Plasma Physics Reports, Vol. 29, No. 8, 2003, pp. 635–641. Translated from Fizika Plazmy, Vol. 29, No. 8, 2003, pp. 691–697.

TOKAMAKS

Effect of Density Variations along Ion Drift Trajectories on the Poloidal and Toroidal Rotation Velocities of a Collisionless Tokamak Plasma

A. N. Romannikov

Troitsk Institute for Innovation and Fusion Research, State Scientific Center of the Russian Federation, Troitsk, Moscow oblast, 142092 Russia

Received December 26, 2002

Abstract—The effect of plasma density variations along ion drift trajectories on the ion velocity distribution function at a given point on a tokamak magnetic surface is studied. The observed distortion of the distribution function can be interpreted as a poloidal (or toroidal) plasma rotation that is additional to the neoclassical rotation. Due to this additional rotation, the velocity of the toroidal plasma rotation is different on the low- and high-field sides of the same magnetic surface. In the case of large ion density gradients, the poloidal rotation velocity on the same magnetic surface can have different signs at different poloidal angles. © *2003 MAIK "Nauka/Interperiodica".*

1. INTRODUCTION

Poloidal and toroidal plasma flows have been studied theoretically since the late 1960s (among the first studies on this problem were the papers by Rosenbluth *et al.* [1] and Stix [2]). However, some problems concerning the difference between the calculated and measured plasma rotation velocities in certain tokamak regimes still remain unresolved (see, e.g., [3]). First of all, this concerns the poloidal rotation velocity. Calculations of the poloidal rotation velocity are based on the expression for the plasma flow velocity at a certain point on a magnetic surface:

$$V_p \cong \left(\frac{B_p}{B_\parallel}\right)V_\parallel + V_\perp, \tag{1}$$

where $V_\perp = -c\frac{E_r}{B_\parallel} + \frac{c}{n_i Z_i e_i B_\parallel}\frac{\partial p_i}{\partial r}$ is the sum of the drift velocity of ions with the charge $Z_i e$ in the radial electric field E_r and the drift velocity caused by the radial gradient of the ion pressure p_i. Here, $B_\parallel$ and B_p are the total magnetic field and its poloidal component at the point under consideration, $V_\parallel$ is the ion velocity along the magnetic field, c is the speed of light, and n_i is the ion density. The calculation of $V_\parallel$ in Eq. (1) is of crucial importance. In neoclassical theory, the approach proposed by Hirshman and Sigmar [4] and based on the moment equations averaged over a magnetic surface is usually used for this purpose.

The plasma rotation velocity was calculated by many authors. Here, we can mention the recent paper [5], in which the plasma poloidal and toroidal rotation velocities were obtained (by the author's assertion, from the first principles) for NBI heating regimes. Unfortunately, in that paper, as well as in most other papers, the expressions are presented in an implicit form. Therefore, the results of [6] (and sometimes [7]) are commonly used for comparison with experiments.

The results of calculations can be summarized as follows:

(i) The rotation velocities of the main plasma component differ markedly from the rotation velocities of the impurity ions.

(ii) The poloidal rotation velocity of the main ions is equal to $V_p \cong \frac{c}{Z_i e B_\parallel} K \frac{\partial T_i}{\partial r}$, where K is a numerical factor dependent on the ion collisional regime (note that the K value used in [6] differs from that used in [7]) and T_i is the ion temperature. The toroidal rotation velocity of the main ions is equal to

$$V_t \cong c\frac{E_r}{B_p} + f\left(\frac{\partial n_i}{\partial r}, \frac{\partial T_i}{\partial r}\right), \tag{2}$$

where f is the linear function of the ion density and temperature gradients. In experiments, the term proportional to E_r usually makes the main contribution.

(iii) The toroidal rotation velocity of impurity ions is equal to $V_t^I \cong c\frac{E_r}{B_p}$, and their poloidal rotation velocity is equal to the poloidal velocity V_p of the main ions (with the other factor K) plus an expression propor-

1063-780X/03/2908-0635$24.00

tional to the difference $\frac{Z_i}{Z_I}\left(\frac{1}{n_I}\frac{\partial n_I}{\partial r}\right) - \left(\frac{1}{n_i}\frac{\partial n_i}{\partial r}\right)$, where I stands for impurities and i stands for the main ions. The temperature of the main ions and impurities is assumed to be the same.

(iv) The toroidal ion-flow velocity is the same at any point on a given magnetic surface. In the general case, however, the main and impurity ions have different velocities.

Since the rotation velocities (first of all, the poloidal rotation velocity) measured in some tokamak regimes (see, e.g., [3]) differed markedly from those calculated in [6], new approaches extending the standard theory were proposed. Among those are the following:

(i) in [3], an additional viscosity due to the charge exchange of the main ions with residual neutrals in a tokamak plasma [8] was introduced to achieve agreement with experiments;

(ii) in [9], in the case of large gradients of E_r, the so-called squeezing effect on the ion trajectory was taken into account, which resulted in an additional term proportional to the ion density gradient in the expression for the poloidal rotation velocity; and

(iii) anomalous viscosities were introduced into the standard theory [10].

The main experimental method for measuring the plasma rotation velocity is charge-exchange recombination spectroscopy (CXRS) [11]. This method is based on measurements of the Doppler shift of the impurity spectral lines emitted in the course of a charge-exchange reaction, e.g., the reaction

$$C^{+6} + H^0 \longrightarrow C^{+5}* + H^{+1} \longrightarrow C^{+5} + H^{+1} + h\nu. \quad (3)$$

The source of hydrogen in this reaction is a probing or heating beam (in the case of active CXRS) or the neutral component of the working gas (in the case of passive CXRS). The CXRS diagnostics enables measurements of the rotation velocity of the main plasma component only for plasmas that do not consist of hydrogen isotopes, e.g., a helium plasma [3]. That is why this method is of limited applicability. New approaches have recently been proposed and used for comparative experiments on studying the rotation of impurities and the main hydrogen or deuterium components. First of all, we should mention the first measurements of the poloidal rotation velocity of deuterium in the T-11M tokamak [12] and the toroidal rotation of deuterium in the TORE-SUPRA tokamak [13, 14], in which a charge-exchange neutral particle analyzer was used, and the measurements of the toroidal rotation velocity of the main ions by the Doppler shift at the frequencies of the radially localized MHD perturbations [15].

The most comprehensive study of poloidal rotation in a small device by the passive CXRS method was carried out in [16] with the purpose of verifying the relations of [6, 7]. The calculated rotation velocities coincided (to within the measurement error) with the experimental results (possibly, with the exception of a collisionless regime). Unfortunately, the measurement accuracy in terms of the dependence on certain addends in the expression for V_p^I was rather low. This is related to the fact that, for the impurities used in those experiments, the density derivative along the line of sight could change its sign twice.

The most pronounced discrepancy between the calculated poloidal rotation velocity and that measured by the active CXRS method was observed in improved confinement regimes (see, e.g., [17, 18]). To achieve agreement between experiment and theory in these regimes, attention has recently been paid to the specific features of the active CXRS method [19–21]. The point is that the excited impurity ions emit radiation a finite time after the charge-exchange event. As a result, the velocity measured by the Doppler shift differs from the actual velocity of the ion flow before charge exchange. For helium, this effect results in an additional term proportional to E_r, which must be taken into consideration in measurements [21]. By properly correcting the experimental data, the measured velocity can approach the value predicted by the theory. In this respect, the results of [22] are rather representative. That paper presents the results of experimental studies of the poloidal rotation velocity of the C^{+5} impurity ions by the active CXRS method in the ASDEX Upgrade device. Discharges with an internal transport barrier were studied. The diagnostic facility allowed the measurements of the shift of the C^{+5} lines on the low-field side of the plasma column (from the central region to the plasma edge). The poloidal rotation velocities of the impurity ions deduced from the measured shifts of the spectral lines differed markedly from the calculated neoclassical values. After a correction was made for the dependence of the charge-exchange cross section on the relative velocity of the C^{+5} ions and the neutral beam particles at the point of their interaction, as well as for the time delay between the charge-exchange event and the emission from the excited state of the C^{+5} impurity ion, the recalculated values of the poloidal rotation velocity became close to the neoclassical values (except for a narrow region near the internal transport barrier [22, Fig. 8]). The difference between the corrected and uncorrected values was nearly 10 km/s. Unfortunately, in order to correctly bring the measured Doppler shift to the actual shift of the ion distribution function, it is necessary to know the actual lifetime of the excited state of the impurity ion in a plasma. Step transitions change the effective transition probability. These processes were disregarded in [22], which increased the measurement error.

Thus, it may be concluded that the problem of the difference between the calculated and measured velocities of the poloidal and toroidal plasma rotation still remains unresolved.

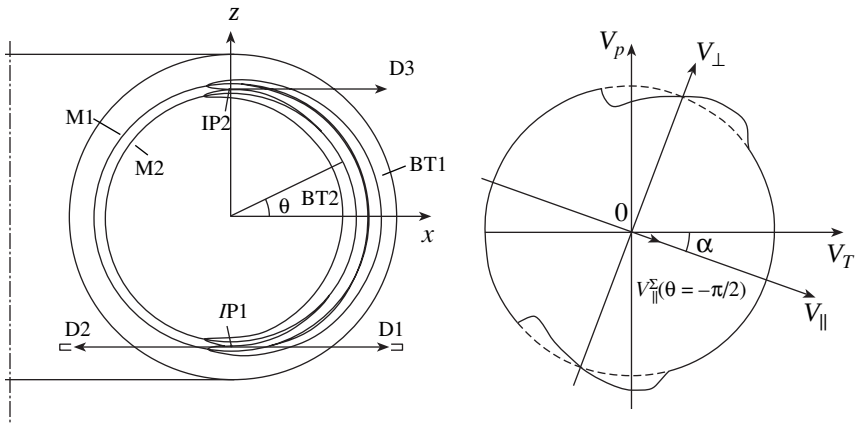

Fig. 1. (a) Layout of the measurements of the IVDF at a given point *I*P1(*I*P2) lying on a magnetic surface of a tokamak by detectors D1 and D2 (detector D3 is equivalent to detector D2): BT1 is the drift banana trajectory that belongs to magnetic surface M1, BT2 is the drift banana trajectory that belongs to magnetic surface M2, and θ is the poloidal angle. (b) Contour line of the IVDF at point *I*P1: V_p and V_t are the poloidal and toroidal velocities, and $V_\parallel$ and $V_\perp$ are the velocity components directed along and across the magnetic field in the plane (V_p, V_t $\alpha = \arctan(B_p/B_t)$. $V_\parallel^\Sigma(\theta = -\pi/2)$ is the averaged shift of the IVDF at the measurement point. The contour line of the Maxwellian distribution function is shown by the dashed line.

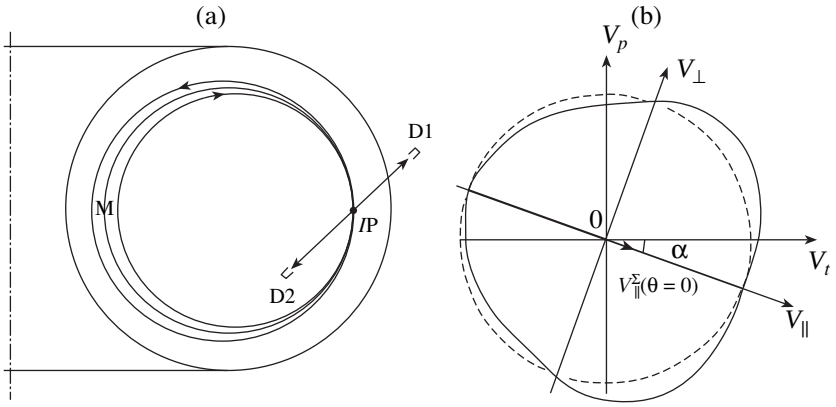

Fig. 2. (a) Layout of the measurements of the IVDF at point *I*P lying on the low-field side of magnetic surface M by detectors D1 and D2. (b) Contour line of the IVDF at point *I*P: $V_\parallel^\Sigma(\theta = 0)$ is the averaged shift of the IVDF at the measurement point. The other notation is the same in Fig. 1.

In this paper, a new and rather simple (from the experimental standpoint) approach is proposed in which an additional term proportional to $\frac{\partial n_{i,I}}{\partial r}$ is introduced in the expression for the flow velocity [23]. This approach is based on a method developed by Gott and Yurchenko [24, 25]. This method allows one to take into account the effect of variations in the plasma parameters along the ion drift trajectories on the poloidal and toroidal rotation velocities in a collisionless tokamak plasma. There is a simple procedure (described below) of taking into account this effect at any point on a given magnetic surface. This effect plays an important role when comparing the experimental data with the calculated poloidal and toroidal rotation velocities. We draw the reader's attention to a certain inconsistency between the traditional experimental and theoretical approaches to studying plasma flows. The plasma rotation velocity is actually measured in some local region on a magnetic surface; at the same time, calculations use the moment equations averaged over the magnetic surface. For weakly collisional plasmas, this inconsistency can become substantial. Here, it is appropriate to consider the following example. It is well known (see, e.g., [26]) that neoclassical diffusion in a collisional tokamak plasma resembles a peculiar

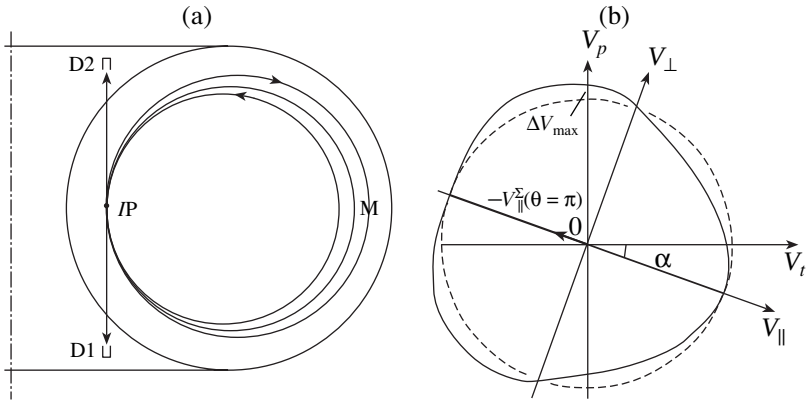

Fig. 3. (a) Layout of the measurements of the IVDF at point *I*P lying on the high-field side of magnetic surface M by detectors D1 and D2. (b) Contour line of the IVDF at point *I*P: $V_\parallel^\Sigma(\theta = \pi)$ is the averaged shift of the IVDF at the measurement point and ΔV_{max} is the maximum shift with respect to the Maxwellian distribution function. The other notation is the same as in Fig. 1.

kind of convection. The plasma is outflowing on the low-field side and inflowing on the high-field side, the plasma flow being closed along the magnetic field lines. Let us imagine that we can measure the velocity of the radial neoclassical diffusion flow. If we measure the flow velocity component normal to the magnetic surface at some points of this surface, we will arrive at a surprising conclusion that the plasma merely moves with a certain velocity toward the region with a weak magnetic field. No diffusion will be observed. The velocity of this flow will be much higher than the expected velocity of the neoclassical diffusion flow averaged over the magnetic surface.

2. ESTIMATE OF THE DISTORTION OF THE ION DISTRIBUTION FUNCTION BY PLASMA DENSITY VARIATIONS ALONG THE ION DRIFT TRAJECTORIES

In order to estimate the distortion of the ion velocity distribution function (IVDF) due to plasma density variations along the ion drift trajectories, we consider the following simple model:

(i) Magnetic surfaces in the poloidal cross section of the tokamak are nested circles.

(ii) The radius r of the magnetic surface on which we measure the poloidal and toroidal rotation velocities of the main plasma ions is much smaller than the major plasma radius R.

(iii) In the plasma regions under consideration, there is only the ion density gradient and $\frac{dT_i}{dr} = 0$.

(iv) The plasma current density is assumed to be uniform.

(v) We consider an ideal situation in which the IVDF on the magnetic surfaces is Maxwellian at the initial time. The poloidal and toroidal rotation velocities are chosen based on the standard neoclassical approach. In view of the assumption that $\frac{dT_i}{dr} = 0$, the poloidal velocity is zero. The toroidal rotation velocity is also set equal to zero by an appropriate choice of E_r. In addition, the field E_r is assumed to be small, so that it does not affect the ion drift trajectories.

(vi) After the ions perform several excursions along the drift trajectories, we begin to measure the IVDF. The measurements are performed using two ideal flow spectral detectors (Figs. 1–3), which provide information about the ion distribution along a given direction. Only the ions with a given velocity direction are detected. By varying the line of sight of the detector, it is possible to measure the IVDF in the entire velocity space.

Let us consider the procedure of the measurements of the IVDF at the point *I*P1 on a chosen magnetic surface as is shown in Fig. 1a. The measurements by detector D2 are equivalent to the measurements by detector D3. It was shown in [23] that, at the instant of measurement, the ion velocities must satisfy the relationships $V_\parallel/V_\perp = B_p/B_t$ for detector D1 and $V_\parallel/V_\perp = -B_p/B_t$ for detector D2, where $V_\parallel$ and $V_\perp$ are the longitudinal and transverse components of the ion velocity with respect to the total magnetic field and B_t is the toroidal component of the tokamak magnetic field. Viewed from above, the plasma current and the toroidal magnetic field are directed counterclockwise. The poloidal direction is chosen as in Fig. 1b. The ions that can be detected by detectors D1 and D2 move along banana drift trajectories BT1 and BT2.

According to [24], after several excursions along a banana trajectory, the IVDF is averaged over the trajectory and, with an accuracy that is satisfactory for our

consideration, on this trajectory we will have a Maxwellian distribution function F_M corresponding to the plasma parameters at the reflection points. As a result, the ions with the parameters on magnetic surface M2 (where the density is higher) will fall into detector D2, whereas detector D1 will detect the ions arriving from magnetic surface M1 (where the density is lower).

It can be shown (see [23]) that the IVDF along a given (in the case at hand, poloidal) direction will be shifted with respect to the Maxwellian distribution function F_M at the measurement point by a value equal to the poloidal rotation velocity

$$V_p \approx \frac{c}{ZeB_t}\frac{T_i}{n_i}\frac{dn_i}{dr}. \quad (4)$$

When deriving this formula, we assumed that, when moving along the drift trajectory, the ions passing through point *I*P1 that lies on a magnetic surface with a radius r are shifted from a certain initial position characterized by the radius r_0, velocities $V_{\|,0}$ and $V_{\perp,0}$, and the poloidal angle $\vartheta = 0$ (which is counted from the point situated on the low-field side) by a distance of $\Delta r = r - r_0 \ll r$. Under these assumptions, we can find the shift of the trajectory at any point (see, e.g., [9]):

$$\Delta r = \frac{Mc}{eB_p}\left[V_\| - V_{\|,0} - V_\|\frac{r}{R}(1-\cos\vartheta)\right], \quad (5)$$

where M is the ion mass. From this relationship and the conservation equations for energy and magnetic moment, it follows that, for the measurement direction shown in Fig. 1a, point *I*P1 is shifted from magnetic surfaces M1 and M2 by $\Delta r \approx \frac{Mc}{eB_t}V_\perp$. Expanding the IVDF into a series with allowance for this shift, we find that, for the given direction, the IVDF at the observation point takes the form $F_{\rm obs} \approx F_{M,\,\rm obs}\exp\left(\frac{MV_\perp}{T_i}\left[\frac{c}{ZeB_t}\frac{T_i}{n_i}\frac{dn_i}{dr}\right]\right)$. The expression in square brackets is identical to expression (4), which, in the given case, can be interpreted as the poloidal velocity.

Varying the direction of the line of sight at a given point *I*P1 and using the procedure described above, we can find the shift of the IVDF along any direction. This shift is illustrated in Fig. 1b by the shape of a given contour line of the IVDF. The dashed circle corresponds to the Maxwellian distribution function F_M. The IVDF is symmetric about the $V_\|$ axis. The maximum shift corresponds to the direction for which $V_\|/V_\perp \approx \sqrt{\frac{r}{R}}$ for detector D1 and $V_\|/V_\perp \approx -\sqrt{\frac{r}{R}}$ for detector D2, which corresponds to banana trajectories with reflection points lying near the region of barely circulating ions. In our approximation, this shift will correspond to the ion flow velocity $V \approx \frac{c}{ZeB_p}\frac{T_i}{n_i}\frac{dn_i}{dr}\sqrt{\frac{r}{R}}$. It can be seen from Fig. 1b that, in this case, the total shift of the IVDF is directed along $V_\|$ (along the magnetic field line). The value of this shift can be estimated as

$$V_\|^\Sigma\left(\vartheta = -\frac{\pi}{2}\right) \approx \frac{c}{ZeB_p}\frac{T_i}{n_i}\frac{dn_i}{dr}\frac{r}{R}. \quad (6)$$

Thus, the IVDF is shifted, and this shift can be measured in the poloidal and toroidal directions, e.g., by the CXRS method.

Figure 2 shows the layout of the measurements of the IVDF at point *I*P lying on the low-field side. In this case, the maximum shift is greater than for the case presented in Fig. 1. Moreover, the shift of the IVDF is maximum at this point. The value of this shift is determined by barely trapped and barely circulating ions and is equal to $V_2 \approx \frac{c}{ZeB_p}\frac{T_i}{n_i}\frac{dn_i}{dr}\sqrt{2\frac{r}{R}}$. After averaging, we find that the total shift of the IVDF along $V_\|$ is equal to

$$V_\|^\Sigma(\vartheta = 0) \approx \frac{c}{ZeB_p}\frac{T_i}{n_i}\frac{dn_i}{dr}\sqrt{2\frac{r}{R}}. \quad (7)$$

The observation points in Figs. 1 and 2 are close to regions actually used in experiments on the measurements of the poloidal and toroidal plasma rotation. Ion collisions lead to the establishment of a Maxwellian distribution function shifted along $V_\|$ by the velocities defined by expressions (6) and (7). This shifted IVDF is nonequilibrium from the neoclassical standpoint; however, in a weakly collisional plasma, the additional poloidal and toroidal rotation velocities will be substantial for times shorter than the collision time. For large ion density gradients, this term can become dominant in the measurements of the poloidal plasma rotation.

Applying this approach to studies of the IVDF at points lying on the high-field side (as is shown in Fig. 3) seems to be most promising. In this case, we have $V_\|^\Sigma(\vartheta = \pi) \approx -V_\|^\Sigma(\vartheta = 0)$.

It can be shown [23] that, using a Maxwellian distribution function F_M initially shifted in the toroidal and poloidal directions (e.g., by the values corresponding to neoclassical velocities), we again arrive at the above estimates, provided that there are no large gradients of the initial velocities. Introducing the ion temperature gradient complicates the consideration; however, on the whole, this gradient can only increase the absolute value of the additional shift of the IVDF. For thermal ions, this additional term, which is proportional to the ion temperature gradient, is nearly zero [23]. We performed numerical calculations of the drift trajectories for intermediate plasma regions of the TORE-SUPRA tokamak (the results of those calculations were par-

tially used in [14], in which the layout of the measurements was similar to that shown in Fig. 1a). After averaging the IVDF over the trajectories, the shift of the IVDF caused by density variations along the ion trajectories coincided with the value calculated by formula (4) to within 10%.

3. CONCLUSIONS

In this paper, we have presented a new approach that is based on the results of [24] and enables one to calculate the distortion of the originally Maxwellian ion distribution function at a given point on a magnetic surface due to density variations along the ion drift trajectories in a collisionless tokamak plasma. In experiments, this distortion can be interpreted as an ion flow along the magnetic field line. The velocity of this flow, which is proportional to the ion density gradient, is added to the velocity predicted by the standard neoclassical theory. The specific features of this approach can be outlined as follows:

(i) According to this approach, the toroidal velocities of the plasma ions at the same magnetic surface on the high- and low-field sides of the plasma column differ by the value $\approx 2\frac{c}{ZeB_p}\frac{T_i}{n_i}\frac{dn_i}{dr}\sqrt{2\frac{r}{R}}$. This difference in the behavior of the toroidal rotation velocity on a magnetic surface from the neoclassical results can be used to experimentally verify our approach.

(ii) The ion poloidal rotation velocity acquires a term proportional to the ion density gradient. Its value varies from $+\frac{c}{ZeB_t}\frac{T_i}{n_i}\frac{dn_i}{dr}\sqrt{2\frac{r}{R}}$ on the low-field side to $-\frac{c}{ZeB_t}\frac{T_i}{n_i}\frac{dn_i}{dr}\sqrt{2\frac{r}{R}}$ on the high-field side. In the case of large ion density gradients, this term can become decisive, in which case the poloidal rotation velocity can have different signs on the same magnetic surface. This difference of the poloidal rotation velocity from the neoclassical velocity can also be used to experimentally verify the approach proposed. Moreover, the additional term, which is omitted in the existing approaches, can lead to a better agreement between the results of experimental and theoretical studies of poloidal plasma flows.

(iii) The additional flow related to $V_\parallel^\Sigma(\vartheta)$ almost completely vanishes after averaging over a magnetic surface.

(iv) Since the velocity $V_\parallel^\Sigma(\vartheta)$ is directed along the magnetic field, this flow does not change the radial electric field E_r in a plasma.

(v) The expression for $V_\parallel^\Sigma(\vartheta)$ is independent of the ion mass. This allows one to extend this approach to the electrons (properly taking into account the sign of the charge).

(vi) The existence of an additional flow related to $V_\parallel^\Sigma(\vartheta)$ results in the change of the poloidal electric field and, as a consequence, the modification of the transport processes in a plasma.

The issues related to collisions and the problem of establishing equilibrium flows on a magnetic surface are beyond the scope of this paper. However, in a weakly collisional plasma, the results obtained can be used as limiting estimates.

It should be noted that most of the existing experiments on studying poloidal and toroidal plasma flows are carried out on the low-field side of the plasma column. The further development of the approach proposed, which has revealed the different behavior of the ions at different points on the same magnetic surface, calls for measurements on the high-field side of the plasma column.

ACKNOWLEDGMENTS

I am grateful to Yu.V. Petrov for providing me with the results of numerical calculations of ion drift trajectories.

REFERENCES

1. M. Rosenbluth, P. Rutherford, J. Taylor, *et al.*, Plasma Phys. Controlled Nucl. Fusion Res. **1**, 495 (1971).
2. T. Stix, Phys. Fluids **16**, 1260 (1973).
3. J. Kim, K. Burrell, P. Gohil, *et al.*, Phys. Rev. Lett. **72**, 2199 (1994).
4. S. Hirshman and D. Sigmar, Nucl. Fusion **21**, 1079 (1981).
5. W. Stacey, Phys. Plasmas **8**, 158 (2001).
6. Y. Kim, P. Diamond, and R. J. Groebner, Phys. Fluids B **3**, 2050 (1991).
7. R. Hazeltine, Phys. Fluids **17**, 961 (1974).
8. P. Monier-Garbet, K. Burrell, F. Hinton, *et al.*, Nucl. Fusion **37**, 403 (1997).
9. F. Hinton and Y.-B. Kim, Phys. Plasmas **2**, 159 (1995).
10. V. Rozhansky and M. Tendler, Phys. Fluids B **4**, 1877 (1992).
11. R. Fonck, R. Goldston, R. Kaita, and D. Post, Appl. Phys. Lett. **42**, 239 (1983).
12. I. Kovan, A. Romannikov, and Yu. Petrov, in *Proceedings of the 24th EPS Conference on Controlled Fusion and Plasma Physics, Berschtesgaden, 1997*; ECA **21A**, 409 (1997).
13. A. Romannikov, C. Bourdelle, J. Bucalossi, *et al.*, Nucl. Fusion **40**, 319 (2000).
14. A. Romannikov, Yu. Petrov, R. Platz, *et al.*, Fiz. Plazmy **28**, 110 (2002) [Plasma Phys. Rep. **28**, 94 (2002)].
15. D. Testa, C. Giroud, A. Fasoli, *et al.*, Phys. Plasmas **9**, 243 (2002).
16. A. Meigs and W. Rowan, Phys. Plasmas **1**, 960 (1994).

17. R. Bell, F. Levinton, S. Batha, *et al.*, Phys. Rev. Lett. **81**, 1429 (1998).
18. K. Ida, Plasma Phys. Controlled Fusion **40**, 1429 (1998).
19. M. Zarnstorff, Princeton Plasma Physics Laboratory, Private Communication (1998).
20. D. Ernst, R. Bell, M. Bell, *et al.*, Phys. Plasmas **7**, 615 (2000).
21. A. Romannikov and A. Chernobaĭ, Fiz. Plazmy **27**, 1050 (2001) [Plasma Phys. Rep. **27**, 994 (2001)].
22. H. Meister, A. Kallenbach, A. Peeters, *et al.*, Nucl. Fusion **41**, 1633 (2001).
23. A. N. Romannikov, in *Proceedings of the 29th EPS Conference on Controlled Fusion and Plasma Physics, Montreux, 2002*, paper P2.119.
24. Yu. Gott and É. Yurchenko, Dokl. Akad. Nauk SSSR **260**, 1352 (1981) [Sov. Phys. Dokl. **26**, 995 (1981)].
25. Yu. Gott and É. Yurchenko, Fiz. Plazmy **13**, 131 (1987) [Sov. J. Plasma Phys. **13**, 71 (1987)].
26. L. Artsimovich and R. Sagdeev, *Plasma Physics for Physicists* (Atomizdat, Moscow, 1979).

Translated by N.F. Larionova

Plasma Physics Reports, Vol. 29, No. 8, 2003, pp. 642–656. Translated from Fizika Plazmy, Vol. 29, No. 8, 2003, pp. 698–713.

DUSTY PLASMA

Experimental Studies of the Dynamics of Dust Grains in Gas-Discharge Plasmas

O. S. Vaulina*, O. F. Petrov*, V. E. Fortov*, A. V. Chernyshev*, A. V. Gavrikov*, I. A. Shakhova*, and Yu. P. Semenov**

**Institute for High Energy Densities, Russian Academy of Sciences, Izhorskaya ul. 13/19, Moscow, 127412 Russia*
***Korolev Space & Rocket Corporation Energiya, Korolev, Moscow oblast, 141070 Russia*

Received December 5, 2002; in final form, February 11, 2003

Abstract—Results of the experimental studies of the dynamics of dust grains in the plasmas of an rf capacitive discharge and a dc glow discharge are presented. The dusty plasma of a dc glow discharge was investigated in both ground-based experiments and experiments carried out under microgravity conditions (on board the *Mir* space station). The pair correlation function, temperature, and diffusion coefficient of dust grains are measured in a wide range of the dusty-plasma parameters. Dimensionless parameters responsible for the microscopic transport of dust-grains in a gas-discharge plasma are determined. A nonintrusive diagnostic technique for determining the dust-grain charges and screening lengths under the assumption of screened interaction between the grains is proposed. This technique is used to estimate the surface potential of dust grains of different size in a gas-discharge plasma. © *2003 MAIK "Nauka/Interperiodica"*.

1. INTRODUCTION

Dusty plasma is an ionized gas containing micron-size charged condensed grains (dust). The charging of nonemitting dust grains in gas discharges proceeds via the absorption of electrons and ions from the surrounding plasma. Due to the high mobility of electrons, micron-size grains acquire a significant negative charge (on the order of 10^3–10^5 elementary charges) and can interact electrostatically with each other. The dissipation of the dust-grain kinetic energy in a weakly ionized gas-discharge plasma is mainly related to the grain collisions with the neutral particles of the buffer gas. The interaction between dust grains in combination with dissipative processes in a dusty plasma can lead to the formation of steady-state dusty structures (similar to liquids or solids) or to the establishment complex vibrational (chaotic) regimes [1–10]. Under ordinary laboratory conditions, the dusty structures are suspended in the Earth's gravity field by the electric field of striations (in a dc glow discharge) or the electrode sheath (in an rf capacitive discharge) [1–3]; in this case, the gravity field imposes certain limitations on the experimental results.

Experimental studies of dusty plasmas under microgravity conditions have recently attracted great attention [6–11]. One of the main advantages of these experiments is the possibility of performing investigations over a wide range of the dusty-plasma parameters, which is not limited by the conditions ensuring grain levitation in the gravity field. The experiments carried out under microgravity conditions allow one to investigate a wide scope of phenomena (such as the charging of atmospheric aerosols, ambipolar diffusion, the dynamics of massive dust grains with a size larger than 100 μm, and the opposite-sign charging of the dust grains) that cannot be studied in ground-based experiments [6–8, 10, 11].

Dusty plasma is a good experimental model for studying various transport processes in systems of interacting grains. These processes are of great interest for both the physics of nonideal plasma and other branches of natural science, such as the physics of condensed matter, chemistry, atmosphere physics, and astronomy. Due to their macroscopic dimensions, dust grains in a laboratory plasma can be recorded with a video camera, which greatly simplifies the use of direct nonintrusive diagnostics.

The dust-grain charge is an important parameter, which significantly affects various transport processes in a dusty plasma, such as diffusion, wave propagation, and instabilities. In the literature, much attention is paid to the methods for measuring dust-grain charges. Many of these methods are based on the measurements of the dynamic response of dust grains to different external perturbations [12–18]. These principally new methods are specific for the diagnostics of dusty plasma. The main drawbacks of these methods are (i) the necessity of having a priori information about the electric fields and external forces acting on the dust grains and (ii) the presence of external perturbations that can significantly change the parameters of dust grains and the surrounding plasma. The dust-grain charge can also be determined without perturbing the plasma–dust system, e.g., from the force balance equation for a nonmoving grain in an electric field and the Earth's gravity field [19, 20]. Passive diagnostics of the dust-grain parameters that do

1063-780X/03/2908-0642$24.00 © 2003 MAIK "Nauka/Interperiodica"

not introduce any perturbations in the system under study can be based on the measurements of transport characteristics of a dusty medium. For example, measurements of the pair correlation function $g(l)$, velocity distribution, and displacements of dust grains can provide information about the kinetic temperature T_d and diffusion coefficient D of the dust grains. Under additional assumptions on the interaction between grains, these measurements allow one to estimate the potential of pair interaction between the grains [21].

One of the nonintrusive methods for determining the dust-grain parameters (the charge and the screening length) under the assumption of screened interaction between the grains is described in this paper. The method is based on the results of numerical simulations of the grain dynamics in three-dimensional systems with screened interaction (Yukawa systems). The paper presents the results of measurements of the spatial correlation, temperature, and diffusion coefficient of dust grains for different plasma parameters in an rf capacitive discharge and a dc glow discharge. The dusty plasma of a dc glow discharge was investigated in both ground-based experiments and experiments carried out under microgravity conditions (on board the *Mir* space station).

2. DUST-GRAIN TRANSPORT CHARACTERISTICS IN A DUSTY PLASMA

2.1. Dust-Grain Charge

In gas-discharge plasmas, the emission processes are usually of minor importance and the dust-grain charge is negative. The orbit motion limited (OML) approximation gives the following estimate for the surface potential of an isolated dust-grain: $\phi_s = -eZ_d/a_d \equiv -zT_e/e$, where Z_d is the equilibrium (time-averaged) charge of a dust-grain; T_e is the electron temperature in eV; and the parameter z is determined by the buffer-gas ions and, for noble gases (such as argon or neon), is $z \approx$ 2–4 under typical gas-discharge conditions [22–24]. Numerical simulations show that, for a dust cloud with the dust-grain number density n_d such that $\chi = n_d Z_d/(zn_e) < 1$ (where n_e is the electron density), the parameter z changes slightly and is close to $z \approx 3$ for an isolated grain.

For large grains with a radius of $a_d > 10$–20 μm and typical buffer-gas pressures of $P \approx 1$ torr, the mean free path of ions (Ar, Ne) at room temperature is on the order of or less than a_d [25]. This results in a decrease in the ion flux I_i onto the dust-grain surface and, consequently, an increase in ϕ_s and z, as was observed in experiments. Thus, in [8], it was shown that, in neon at a pressure of $P \approx 0.5$–1.5 torr, the increase in the grain radius from 2 to 7 μm leads to the decrease in the grain surface potential from ~9 to ~30 V, which corresponds to the increase in z from ~2 to ~(4–10) at electron temperatures of $T_e = 3$–7 eV, which are typical of striations in a glow discharge in neon [26, 27].

In a dense dust cloud with $\chi > 1$, the parameters z and ϕ_s are somewhat lower [23, 24]. In some cases, this decrease can be balanced by an increase in the electron temperature under the conditions of equilibrium ionization in the gas discharge [11]. Since the discharges in noble gases are generally dominated by the processes of ambipolar diffusion and plasma recombination on the gas-discharge tube wall, the influence of dust-grains on the ionization processes is only significant when the rate ν_{ed} of electron losses on the dust-grains is comparable to or much larger than the diffusion loss rate ν_{ab} [11, 25],

$$\nu_{ab} \cong D_a/\Lambda_d^2, \tag{1}$$

where $D_a \cong \mu_i T_e/e$ is the ambipolar diffusion coefficient at $T_e \gg T_i$, μ_i is the ion mobility ($P\mu_i \approx 3200$ torr cm^2/(V s) for single-charged neon ions, and $P\mu_i \approx 1250$ torr cm^2/(V s) for argon [25]), and Λ_d is a characteristic scale length. For a cylinder with radius R and length L, we have $\Lambda_d^2 \approx [(2.4/R)^2 + (\pi/L)^2]^{-1}$ [25]. The rate ν_{ed} of electron losses on the dust cloud grains can be estimated as

$$\nu_{ed} \cong \pi a_d^2 n_d \nu_{Te} \exp(-z). \tag{2}$$

Hence, under the conditions of a stratified glow discharge in neon ($P \approx 1$ torr and $T_e \approx 5$–10 eV) and for $\Lambda_d \approx 1$ cm and $z = 2$–4, we have that the rate ν_{ed} of electron losses on the dust cloud grains is comparable with or larger than the diffusion loss rate ν_{ab} ($\nu_{ed} > \nu_{ab}$) if n_d [cm^{-3}] a_d^2 [μm^2] $> 3 \times 10^5$. For grains with a radius $a_d \approx$ 2 μm, this corresponds to a dust density of $n_d > 7.5 \times 10^4$ cm^{-3}, whereas for large grains with $a_d \approx 60$ μm, we have $n_d > 10^2$ cm^{-3}. Thus, it is reasonable to assume that, at a typical mean intergrain spacing of $l_d \equiv n_d^{-1/3} =$ 200–1000 μm, the discharge operation can significantly be affected by plasma recombination on the dust-grains.

2.2. Intergrain Interaction Potential

It is generally accepted that dust-grains in plasma interact with each other via the screened Coulomb potential (a Yukawa-type potential)

$$\phi = eZ_d \exp(-l/\lambda)/l, \tag{3}$$

where l is the distance from a grain. This assumption agrees with the results of measurements of the radial (perpendicular to the Earth's gravity force) interaction force between two dust-grains [13, 28]. However, there are at least two important reasons why the shape of the potential that determines the intergrain interaction energy $\sim eZ_d\phi$ can significantly differ from that given by formula (3) [29–34]. One of these reasons is related to the attraction force caused by the polarization of the

ambient plasma or by the shading of the plasma flow onto one grain by another grain [29–32]. The problem of intergrain attraction has been investigated in a number of theoretical and experimental studies. However, credible experimental confirmation of the existence of such forces is still absent. The second reason is that the floating grain potential ϕ_s, which is on the order of the electron thermal energy, greatly exceeds the ion energy and, hence, the grain screening is strongly nonlinear. The asymptotic behavior of the potential ϕ at large distances from the grain is not described by formula (3) and decreases with distance according to a power law: $\phi \approx eZ_d a_d/l^2$ [34]. In [33], the structure of the screening cloud was calculated with allowance for the nonlinearity in Poisson's equation and the non-Maxwellian velocity distribution of the plasma particles. It was shown that, at distances $l < l_D \approx 5$–$7\lambda_i$ from the grain surface, the screening of an isolated grain with the size a_d lying in the range from $2\lambda_i$ to λ_e (where λ_i and λ_e are the ion and electron Debye radii) is determined by λ_e, whereas for grains with the size $a_d \ll \lambda_i$, it is determined by λ_i. At grain sizes satisfying the inequality $a_d > \lambda_e$, the effective screening length λ can be much larger than λ_e. At distances on the order of the mean distance between the grains $l_d = n_d^{-1/3} > l_D$, the presence of a "non-Debye" screening can reduce the effect of the ambient plasma on the interaction between the grains and, as a consequence, increase the repulsion between them.

2.3. Modeling of the Dust-Grain Dynamics in Dusty Plasma

The correct modeling of the dust-grain transport in a dusty plasma calls for applying the molecular dynamics methods based on solving a system of ordinary differential equations with the Langevin force F_{br} that takes into account random impacts of the ambient gas molecules and other stochastic processes, e.g., random fluctuations of the grain charge that result in an increase in the grain kinetic temperature T_d to a value higher than the temperature T_n of the ambient gas [3, 5, 24, 35]. Microscopic processes in an extended homogeneous cloud consisting of N_d interacting dust-grains are described by a set of N_d equations of motion. To model these processes, one should take into account, along with the random forces F_{br} that result in the grain thermal motion, the pair interaction forces F_{int}:

$$m_d \frac{d^2\mathbf{l}_k}{dt^2} = \sum_j F_{\text{int}}(l)|_{\mathbf{l}=|\mathbf{l}_k-\mathbf{l}_j|} \frac{\mathbf{l}_k-\mathbf{l}_j}{|\mathbf{l}_k-\mathbf{l}_j|} - m_d \nu_{\text{fr}} \frac{d\mathbf{l}_k}{dt} + \mathbf{F}_{br}. \quad (4)$$

It is also necessary to impose periodical boundary conditions that allow one to maintain a constant number and mean kinetic energy of the grains. In (4), $F_{\text{int}}(l) = -eZ_d \partial\phi/\partial l$, $\mathbf{l} = |\mathbf{l}_k - \mathbf{l}_j|$ is the intergrain distance, m_d is the grain mass, and ν_{fr} is the friction coefficient of dust-grains (the effective collision frequency of dust-grains with the neutral particles of the ambient gas). For $l_n \ll a_d$, the friction coefficient is equal to [36, 37]

$$\nu_{\text{fr}} \approx 6\pi a_d \eta \{1 - l_n[1 - \exp(-2a_d/l_n)]/2a_d\}/m_d, \quad (5a)$$

where l_n is the mean free path of neutral particles and η is the gas viscosity. For $a_d \ll l_n$, the friction coefficient can be obtained using the free molecule approximation [34]:

$$\nu_{\text{fr}}\ [\text{s}^{-1}] \approx C_n P\ [\text{Pa}]/(a_d\ [\mu\text{m}]\ \rho_p\ [\text{g/cm}^3]), \quad (5b)$$

where ρ_d is the mass density of the grain substance and the coefficient C_n depends on the sort of gas used. For argon at room temperature, we have l_n [μm] ≈ 6200/P [Pa] and $C_n \approx 8.6$ and, for neon, l_n [μm] ≈ 9400/P [Pa] and $C_n \approx 6.3$.

Under conditions of local thermodynamic equilibrium in a dusty system, the average random force is zero ($\langle F_{br} \rangle = 0$) and the autocorrelation function $\langle F_{br}(0)F_{br}(t)\rangle = 6T_d m_d \nu_{\text{fr}} \delta(t)$ [38, 39] describes a δ-correlated Gaussian process. Here, $\delta(t)$ is the δ function and the angular brackets stand for time averaging. Equilibrium random processes in a dust cloud can be modeled using random increments of the grain momentum: $p_{br} = m_d(2T_d \nu_{\text{fr}} \Delta t/m_d)^{1/2}\psi_j$, where p_{br} is the momentum increment per degree of freedom and ψ_j is a certain random quantity distributed by a normal law with an r.m.s. deviation equal to one. To correctly model random forces when numerically solving Eqs. (4), the time step Δt must satisfy the inequality $\Delta t \ll \max\{\nu_{\text{fr}}, \omega^*\}$, where ω^* is the characteristic collision frequency between the charged dust-grains.

For fluid Yukawa systems with the screening parameter $\kappa = l_d/\lambda < 6$–7, the frequency ω^* can be written in the form [40]

$$\omega^* = eZ_d^*(n_d/\pi m_d)^{1/2}, \quad (6)$$

where Z_d^* is the effective grain charge,

$$Z_d^* = Z_d[(1 + \kappa + \kappa^2/2)\exp(-\kappa)]^{1/2}. \quad (7)$$

The relationship between the intergrain interaction and dissipation in a dusty system is determined by the ratio

$$\xi = \omega^*/\nu_{\text{fr}}, \quad (8)$$

which is a scaling parameter for different dynamics processes in dissipative dusty structures, e.g., the thermal diffusion of dust-grains and the formation of vortices [35, 39–41]. For gas-discharge plasmas and a grain radius of $a_d \approx 2$ μm, this ratio varies in the range $\xi \approx$ 0.02–5, as the grain density n_d varies from 10^3 to 10^6 cm^{-3} and the gas pressure P varies from 1 to 0.01 torr.

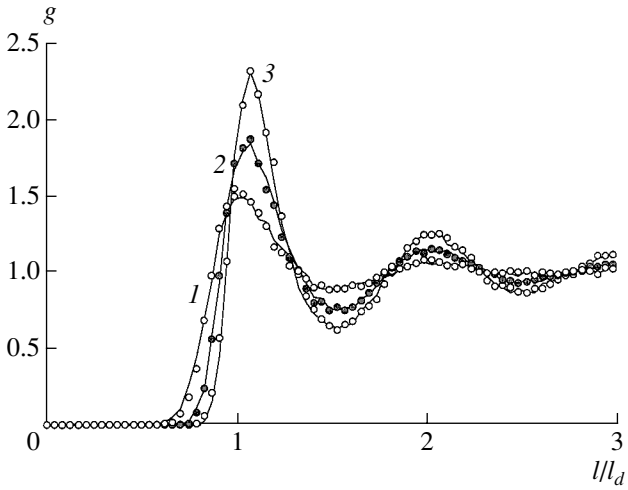

Fig. 1. Pair correlation function $g(l/l_d)$ determined from numerical simulations of Yukawa systems with the screening parameter $\kappa = 4.8$ (symbols) and 2.4 (solid curves) for $\xi = 0.133$ and $\Gamma^* =$ (*1*) 17.5, (*2*) 38, and (*3*) 77.

The grain dynamics in dispersive ($\nu_{fr} = 0$) and dissipative ($\nu_{fr} \neq 0$, $\xi \approx 0.02$–4) extended Yukawa systems was studied in [39–46]. The results of numerical simulations show that the buffer-gas viscosity only slightly affects the degree of correlation of dust-grains in such systems. To analyze the phase state of a three-dimensional system, one can use the effective coupling parameter

$$\Gamma^* = (Z_d^* e)^2/(T_d l_d). \quad (9)$$

The coupling parameter Γ^* determines the formation of both long- and short-range orders in Yukawa systems (from $\Gamma^* < 1$ up to the values corresponding to the crystallization point; see Fig. 1). When Γ^* increases to $\Gamma_m^* = 106$ (for $\kappa < 6$), a body-centered crystal structure is formed. Figure 2 shows the dependences of the first maximum g_{max} of the pair correlation function $g(l)$ and its position ($l = d_{max}$) on the parameter Γ^* for the scaling parameter ξ varying within the range 0.04–1.2. As the parameter Γ^* varies from the value corresponding to the crystallization point ($\Gamma_c^* \cong 102$–104) to that corresponding to the melting point ($\Gamma_m^* \cong 106$–107), the g_{max} value steeply increases from 2.65 to 3.1 and the position of the first maximum of the $g(l)$ function shifts from $l \approx 1.075 l_d$ to the characteristic spacing of a body-centered lattice $d_{max} \cong (3\sqrt{3}/4n_d)^{1/3} \approx 1.092 l_d$ (see Fig. 2b) [42, 43]. In the same range ($\Gamma^* \cong 102$–107), the grain diffusion coefficient obtained in numerical simulations sharply decreases (by more than two orders of magnitude) [39, 42, 43].

The diffusion coefficient of the interacting grains is defined by the formula [39]

$$D(t) = \langle \langle \mathbf{l}(t) - \mathbf{l}(0) \rangle_N^2 \rangle_t / 6t$$
$$\cong \frac{1}{N_d 6 N_t t_{jk}} \sum_{\substack{k=1 \\ (j-k)=\text{const}}}^{N_t} \sum_{i=1}^{N_d} [\Delta \mathbf{l}_i(t_{jk})]^2, \quad (10)$$

where $\Delta_i \mathbf{l}(t_{jk}) = \mathbf{l}(t_j) - \mathbf{l}(t_k)$ is the distance the ith grain shifts during the time $t \equiv t_{jk} = (j-k)\Delta t$ from the position $\mathbf{l}(t_k)$ that it has at the instant t_k; $k = 1, \ldots, N_t$; $j = k, \ldots, (N_t + k)$; Δt is the time resolution (which is determined, e.g., by the frame frequency of a video camera or the time interval between successive outputs of the data on

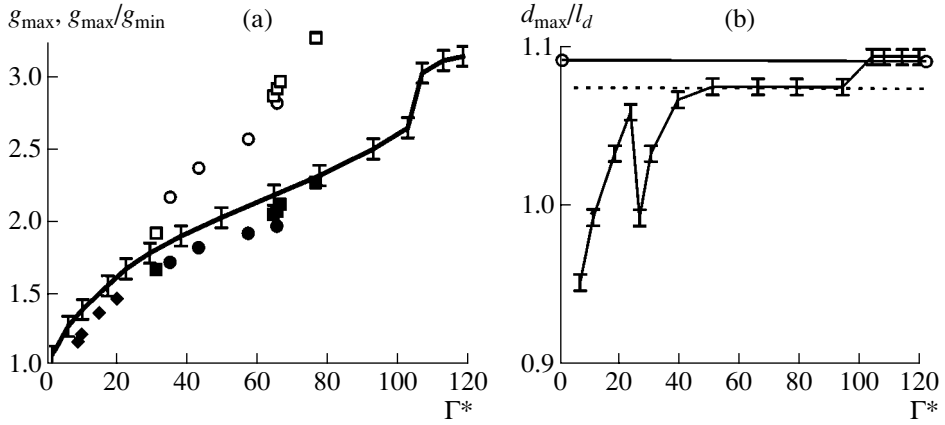

Fig. 2. (a) The first maximum g_{max} of the pair correlation function (solid curve) and (b) its relative position d_{max}/l_d as functions of Γ^*. The bars correspond to the results of calculations with the scaling parameter varying in the range $\xi = 0.04$–1.2. The closed and open symbols in plot (a) show the maximum value g_{max} of the measured function $g(l)$ and the ratio g_{max}/g_{min}, respectively, vs. parameter Γ^* deduced from the measurements of the grain diffusion coefficient in a dc glow discharge under Earth's gravity conditions (diamonds) and microgravity conditions (squares) and in an rf discharge (circles).

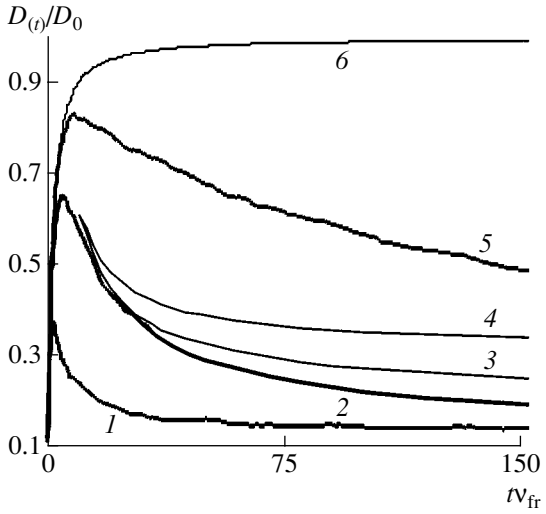

Fig. 3. Ratio $D(t)/D_0$ as a function of $t\nu_{fr}$ for different values of ξ and Γ^*: (*1*) $\xi = 1.2$ and $\Gamma^* = 80$, (*2*) $\xi = 0.133$ and $\Gamma^* = 80$, (*3*) $\xi = 0.133$ and $\Gamma^* = 60$, (*4*) $\xi = 0.133$ and $\Gamma^* = 30$, and (*5*) $\xi = 0.04$ and $\Gamma^* = 80$. Curve *6* is the ratio $D(t)/D_0$ calculated by formula (11).

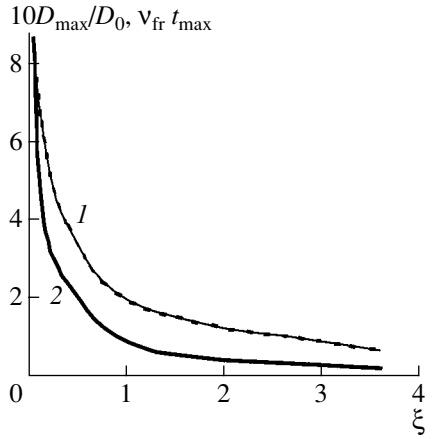

Fig. 4. (*1*) Magnitude D_{max}/D_0 of the maximum of the function $D(t)/D_0$ and (*2*) its time position $t_{max}\nu_{fr}$ as functions of ξ. The dashed line shows the approximation of the ratio D_{max}/D_0 by formula (12).

the grain position in numerical simulations); $t_\Sigma = 2N_t\Delta t$ is the total measurement time (e.g., the duration of a video recording or numerical simulation); and the angular brackets stand for averaging over either the grain ensemble (N) or time (t). We note that the analysis of two-dimensional images ($\Delta\mathbf{l}(t)^2 \sim x^2 + y^2$) requires either certain assumptions about the grain displacement along the third coordinate (e.g., $z^2 \approx y^2$ in the case of cylindrical symmetry) or taking into account the number of spatial dimensions in formula (10) by replacing the coefficient 6 by 4.

Formula (10) can be derived by considering the diffusion of grains through a unit area in a homogeneous medium. At $t \longrightarrow \infty$, it is similar to the known Green–Kubo relation [44]. When deriving this formula, no suggestions about the nature of thermal motion were made; hence, it is equally valid for gases, liquids, and solids.

Figure 3 shows the ratio of the diffusion coefficient $D(t)$ for interacting grains to that for noninteracting (Brownian) grains, $D_0 = T_d/(\nu_{fr}m_d)$, as a function of time (in units of the deceleration time ν_{fr}^{-1}) for dissipative systems with different values of the parameters ξ and Γ^*. Curve *6* is the exact solution to the Langevin equation for noninteracting grains [39]:

$$D(t)/D_0 = 1 - [1 - \exp(-\nu_{fr}t)]/\nu_{fr}t. \qquad (11)$$

Hence, for the times longer than the reciprocal friction frequency ($\nu_{fr}t \gg 1$), we have $D(t) = D_0$, whereas at the shorter times ($\nu_{fr}t \ll 1$), the grain motion is ballistic in character: $\langle r(t)^2\rangle = \langle\langle \mathbf{l}(t) - \mathbf{l}(0)\rangle_N^2\rangle_t \approx 3\nu_{Tp}t^2$ and $D(t) \propto t$. In the presence of interaction (see Fig. 3), the behavior of $D(t)$ at short times remains the same. As the time increases, the diffusion coefficient reaches its maximum value D_{max}, which can be used to analyze the particle transport at short observation times. Note that D_{max} is smaller than D_0 and tends to the latter as the viscosity of the medium increases. The dependences of the maximum value of the ratio D/D_0 and its time position $t_{max}\nu_{fr}$ on the parameter ξ are shown in Fig. 4. An important result of numerical simulations is that neither the ratio D_{max}/D_0 nor the value of $t_{max}\nu_{fr}$ depend on Γ^* and the time dependence of the ratio $D(t)/D_0$ at times $t < t_{max}$ is determined by expression (11) for noninteracting grains. An empiric fit of the calculated curves $D(t)$ that monotonically decrease after reaching their maximum value D_{max} gives the following dependence $D_{max}(\xi)$:

$$D_{max} \approx D_0/(1 + 4\pi\xi/3), \qquad (12)$$

which coincides with the numerical data with an accuracy of up to 5% (Fig. 4). An analysis of the time dependence of the ratio $D(t)/D_0$ at short observation times can be used to find the coefficient D_0 or the dust-grain temperature T_d from the measured values of $D(t)$ when the resolution of the measuring device does not allow one to correctly determine the velocity distribution of dust-grains. Thus, if the grain displacements are recorded with a video camera with a frame frequency smaller than the friction coefficient ν_{fr}, the measurements of the instant velocities of dust-grains give an underestimated value of the grain temperature [47].

As time elapses, the diffusion coefficient $D(t)$, determined by formula (10), tends to its steady-state value $D = \lim_{t\to\infty} D(t)$, which is generally treated as the grain thermal diffusion coefficient and is one of the

main transport coefficients. The coefficient D can be determined experimentally [7, 11]. The results of numerical simulations of the ratio of the diffusion coefficient D of the interacting dust-grains to the coefficient D_0 for $\xi \approx 0.02$–4 are shown in Fig. 5. One can see that the function $D(1 + \xi)/D_0$ depends only on the effective parameter Γ^* for both weakly correlated and strongly nonideal systems. In the latter case (for $\Gamma^* > 50$), the diffusion coefficient of the interacting dust-grains can be represented in the form [40, 43]

$$D \cong \frac{T_d \Gamma^*}{12\pi(\omega^* + \nu_{fr}) m_d} \exp\left(-c_1 \frac{\Gamma^*}{\Gamma_c^*}\right), \qquad (13)$$

where $c_1 = 2.9$ for $\xi > 0.3$ and $c_1 = 3.15$ for $\xi < 0.3$. The approximation of the calculated results by formula (13) with allowance for the difference between the coefficients c_1 is also shown in Fig. 5. The error of this approximation is less than 5% for $\Gamma^* > 50$ and increases to 20–35% as the parameter Γ^* decreases to 30. Thus, for $\Gamma^* > 50$, one can obtain two simple expressions for the diffusion coefficient D in the two limiting cases:

$$D \cong \frac{l_d}{12}\sqrt{\frac{T_d \Gamma^*}{\pi m_d}} \exp\left(-2.9 \frac{\Gamma^*}{\Gamma_c^*}\right), \quad \omega^* \gg \nu_{fr}, \qquad (14a)$$

$$D \cong D_0 \frac{\Gamma^*}{12\pi} \exp\left(-3.15 \frac{\Gamma^*}{\Gamma_c^*}\right), \quad \omega^* \ll \nu_{fr}. \qquad (14b)$$

These formulas allow one to determine the effective parameter Γ^* from the results of measurements of the mean intergrain spacing l_d, temperature T_d, and grain diffusion coefficient D in liquid systems. They can also be used to determine the grain charge Z^* and the grain screening radius λ from experimental data. To diagnose weakly correlated systems ($\Gamma^* < 50$), one can use the results of numerical calculations of the function $D(1 + \xi)/D_0$ (see Fig. 5).

In the case of screened interaction between grains, formula (7) allows one to determine either the dust-grain charge Z_d or the quantity $\lambda = l_d/\kappa$, provided that one of these parameters is given. To determine one of these parameters, one can use the results of numerical simulations or the available experimental data obtained under the conditions close to those analyzed. The existence of additional relations between the charge Z_d, screening length λ, and parameters monitored in the experiment significantly simplifies this problem. For instance, by analyzing the positions of dust-grains in a two-dimensional dust crystal in the electrode sheath of an rf discharge, an additional relation was found between screened potential (3), the screening length λ, and the number of dust-grains assuming that the potential of the radial electric field is parabolic [21]. The determination of such a relationship for fluid dusty structures, in which the grain positions are not fixed

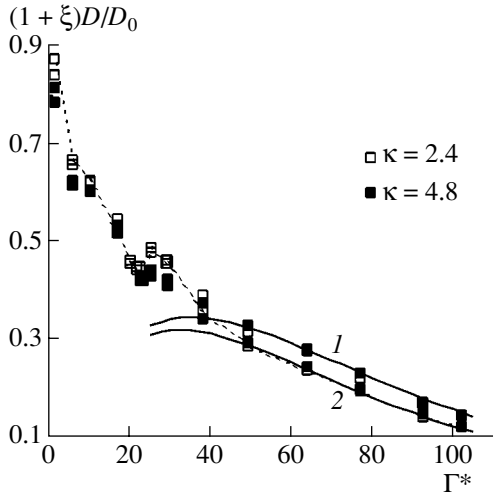

Fig. 5. Quantity $(1 + \xi)D/D_0$ as a function of Γ^* for different values of the screening parameter κ and the approximation of this quantity by formula (13) for (*1*) $\xi > 0.3$ and (*2*) $\xi < 0.3$.

($D \neq 0$), or for another shape of the electric potential calls for additional numerical simulations.

The results of [13, 28, 33] (see Section 2.2) allow us to made an assumption about the screening length λ of dust-grains. According to those results, the screening length of dust-grains with radius $a_d \gg \lambda_i$ in the electrode sheath of an rf discharge is close to the electron Debye radius ($\lambda \approx \lambda_e$). Then, for characteristic intergrain spacings l_d and plasma parameters typical of experiments ($n_i \sim n_e \sim 10^8$–10^9 cm^{-3}, $T_e \sim 1$–7 eV), we have $\kappa = l_d/\lambda \lesssim 1$. In this case, the effective parameter Γ^* is close to the Coulomb coupling parameter, $\Gamma^* \approx \Gamma = (Z_d e)^2/T_d l_d$, and the measurements of D, T_d, and l_d enable the determination of the grain charge without additional information about λ. When the grain charge is not directly related to the screening parameter κ and/or $\kappa \gg 1$, the data on the parameters of the ambient plasma can be obtained by preliminarily studying the discharge plasma in the absence of dust, because diagnosing this plasma under the actual experimental conditions introduces strong perturbations in the plasma–dust system.

To conclude, we note that the determination of the parameters Γ^* and ξ is of interest by itself, because it allows one to verify how the numerical model agrees with experimentally observed dusty structures. A comparison of independent measurements of the grain-transport characteristics, such as the pair correlation function $g(l)$, diffusion coefficient $D = \lim_{t \to \infty} D(t)$, and magnitude D_{max} and time position t_{max} of the maximum of the function $D(t)$, allow one to judge the physical parameters that are responsible for the phase state of a dusty structure and the transport of dust-grains in a real

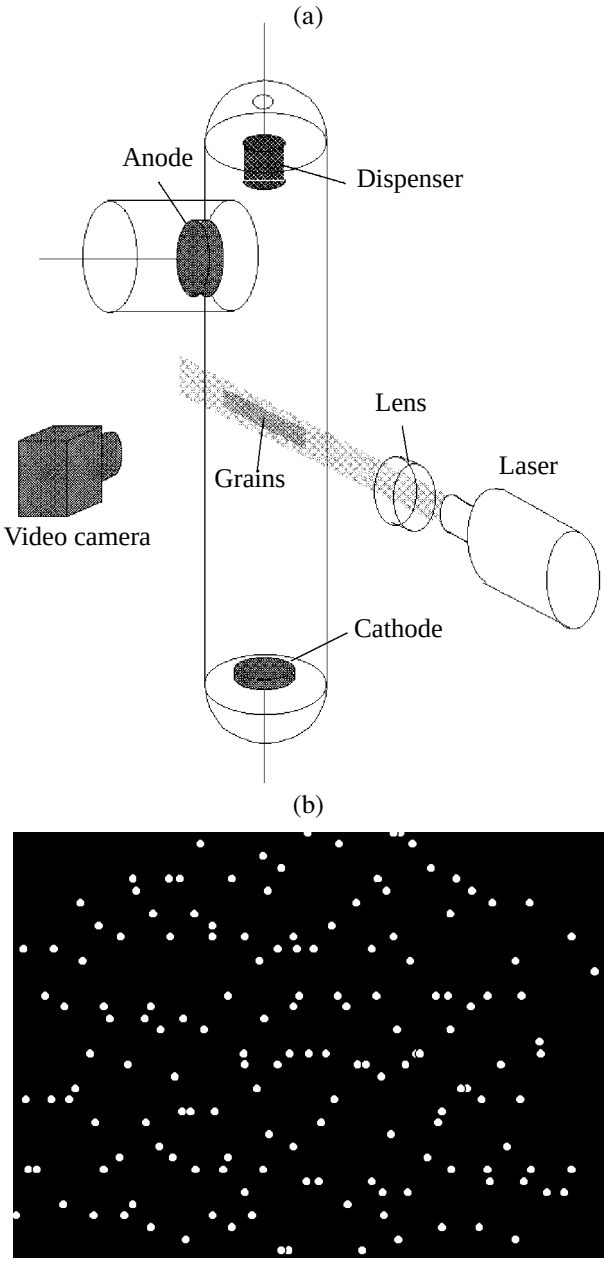

Fig. 6. (a) Schematic of ground-based experiments with a dc glow discharge and (b) the video recording of dust grains in a glow discharge striation.

plasma. Remember that, in numerical simulations of a homogeneous extended three-dimensional system of grains with the screened pair interaction potential, the above four characteristics are completely determined by the grain kinetic temperature and the two effective parameters Γ^* and ξ (see Section 2.3). Thus, one can answer questions as to whether these parameters describe a real dusty system and whether the attraction forces between the grains, the plasma inhomogeneity, the preferred spatial orientation of grains, etc., are of significance under the conditions of an experiment.

3. EXPERIMENT

Experiments on dust-grain dynamics were carried out in the plasmas of an rf capacitive discharge and a dc glow discharge (both on the Earth and under microgravity conditions). The visualization method (see Section 3.1) and the nonintrusive method for determining dust-grain parameters that was described in the previous section were used to diagnose dust-grains. Schematics of the experimental facilities are shown in Figs. 6, 9, and 12; a description of the experiments is given in Section 3.2; and the experimental results are presented in Figs. 7, 8, 10, 11, 13, and 14 and Tables 1 and 2.

3.1. Dust-Grain Diagnostics by the Visualization Method

The visualization method was used to study dust-grain dynamics in gas-discharge plasmas. The dust cloud was illuminated with a ribbon laser beam and then shot with a CCD video camera with a frame frequency of 25 s^{-1}). In ground-based experiments, a 0.633-μm He–Ne laser, whose radiation was focused by cylindrical lenses in a ribbon beam (laser blade) with a thickness from 150 to 300 μm, was used as an illumination source. To diagnose dust-grains under microgravity conditions, a 300-μm-thick laser blade produced by a 0.67-μm semiconductor laser and the additional illumination of the dust cloud with a filament lamp were used [11].

Video recordings were processed with a PC using a special program by dividing the recordings into half-frames with a frequency of 50 s^{-1}, which enabled the identification of the displacements of individual grains that resided in the viewing field of the video camera. Using this program, we determined the displacements and velocity distributions of grains in the dusty structures observed. All the results presented below refer to quasi-steady fluid dusty structures. The recorded grain motion was nearly thermal (the grain velocity distribution was close to Maxwellian).

By processing the video recordings, we determined the density, diffusion coefficient, temperature, and pair correlation function of the dust-grains in a wide range of gas-discharge parameters. The results obtained were used to find the effective coupling parameter Γ^*, scaling parameter ξ, and effective surface potential $\phi_s^* = eZ_d^*/a_d$. The estimates of the grain surface potential $\phi_s = eZ_d/a_d$ were made under the assumption of a screened intergrain interaction.

The mean intergrain spacing $l_d = n_d^{-1/3}$ and the dust-grain density n_d were determined from the position of the maximum of the pair correlation function. The dust-grain temperature was found by fitting the measured grain velocity distribution by a Maxwellian distribution. A similar procedure was used in [7, 47]. The dust-

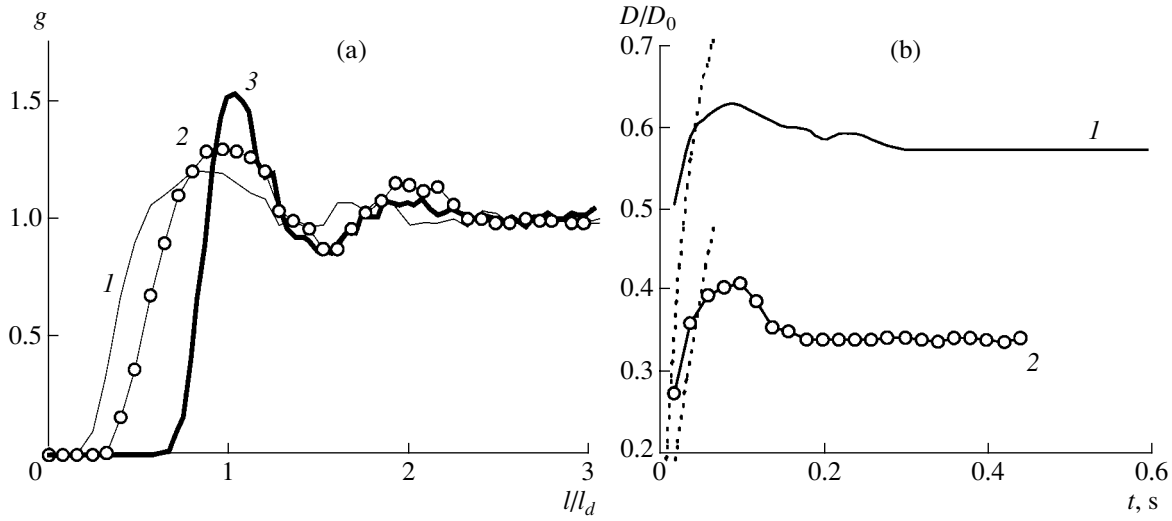

Fig. 7. (a) Pair correlation function $g(l/l_d)$ and (b) the evolution of the function $D(t)/D_0$ for the pressures P = (*1*) 128 and (*2*) 56 Pa. Curve *3* shows the function $g(l/l_d)$ obtained from numerical simulations at $\Gamma^* \approx 18$. The dashed lines in plot (b) show the evolution of the function $D(t)$ for noninteracting grains.

grain temperature determined from the dispersion of the velocity distribution function was corrected by matching the measured dust-grain diffusion coefficient to the results of calculations for short observation times (see Section 2.3). The measured time dependences of the diffusion coefficient D are shown in Figs. 7b, 10b, and 13b (the dashed curves show the ratio $D(t)/D_0$ for noninteracting grains with the friction coefficient ν_{fr} and temperature T_d close to the measured ones). The dust-grain temperature T_d and the mean intergrain spacing l_d measured in three experiments with different discharge parameters are listed in Table 1. The table also presents the values of the parameter Γ^*, surface potentials (ϕ_s^*, and ϕ_s), and scaling parameter ξ deduced from the measured diffusion coefficient D.

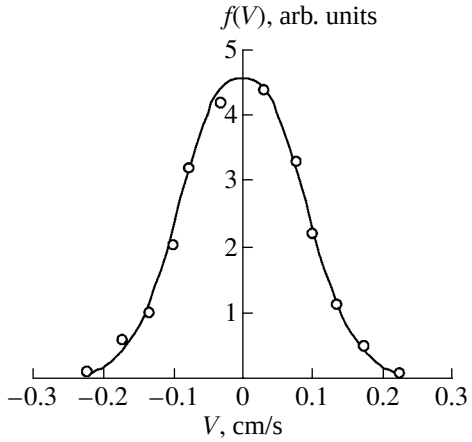

Fig. 8. Velocity distribution function $f(V)$ of dust grains at a pressure of P = 56 Pa. The symbols show the results of measurements and the solid curve shows the Maxwellian distribution with the temperature T_d = 1 eV.

3.2. Description of the Experiments

3.2.1. Ground-based experiments in the striations of a dc glow discharge. Figure 6a shows a sche-

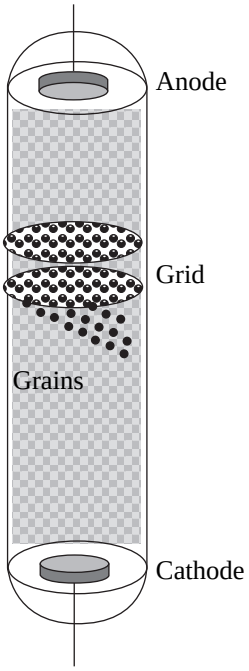

Fig. 9. Schematic of a gas-discharge tube for experiments in a dc glow discharge under microgravity conditions.

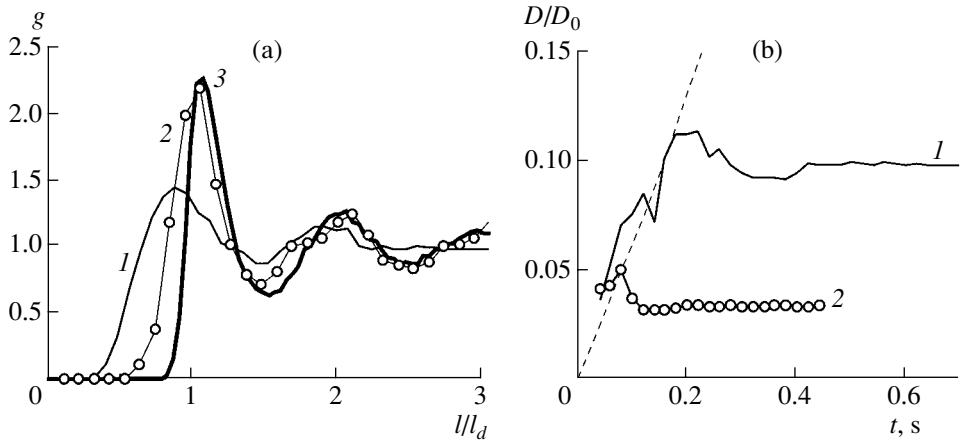

Fig. 10. (a) Pair correlation function $g(l/l_d)$ and (b) the time evolution of the diffusion coefficient $D(t)/D_0$ in a dusty structure near the grid electrodes for different discharge currents: I = (*1*) 0.8 and (*2*) 0.1 mA. Curve *3* shows the function $g(l/l_d)$ obtained from numerical simulations at $\Gamma^* \approx 77$.

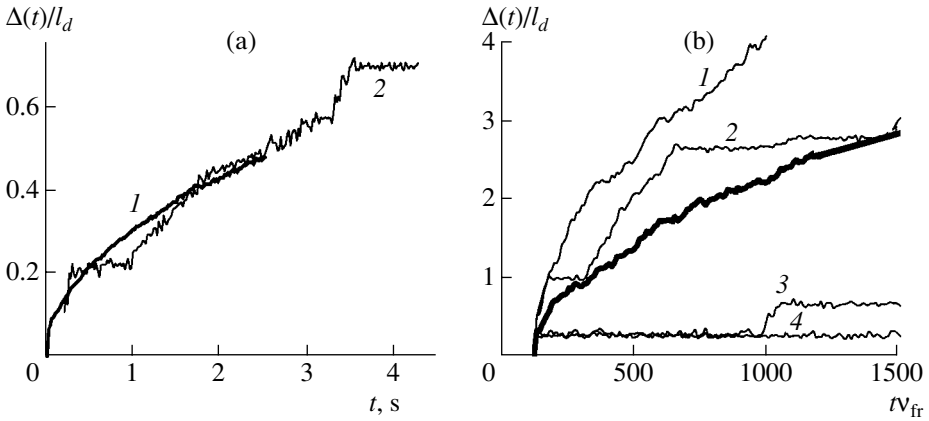

Fig. 11. (a) Measured time dependence of the Lindemann parameter $\delta_c = \Delta(t)/l_d$ for I = 0.4 mA and different averaging methods: (*1*) $\Delta(t) \equiv \Delta_N$ and (*2*) $\Delta(t) \equiv \Delta_N^t$. (b) An illustration of the jumplike changes in the modeled Yukawa system for $\Delta(t) = \Delta_N$ and Γ^* = (*1*) 77, (*2*) 92, (*3*) 102, and (*4*) 106; the solid curve shows $\Delta_N^t(t)$ for $\Gamma^* = 92$.

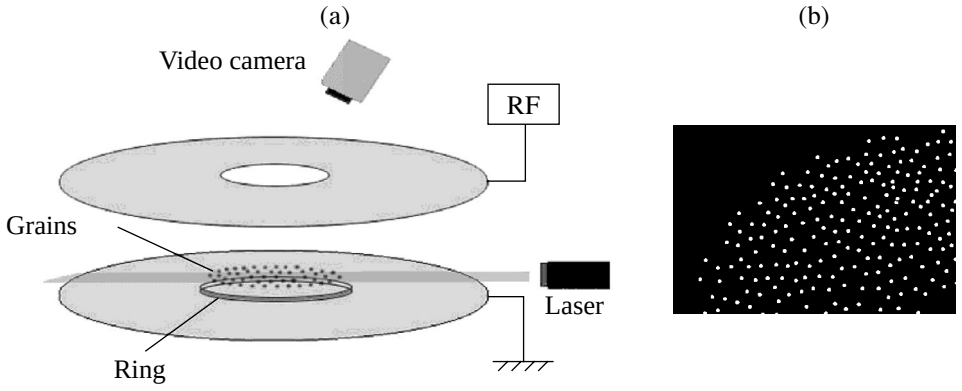

Fig. 12. (a) Schematic of experiments with an rf discharge and (b) the video recording of dust grains in the electrode sheath.

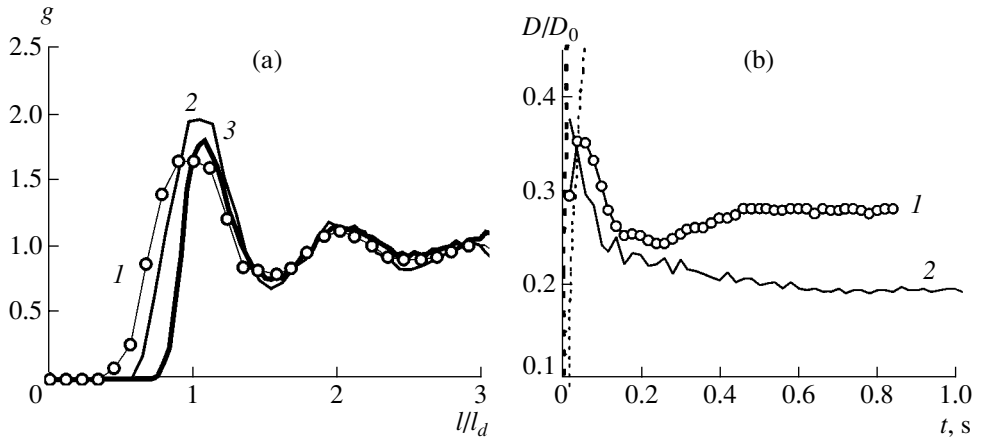

Fig. 13. (a) Pair correlation function $g(l/l_d)$ and (b) the time evolution of the diffusion coefficient D/D_0 of grains in a dust monolayer at pressures P = (*1*) 40 and (*2*) 10 Pa. Curve *3* in plot (a) shows the function $g(l/l_d)$ obtained from numerical simulations at $\Gamma^* \approx 35$.

matic of the experimental setup. A fragment of the video recording of a dust cloud (side view) in the striations of a glow discharge is shown in Fig. 6b. The main component of the working chamber was a 3.2-cm-radius gas-discharge tube filled with neon. The experiments with polydisperse iron grains with the mass density $\rho_d \approx 8$ g/cm^3 and radii a_d = 1–3 μm (the average grain radius was $\langle a_d \rangle \approx 2$ μm, which corresponded to $\langle m_d \rangle \approx 2.7 \times 10^{-10}$ g) were performed at a gas pressure of P = 50–130 Pa and a dc discharge current of $I \approx 3$ mA.

The experiments were aimed at the observation of weakly correlated quasi-steady dusty structures. The main difficulty was to choose the discharge parameters at which no instability developed and no large-scale dust motions (such as dust waves or vortices, which are typical of experiments in glow discharge striations [3, 35, 41]) occurred.

Figure 7 shows in the pair correlation function $g(l/l_d)$ and the time evolution of the diffusion coefficient $D(t)/D_0$ for two different pressures. An example of the dust-grain velocity distribution is presented in Fig. 8. The effective coupling parameter Γ^* deduced from the measured diffusion coefficient by computing the function $D(1 + \xi)/D_0$ (Fig. 5) varied in the range 10–20 (see Table 1).

3.2.2. Experiments in a dc glow discharge under microgravity conditions. A detailed description of the experimental setup and the experimental data on the dynamics of large dust-grains under microgravity conditions were presented in [11]. The scheme of video recording of a dust cloud was similar to that shown in Fig. 6a. The main component of the working chamber was a 1.6-cm-radius gas-discharge tube filled with neon at a pressure of P = 133 Pa (see Fig. 9). The discharge current I was varied from 0.1 to 0.8 mA. Inside the gas-discharge tube (at a certain distance from the anode), an insulated electrode consisting of two steel grids (made from a 60-μm-diameter wire) with a cell size of 150 × 150 μm was installed. The electrode was at the floating potential and prevented the negatively charged dust-grains from escaping to the anode. Spherical bronze grains with a specific mass density $\rho_d \approx 8.2$ g/cm^3 and diameters of 70–180 μm (the average radius was $\langle a_d \rangle$ = 62.5 μm, which corresponded to $\langle m_d \rangle \approx 8.4 \times 10^{-6}$ g) were placed between the grid electrode and cathode.

As was discussed above, the experiments carried out under microgravity conditions allow one to study the dynamics of large dust-grains with dimensions comparable to or larger than the Debye radius and the mean free path of plasma ions. Note that it is practically impossible to ensure the levitation of such massive grains under the conditions of ground-based experiments.

The pair correlation function $g(l/l_d)$ and the time evolution of the diffusion coefficient $D(t)/D_0$ are shown in Fig. 10 for two different discharge currents I. The effective coupling parameter Γ^* varied from ~20 to 80 (see Table 1). In regimes with $I \geq 0.5$ mA, the deduced value of the parameter Γ^* changed slightly (by no more than 10%) when varying the dust-grain radius that was taken in calculating the grain friction coefficient. Note that this radius was varied from the average radius $\langle a_d \rangle$ = 62.5 μm to the minimum radius of 35 μm (see Table 1). Such a weak dependence is explained by the fact that the friction coefficient ν_{fr} only slightly affects the value of the effective parameter Γ^* under the experimental conditions at $\xi \gg 1$ or $\nu_{fr} \ll \omega^*$ [see Eqs. (13), (14)].

An interesting experimental observation is the jumplike time evolution of the r.m.s. dust-grain displacement $\Delta_N(t) = \sqrt{\langle \mathbf{l}(t) - \mathbf{l}(0) \rangle_N^2}$ (where $\langle\ \rangle_N$ stands for the averaging over N grains) when the dynamic characteristics are averaged over an ensemble consisting of a

Table 1. Mean intergrain spacing l_d, grain temperature T_d, effective parameters Γ^* and ξ, and grain surface potential ϕ_s^* obtained from the diffusion measurements and the potential ϕ_s deduced under the assumption of screened interaction for different gas-discharge experiments (the experimental data are given for $a_d = \langle a_d \rangle$)

Ground-based experiments in striations of a dc glow discharge							
P, Pa	ν_{fr}, s^{-1}	l_d, μm	T_d, eV	Γ^*	ξ	ϕ_s^*, eV	ϕ_s, eV
56	22	250	1	20	0.36	1.35	5.9–14.6
80	33	230	1	15	0.22	1.10	4–9.1
109	44	220	1	10	0.145	0.90	3–6.5
128	50	190	1.2	9	0.15	0.85	2.2–4.2
Experiments in a dc glow discharge under microgravity conditions (the values in braces correspond to the minimum grain size a_d = 35 μm)							
I, mA	ν_{fr}, s^{-1}	l_d, μm	$T_d \times 10^{-5}$, eV	Γ^*	ξ	ϕ_s^*, eV	ϕ_s, eV
0.1	1.6{3.3}	710	0.95{0.17}	76{72}	5.8{2.8}	43.5{31.5}	43.6{31.6}
0.2	1.6{3.3}	800	1{0.18}	64{60}	4.9{2.3}	44{32}	44{32}
0.4	1.6{3.3}	825	1{0.18}	66{62}	4.9{2.3}	45.5{33}	45.5{33}
0.5	1.6{3.3}	810	1{0.18}	65{60}	4.95{2.35}	45{33}	45{33}
0.8	1.6{3.3}	1010	1.2{0.22}	31{22}	3.0{1.3}	37.5{24.5}	37.5{24.5}
Ground-based experiments in an rf discharge							
P, Pa	ν_{fr}, s^{-1}	l_d, μm	T_d, eV	Γ^*	ξ	ϕ_s^*, eV	ϕ_s, eV
10	24	550	1.43	35	0.66	4.2	4.4–4.8
20	48	400	2.65	43	0.68	5.4	5.5–5.7
30	72	350	2.65	57	0.60	5.8	5.9–6.1
40	96	300	2.80	65	0.57	5.9	6.0–6.1

Table 2. Estimates of the scaling parameter ξ by the time position $t_{max}\nu_{fr}$ of the maximum of the measured function $D(t)/D_0$ (ξ_1) and by the magnitude of this maximum D_{max}/D_0 (ξ_2)

DC glow discharge under the Earth's gravity conditions			DC glow discharge under microgravity conditions			RF discharge		
P, Pa	ξ_1	ξ_2	I, mA	ξ_1	ξ_2	P, Pa	ξ_1	ξ_2
56	0.41	0.34	0.1	2.4	1.9	10	0.68	0.45
128	0.15	0.14	0.8	5.8	4.55	40	>0.48	0.4

small number of grains [11]. The time dependence of the parameter $\delta_c = \Delta_N(t)/l_d$ is shown in Fig. 11a. The figure also shows the r.m.s. dust-grain displacement $\Delta_N^t = \sqrt{\langle \langle \mathbf{l}(t) - \mathbf{l}(0) \rangle_N \rangle_t^2}$ (averaged over both ensemble and time) used in calculations of the grain diffusion coefficient D [see Eqs. (14)]. We also note that, at short observation times, the ratio $\Delta_N(t)/l_d$ (see Fig. 11a) corresponds to the Lindemann criterion, according to which the solid phase starts melting when the ratio of the r.m.s. displacement Δ_0 of a grain from its equilibrium position to the mean intergrain spacing l_d reaches ~0.15 [48]. Since the grain displacement is usually measured from the center of mass of the system ($\Delta = \sqrt{2}\Delta_0$), the value of the Lindemann parameter on the melting line should be $\delta_c = \Delta/l_p \approx 0.21$.

A similar picture was observed in numerical simulations of dust-grain dynamics in strongly nonideal Yukawa systems [38]. The jumps observed in the systems under study are illustrated in Fig. 11b, which demonstrates the difference between the r.m.s. displacement $\Delta_N(t)/l_d$ averaged over ensemble and the time-averaged r.m.s. displacement Δ_N^t/l_d near the crystallization line, at which the effective coupling parameter

Γ^* is equal to 102. As Γ^* decreases, this difference vanishes and the system under study becomes ergodic.

3.2.3. Ground-based experiments in an rf capacitive discharge. Figure 12a shows a schematic of the experimental setup for studying the transport characteristics of grains in a dust monolayer formed in an rf discharge. A fragment of the video recording of the dust layer (top view) is shown in Fig. 12b. To prevent the grains from expanding beyond the electrode edges, a ring 2 mm tall and 4 cm in diameter was placed at the lower electrode. The experiments were performed in argon at a pressure of P = 10–40 Pa. The discharge power was $W \approx 5$ W. The dust component consisted of aluminum oxide (Al_2O_3) grains with the mass density $\rho_d \approx 2.4$ g/cm^3 and radii a_d = 1–2.5 μm (the average radius was $\langle a_d \rangle \approx 1.5$ μm, which corresponded to $\langle m_d \rangle \approx 3.4 \times 10^{-11}$ g).

The pair correlation function $g(l/l_d)$ and the time evolution of the diffusion coefficient $D(t)/D_0$ for two different pressures P are shown in Fig. 13. The effective coupling parameter Γ^* deduced from the measurements of the diffusion coefficient varied from 35 to 65 (see Table 1).

We note that applying the results of three-dimensional numerical simulations to analyzing the effective parameters of a dusty system is not well justified under conditions of this experiment because the observed dusty structures are two-dimensional. At present, no simulation data are available that can be used for the nonintrusive diagnostics of the grain-transport characteristics in two-dimensional fluid dusty systems. Hence, applying the above method to analyzing the grain transport in a dust monolayer is of interest by itself from the standpoint of comparing the grain dynamics in two- and three-dimensional dusty systems.

3.3. Analysis of the Measured Grain-Transport Characteristics

In the experiments, we determined four transport characteristics of the dusty structures: g_{max}, D, D_{max}, and t_{max}, each of which carries information about the effective parameter Γ^*. The measurements of the diffusion coefficient D provide the highest accuracy in determining this parameter. The number of grains and the frame frequency of video recording only slightly affect the D value because the function $D(t)$ defined by expression (10) can be recorded over the time during which it reaches its steady-state value, $D = \lim_{t \to \infty} D(t)$. In contrast, the number of grains and the frame frequency do affect the accuracy of measuring the other three characteristics. The inaccuracy with which the parameter Γ^* is determined from the measurements of the grain diffusion coefficient D depends mostly on the error in measuring the temperature T_d. At a relative error of $|\Delta T_d/T_d| < 20\%$, the inaccuracy in determining Γ^* is no higher than 5–10%. The systematic error in determining the Γ^* can be related to the mismatch of the model used (see Section 2.3) and the actual experimental conditions.

We have analyzed the measured pair correlation function $g(l)$ and the parameter Γ^* deduced from the measurements of the diffusion coefficient D. These measurements are independent and their comparison allows us to draw a conclusion about the correctness of determining the transport characteristics and the applicability range of the discussed method for deducing the effective parameters of the system under study (the coupling parameter Γ^* and the scaling parameter ξ). The dependences of the maximum value g_{max} of the function $g(l)$ and the ratio g_{max}/g_{min} (where g_{min} is the first minimum of the function $g(l)$ at $l \neq 0$) on the deduced parameter Γ^* are shown in Fig. 2a. It can be seen that, in all the experiments, the degree of correlation (g_{max}/g_{min}, g_{max}) of dust-grains agrees well with the deduced value of the parameter Γ^*, including experiments with dust-grains in two-dimensional dusty structures in an rf discharge. We note, however, that the maximum values g_{max} of the measured function $g(l)$ are somewhat lower than those obtained from numerical simulations (see Fig. 2a) and the functions $g(l)$ themselves are extended to the region corresponding to short intergrain spacings. The measured correlation function and the function $g(l)$ obtained from numerical simulations for Γ^* values close to the measured ones are shown in Figs. 7a, 10a, and 13a. The discrepancy between these data can be related to both the procedure of measuring the function $g(l)$ in a volume containing the limited number of grains and the spatial inhomogeneity of the dusty structures under study. The parameters Γ^* and ξ deduced from the measured diffusion coefficient are listed in Table 1.

According to the simulation results (see Section 2.3), the time evolution of the diffusion coefficient $D(t)$ at short observation times is determined by the scaling parameter ξ. Hence, the parameter $\xi = \omega^*/\nu_{fr}$ can be independently estimated from the measurements of the time position t_{max} and magnitude D_{max} of the maximum of the function $D(t)$. We note, however, that, under the given experimental conditions, the accuracy of these measurements was unsatisfactory. For example, the accuracy in determining the time position t_{max} was significantly affected by the fact that, in all the experiments, these positions were close to the time resolution of video recordings (50 s^{-1}). Moreover, the magnitude D_{max} of the maximum strongly depended on the spatial resolution D_{max} of video recordings (in our experiments, Δ_s = 10–40 μm/pixel) and the procedure of processing these recordings. These factors can lead to either an underestimation of the measured D_{max} value as compared to its true value (because the grain displacements with the magnitude less than Δ_s are not taken into account) or an overestimation of it (because of the incorrect determination of the position of grains with

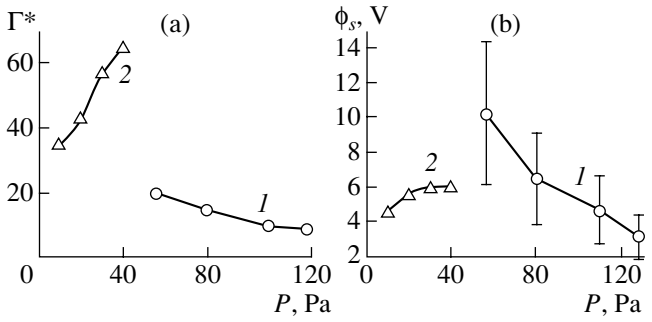

Fig. 14. (a) Parameter Γ* deduced from the measured diffusion coefficients and (b) the surface potential $\phi_s = eZ_d/a_d$ vs. pressure for ground-based experiments in (*1*) a dc glow discharge and (*2*) an rf discharge. The bars in plot (b) show the error in determining ϕ_s caused by an uncertainty in the choice of the screening parameter ($\lambda_i \approx 29$–40 μm).

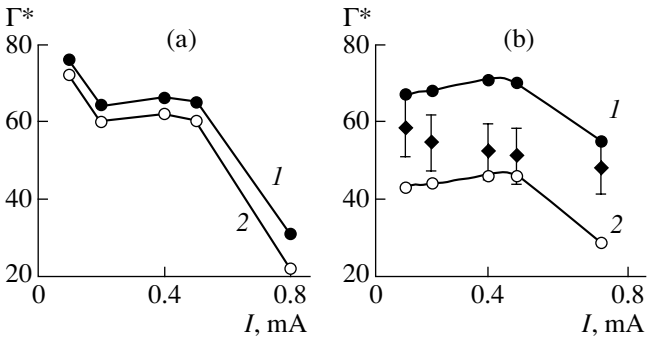

Fig. 15. (a) Parameter Γ* deduced from the measured diffusion coefficients and (b) the surface potential $\phi_s = eZ_d/a_d$ vs. discharge current in a dc glow discharge under microgravity conditions for different grain radii: a_d = (*1*) 62.5 and (*2*) 35 μm. The closed diamonds in plot (b) show the grain surface potential ϕ_s obtained in [11] by tracing the grain motion toward the grid electrodes. The bars in plot (b) show the error in determining ϕ_s caused by an uncertainty in the choice of the screening parameter.

sizes larger than Δ_s when numerically analyzing video recordings). Therefore, under our experimental conditions, the measurements of $D_{\max}$ and $t_{\max}$ allow us to determine only the range of the possible values of the parameter ξ, rather than its exact value. For the experiments whose results are illustrated in Figs. 7b, 10b, and 13b, the deduced ξ values are presented in Table 2. The quantity ξ_1 was determined from the position of the maximum of the measures function $D(t)/D_0$ (see Fig. 4), whereas the quantity ξ_2 was determined from the magnitude of this maximum using relation (12). We can see that the time evolution of the grain diffusion coefficient measured at short observation times agrees well with the data obtained from the measurements of $D = \lim_{t \to \infty} D(t)$ (see Table 1). This additionally confirms the correctness of the measurements and the absence of any significant difference between the modeled and experimentally observed systems.

The effective surface potential $\phi_s^* = eZ_d^*/a_d$ obtained from the deduced Γ* value and the dust-grain temperature T_d are presented in Table 1 for all three experiments and different discharge parameters. In the case of the screened interaction between grains, relation (7) allows one to estimate either the dust-grain charge or the parameter $\kappa = l_d/\lambda$, provided that one of these parameters is given. To estimate the dust-grain charge Z_d, one can use the results of numerical simulations [33] and the experimental data from [13, 28] (see Section 2.1).

We will assume that the screening of small grains with $a_d \ll \lambda$ in a dc glow discharge under Earth's gravity conditions is provided by the ions of the ambient plasma [33]. We also assume that the ion temperature is close to room temperature, $T_i \sim 0.027$ eV. Then, for the plasma ion density $n_i \approx (1$–$2) \times 10^9$ cm^{-3}, the screening radius is $\lambda_i \approx 29$–40 μm [26, 27]. The deduced values of the grain potential $\phi_s = eZ_d/a_d$ in a dc glow discharge under Earth's gravity conditions are presented in Table 1 and Fig. 4b for $\lambda = \lambda_i \approx 29$–$40$ μm. The error in determining ϕ_s caused by an uncertainty in the choice of λ is about 40%.

In the case of large bronze grains ($a_d > \lambda_i$, $n_i \approx 5 \times 10^9$ cm^{-3}, and $n_e \approx 10^8$ cm^{-3} [11]), the ions do not contribute to the screening of the grains [33] ($\kappa < 1$) and, consequently, we have $\phi_s \approx \phi_s^* = (\Gamma^* T_d l_d)^{1/2}/a_d$ (see Table 1). Figure 15b compares the deduced potential ϕ_s with the surface potential obtained under the given experimental conditions by analyzing the dust-grain motion from the discharge positive column toward the grid electrodes [11].

It can be seen that the difference between the results of these measurements is no larger than 20% even if the plasma parameters in the positive column differ from those near the grid electrodes.

In the electrode sheath of an rf discharge, the ions also slightly affect the dust-grain screening [13, 28]; hence, the grain screening radius is $\lambda \approx \lambda_e$. Then, under our experimental conditions ($n_e \approx (0.5$–$1) \times 10^9$ cm^{-3} and $T_e \approx 2$ eV [49, 50]), we have $\lambda \approx \lambda_e \approx 336$–$470$ μm. Thus, in this case, $\kappa = l_d/\lambda \approx 1$ and the dust-grain surface potential ϕ_s does not significantly differ from the effective surface potential ϕ_s^* (see Table 1 and Fig. 15b). The error in determining ϕ_s caused by an uncertainty in the choice of λ is less than 5%.

In turn, the deduced value of ϕ_s allows us to estimate the electron temperature T_e. We may assume that the accuracy of the above estimates of the grain surface potential is acceptable when the obtained T_e value

agrees with the available data on the mean electron energy under the given experimental conditions.

The experiments with grains whose size is much less than the plasma electron (ion) mean free path can be analyzed using the results of numerical simulations performed in the OML approximation. Then, for a dense dust cloud ($\chi > 1$, see Section 2.1) consisting of iron grains in striations of a dc glow discharge, the surface potential can be set at $\phi_s \approx 2T_e/e$ [23, 24]. In this case, the mean electron energy is $T_e \sim 2$–7 eV. In the case of an rf discharge in argon, we can assume that, in the electrode sheath, $\phi_s \approx 4T_e/e$ [24] and, consequently, the electron temperature is $T_e \sim 1$–1.5 eV. Since the OML approximation is not appropriate for estimating the charges of dust-grains with radii $a_d > l_i$, one can use the results obtained in [17] (see Section 2.1) to analyze the electron mean energy T_e in experiments with large bronze grains ($\langle a_d \rangle = 62.5$ μm $> l_i \approx 15$–25 μm) in a neon plasma at a pressure of $P = 133$ Pa. Then, we have $\phi_s \approx 4$–$10T_e/e$, which gives the electron temperature $T_e \sim 4$–10 eV. Thus, in all of the above cases, the obtained electron temperature agrees with the experimental and calculated data on the electron mean energy obtained under conditions close to the experimental ones [11, 25–27, 49, 50].

4. CONCLUSIONS

We have presented experimental results on the dynamics of dust-grains in the plasmas of an rf capacitive discharge and a dc glow discharge. The dusty plasma of a glow discharge was investigated in both ground-based experiments and experiments carried out under microgravity conditions (on board the *Mir* space station). The pair correlation function, velocity distribution, and diffusion coefficient of the dust-grains were measured. Based on these measurements, the number density and temperature (the kinetic energy of Brownian motion) of the dust-grains were determined. The effective parameters (ϕ_s^*, Γ^*) of the dusty structures were deduced for different discharge conditions. It is found that the phase state of the observed dusty structures changes from weakly correlated systems to strongly nonideal dust fluids ($\Gamma^* \sim 10$–80).

The degree of grain correlation determined from the form of the pair correlation function, the grain dynamics over short observation times, and the effective coupling parameter Γ^* deduced from the measurements of dust-grain diffusion are found to be in good agreement with each other. An analysis of the experimental data shows that the microscopic motion of dust-grains in a weakly ionized gas-discharge plasma can be described by the two main parameters: the effective coupling parameter Γ^* and the scaling parameter ξ.

A nonintrusive method has been proposed for determining the dust-grain charge or the screening length, provided that one of these parameters is given. This method does not introduce perturbations in the plasma–dust system under study and can be used to analyze the dust-grain parameters directly in the course of experiments. The necessary data on the unknown parameter can be obtained by either preliminary diagnosing the plasma in the absence of dust or analyzing the available literature data on the plasma parameters under conditions close to the experimental ones. In the latter case, this method can only be used to estimate the unknown quantities. In this study, we made certain assumptions about the screening length and estimated the surface potential of dust-grains from the measured values of the grain temperature, mean intergrain distance, and diffusion coefficient. The results obtained are in good agreement with the results of the analysis of the above experimental data by using the existing theoretical models.

It should be noted that the analysis of the experimental data has not revealed any significant difference between the dynamics of dust-grains in three-dimensional dusty structures in a glow discharge and their dynamics in a dust layer formed in the electrode sheath of an rf discharge. This allows us to suggest that, in both cases, the character of dust-grain diffusion is the same.

ACKNOWLEDGMENTS

This study was supported in part by the Russian Foundation for Basic Research (project no. 01-02-16658) and INTAS (grant nos. 01-0391 and 00-0522).

REFERENCES

1. H. Thomas, G. E. Morfill, V. Demmel, *et al.*, Phys. Rev. Lett. **73**, 652 (1994).
2. A. Melzer, T. Trottenberg, and A. Piel, Phys. Lett. **191**, 301 (1994).
3. V. V. Zhakhovskiĭ, V. I. Molotkov, A. P. Nefedov, *et al.*, Pis'ma Zh. Éksp. Teor. Fiz. **66**, 392 (1997) [JETP Lett. **66**, 419 (1997)].
4. S. Nunomura, T. Misawa, N. Ohno, and S. Takamura, Phys. Rev. Lett. **83**, 1970 (1999).
5. O. Vaulina, S. Khrapak, A. Nefedov, *et al.*, Phys. Rev. E **60**, 5959 (1999).
6. V. E. Fortov, A. P. Nefedov, O. S. Vaulina, *et al.*, Zh. Éksp. Teor. Fiz. **114**, 2004 (1998) [JETP **87**, 1087 (1998)].
7. O. S. Vaulina, A. P. Nefedov, O. F. Petrov, *et al.*, Phys. Rev. Lett. **88**, 035001 (2002).
8. V. E. Fortov, A. P. Nefedov, V. I. Molotkov, *et al.*, Phys. Rev. Lett. **87**, 205002 (2001).
9. G. Morfill, H. Thomas, U. Konopka, *et al.*, Phys. Rev. Lett. **83**, 1598 (1999).
10. T. Stuffler, G. Schmitt, H. Pfeuffer, *et al.*, in *Proceedings of the 52nd International Astronautical Congress, Toulouse, 2001*, paper IAF-01-J.6.02.
11. A. P. Nefedov, O. S. Vaulina, O. F. Petrov, *et al.*, Zh. Éksp. Teor. Fiz. **122**, 778 (2002) [JETP **95**, 673 (2002)].
12. B. Pieper and J. Goree, Phys. Rev. Lett. **77**, 3137 (1996).

13. U. Konopka, L. Ratke, and H. M. Thomas, Phys. Rev. Lett. **79**, 1269 (1997).
14. A. Homann, A. Melzer, and A. Piel, Phys. Rev. E **59**, 3835 (1999).
15. E. B. Tomme, B. M. Anaratone, and J. E. Allen, Plasma Sources Sci. Technol. **9**, 87 (2000).
16. A. A. Samarian, A. V. Chernyshev, A. P. Nefedov, *et al.*, Zh. Éksp. Teor. Fiz. **119**, 524 (2001) [JETP **92**, 454 (2001)].
17. V. Fortov, A. Nefedov, V. Molotkov, *et al.*, Phys. Rev. Lett. **87**, 205002 (2001).
18. S. Nunomura, D. Samsonov, and J. Goree, Phys. Rev. Lett. **84**, 5141 (2000).
19. C. Zafiu, A. Melzer, and A. Piel, Phys. Rev. E **63**, 066403 (2001).
20. E. B. Tomme, D. A. Low, B. M. Anaratone, and J. E. Allen, Phys. Rev. Lett. **85**, 2518 (2000).
21. E. Thomas, B. Annaratone, G. Morfill, and H. Rothermel, Phys. Rev. E **66**, 016405 (2002).
22. T. Nitter, Plasma Sources Sci. Technol. **5**, 93 (1996).
23. J. Goree, Plasma Sources Sci. Technol. **3**, 400 (1994).
24. O. S. Vaulina, S. A. Khrapak, A. A. Samarian, and O. F. Petrov, Phys. Scr. **84**, 292 (2000).
25. Yu. P. Raizer, *Gas Discharge Physics* (Nauka, Moscow, 1987; Springer-Verlag, Berlin, 1991).
26. Yu. B. Golubovskiĭ and S. U. Nisimov, Zh. Tekh. Fiz. **65** (1), 46 (1995) [Tech. Phys. **40**, 24 (1995)].
27. Yu. B. Golubovskiĭ and S. U. Nisimov, Zh. Tekh. Fiz. **66** (7), 20 (1996) [Tech. Phys. **41**, 645 (1996)].
28. U. Konopka, G. E. Morfill, and L. Ratke, Phys. Rev. Lett. **84**, 891 (2000).
29. V. N. Tsytovich, Usp. Fiz. Nauk **167**, 57 (1997) [Phys. Usp. **40**, 53 (1997)].
30. S. A. Khrapak, A. V. Ivlev, and G. Morfill, Phys. Rev. E **64**, 046403 (2001).
31. D. P. Resendes, J. T. Mendonca, and P. K. Shukla, Phys. Lett. A **239**, 181 (1998).
32. A. S. Ivanov, Phys. Lett. A **290**, 304 (2001).
33. J. E. Daugherty, R. K. Porteous, M. D. Kilgore, *et al.*, J. Appl. Phys. **72**, 3934 (1992).
34. J. E. Allen, Phys. Scr. **45**, 497 (1992).
35. O. S. Vaulina, A. P. Nefedov, O. F. Petrov, *et al.*, Zh. Éksp. Teor. Fiz. **118**, 351 (2000) [JETP **91**, 307 (2000)].
36. E. M. Lifshitz and L. P. Pitaevskii, *Physical Kinetics* (Nauka, Moscow, 1979; Pergamon, Oxford, 1981).
37. N. A. Fuchs, *The Mechanics of Aerosols* (Dover, New York, 1964).
38. A. A. Ovchinnikov, S. F. Timashev, and A. A. Belyĭ, *Kinetics of Diffusion-Controlled Chemical Processes* (Khimiya, Moscow, 1986).
39. O. S. Vaulina and S. A. Khrapak, Zh. Éksp. Teor. Fiz. **119**, 264 (2001) [JETP **92**, 228 (2001)].
40. O. S. Vaulina and S. V. Vladimirov, Phys. Plasmas **9**, 835 (2002).
41. O. S. Vaulina, A. P. Nefedov, O. F. Petrov, *et al.*, Zh. Éksp. Teor. Fiz. **120**, 1369 (2001) [JETP **93**, 1184 (2001)].
42. O. S. Vaulina, S. V. Vladimirov, O. F. Petrov, *et al.*, Phys. Rev. Lett. **88**, 245002 (2002).
43. O. S. Vaulina, Zh. Éksp. Teor. Fiz. **121**, 35 (2002) [JETP **94**, 26 (2002)].
44. S. Hamaguchi, R. T. Farouki, and D. H. E. Dubin, Phys. Rev. E **56**, 4671 (1997).
45. M. J. Stevens and M. O. Robbins, J. Chem. Phys. **98**, 2319 (1993).
46. N. Ohta and S. Hamaguchi, Phys. Plasmas **7**, 4506 (2000).
47. A. Melzer, A. Homann, and A. Piel, Phys. Rev. E **53**, 2757 (1996).
48. F. A. Lindemann, Z. Phys. **11**, 609 (1910).
49. Yu. P. Raĭzer, M. N. Shneĭder, and N. A. Yatsenko, *RF Volume Discharge: Physics, Experimental Methods, Applications* (Mosk. Fiz.-Tekh. Inst., Moscow, 1995).
50. M. R. Akdim and W. J. Goedheer, Phys. Rev. E **65**, 015401 (2002).

Translated by N.N. Ustinovskiĭ

Plasma Physics Reports, Vol. 29, No. 8, 2003, pp. 657–663. Translated from Fizika Plazmy, Vol. 29, No. 8, 2003, pp. 714–721.

PLASMA DYNAMICS

Generation and Interaction of Intense Counterpropagating Plasma Flows

G. N. Dudkin*, B. A. Nechaev*, V. N. Padalko*, V. M. Bystritsky, V. A. Stolupin**, Vit. M. Bystritskii***, and J. Voznyak******

** Nuclear Physics Institute, Tomsk Polytechnical University, pr. Lenina 2a, Tomsk, 634050 Russia*

*** Joint Institute for Nuclear Research, Dubna, Moscow oblast, 141980 Russia*

**** University of California, Irvine, California, USA*

***** Faculty of Physics and Nuclear Technology, Mining and Smelting Academy, Krakov, Poland*

Received June 19, 2002; in final form, January 22, 2003

Abstract—Results are presented from experimental studies of the parameters of two counterpropagating (colliding) plasma flows generated by discharges in crossed electric and magnetic fields. It is shown that the conversion efficiency of the energy deposited in the discharges into the energy of directed plasma flows is 0.3–0.6. For discharge current pulses with a duration of ~10 μs, the energy flux density in the plasma flow reaches ~10 J/cm^2 and the total energy of the flow is on the order of 300 J. The density of deuterons in the flows is ~10^{15} cm^{-3}, and the flow velocity is $\leq 2 \times 10^7$ cm/s. The total number of particles carried by the flows is about 10^{19}. The possibility of using counterpropagating plasma flows to study reactions involving light nuclei (*dd*, *pd*, *dt*, and *d*He reactions) in the range of ultralow collision energies is discussed. © *2003 MAIK "Nauka/Interperiodica".*

1. INTRODUCTION

Experimental studies of reactions between light nuclei (*dd*, *pd*, *dt*, and dHe reactions) in the range of ultralow collision energies (~1 keV) with the use of conventional accelerators are rather problematic. This is related to the low cross sections for these processes in the given energy range ($\sigma \approx 10^{-35}$–10^{-43} cm^2) and the low intensities of charged particle beams. To obtain necessary information about the parameters of reactions between light nuclei in the range of ultralow energies, intense particle flows are required.

In the experimental studies of *dd* processes at ultralow energies (≤3 keV in the center-of-mass frame), the efficient interaction of charged particles is achieved by using intense radially converging ion flows generated in direct and inverse Z-pinches produced with the help of high-current ($I \sim 1$ MA) generators [1, 2]. In this case, the current pulse duration is ~100 ns and the number of ions in the accelerated plasma flow attains ~10^{19}. On the whole, the experiments have shown that Z-pinches are fairly promising for these purposes. However, at high energy densities, the liner undergoes rapid nonlinear processes, including explosive instabilities. These processes are accompanied by a background radiation (neutrons and γ rays), which substantially complicates measurements of the reaction yield and the processing and interpretation of the results of experiments on the interaction of deuterium flows with solid targets at collision energies of ≤3 keV (in the center-of-mass frame). We note that the range of interaction energies from 3 to 6 keV in the center-of-mass frame has not been explored by this method because it is problematic to obtain ions with an energy of 12 keV (6 keV in the center-of-mass frame) in the liner. Meanwhile, the cross section for, e.g., the *dd* reaction, was measured only for energies higher than 6 keV in the center-of-mass frame [3]. Moreover, the efficiency with which the energy deposited in a Z-pinch is converted into the kinetic energy of the accelerated ions is rather low.

These problems stimulated a search for alternative methods for generating intense flows of low-energy light nuclei. It is well known that pulsed plasma accelerators are characterized by a large fraction of the kinetic energy (>60%) of the plasma flow in the total energy balance of the system [4, 5]. On the other hand, the interaction of intense counterpropagating (colliding) plasma flows makes it possible to substantially decrease the deposited energy that is necessary for achieving the required values of the particle interaction energy in the center-of-mass frame. The aim of the present paper is to analyze and experimentally verify this approach to solving the above problems.

Intense counterpropagating plasma flows are generated by discharges in crossed electric and magnetic fields. In this case, Ampère's force, which acts on a unit plasma volume with the current density **J** in an external magnetic field **H**, is equal to

$$\mathbf{F} = \frac{1}{c}\mathbf{J} \times \mathbf{H}. \quad (1)$$

1063-780X/03/2908-0657$24.00 © 2003 MAIK "Nauka/Interperiodica"

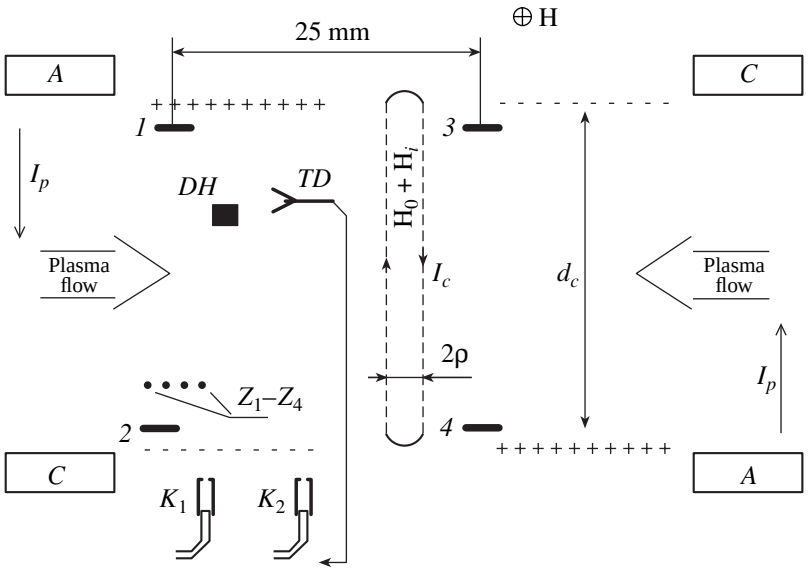

Fig. 1. Arrangement of the detectors in the propagation region of the plasma flows: (*A*) anode, (*C*) cathode, (*H*) magnetic field, (*TD*) calorimeter, (*DH*) Hall detector of the magnetic field, (*1–4*) plates for measuring the induced voltage, (Z_1–Z_4) probes for measuring the Hall potential, and (K_1, K_2) collimators of the optical detectors.

Under the action of this force, a plasma with the density N_i and ion mass M_i accelerates in the direction transverse to the magnetic field and, over a distance l, gains the velocity

$$V_i = \left(\frac{2lJ_pH}{cN_iM_i}\right)^{1/2}. \quad (2)$$

The current density can be expressed in terms of the total discharge current,

$$J = \frac{I_p}{l_H l'}, \quad (3)$$

where l' and l_H are the transverse and longitudinal (with respect to the magnetic field) dimensions of the current-carrying region.

Since the acceleration occurs in the current-carrying region, we have $l \simeq l'$ and

$$V_i \simeq 7.7 \times 10^4 \left(\frac{I_pH}{cN_iM_il_H}\right)^{1/2}, \quad (4)$$

where the current is expressed in amperes.

For two counterpropagating flows accelerated in such a way, the particle collision energy in the center-of-mass frame is equal to $2\varepsilon_0$, where ε_0 is the particle energy in each flow. Then, in the laboratory frame, the maximum particle energy in each flow should be ≤3 keV. The use of counterpropagating flows with a duration of ~10 μs makes it possible to substantially decrease the deposited energy; the energy and density of the plasma flows; and, hence, the intensity of the background radiation.

2. EXPERIMENT

Two pairs of electrodes (24 cm long and 4 cm wide) with interelectrode distances of $d_p \approx 2$ cm are placed in a ceramic chamber (150 cm long and 18 cm in diameter). The chamber is in a solenoidal magnetic field with a strength of $H_{max} = 2 \times 10^4$ Oe. The distance between the centers of the discharge gaps is 10 cm. After filling the preevacuated chamber with a working gas at a pressure of $P_0 \sim 1$ torr, the discharge is ignited. The discharge currents in two discharge gaps flow in the opposite directions across the magnetic field (see Fig. 1). The hydrodynamic acceleration of the plasma in the discharge gaps results in the generation of two plasma flows that move across the magnetic field toward each other and collide at the center of the chamber. The sizes of the flows along the magnetic field are determined by the sizes of the regions where the discharge currents flow in this direction: $l_H \simeq$ 6–10 cm. In turn, the size l_H is determined by the shape and depth of the magnetic well formed in the discharge region.

The parameters of the plasma and ion flows were measured using the diagnostic techniques tested in studying the processes of the interaction of counterpropagating plasma flows in the presence of a magnetic field [6, 7]. We also used the method proposed in [8], in which the possibility was demonstrated of measuring the liner velocity and the particle velocity distribution in the liner with the help of collimated optical detectors positioned a certain distance from each other. The liner radiation was observed near the H_α Balmer spectral line emitted by deuterium atoms produced by the charge

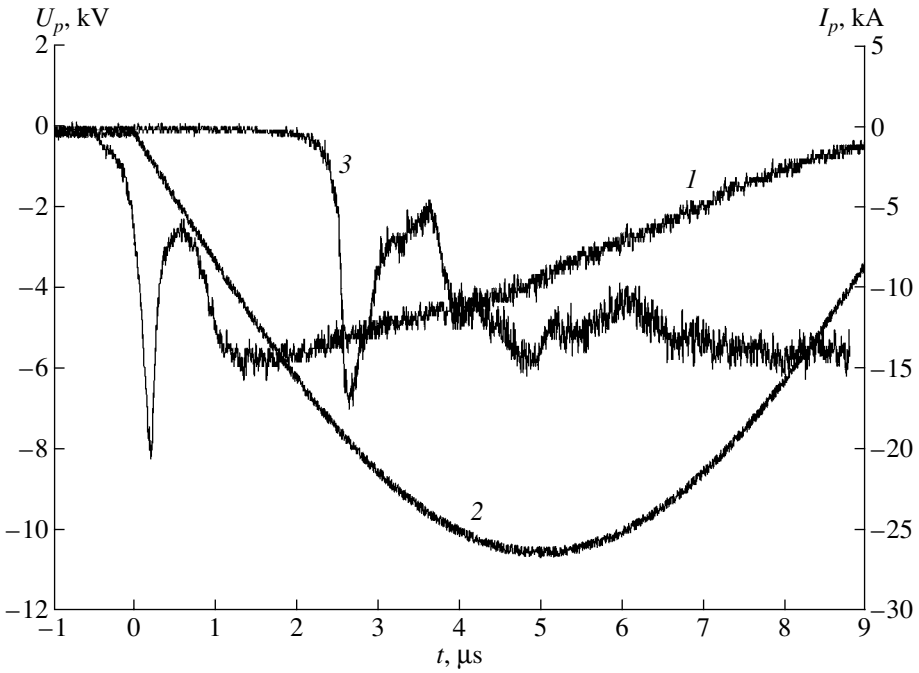

Fig. 2. Waveforms of (*1*) the electrode voltage U_p, (*2*) the discharge current I_p, and (*3*) the signal from the collimated optical detector K_1.

exchange of deuterium ions with the neutrals of the residual gas.

A comparison of the energy deposited in the discharge (Fig. 2) and the flow energy measured with a calorimeter shows that the conversion efficiency K of the energy deposited in the discharge into the energy of the directed motion depends on the initial deuterium pressure. As the initial gas pressure varies from 0.5 up to 1.5 torr, the conversion efficiency K varies within the range 0.3–0.6.

In the course of acceleration, the cold gas enters the discharge region through the inlet cross section, passes through the discharge, and flows out from the outlet cross section. Knowing the dimensions of the discharge region and using the continuity equation for the gas and plasma flows, we can write

$$V_0 N_0 S_0 = V_i N_i S_i , \quad (5)$$

where V_0 and N_0 are the velocity and density of the neutral gas, V_i and N_i are the velocity and density of the ionized gas, $S_i = d_p l_H$ is the cross-sectional area of the gap through which the ionized gas flows out (d_p being the distance between the electrodes), and S_0 is the cross-sectional area of the gap through which the neutral gas enters the discharge. The results of the experimental investigations of the discharge structure in crossed magnetic and electric fields [9] and an analysis of the discharge photographs allows us to conclude that, at the entrance to the interelectrode gap, the discharge is shaped as a semicylinder with the radius $\sim d_p/2$. Thus, we have $S_0 \simeq \pi d_p l_H/2$ and, hence,

$$2 V_i N_i \simeq \pi V_0 N_0 . \quad (6)$$

The expression relating the parameters of the plasma flow and the energy flux measured by a calorimeter has the form

$$\frac{Q}{S_T t_p} = \frac{M_i V_i^2}{2} V_i N_i , \quad (7)$$

where Q is the energy measured by the calorimeter, S_T is the inlet cross section of the calorimeter, and t_p is the FWHM duration of the discharge current pulse.

For a particular shot in an experiment carried out with deuterium at room temperature, the measured parameters were the following: $N_0 \simeq 4 \times 10^{16}$ cm^{-3}, $t_p \simeq 10$ μs, $V_0 \simeq 2 \times 10^5$ cm/s, $S_T = 1$ cm^2, and $Q \simeq 10^8$ erg. In this case, from Eqs. (6) and (7), we find that the flow velocity and density are $V_i \simeq 2 \times 10^7$ cm/s and $N_i \simeq 10^{15}$ cm^{-3}, respectively. The total number of particles in the flows amounts to $\sim 2 \times 10^{19}$.

The plasma bunch velocity measured for the same shot with the help of optical detectors (with a spatial resolution of ~4 mm) is nearly the same (Fig. 3).

The plasma flow velocity can also be estimated from the relation $U/d = V_i H/c$, where U is the voltage induced between 1×1-cm copper plates *1* and *2* located near the electrodes (see Fig. 1), $d = 0.8$ cm is the distance between the plates, and H is the magnetic field strength in the plasma. In order to reduce interferences

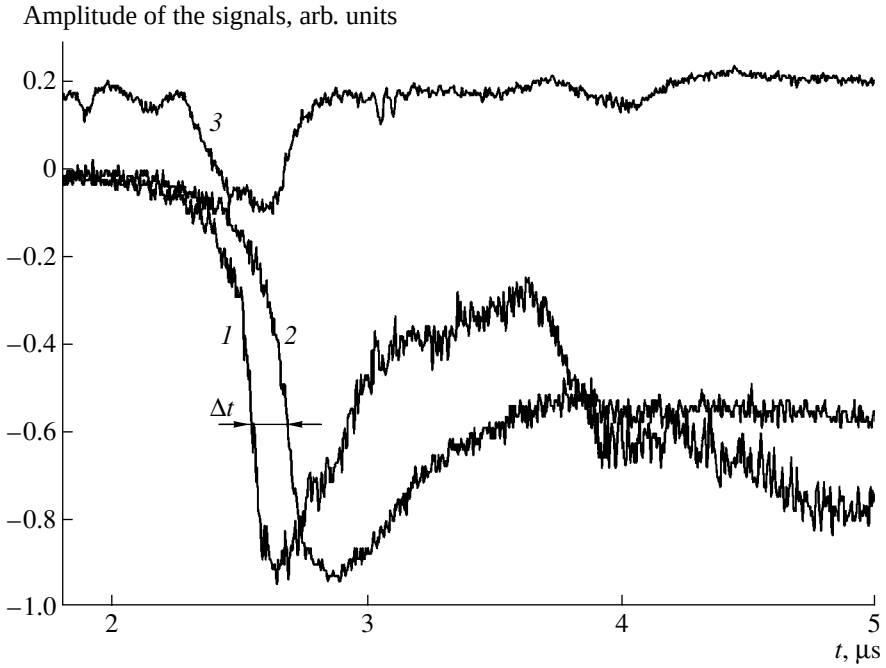

Fig. 3. Waveforms of (*1*, *2*) the signals from optical detectors K_1 and K_2 and (*3*) the Hall potential between probes Z_3 and Z_4.

when measuring the induced voltage and exclude the galvanic coupling between the plasma and the recording devices (Tektronix TDS 224 oscilloscopes), we used optical isolators, whose time resolution (50 ns) was limited by the speed of the light-emitting diode.

Figure 4 shows the waveforms of (*1*) the induced voltage U_{1-2} between plates *1* and *2*, (*2*) the signal from optical detector K_2, and (*3*) the signal from the Hall detector of the magnetic field. The magnetic field detector was fed and the signals from it were read through decoupling transformers. As the absolute value of the voltage U_{1-2} decreased in the time interval 3–4.5 μs, the magnetic field detector showed that the magnetic field decreased with respect to its initial value $H_0 = 10^4$ Oe due to the displacement of the plasma. The residual magnetic field was $\simeq 0.4H_0$. Therefore, the measured voltage $U_{1-2} \simeq -700$ V corresponds to the plasma flow velocity $V_i \simeq cU_{1-2}/(0.4H_d) \simeq 2 \times 10^7$ cm/s.

We also studied the time evolution of the plasma flows with the above parameters in the region where the plasma flows collide with each other. Curve *2* in Fig. 5 shows the waveform of the voltage induced between plates *3* and *4* (see Fig. 1), which are placed in the collision region but are slightly displaced (by ~2–3 mm) from the symmetry axis toward one pair of the electrodes. The negative voltage pulse corresponds to the plasma motion from the electrodes toward the center of the chamber. After the rapid decrease in the signal at the instant of collision, the voltage becomes positive, which means that the plasma flows begin to move away from the center of the chamber. At the same time, the signals from plates *1* and *2*, located at a distance of ~1 cm from the symmetry axis, show that the plasma flows do not reverse their direction in this region (Fig. 5, curve *1*).

3. DISCUSSION

It follows from Fig. 2 that, in spite of the relatively high discharge power, the efficiency with which the energy deposited in the discharge is converted into the directed motion of the flow in the time interval 0–2 μs is rather low; i.e., in terms of [10], the exchange coefficient is small. Without going into the details of the flow formation (such as the time variations in the plasma density and temperature), we call the reader's attention to one important circumstance. For $V_d \neq V_i$ (where V_d is the drift velocity), the drift motion in the discharge is cyclic in character; consequently, there is a velocity component perpendicular to the electrode plane (i.e., the direction of the flow as a whole). When the velocity acquired by the plasma under the action of the Ampère force is close to the drift velocity, the particle trajectories are nearly straight [11]. In this case, the velocity component perpendicular to the electrode plane is minimum; hence, the particle and energy losses on the electrodes are minimum. If we compare the energy deposited in the discharge with the energy measured by a calorimeter and take into account the conversion efficiency in a particular shot ($K \simeq 0.5$), then the above condition can be written the form

$$V_i \simeq V_d = \frac{U_p c}{d_p H_0} \simeq 7.7 \times 10^4 K^{1/2} \left(\frac{I_p H_0}{c N_i M_i l_H} \right)^{1/2}. \quad (8)$$

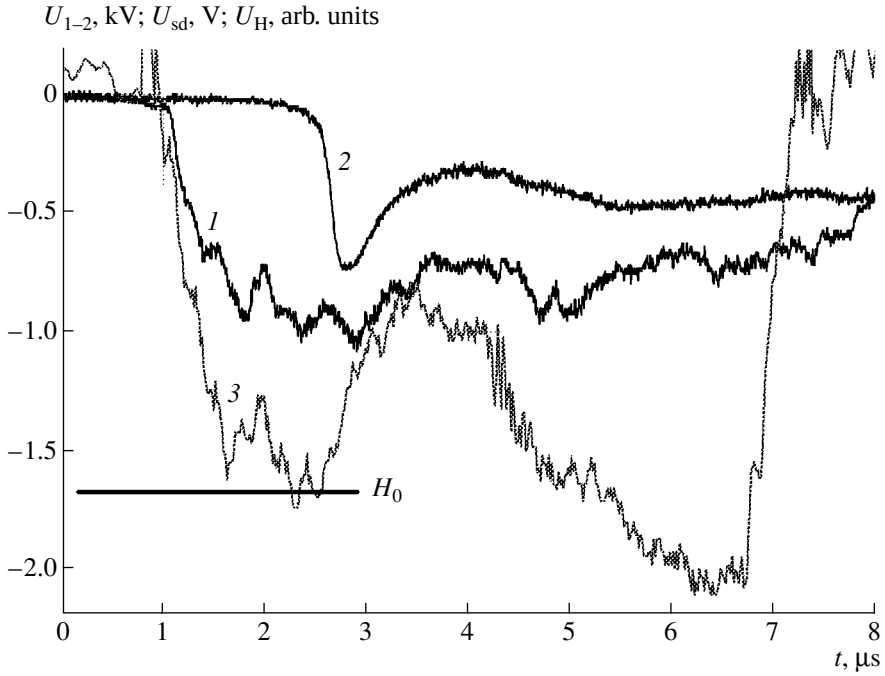

Fig. 4. Waveforms of (*1*) the voltage U_{1-2} induced between plates *1* and *2*, (*2*) the signal U_{sd} from optical detector K_2, and (*3*) the signal U_H from the Hall detector.

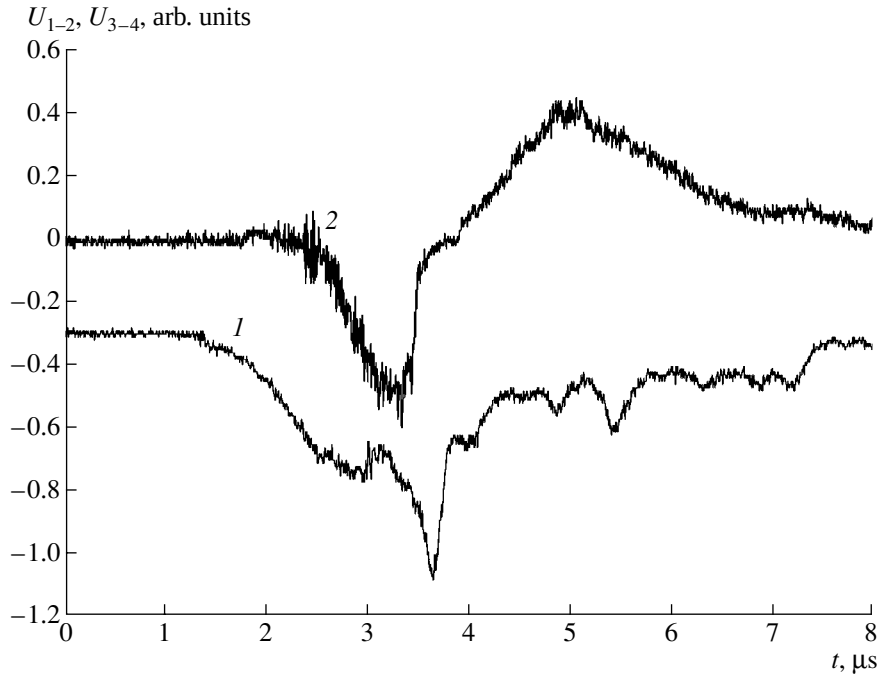

Fig. 5. Waveforms of (*1*) the voltage U_{1-2} induced between plates *1* and *2* and (*2*) the voltage U_{3-4} induced between plates *3* and *4*.

It follows from here that

$$I_p \simeq 1.9 \times 10^{-13} \frac{N_i M_i c^3 U_p^2 l_H}{K H_0^3 d_p^2}, \qquad (9)$$

where U_p is the electrode voltage (in V) and $d_p \simeq 2$ cm is the interelectrode distance.

It can be seen in Fig. 2 that the formed plasma bunch is detected at time $t = t_{eff} \simeq 2.5$ μs. Substituting the

value of the electrode voltage $U_p \simeq 4.7 \times 10^3$ V measured at this time into expression (9) and assuming that $l_H \simeq 10$ cm, $N_i = 10^{15}$ cm^{-3}, and $H_0 = 10^4$ Oe, we find that the discharge current is $I_p \simeq 1.8 \times 10^4$ A. This value agrees well with the current I_p measured at this time. For times $t < t_{\text{eff}}$, we have $V_i < V_d$, because the discharge current is lower than that required to satisfy condition (8). At $t > t_{\text{eff}}$, the discharge current exceeds the optimal value; i.e., $V_i > V_d$ in this case. The efficiency of plasma acceleration and transportation in both cases is lower than the optimal efficiency. According to condition (8), the acceleration is optimum when the following relationship is satisfied: $U_p \sim I_p^{1/2}$, all the other factors being the same.

According to Fig. 3 (curve *3*), the optimum acceleration conditions correspond to the maximum Hall potential (and, accordingly, the minimum Hall current) measured near the electrodes with the help of probes Z_3 and Z_4 (see Fig. 1). It is believed that it is the electrodynamic force component perpendicular to the flow direction (i.e., the electrode plane) that substantially impairs the characteristics of the plasma accelerator (see [10], p. 193).

As the plasma flow moves across the magnetic field outside the interelectrode gap, it becomes polarized. The voltage induced between the flow boundaries corresponds to the electric field $\mathbf{E}_{\text{in}} \sim \mathbf{V}_i \times \mathbf{H}/c$, which is perpendicular to the magnetic field. Thus, outside the discharge region, the plasma flow continues to drift in the crossed fields $\mathbf{E}_{\text{in}}$ and $\mathbf{H}$ in the direction transverse to the magnetic field. When the drift channel is formed, the kinetic energy of the plasma flow is spent on the ionization of the neutral gas (change exchange), the generation of the electric and magnetic fields, Joule losses, and the excitation of oscillations [12].

In the collision region, two counterpropagating flows are partially or completely depolarized, because the polarization fields of the flows point in the opposite directions. We may consider the polarized flows as plasma capacitors with capacitances C_p. When the flows come into contact, the plasma capacitors discharge into each other. The voltage between plates *1* and *2*, as well as plates *3* and *4*, is maintained at a certain level that depends on the parameters of the capacitor discharge circuit (the equivalent inductance and resistance) and the intensity of recharging at the expense of the plasma flow energy, which is determined by the flow density and velocity. Obviously, if the inductance and resistance of the discharge circuit are minimum and the discharge current is much higher than the recharge current, the flows can be completely depolarized. The electric parameters of the discharge circuit are determined by the flow parameters, as well as by the geometry of the region in which the flows collide and interact (see Fig. 1). It is reasonable to assume that the penetration depth of the flows into each other is determined by the flow velocity and the time during which they become completely depolarized. In the case of complete depolarization in the collision region, we have $E \longrightarrow 0$ and, consequently, the drift velocity $V_d \longrightarrow 0$; as a result, the translational motion of the plasma particles transforms into their rotational motion. It is this case that is realized under our experimental conditions when we observe the collision of plasma flows formed under the optimum conditions discussed above (Fig. 5).

When the fronts of the flows are plane and the conditions for the complete depolarization are satisfied, the minimum depth to which the flows penetrate into each other is equal to the doubled ion Larmor radius $\rho_i = M_i V_i c/(eH)$.

The depolarization of the flows during their collision may be treated as the oscillatory motion of charges in a circuit consisting of plasma capacitors and inductances whose parameters are determined by the geometry of the collision region [7]. If the Q factor of the circuit is high enough, then the charge at the plasma capacitor can change its polarity. In the first half-period of the oscillation process, the increase in the current through the circuit (the charge flows from one the plasma capacitor to another) corresponds to an increase in the magnetic field as compared to this initial value; i.e., the Larmor radius in the collision region decreases and the plasma is compressed. To illustrate, we will give some quantitative estimates.

The average current flowing through the circuit during the discharge of the plasma capacitances C_p charged to the voltage U_c can be estimated from the expression $I_c \simeq 0.5 C_p U_c/t_c$, where t_c is the time during which the capacitances are discharged. When the size of the collision region along the direction of the flow is smaller than the transverse size of the plasma flows, the magnetic field produced the discharge current is equal to

$$H_I \approx 0.4\pi C_p U_c/l_H t_c. \tag{10}$$

According to [5], the plasma capacitance is equal to

$$C_p \simeq \frac{M_i N_i c^2 L l_H}{H_0^2 d_c}, \tag{11}$$

where l_H and $d_c \simeq d_p$ are the sizes of the flows along and across the magnetic field, respectively, and L is the plasma capacitance per unit length along the flow direction. When the plasma flows collide, the length over which they are depolarized is equal to

$$L \simeq 2(2V_i t_c + 2\rho_i) = 4V_i(t_c + \omega_i^{-1}), \tag{12}$$

where t_c is the depolarization time and ω_i is the ion cyclotron frequency. Substituting expressions (10) and

(11) into Eq. (9) and taking into account that $U_c = V_i H_0 d_c/c$, we find

$$H_I \simeq 1 \times 10^{-9} \pi \frac{M_i N_i c}{H_0} V_i^2 \left(1 + \frac{1}{\omega_i t_c}\right). \quad (13)$$

Substituting here the above values of H_0, N_i, and V_i and assuming that $t_c \simeq 1/\omega_i \simeq 20$ ns, we obtain $H_I \simeq 10^4$ Oe. Actually, the measured depolarization time is less than 50 ns. However, as was indicated above, the time resolution of optical isolators is $\simeq 50$ ns. On the other hand, the discharge time varies only slightly from shot to shot. Therefore, there is a reason to believe that the actual depolarization time is shorter than the measured one.

Thus, for the given flow parameters, the magnetic field in the collision region doubles; i.e., the plasma is compressed. For the given geometry, the plasma compression ratio is approximately equal to 4. Then, plasma compression in the collision region changes to expansion. The time interval between the collision of the plasma flows ($t \simeq 3.3$ μs) and the time at which the plasma expansion velocity is maximum ($t \simeq 5$ μs) corresponds to the interaction time of certain cut off fractions of the flows (see Fig. 5, curve *2*).

When studying *dd* processes, it is important that the residence time of the particles (ions) in the interaction region be comparable with the average time of the binary collisions τ_{ii}. In other words, the path traveled by the ions during their rotation should be comparable with their mean free path.

It can be seen from Fig. 5 that the interaction time of the plasma flows is ~1.7 μs. This time exceeds the average time of binary collisions.

Estimates show that the mean free path of deuterium ions moving with the velocity $V_i \simeq 5 \times 10^7$ cm/s in a gaseous medium with the density $N_0 \simeq 4 \times 10^{16}$ cm^{-3} is a few tens of centimeters. For the straight-line motion of a single flow, this path would exceed the chamber diameter (18 cm). For a deuterium ion velocity of $V_i \simeq 5 \times 10^7$ cm/s and magnetic field strength of $H_0 = 10^4$ Oe, the depth to which the flows penetrate into each other is $\geq 2\rho_i \simeq 1$ cm.

From the standpoint of studying the *dd* processes, it is desirable that the plasma flows be relatively cold in order to ensure the minimum spread in the ion velocities. The measurements with a calibrated calorimeter showed that the energy transferred by the flow in the acceleration direction was higher than the energy transferred in the opposite direction by more than one order of magnitude. Based on these measurements, we can conclude that the plasma temperature is much lower than the directed kinetic energy of the flows.

In the above experiments, the maximum discharge current was $I_p \simeq 25$ kA. To achieve the desired flow velocity $V_i \simeq 5 \times 10^7$ cm/s (assuming that the energy and the energy flux density in each flow are ~1 kJ and ~25 J/cm^2, respectively), the discharge current estimated from the measured conversion efficiency should be $I_p \simeq 1.5 \times 10^5$ A.

On the whole, the results obtained in this study allow us to conclude that the method proposed is promising for the generation of intense low-*Z* ion flows with energies ≤3 keV.

ACKNOWLEDGMENTS

This work was supported in part by the Russian Foundation for Basic Research (project no. 03-02-17278) and by a grant of the Plenipotentiary of the Republic of Poland at the Joint Institute for Nuclear Research.

REFERENCES

1. V. M. Bystritsky, Vit. M. Bystritskii, V. M. Grebenyuk, *et al.*, Laser Part. Beams **18**, 325 (2000).
2. V. M. Bystritsky, Vit. M. Bystritskii, V. M. Grebenyuk, *et al.*, Nucl. Instrum. Methods **455**, 706 (2000).
3. A. Krauss, H. W. Becker, H. P. Trautvetter, and C. Rolps, Nucl. Phys. A **465**, 150 (1987).
4. A. S. Kamrukov, N. P. Kozlov, E. P. Myshelov, and Yu. S. Protasov, Fiz. Plazmy **7**, 1234 (1981) [Sov. J. Plasma Phys. **7**, 678 (1981)].
5. A. S. Kamrukov, E. P. Myshelov, and Yu. S. Protasov, Fiz. Plazmy **5**, 368 (1979) [Sov. J. Plasma Phys. **5**, 206 (1979)].
6. B. A. Nechaev and A. V. Peshkov, Zh. Tekh. Fiz. **63** (8), 181 (1993) [Tech. Phys. **38**, 725 (1993)].
7. G. N. Dudkin, B. A. Nechaev, and V. N. Padalko, Fiz. Plazmy **23**, 258 (1997) [Plasma Phys. Rep. **23**, 237 (1997)].
8. G. N. Dudkin, B. A. Nechaev, V. N. Padalko, and E. G. Furman, Fiz. Plasmy **27**, 599 (2001) [Plasma Phys. Rep. **27**, 563 (2001)].
9. V. M. Bystritsky, Vit. M. Bystritskii, G. N. Dudkin, *et al.*, in *Proceedings of the Conference on Pulsed Power Plasma Science, Las Vegas, NV, 2001*.
10. A. I. Morozov and A. P. Shubin, *Plasma Accelerators* (Nauka, Moscow, 1984).
11. E. Levi and M. Panzer, *Electromechanical Power Conversion* (McGrow-Hill, New York, 1966; Mir, Moscow, 1969).
12. A. G. Belikov and N. A. Khizhnyak, Fiz. Plazmy **21**, 723 (1995) [Plasma Phys. Rep. **21**, 685 (1995)].

Translated by E.L. Satunina

Plasma Physics Reports, Vol. 29, No. 8, 2003, pp. 664–668. Translated from Fizika Plazmy, Vol. 29, No. 8, 2003, pp. 722–726.

PLASMA DYNAMICS

Synchronization of Parallel-Connected Plasma Opening Switches and Switching the Current to the Load

A. A. Altukhov, P. I. Blinov, G. I. Dolgachev, D. D. Maslennikov, A. S. Fedotkin, and I. A. Khodeev

Russian Research Centre Kurchatov Institute, pl. Kurchatova 1, Moscow, 123182 Russia

Received November 21, 2002

Abstract—The possibility of using plasma opening switches (POSs) to create superpower generators is considered. To decrease the linear density of the charge passed through a POS of reasonable size, it is proposed to use a compact multimodule POS system. The design of an individual POS module is presented. The compact arrangement of the modules is ensured by an external magnetic field. It is proposed to use a sharpening spark gap to increase the efficiency of a multimodule POS operating with a low-inductance load. The results are presented of experiments on synchronizing two POS modules and switching the current to a low-inductance load. *© 2003 MAIK "Nauka/Interperiodica".*

1. INTRODUCTION

The Baikal program envisions the creation of a superpower pulsed current generator with an output voltage of ~10 MV, a current of ~50 MA, and a pulse duration of ~150 ns. As an output stage (power sharpener), it is proposed to use a plasma opening switch (POS) with a rise time of the main current pulse of ~2 μs and a fairly long (~40 μs) prepulse. At present, an MOL device (4–6 MV, 3 MA, 100 ns) is being created for the purpose of modeling the main units of the future generator [1]. As was shown in [2–4], the efficient switching of the current can only be achieved by applying an external axial magnetic field and limiting the linear (along the perimeter of the outer POS electrode) density of the charge passed through the POS ($q_L \leq$ 5 mC/cm). In those papers, it was shown that the suppression of the electron current by an axial magnetic field intensifies plasma erosion and increases the output POS voltage. The increase in the linear charge density q_L by reducing the POS diameter and increasing its length leads to an increase in the self-magnetic field of the POS and to the contraction of the plasma. As a result, the plasma density increases and the POS passes into a less efficient (in terms of the output voltage) magnetohydrodynamic regime. The limitation on the linear charge density means that the perimeter a POS with a current of 50 MA should be $l_0 \sim 100$ m and, accordingly, the POS diameter should be $d_0 \sim 30$ m, which seems unrealistic. For this reason, it was proposed to use a compact multimodule POS system. The total perimeter of a set of n POS modules with the diameter $d_m = d_0/n$ will be equal to l_0; in this case, all the modules can be arranged inside a cylinder of diameter $d_c \approx d_0/n^{0.5}$. In other words, the POS diameter is reduced by a factor of $n^{0.5}$. Thus, 100 modules with a diameter of $d_m = 30$ cm can be arranged inside a cylinder of diameter $d_c \approx 3$ m, the total perimeter being $l_0 \approx 100$ m. It is planned to implement this idea in the MOL device [1]. The device will have seven closely spaced POS modules. This will allow one to halve the outer diameter of the device and decrease the diameter of a vacuum chamber to 1.4 m. To create an efficient multimodule POS for the Baikal program, it is necessary to design a POS module with an applied external magnetic field (which will allow the compact arrangement of such modules), synchronize the modules, and avoid the short-circuiting of the modules after switching the current to a low-inductance load. This study is aimed at solving these problems.

2. DESIGN OF THE MODULE

The compact arrangement of the POS modules is provided by applying an external quasi-steady longitudinal magnetic field produced by a solenoid located at the inner electrode (the POS anode). The magnetic field is screened by the outer electrode (the POS cathode) made of copper. Since the cathode thickness is several times larger than the skin depth, the magnetic field of the solenoid is concentrated inside the cathode–anode gap of the POS. This allows one to compactly arrange the modules without perturbing the magnetic field produced by the solenoid in the POS.

Figure 1 shows a schematic of the module and the configuration of the external magnetic field. The magnetic field topology was chosen so as to prevent the drift of electrons from the cathode to the anode along the magnetic field lines. Thus, the field line passing along the cylindrical surface of the cathode is curved near its end away from the anode. Hence, near the cathode,

1063-780X/03/2908-0664$24.00 © 2003 MAIK "Nauka/Interperiodica"

there are no magnetic field lines along which electrons could be accelerated by the electric field.

The interelectrode gap is filled with a plasma produced by plasma guns with the successive breakdown of ten to twelve gaps. The plasma enters the POS gap from the buffer volumes of the guns through holes in the copper cathode [5]. It is planned to use such plasma guns in the MOL device because they are compact and the dielectric (organic glass) target is protected from the bombardment by the charged particles accelerated in the POS. Moreover, such guns enable the controllable filling of the POS gap with a plasma, which is necessary for transmitting a prepulse [5]. To diminish the plasma production on the POS electrodes in the MOL device, it is proposed to cover them with a pyrocarbon coating.

3. EXPERIMENTAL SETUP

Experiments on the synchronization of two POS modules and the switching of the current to a low-inductance load were carried out in the RS-20 device [6]. The pyrocarbon protection of the POS electrodes was not applied. For this reason and because of the moderate strength of the external magnetic field, the energy potential of the Marx generator (MG) of the device was used only partially. We used only two MG units with eight or two stages; the MG voltage was 320 or 80 kV, the current amplitude was 80 or 150 kA, and the current rise time was 2 or 4 μs, respectively. Figure 2 shows the arrangement of the POS modules and the measurement units. The magnetic field coils located on the high-voltage electrodes (anodes) of the POS modules were fed through a 6-μH decoupling choke. The rise time of the magnetic field was ~0.2 ms, and the averaged (over the POS gap) amplitude of the magnetic field was up to 3.6 kOe. The input (I_1, I_3) and output (I_2, I_4) currents of the POS modules and the current through the load (I_5) were measured with Rogowski coils. The total current I_0 in the MG–POS circuit was measured with the help of a shunt, and the POS current I_{POS} was determined from the difference between the total current I_0 (the input current) and the load current I_5 (the output current). The MG output voltage was measured with a voltage divider, and the signal proportional to the voltage LdI_0/dt in the MG–POS circuit was measured with a *B*-field loop. The signals from the divider (U_d) and the loop (U_l) were used to determine the voltage across the POS [6]. The load inductance was $L_{load} \approx 0.4$ μH, and the inductance of the connection between the POS modules was $L_c \approx 0.2$ μH.

We note that the possibility of POS synchronization was first demonstrated in the experiments of [7], in which two parallel-connected POSs with a common cathode and magnetic-field solenoid were connected to identical loads. The instants of switching of the POSs were determined from the appearance of the current in the corresponding load. Our scheme allows one to use individual POS modules, examine in detail the synchronization process and the dynamics of the current redistribution between the POS modules, and use a common load.

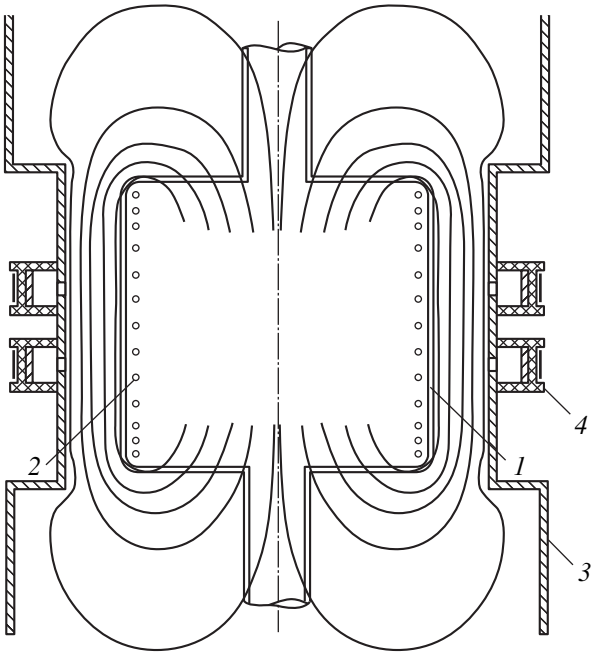

Fig. 1. Schematic of the POS module and the configuration of the external magnetic field in its gap: (*1*) high-voltage electrode (the POS anode), (*2*) solenoid producing the external magnetic field, (*3*) POS cathode, and (*4*) plasma guns.

To prevent the short-circuiting of the POS immediately after the current is switched to the low-inductance load, it was proposed to use a separating spark gap between the POS output and the load. It was supposed that the operation of the gap will be preceded by a sufficiently deep plasma erosion; under the condition of magnetic insulation by an external magnetic field, this should substantially increase the time interval before the second short-circuiting of the POS.

4. EXPERIMENTAL RESULTS AND DISCUSSION

At the elevated density of the plasma produced by the plasma guns (the operating regime of the guns is controlled by the gun voltage and the time delay between the instants at which the guns and the MG are switched on) and without an external magnetic field, the POS modules are shorted and no current breaking occurs. The POS current oscillates with a period T_0, which depends on the inductance L_0 of the MG–POS circuit. In this case, the signals from the Rogowski coils and the shunt satisfy the equalities $I_1 = I_3$, $I_0 = I_1 + I_3$, and $I_2 = I_4 = I_5 = 0$. When the plasma guns are switched off and the separating gap is shorted, the current flows through the load and is oscillatory in character; the

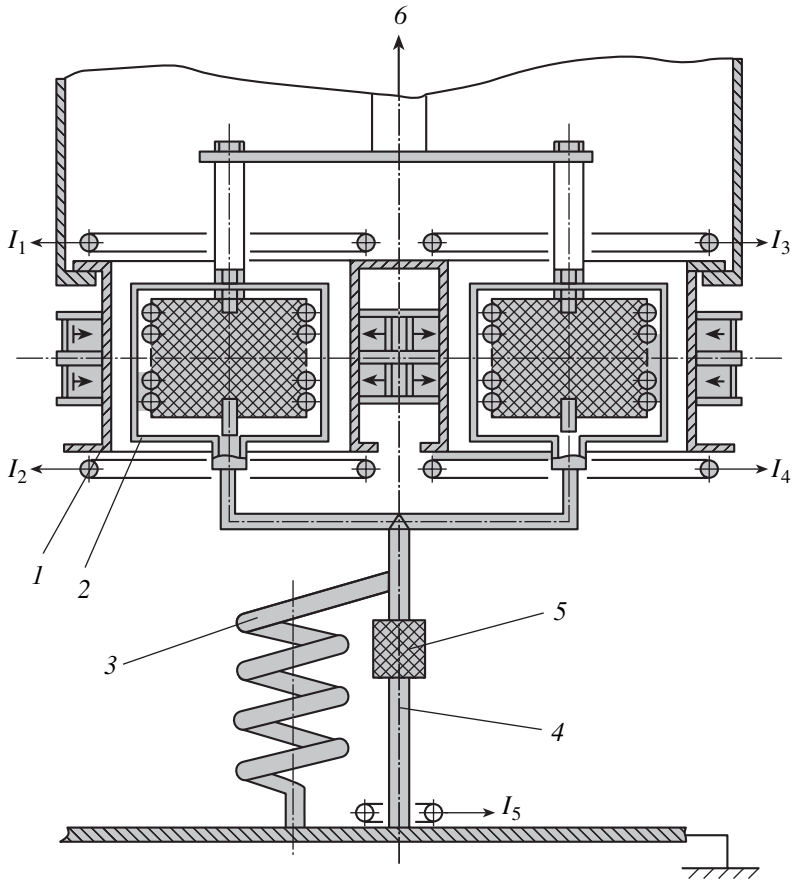

Fig. 2. Layout of an experiment on the synchronization of two POS modules and the switching of the current to a low-inductance load: (*1*) cathode of the POS module with plasma guns, (*2*) anode of the POS module with a magnetic field solenoid, (*3*) decoupling choke for powering the solenoid, (*4*) load, (*5*) separating spark gap, (*6*) to the high-voltage electrode of the MG, (I_1, I_3) signals from Rogowski loops at the inputs of the POS modules, (I_2, I_4) signals from Rogowski loops at the outputs of the POS modules, and (I_5) signal from a Rogowski loop for measuring the load current.

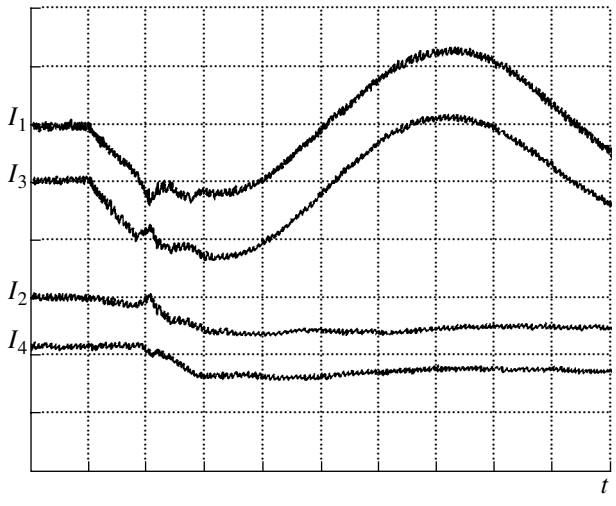

Fig. 3. Oscillograms of the currents at the inputs (I_1, I_3) and outputs (I_2, I_4) of the POS modules (50 kA/division); the time scale is 1 μs/division. Operating conditions: eight MG stages, H_z = 2 kOe.

oscillation period T_{load} depends on the inductance of the MG–load circuit, $L_0 + L_{load} + L_c$. In this case, the MG current flows successively through the shunt, the input and output Rogowski coils, and the load loop and the detector signals satisfy the equalities $I_0 = I_5 = I_1 + I_3 = I_2 + I_4$ and $I_1 = I_2 = I_3 = I_4$. These experiments allowed us to calibrate the current detectors and check the design value of the load inductance.

The synchronization of the POS modules consists in the redistribution of the currents through the modules. This is most evidently demonstrated by the example of the passive break of the POS, when the plasma density is sufficiently high and the external magnetic field is relatively low. In this case, only a small fraction of energy is spent on the acceleration of ions (i.e., plasma erosion). Under these conditions, the partial break of the current through the POS module is not irreversible and the POS conductivity is restored. It can be seen from Fig. 3 that the increase in the resistance of one of the modules results in a decrease in the current flowing through it, because some fraction of the current is switched to the other module. Due to the finite induc-

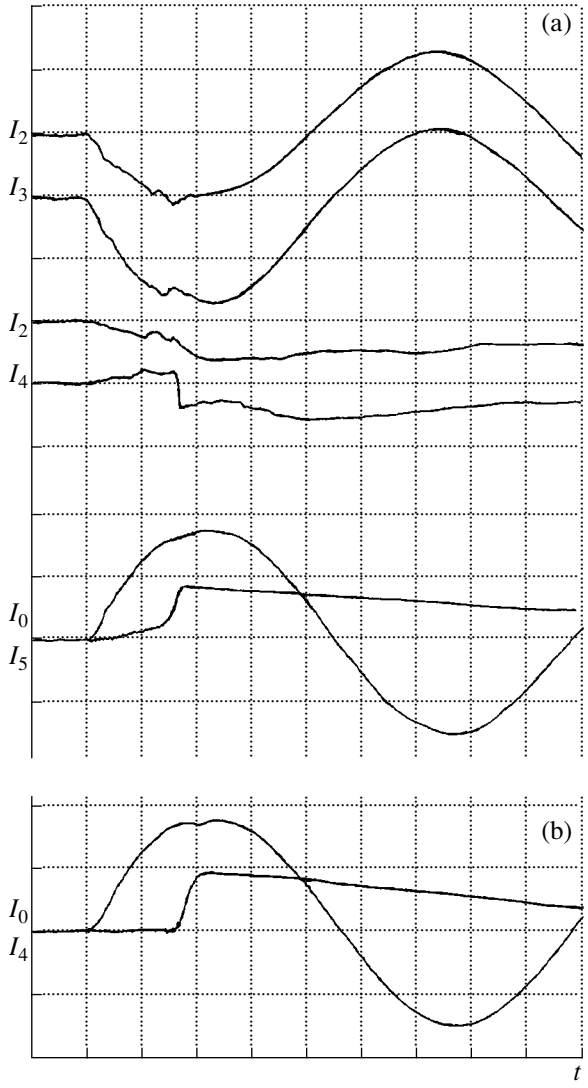

Fig. 4. Oscillograms of the currents at the inputs (I_1, I_3) and outputs (I_2, I_4) of the POS modules (50 kA/division), the total current I_0, and the load current I_5 (75 kA/division): (a) without and (b) with a separating spark gap; the time scale is 1 μs/division. Operating conditions: eight MG stages, H_z = 3.6 kOe.

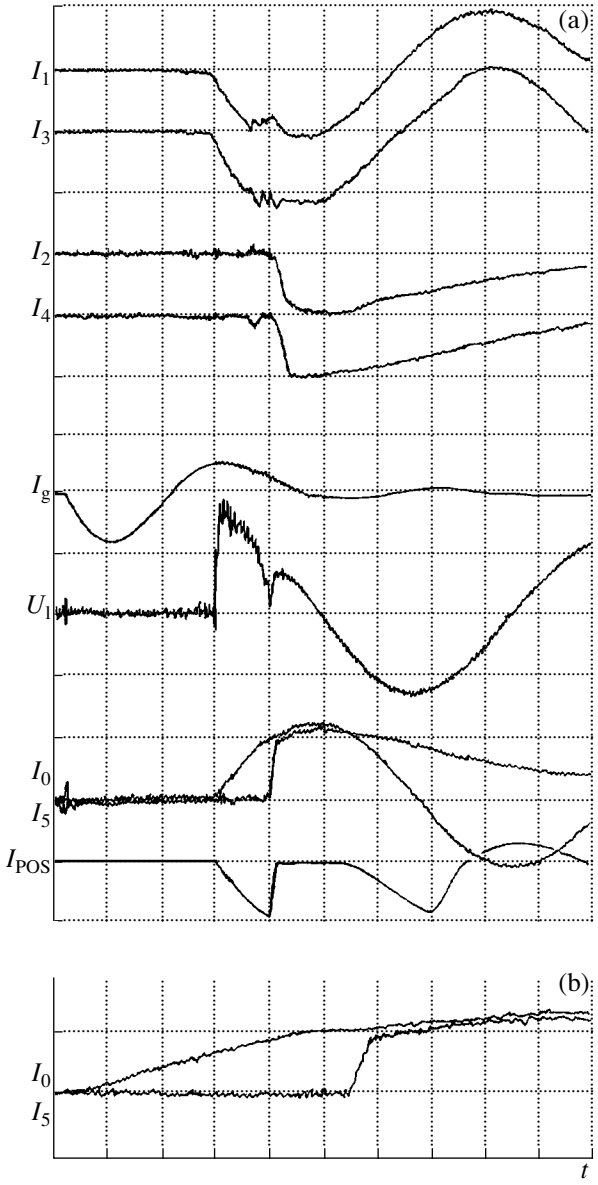

Fig. 5. (a) Oscillograms of the currents at the inputs (I_1, I_3) and outputs (I_2, I_4) of the POS modules (50 kA/division), the plasma-gun current I_g (arb. units), the *B*-field loop signal U_l, the total current I_0, the load current I_5 (100 kA/division), and the POS current $I_{POS} = I_0 - I_5$ (100 kA/division); the time scale is 2 μs/division. (b) Oscillograms of the total current I_0 and load current I_5 (100 kA/division); the time scale is 0.4 μs/division. Operating conditions: two MG stages, H_z = 3.6 kOe; the separating spark gap is switched on.

tance of the connection between the POS modules, this process occurs with a time delay. Since the current flowing through the other module increases, its resistance increases and the conductivity of the first module is restored. As a result, a fraction of the current is switched to the first module. This process resembles the operation of an *LC* oscillator: the current that is switched from the first POS module to the second one initiates plasma erosion in the second module. This is accompanied by the generation of a voltage, which, in turn, results in the change of the current direction. The exchange by the currents between the POS modules lasts nearly 1 μs and ends after the final short-circuiting of both modules. The exchange by the currents is accompanied by energy losses in the POS. Also, there is a small voltage drop across the POS and a fraction of the current is switched to the load. In this case, the current in the MG–POS *LC* circuit oscillates with the period $T = 2\pi(LC)^{1/2}$, whereas the current in the POS–load *LR* circuit decreases as $e^{-tR/L}$, so that both currents flow through the POS. We note that, under the same

operating conditions (i.e., the same voltages at the guns and the MG and the same time delay between the instants at which the guns and the MG are switched on), sometimes one of the identical POS modules is switched on first and sometimes another one is.

When an asymmetry of the POS modules was artificially introduced (the number of the operating guns in the first POS module was halved), most of the current flowed through the second POS module (see Fig. 4a). Note that the current enters the second module both through the upper (high-voltage) and lower (grounded through the load and the separating spark gap) connections between the modules. As a result, the signal I_4 from Rogowski coil *4* (see Fig. 2) is opposite in sign. Simultaneously, the load current begins to grow. After the second module is switched on, the current I_4 abruptly changes its sign and both modules operate as a single POS. In this case, after a relatively long prepulse, the current is rapidly switched to the load. Since the magnetic field is insufficiently strong, the POS gap is bridged again when the load current reaches only ~60% of the current flowing in the MG–POS circuit. In the presence of a separating spark gap, two asymmetric modules operate as a single POS (Fig. 4b). The synchronization process ends before the breakdown of the separating gap and the disappearance of the current prepulse in the load.

In order to achieve the required magnetic insulation in the POS gap at a moderate magnetic field strength, we had to decrease the MG voltage and keep only two stages, which provided a voltage of 80 kV. Although in this case the current rise time increased to ~4 μs, we achieved the fast switching of the current to the load in ~0.2 μs and the second short-circuiting of the POS was delayed by nearly 3 μs (Fig. 5). This means that, for these three microseconds, the POS remained open and no current flowed through it. At the instant of current breaking, 30–40% of the energy stored in the inductance was liberated in the POS, which ensured a fairly long pause in the POS current.

5. CONCLUSIONS

(i) Current spikes with an amplitude of 10–20% of the maximum current value and a duration of ~10% of the current rise time result in the equalization of the resistances of the parallel-connected POS modules. Hence, in order to synchronize the POS modules, it is sufficient that the difference between the charges passed through the POS modules be at a level of 1% of the charge passed through each module. In this case, the inductance of the connection between the modules, as well as the inductance of the MG–POS circuit, should satisfy the inequality $L_c \le 0.2L_0$.

(ii) The use of a separating spark gap in the load circuit makes it possible to switch the current to the load after the end of the synchronization process. In this case, two POS modules with a different number of plasma guns operate as a single POS with the total number of plasma guns.

(iii) As the external magnetic field H_z increases within the range $(1–4)H_{cr}$ (where H_{cr} is the critical magnetic field that ensures the cutoff of electrons in the POS gap and allows one to attain the maximum voltage across the gap), the current flowing through the load increases from 40 to 100%. For the maximum magnetic field ($H_z \approx 4H_{cr} \approx 2H_\varphi$, where H_φ is the self-magnetic field of the POS), the use of a separating spark gap allows one to reduce the rise time of the load current to 10% of the current rise time in the MG–POS inductive storage circuit and, more importantly, delay the second short-circuiting of the POS by a time comparable to the POS current rise time.

ACKNOWLEDGMENTS

We thank A.I. Zhuzhunashvili for designing and manufacturing the Rogowski loops. This work was supported in part by the Russian Foundation for Basic Research (project no. 03-02-16766) and the Russian Federal Program "Government Support of the Leading Scientific Schools" (project no. 2292.2003.2).

REFERENCES

1. É. A. Azizov, S. G. Alikhanov, E. P. Velikhov, *et al.*, Vopr. At. Nauki Tekh., Ser. Termoyad. Sint., No. 3, 3 (2001).
2. G. I. Dolgachev, L. P. Zakatov, and A. G. Ushakov, Fiz. Plazmy **17**, 1171 (1991) [Sov. J. Plasma Phys. **17**, 679 (1991)].
3. G. I. Dolgachev and A. G. Ushakov, Fiz. Plazmy **27**, 121 (2001) [Plasma Phys. Rep. **27**, 110 (2001)].
4. N. U. Barinov, S. A. Budkov, G. I. Dolgachev, *et al.*, Fiz. Plazmy **28**, 202 (2002) [Plasma Phys. Rep. **28**, 177 (2002)].
5. G. I. Dolgachev, D. D. Maslennikov, and D. V. Ryzhov, in *14th International Conference on High-Power Particle Beams and the 5th International Conference on Dense Z-Pinches, Albuquerque, NM, 2002*, Book of Abstracts, paper 93.
6. S. A. Budkov, N. U. Barinov, S. A. Dan'ko, *et al.*, Prib. Tekh. Éksp., No. 2, 112 (2002).
7. Yu. P. Golovanov, L. P. Zakatov, G. I. Dolgachev, *et al.*, Vopr. At. Nauki Tekh., Ser. Termoyad. Sint., No. 2, 35 (1987).

Translated by N.F. Larionova

Plasma Physics Reports, Vol. 29, No. 8, 2003, pp. 669–674. Translated from Fizika Plazmy, Vol. 29, No. 8, 2003, pp. 727–733.

PLASMA OSCILLATIONS AND WAVES

Parametric Excitation of Surface Waves at the Boundary between a Magnetized Plasma and a Metal

N. A. Azarenkov, Yu. A. Akimov, and V. P. Olefir

Karazin National University, pl. Svobody 4, Kharkov, 61077 Ukraine

Received January 9, 2003; in final form, February 18, 2003

Abstract—A study is made of the parametric excitation of potential surface waves propagating in a planar plasma–metal waveguide structure in a magnetic field perpendicular to the plasma–metal boundary. An external, spatially uniform, alternating electric field at the second harmonic of the excited wave is used as the source of parametric excitation. A set of equations is derived that describes the excitation of surface waves due to the onset of decay instability. Expressions for the growth rates in the linear stage of instability are obtained, and the threshold amplitudes of the external electric field above which the parametric instability can occur are found. Analytic expressions for the saturation amplitudes are derived with allowance for the self-interaction of each of the excited waves and the interaction between them. The effect of the plasma parameters and the strength of the external magnetic field on the saturation amplitude, growth rates, and the threshold amplitudes of the pump electric field are analyzed. © *2003 MAIK "Nauka/Interperiodica".*

1. INTRODUCTION

At present, plasma–metal waveguides are widely used in plasma electronics, semiconductor electronics, gas discharges, and various plasma technologies [1]. In this connection, the physical processes occurring in plasma–metal structures are actively studied both theoretically and experimentally [1–5]. A characteristic feature of such waveguide structures is the presence of surface waves (SWs) propagating in them, whose parameters are essentially governed by the external magnetic field. The linear theory of SWs in a waveguide in a magnetic field parallel to the plasma–metal boundary has been developed fairly well both in the Voigt geometry (in which the external magnetic field is perpendicular to the propagation direction of the wave) and in the Faraday geometry (in which the magnetic field is parallel to the propagation direction of the wave) [3–6]. In practice, however, many types of waveguide structures operate with a magnetic field oriented perpendicular to plasma–metal boundary [7–9]. Such waveguides are typical of rf and microwave discharge devices, magnetrons, Penning sources, magnetic discharge pumps, Hall detectors, divertor- and limiter-equipped fusion systems, devices for the plasma processing of metal surfaces, and so on.

The linear theory of potential SWs at the plasma–metal boundary in such magnetic field configurations has been developed fairly well [8, 9], and some nonlinear mechanisms for the self-interaction of these SWs have also been investigated [10, 11]. However, the construction of a nonlinear theory of SWs requires a detailed study of the mechanisms for their excitation. In the waveguide structures in question, SWs are difficult to excite by charged particles because of the presence of an external magnetic field perpendicular to the plasma–metal boundary. In this situation, a more promising way is to excite SWs parametrically [12, 13]. Our objective here is to investigate the efficiency of this excitation method.

2. FORMULATION OF THE PROBLEM

We analyze the parametric excitation of a high-frequency SW propagating along a plane plasma–metal boundary in the y direction (Fig. 1). A highly nonisothermal plasma ($T_e \gg T_i$, where T_e and T_i are the electron and ion plasma temperatures, respectively) occupies the half-space $x > 0$ and is bounded at $x = 0$ by a perfectly conducting metal surface. A constant magnetic field $\mathbf{H}_0$ is directed along the x-axis, which is perpendicular to the plasma–metal boundary.

It is well known that the properties of SWs in an inhomogeneous plasma are strongly influenced by the spatial distribution of plasma density in the boundary layer. In plasmas with large and small density inhomogeneities, the properties of SWs are determined by the integral parameters of the plasma in the region where

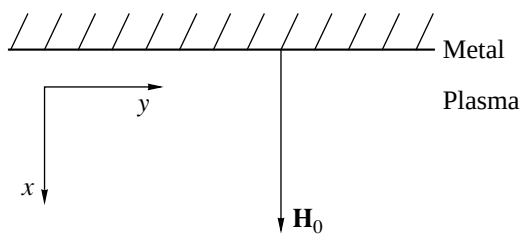

Fig. 1. Geometry of the problem.

1063-780X/03/2908-0669$24.00 © 2003 MAIK "Nauka/Interperiodica"

the wave field is localized. [4]. In these cases, the plasma–metal boundary can be assumed to be sharp and the plasma density can be treated as uniform and set equal to its mean value in the localization region of the SW. This approach was found to be effective and to agree well with the experimental data, in particular, with those from experimental investigations of gas discharges maintained by SWs [14, 15]. Below, the efficiency of the parametric excitation of SWs will be determined under the assumptions that the plasma–metal boundary is sharp and the plasma is homogeneous.

In [8], it was shown that, in the waveguide structure under consideration, high-frequency potential SWs can be excited at frequencies higher than the electron cyclotron frequency, $\omega > \omega_{ce}$. In what follows, we consider the parametric excitation of such waves at the boundary between a weakly collisional dense plasma ($\omega^2 \ll \omega_{pe}^2$, where ω_{pe} is the electron plasma frequency) and a metal. In this case, the wavenumber and frequency of the excited SW are related by [8]

$$k^2 = \omega^2(\omega^2 - \omega_{ce}^2)/(V_{Te}^2\omega_{pe}^2), \quad (1)$$

where V_{Te} is the electron thermal velocity. Analysis of relationship (1) shows that the phase velocity of an SW is much higher than the electron thermal velocity. This agrees with the condition that was adopted in [8] in order to describe the plasma properties in the hydrodynamic approach. At the same time, in the case of a dense plasma, the condition that the SWs be potential imposes the following restriction on the intensity of the thermal motion of plasma electrons: $V_{Te} \ll c(\omega^2 - \omega_{ce}^2)^{1/2}/\omega_{pe}$, where c is the speed of light in vacuum.

Note that an important property of the waves under study is that they are reciprocal [8]. This means that there exist two oppositely propagating waves with the same frequency ω and the same (in absolute value) wavenumbers $k_1 = k(\omega)$ and $k_2 = -k(\omega)$. It is this property that makes possible parametric excitation of the waves in question due to decay instability [12]. That this method is efficient is evidenced by the fact that the self-interaction of SWs [10] is accompanied by the excitation of both the modes at the second harmonic and static, purely surface perturbations. Consequently, SWs excited at a plasma–metal boundary are not subject to the nonlinear damping associated with the excitation of internal modes, which can result in a loss of energy.

We assume that the source of parametric excitation is an external, spatially uniform electric field oscillating at a frequency ω_0 and directed along the external magnetic field:

$$E = E_0\cos(\omega_0 t). \quad (2)$$

In this case, the spatiotemporal synchronization condition [12] takes the form

$$\omega_0 = \omega + \omega, \quad 0 = k_1(\omega) + k_2(\omega). \quad (3)$$

We can see that the interaction between SWs with the frequency $\omega = \omega_0/2$ and a pump wave is the most efficient.

The parametric excitation of SWs will be investigated in a weakly nonlinear approximation [4, 12], which is valid for sufficiently small SW amplitudes and in which the small nonlinearity parameters are $\mu_{1,2} = e|A_{1,2}|/(m_e V_{Te}^2) \ll 1$, where $A_{1,2}$ are the amplitudes of the excited SWs and e and m_e are the charge and mass of an electron, respectively. In this approximation, Poisson's equation and the nonlinear quasi-hydrodynamic equations for electron motions in the SW field can be written as

$$\begin{aligned}
\Delta\varphi &= 4\pi e n_e, \\
\frac{\partial n_e}{\partial t} + \nabla\cdot(n_e\mathbf{V}_e) &= 0, \\
\frac{\partial \mathbf{V}_e}{\partial t} + (\mathbf{V}_e\cdot\nabla)\mathbf{V}_e &= \frac{e}{m_e}\nabla\varphi - \frac{e}{m_e c}\mathbf{V}_e\times\mathbf{H}_0 \\
&\quad - V_{Te}^2\frac{\nabla n_e}{n_e} - \nu\mathbf{V}_e,
\end{aligned} \quad (4)$$

where φ is the wave potential, $\mathbf{V}_e$ and n_e are the hydrodynamic velocity and density of the plasma electrons, and ν is the effective frequency of their collisions. The solution to this set of equations can be expanded in harmonics of the SW frequency ω:

$$\mathbf{W}(\mathbf{r}, t) = \sum_{s=0}^{\infty}\mathbf{W}^{(s)}(\mathbf{r}, t), \quad (5)$$

where $\mathbf{W}^{(s)}(\mathbf{r}, t)$ is the amplitude of the sth harmonic.

The first harmonic $\mathbf{W}^{(1)}(\mathbf{r}, t)$ can be expressed as $\mathbf{W}^{(1)}(\mathbf{r}, t) = \mathbf{W}_1^{(1)}(\mathbf{r}, t) + \mathbf{W}_2^{(1)}(\mathbf{r}, t)$, where $\mathbf{W}_1^{(1)}(\mathbf{r}, t)$ and $\mathbf{W}_2^{(1)}(\mathbf{r}, t)$ are perturbations with the frequency ω and the wavenumbers $k_1 = k(\omega)$ and $k_2 = -k(\omega)$, respectively. According to [8], these perturbations can be represented in the form

$$\begin{aligned}
&\mathbf{W}_j^{(1)}(\mathbf{r}, t) \\
&= 0.5[\mathbf{W}_{1j}(x)\exp(i\psi_{1j}) + \mathbf{W}_{1j}^*(x)\exp(-i\psi_{1j})], \\
&\mathbf{W}_{1j} = (\varphi_{1j}, n_{1j}, \mathbf{V}_{1j}), \quad \psi_{1j} = k_j y - \omega t, \\
&\varphi_{1j}(x) = A_j[\exp(-\lambda_1 x) - \exp(-\lambda_2 x)], \\
&n_{1j}(x) = [eA_j/(m_e V_{Te}^2)] \\
&\times n_0[\exp(-\lambda_1 x) - \omega^2\omega_{ce}^2/\omega_{pe}^4\exp(-\lambda_2 x)], \\
&V_{x1j}(x) = -[ieA_j\omega/(m_e V_{Te}\omega_{pe})] \\
&\times[\exp(-\lambda_1 x) - \exp(-\lambda_2 x)],
\end{aligned} \quad (6)$$

$$V_{y1j}(x) = -\{eA_j\omega k_j/[m_e(\omega^2-\omega_{ce}^2)]$$
$$\times[\omega^2/\omega_{pe}^2\exp(-\lambda_1 x)-\exp(-\lambda_2 x)]\},$$
$$V_{z1j}(x) = \{ieA_j\omega_{ce}k_j/[m_e(\omega^2-\omega_{ce}^2)]\}$$
$$\times[\omega^2/\omega_{pe}^2\exp(-\lambda_1 x)-\exp(-\lambda_2 x)],$$
$$\lambda_1 = \omega_{pe}/V_{Te},\quad \lambda_2 = \omega^2/(V_{Te}\omega_{pe}),$$
$$\lambda_1 \gg \lambda_2,\quad j = 1,2,$$

where ψ_{1j} are the phases of SWs and the asterisk denotes the complex conjugate. Note that the above linearized expressions were obtained under the assumption that the plasma is weakly collisional, $\nu \ll \omega$.

In the weakly nonlinear approximation [12], we can substitute expressions (6) into the nonlinear terms in quasi-hydrodynamic equations (4) to obtain a set of nonlinear equations describing the dependence of the amplitudes of SWs on time in their interaction with the pump field. In investigating the parametric excitation, it should be kept in mind that, in a weakly collisional plasma, the damping of SWs can have a strong impact on their excitation. That is why, in analogy with [12], we introduce additional terms that take into account a weak nonlinear damping of the excited waves. Thus, the spatiotemporal dynamics of the excitation of SWs by an external, spatially uniform, alternating electric field at the second harmonic of the frequency of the excited wave can be described by the following set of nonlinear equations:

$$\left.\begin{aligned}\frac{\partial A_1}{\partial t}\pm V_g\frac{\partial A_1}{\partial y}+\nu A_1 &= -i\alpha A_0 A_2^*\\ \frac{\partial A_2}{\partial t}\mp V_g\frac{\partial A_2}{\partial y}+\nu A_2 &= -i\alpha A_0 A_1^*\end{aligned}\right\}, \quad (7)$$

where the coefficient $\alpha = e\omega F/(4m_e V_{Te}^2)$ characterizes the interaction of the excited SWs with the pump field, the parameter $F = \omega_{pe}^2(\omega^2-\omega_{ce}^2)/[\omega^2(2\omega^2-\omega_{ce}^2)]$ accounts for the influence of the magnetic field and plasma density on the efficiency of the wave excitation, $V_g = V_{Te}\omega_{pe}(\omega^2-\omega_{ce}^2)^{1/2}/(2\omega^2-\omega_{ce}^2)$ is the group velocity of the SWs, and $A_0 = r_{de}E_0$ with $r_{de} = V_{Te}/\omega_{pe}$ being the electron Debye radius. The upper (lower) sign in Eqs. (7) corresponds to the propagation of the first wave in the positive (negative) direction along the *y*-axis and the propagation of the second wave in the negative (positive) direction. In what follows, we consider the temporal dynamics of the SW amplitudes in a case in which the second terms on the left-hand sides of Eqs. (7) can be neglected.

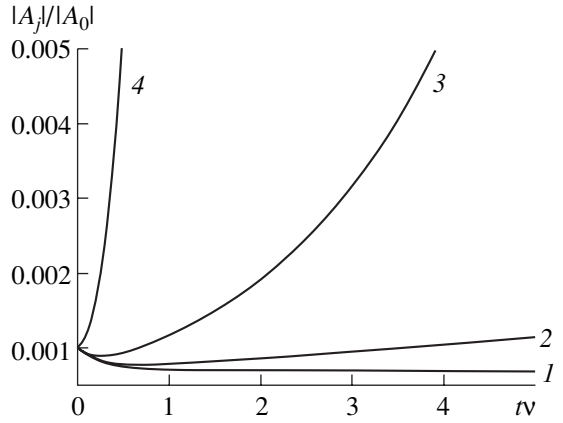

Fig. 2. Time evolution of the SW amplitudes for different values of the parameter $\alpha|A_0|/\nu$: (*1*) 1.0, (*2*) 1.1, (*3*) 1.5, and (*4*) 5.0. The initial SW amplitudes are $A_1(0) = A_2(0) = 10^{-3}A_0$.

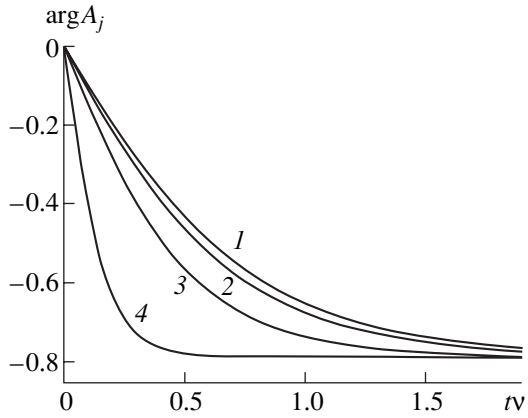

Fig. 3. Time evolution of the SW phases for different values of the parameter $\alpha|A_0|/\nu$: (*1*) 1.0, (*2*) 1.1, (*3*) 1.5, and (*4*) 5.0. The initial SW amplitudes are $A_1(0) = A_2(0) = 10^{-3}A_0$.

3. THRESHOLD AMPLITUDE OF THE PUMP FIELD

It is well known that the process of the parametric excitation of SWs is threshold in nature. Numerical integration of Eqs. (7) showed that SWs can be excited under the condition $\alpha|A_0|/\nu > 1$. A further increase in the parameter $\alpha|A_0|/\nu$ leads to a sharper increase in the amplitude $|A_j|$ of the excited waves (Fig. 2) and a sharper decrease in their phase $\arg A_j$ (Fig. 3). In the opposite case when $\alpha|A_0|/\nu < 1$, the parametric instability does not develop.

Analysis of Eqs. (7) yields the following time dependence of the amplitudes of the excited waves:

$$|A_j(t)|^2 = |A_j(0)|^2$$
$$+(|A_1(0)|^2+|A_2(0)|^2)\sinh^2(\alpha|A_0|t)\exp(-2\nu t), \quad (8)$$
$$j = 1,2.$$

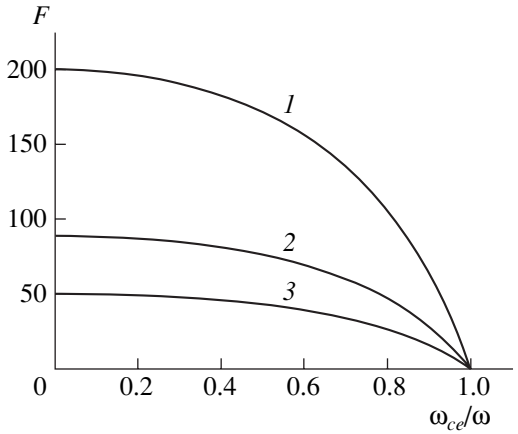

Fig. 4. Dependence of the coefficient F on the magnetic field strength for different values of the parameter ω/ω_{pe}: (*1*) 0.05, (*2*) 0.075, and (*3*) 0.1.

For $\alpha|A_0|t > 2$, this expression becomes

$$|A_j(t)| = 1/2\sqrt{|A_1(0)|^2 + |A_2(0)|^2}\exp(\alpha|A_0| - \nu)t, \quad (9)$$

in which case the phases of the SWs are seen to approach a steady-state value $\pi/4$ (Fig. 3).

Expression (9) implies that SWs can be excited under the condition $\gamma = \alpha|A_0| - \nu > 0$. This condition determines the threshold amplitude of the pump field $|A_0|_{cr}$, above which the SWs can be excited parametrically:

$$|A_0|_{cr} = 4\nu m_e V_{Te}^2/(eF\omega). \quad (10)$$

According to this expression, the threshold pump field amplitude increases linearly with increasing electron temperature and collision frequency and with decreasing plasma density n_0:

$$|A_0|_{cr} \propto T_e\nu/[n_0(\omega_0^2 - 4\omega_{ce}^2)]. \quad (11)$$

As the pump field frequency approaches the value $2|\omega_{ce}|$, the threshold amplitude increases. It should be noted that the above expression for $|A_0|_{cr}$ is valid for a weakly collisional plasma far from the cyclotron resonance: $\nu\omega/(\omega^2 - \omega_{ce}^2) \ll 1$.

Estimates of pump field amplitude (2) at which SWs can be excited parametrically show that, in a low-pressure gas-discharge plasma (such that the electron density is $n_0 \approx 10^{12}$ cm^{-3}, the electron temperature is T_e = 1 eV, the normalized frequency of plasma electron collisions is $\nu/\omega = 0.05$, and the external magnetic field is $H_0 \approx 1$ kOe), SWs can be excited at frequencies $\omega \approx 1.23\omega_{ce}$ by pump fields with amplitudes $|A_0| > 0.23$ V (corresponding to electric field strengths of $|E_0| >$ 320 V/cm). In this case, a pump field with the amplitude $|A_0| = 0.7$ V ($|E_0| \approx 950$ V/cm) excites SWs with the relative growth rate $\gamma/\omega \approx 0.1$.

Analysis of the effect of the magnetic field on the coefficient F (Fig. 4) in the expressions for α and $|A_0|_{cr}$ shows that, as the magnetic field increases, the growth rate γ decreases and the threshold amplitude $|A_0|_{cr}$ increases.

4. SATURATION LEVELS OF THE SURFACE WAVES

It is well known that the saturation of the parametric instability is governed by the processes that destroy spatiotemporal synchronization condition (3). These include the self-interaction of each of the excited waves and the interaction between them. The self-interaction of the SWs under discussion, which was studied earlier in [10], is a result of nonlinearities described by the quasi-hydrodynamic equations [4].

In analogy with [10], we can consider, to second order in the amplitudes of the fields of the excited waves, the interaction of two SWs that results in the excitation of waves at the second harmonic of the pump frequency ($\omega + \omega = 2\omega$, $k + (-k) = 0$):

$$\mathbf{W}^{(2)}(\mathbf{r}, t) = 0.5[\mathbf{W}_2(x)\exp(i\psi_2) + \mathbf{W}_2^*(x)\exp(-i\psi_2)],$$

$$\mathbf{W}_2 = (\varphi_2, n_2, \mathbf{V}_2), \quad \psi_2 = -2\omega t,$$

$$\varphi_2(x) = eA_1A_2/(m_eV_{Te}^2)[-(1/3)\exp(-\lambda_1 x)$$

$$+ (1/6)\exp(-2\lambda_1 x) - (1/2)\exp[-(\lambda_1 + \lambda_2)x]$$

$$- \omega^2/\omega_{pe}^2\exp(-2\lambda_2 x)],$$

$$n_2(x) = e^2A_1A_2/(m_e^2V_{Te}^4)n_0[-(1/3)\exp(-\lambda_1 x) \quad (12)$$

$$+ (2/3)\exp(-2\lambda_1 x) - (1/2)\exp[-(\lambda_1 + \lambda_2)x]$$

$$- 4\omega^6/\omega_{pe}^6\exp(-2\lambda_2 x)],$$

$$V_{x2}(x) = -ie^2A_1A_2\omega/(m_e^2V_{Te}^3\omega_{pe})\{-(8/3)\exp(-\lambda_1 x)$$

$$+ (8/3)\exp(-2\lambda_1 x) + \omega^2/\omega_{pe}^2\exp[-(\lambda_1 + \lambda_2)x]\},$$

$$V_{y2}(x) = V_{z2}(x) = 0.$$

The excitation of waves at the second harmonic is accompanied by the generation of static, purely surface perturbations ($\omega - \omega = 0$, $k - (-k) = 2k$):

$$\mathbf{W}^{(0)}(\mathbf{r}, t)$$

$$= 0.5[\mathbf{W}_0(x)\exp(i\psi_0) + \mathbf{W}_0^*(x)\exp(-i\psi_0)],$$

$$\mathbf{W}_0 = (\varphi^{(0)}, n^{(0)}, \mathbf{V}^{(0)}), \quad \psi_0 = 2ky,$$

$$\varphi^{(0)}(x) = eA_1A_2/(m_eV_{Te}^2)[-(2/3)\exp(-\lambda_1 x)$$

$$+ (1/6)\exp(-2\lambda_1 x) + (1/2)\exp[-(\lambda_1 + \lambda_2)x]$$

$$- \omega^4\omega_{ce}^4/(2\omega_{pe}^8)\exp(-2\lambda_2 x)],$$

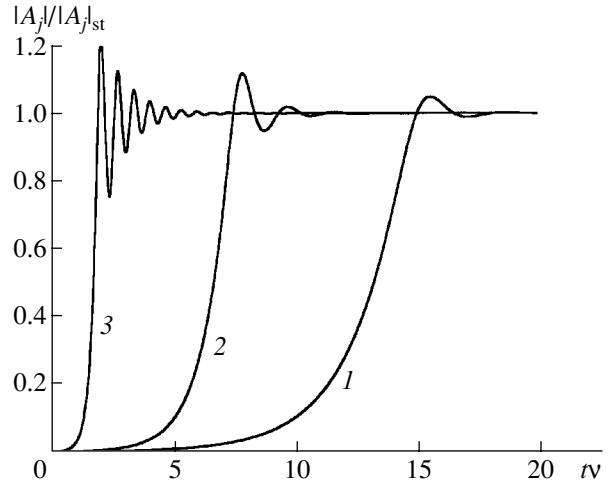

Fig. 5. Time evolution of the SW amplitudes for different values of the parameter $\alpha|A_0|/\nu$: (*1*) 1.5, (*2*) 2.0, and (*3*) 5.0.

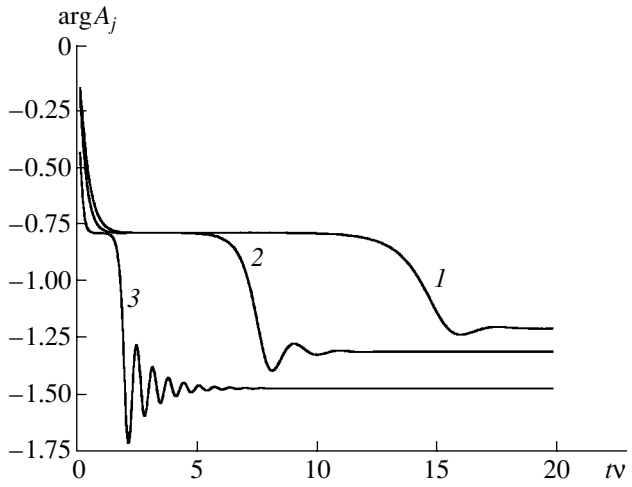

Fig. 6. Time evolution of the SW phases for different values of the parameter $\alpha|A_0|/\nu$: (*1*) 1.5, (*2*) 2.0, and (*3*) 5.0.

$$n^{(0)}(x) = e^2 A_1 A_2/(m_e^2 V_{Te}^4) n_0 [(2/3)\exp(-\lambda_1 x) \quad (13)$$
$$+ (2/3)\exp(-2\lambda_1 x) + (1/2)\exp[-(\lambda_1 + \lambda_2)x]$$
$$- 2\omega^6 \omega_{ce}^6/\omega_{pe}^{12}\exp(-2\lambda_2 x)],$$
$$V_x^{(0)}(x) = V_y^{(0)}(x) = 0,$$
$$V_z^{(0)}(x) = ie^2 A_1 A_2 \omega^4/(m_e^2 V_{Te}^4 k \omega_{ce}\omega_{pe}^2)$$
$$\times \{-[8(\omega^2 - \omega_{ce}^2)/(3\omega^2)]\exp(-\lambda_1 x)$$
$$- (\omega^2/\omega_{pe}^2)\exp(-2\lambda_1 x) + (\omega^2/\omega_{pe}^2)\exp[-(\lambda_1 + \lambda_2)x]\}.$$

The interaction of SWs at the first harmonic with SWs at the second harmonic ($2\omega - \omega = \omega$, $0 - (-k) = k$; $2\omega - \omega = \omega$, $0 - k = -k$) and with static perturbations ($0 + \omega = \omega$, $2k + (-k) = k$; $0 + \omega = \omega$, $-2k + k = -k$) gives rise to a nonlinear response at the fundamental frequency. Note that the response at the same frequency also results from the term $-V_{Te}^2 \nabla n_e/n_e$ in the equation of electron motion.

Taking into account this response, we can write, to third order in the field amplitude, the following nonlinear equations for the amplitudes of the excited SWs:

$$\left.\begin{aligned} \frac{\partial A_1}{\partial t} \pm V_g \frac{\partial A_1}{\partial y} + \nu A_1 \\ = -i\alpha A_0 A_2^* - i\beta_1 |A_1|^2 A_1 - i\beta_2 |A_2|^2 A_1, \\ \frac{\partial A_2}{\partial t} \mp V_g \frac{\partial A_2}{\partial y} + \nu A_2 \\ = -i\alpha A_0 A_1^* - i\beta_1 |A_2|^2 A_2 - i\beta_2 |A_1|^2 A_2, \end{aligned}\right\} \quad (14)$$

where the self-interaction of SWs of this type is characterized by the coefficient $\beta_1 = 10e^2/(m_e^2 V_{Te}^4) F\omega$, which was derived in [10], and the coefficient $\beta_2 = 13e^2\omega^2/(96 m_e^2 V_{Te}^4 \omega_{pe}^2) F\omega$ characterizes the interaction of two excited waves. Note that the value of the interaction coefficient β_2 is equally determined by the interaction of SWs at the first harmonic with SWs at the second harmonic and with static surface perturbations and by the interaction between SWs at the first harmonic, which is described by the cubic nonlinearity related to the term $-V_{Te}^2 \nabla n_e/n_e$ in the equation of electron motion.

Accounting for the self-interaction of each of the SWs and the interaction between them violates spatiotemporal synchronization condition (3). For the dense plasma under consideration, we have $|\beta_2| \ll |\beta_1|$; hence, the nonlinear frequency shifts of both the first ($\Delta\omega_{NL1} = \beta_1|A_1|^2 + \beta_2|A_2|^2$) and the second ($\Delta\omega_{NL2} = \beta_1|A_2|^2 + \beta_2|A_1|^2$) excited SWs are governed primarily by their self-interaction. The frequency mismatch between the excited SWs and the pump field increases with time. As a result, SWs saturate at the same amplitude (Figs. 5, 6), which is independent of the initial conditions:

$$\frac{|A_1|_{st}}{|A_0|} = \frac{|A_2|_{st}}{|A_0|}$$
$$= \left[\frac{\alpha^2 A_0^2 - \nu^2}{A_0^4(\beta_1 + \beta_2)^2}\right]^{1/4} \approx \left(\frac{m_e V_{Te}^2}{40e|A_0|}\right)^{1/4}\left(1 - \frac{\nu^2}{\alpha^2 A_0^2}\right)^{1/4}. \quad (15)$$

As time elapses, the phases of the SWs approach the value $\arg A_{jst} = -0.5\arccos[-\sqrt{1 - \nu^2/(\alpha^2 A_0^2)}]$. Numerical solution of equations (14) shows (Figs. 5, 6)

that the time required for the phases to reach this value decreases as the pump field amplitude and plasma density increase and the electron temperature decreases.

Hence, the development of parametric instability leads to the excitation of two oppositely propagating SWs with the same frequency and amplitude. The superposition of these waves produces a standing SW.

Analysis of the effect of the magnetic field and plasma density on saturation amplitudes (15) has shown that, for the same amplitude A_0 of the pump field, the strengthening of the external magnetic field, as well as a reduction in the plasma density, results in a decrease in the amplitude at which the SWs saturate. Estimates of the saturation amplitudes indicate that, in a plasma with the above parameters, a pump field with the amplitude $|A_0| = 0.7$ V ($|E_0| \approx 950$ V/cm) can excite SWs with amplitudes of up to 0.5 V, which corresponds to an electric field amplitude of about 680 V/cm at the plasma–metal boundary.

5. CONCLUSIONS

We have considered the parametric excitation of SWs propagating along a plasma–metal boundary by a pump field of frequency ω_0. The excitation process is shown to be threshold in nature. We have determined the threshold pump field amplitude above which the parametric instability develops, giving rise to two oppositely propagating SWs with the same frequencies $\omega_0/2$ and the same linear growth rates $\gamma = \alpha|A_0| - \nu$.

We have analyzed the effect of two nonlinear processes—the self-interaction of each of the excited SWs and the interaction between them—on the development of instability. These processes violate the temporal synchronization conditions and lead to the saturation of instability. The effect of the pump field amplitude, plasma parameters, and external magnetic field strength on the dynamics of the amplitudes and phases of the excited SWs has been analyzed numerically. We have shown that, in the dense plasma under consideration, the main saturation mechanism is the nonlinear self-interaction of SWs, in which case, the SW amplitudes in the saturation stage are the same and are independent of their initial values. Hence, the parametric instability results in the excitation of a standing SW.

The above analysis has shown that, at a fixed amplitude of the pump field, the strengthening of the external magnetic field, as well as reduction in the plasma density, leads to an increase in the threshold pump field amplitude and a decrease in both the linear growth rate and the saturation amplitude of the excited SWs. An increase in the plasma electron temperature also leads to an increase in the threshold pump field amplitude and a decrease in the linear growth rate.

Hence, the parametric excitation of the SWs under study is found to be most efficient for waveguide structures with a sufficiently dense plasma in weak magnetic fields.

ACKNOWLEDGMENTS

This work was supported in part by the Science and Technology Center in Ukraine, project no. 1112.

REFERENCES

1. M. Moisan, J. Hurbert, J. Margot, and Z. Zakrzewski, *The Development and Use of Surface-Wave Sustained Discharges for Applications in Advanced Technologies Based on Wave and Beam Generated Plasmas* (Kluwer, Amsterdam, 1999).
2. N. A. Azarenkov, K. N. Ostrikov, and M. Y. Yu, J. Appl. Phys. **84**, 4176 (1998).
3. N. A. Azarenkov, A. N. Kondratenko, and K. N. Ostrikov, Izv. Vyssh. Uchebn. Zaved., Radiofizika **36**, 32 (1993).
4. A. N. Kondratenko, *Plasma Waveguides* (Atomizdat, Moscow, 1976).
5. A. W. Trivelpiece and R. W. Gould, J. Appl. Phys. **30**, 1784 (1959).
6. N. A. Azarenkov and K. N. Ostrikov, Phys. Rep. **308**, 333 (1999).
7. D. P. Schmidt, N. B. Meezan, W. A. Hargus, Jr., and M. A. Cappelli, Plasma Sources Sci. Technol. **9**, 68 (2000).
8. N. A. Azarenkov, A. N. Kondratenko, and Yu. O. Tyshetskiĭ, Zh. Tekh. Fiz. **69** (11), 30 (1999) [Tech. Phys. **44**, 1286 (1999)].
9. N. A. Azarenkov, Yu. A. Akimov, and V. P. Olefir, Vestn. Kharkov. Natsion. Univ. im. V.N. Karazina, Ser. Fiz. Yad., Chast., Polya, No. 3/19, 23 (2002).
10. N. A. Azarenkov, Yu. A. Akimov, and A. V. Gapon, Vestn. Kharkov. Natsion. Univ. im. V.N. Karazina, Ser. Fiz. Yad., Chast., Polya, No. 4/12, 29 (2000).
11. Yu. A. Akimov, N. A. Azarenkov, and V. P. Olefir, in *Proceedings of the International Conference and School on Plasma Physics and Controlled Fusion, Alushta, 2002*, p. 96.
12. J. Weiland and H. Wilhelmsson, *Coherent Nonlinear Interaction of Waves in Plasmas* (Pergamon, Oxford, 1976; Énergoizdat, Moscow, 1981).
13. A. I. Akhiezer, V. S. Mikhaĭlenko, V. V. Ol'shansky, and K. N. Stepanov, Fiz. Plasmy **26**, 615 (2000) [Plasma Phys. Rep. **26**, 575 (2000)].
14. I. Peres, M. Fortin, and J. Margot, Phys. Plasmas **3**, 1754 (1996).
15. I. Peres, A. Dallaire, P. Jones, and J. Margot, J. Appl. Phys. **82**, 4211 (1997).

Translated by I.A. Kalabalyk

Plasma Physics Reports, Vol. 29, No. 8, 2003, pp. 675–682. Translated from Fizika Plazmy, Vol. 29, No. 8, 2003, pp. 734–741.

PLASMA OSCILLATIONS AND WAVES

Formation of a Steady-State Shock Front of a Long-Wavelength Fast Magnetosonic Wave in Space Plasma with Strong Alfvén Turbulence

V. R. Zemskov

Received April 18, 2002; in final form, November 27, 2002

Abstract—A study is made of the propagation of a long-wavelength fast magnetosonic wave in a space plasma with a low particle density and high temperature ($\beta_e \approx \beta_i \approx 1$) in a direction perpendicular to the magnetic field, along which the structures originating from a nonlinear Alfvén wave due to the modulational instability propagate. It is shown that, in the case of an Alfvén wave with certain parameters, a fast magnetosonic wave can be described by the Korteweg–de Vries–Burgers equation. It is pointed out that the fast magnetosonic wave may be in resonance with the structures originating from the Alfvén wave. © *2003 MAIK "Nauka/Interperiodica".*

1. INTRODUCTION

Mikhaĭlovskiĭ and Smolyakov [1] studied the propagation of a long-wavelength ($kr_{e,i} < 1$, where k is the wavenumber and $r_{e,i}$ are the electron and ion gyroradii) fast magnetosonic wave (FMS) in the direction of the unit vector $\mathbf{e}_x$, which is strictly transverse to the magnetic field $\mathbf{B}_0 = \mathbf{e}_z B_0$. They showed that the evolution of the magnetic field of an FMS wave propagating in a plasma with a low density ($n_e \approx n_i \approx 1$–$5$ cm^{-3}) and a sufficiently high temperature ($\beta_e \approx \beta_i \approx 1$) can be described by the Korteweg–de Vries (KdV) equation.

In space plasmas in which the particle density is low, dissipation due to collisions between the particles is negligible. Consequently, a long-wavelength FMS wave may be subject to anomalous dissipation only in a turbulent plasma [2]. In [2], it was shown that, if the plasma turbulence is modeled by Alfvén waves whose magnetic fields have the form $\tilde{\mathbf{b}} = \mathbf{e}_x b_x + \mathbf{e}_y b_y$ and are described by certain correlation functions (see also [3]), then the evolutionary equation for the magnetic field of an FMS wave can be reduced to the Korteweg–de Vries–Burgers (KdVB) equation, which implies the development of a steady-state shock front. It was also shown that the shock front forms in the interaction of an FMS wave with small-scale Alfvén turbulence, which was assumed to be weak and to have certain properties.

The objective of the present paper is to determine the conditions of formation of the steady-state shock front of an FMS wave propagating in a plasma with the above parameters but with strong Alfvén turbulence.

The theory of strong Alfvén turbulence has been actively developed in recent years. Thus, Kennel *et al.* [4] calculated steady-state structures in the form of shock wave trains with rotational discontinuities and accompanying hyperbolic solitons by solving the nonlinear Schrödinger equation (NSE)

$$i\frac{\partial q}{\partial \tau} - \frac{\partial^2 q}{\partial \xi^2} + i\frac{\partial}{\partial \xi}(|q|^2 q) = 0 \qquad (1)$$

accounting for resonant particles in the space plasma. In Eq. (1), the dimensionless time τ and the dimensionless coordinate ξ along the z-axis are defined by the relationships

$$\tau = \frac{\omega_{Bi} t}{2}, \quad \xi = \frac{z - c_\perp t}{r_i}, \quad c_\perp = c_A(1 + \beta_e + \beta_i)^{1/2},$$

$$q = \frac{\tilde{b}_x + i\tilde{b}_y}{B_0},$$

and $\tilde{b}_x$ and $\tilde{b}_y$ are the transverse components of the magnetic field of a nonlinear Alfvén wave (Fig. 1).

Steady-state Alfvén structures in the form of shock wave trains can be produced by the fluxes of cosmic-ray particles that are in resonance with the Alfvén wave [4,

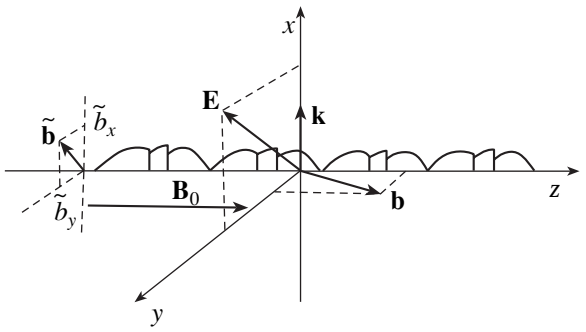

Fig. 1. Geometry of the problem.

1063-780X/03/2908-0675$24.00 © 2003 MAIK "Nauka/Interperiodica"

5]. The presence of plasma particles interacting with an Alfvén wave whose field geometry is like that shown in Fig. 1 gives rise to nonlinear Landau damping. Medvedev and Diamond [6, 7] took into account this damping and applied the kinetic method to derive, instead of Eq. (1), a kinetic NSE and calculate the structure of the nascent rotational discontinuities. The objective of this paper is to consider the case in which strong turbulence is driven by the modulational instability of Alfvén waves. The modulational instability generates steady-state structures extended along the magnetic field $\mathbf{B}_0$. Here, attention is drawn to the fact that, in a highly unstable turbulent plasma, such structures may serve as objects that scatter a long-wavelength FMS wave and cause it to dissipate as described by the KdVB equation, but under the assumption that Alfvén turbulence is strong.

Alfvén waves that are subject to the modulational instability can be described by Eq. (1). It is well known [8] that this equation has solutions in the form of monochromatic waves and hyperbolic and algebraic solitons. Hyperbolic solitons are more stable [9]. Hyperbolic solitons in the form of wells of the magnetic field of an Alfvén wave describe rotational discontinuities in which the field components $\tilde{b}_x$, and $\tilde{b}_y$ rotate through an angle of 180° in a counterclockwise sense (see, e.g., [8]).

2. EVOLUTION OF A FAST MAGNETOSONIC WAVE

We consider an FMS wave with the wave vector $\mathbf{k} = \mathbf{e}_x k$ (Fig. 1) that propagates along the x-axis, which is strictly transverse to the magnetic field $\mathbf{B}_0 = \mathbf{e}_z B_0$, through the structures originating from an unstable nonlinear Alfvén wave propagating along the z-axis and possessing the growth rate Γ. The evolution of the magnetic field $\mathbf{b} = \mathbf{e}_z b$ of this FMS wave is described by the equation [2]

$$\frac{\partial h}{\partial T} + im\frac{\partial h}{\partial \Sigma} + in\frac{\partial^2 h}{\partial \Sigma^2} - ip\frac{\partial^3 h}{\partial \Sigma^3} + \frac{\partial^3 h}{\partial \Sigma^3} + h\frac{\partial h}{\partial \Sigma} = k_2\frac{\partial^2 h}{\partial \Sigma^2} - k_3 h. \tag{2}$$

Here,

$$T = \frac{c_\perp t}{a_*},\quad h = \frac{b}{B_0}\frac{3+\beta-3\beta_i}{1+\beta},\quad b < B_0,\quad \Sigma = \frac{x - c_\perp^* t}{a_*},$$

$$c_\perp^* = c_\perp\left[1 + \omega_{Be}\left(1 - \frac{3v_{Ti}^2}{c_\perp^2}\right)(6A + B) + \frac{2m_i}{m_e}\omega_{Bi}^2 C\right],$$

$$a_*^2 = a_D^2 + \tilde{a}^2,\quad a_D^2 = \frac{r_i^2(2 + 2\beta + 3\beta_i)}{16(1+\beta)},$$

$$\beta = \beta_e + \beta_i,\quad \beta_{e,i} = \frac{8\pi n T_{e,i}}{B_0^2},\quad c_\perp = c_A(1+\beta)^{1/2},$$

$$\tilde{a}^2 = \frac{3v_{Ti}^2 - 2c_\perp^2}{12\omega_{Bi}}\left(B - \frac{6\varepsilon}{\omega_{Bi}}\right) - c_\perp^2 C,$$

and the following notation is introduced:

$$m = 4\varepsilon,\quad n = \frac{4\varepsilon(3v_{Ti}^2 - 2c_\perp^2)}{a_*\omega_{Bi}c_\perp},\quad p = \frac{8c_\perp^2 A}{\omega_{Bi}a_*^2},$$

$$k_3 = \frac{2m_i\omega_{Bi}a_*}{m_e c_\perp}(B - A), \tag{3}$$

$$k_2 = \frac{c_\perp}{a_*}\left(6\omega_{Be}C - 2B - A - \frac{4\varepsilon}{\omega_{Bi}}\right),$$

where ω_{Bi} and ω_{Be} are the ion and electron gyrofrequencies. In [2], the quantities A, B, C, and ε are defined in terms of the parameters of the nonlinear Alfvén wave that serves to model plasma turbulence. The formulas for these quantities are as follows:

$$A = \int_{-\infty}^{+\infty}\langle\tilde{b}_1^2\rangle\Gamma(\kappa)\left(\frac{1}{\Gamma^2 + \Omega_1^2} + \frac{1}{\Gamma^2 + \Omega_2^2}\right)d\kappa,$$

$$B = \int_{-\infty}^{+\infty}\langle\tilde{b}_1^2\rangle\left(\frac{\Omega_1}{\Gamma^2 + \Omega_1^2} + \frac{\Omega_2}{\Gamma^2 + \Omega_2^2}\right)d\kappa, \tag{4}$$

$$C = \int_{-\infty}^{+\infty}\langle\tilde{b}_1^2\rangle\left(\frac{1}{\Gamma^2 + \Omega_1^2} + \frac{1}{\Gamma^2 + \Omega_2^2}\right)d\kappa,$$

$$\varepsilon = \int_{-\infty}^{+\infty}\langle\tilde{b}_1^2\rangle d\kappa,$$

where the frequencies Ω_1 and Ω_2 are expressed in terms of the Alfvén wave parameters, κ is the wavenumber of the longitudinal perturbation of the Alfvén wave, and $\langle\tilde{b}_1^2\rangle$ is the correlation function of the Alfvén wave perturbations.

Evolutionary equation (2) was derived under the assumption that the wavenumber of the FMS wave satisfies the conditions

$$kr_{e,i} \ll 1,\quad \lambda = 2\pi k^{-1} \gg r_{e,i},$$

where λ is the wavelength of the FMS wave.

If the perturbation spectrum of the Alfvén wave that models Alfvén turbulence consists of perturbations with a sufficiently short wavelength, then some of integrals (4) vanish and the terms with imaginary coefficients can be neglected [2]. In this case, Eq. (2) takes the form of the KdVB equation, which is known to have a solution describing a steady-state shock front [10]. Below, it will be shown that, in the case of large-scale

Alfvén turbulence, Eq. (2) also reduces to the KdVB equation.

3. ALFVÉN TURBULENCE

In order to analyze plasma turbulence in the situation described in the previous sections, we consider an Alfvén wave that propagates exactly along the magnetic field $\mathbf{B}_0$ and whose magnetic field is a solution to Eq. (1),

$$\begin{aligned}\tilde{b} &= \tilde{b}_x + i\tilde{b}_y \\ &= A_0\cos(k_0\zeta + \delta_1) + iA_0\sin(k_0\zeta + \delta_1),\end{aligned} \tag{5}$$

where $k_0 = A_0^2 - u$, ζ is the dimensionless coordinate along the z-axis, δ_1 is the constant part of the phase, and A_0 and u are the amplitude of the Alfvén wave and its phase velocity. We assume that an Alfvén wave with magnetic field (5) is subject to the modulational instability. The frequency ν and wavenumber κ of the longitudinal perturbations of wave (5) are related by the dispersion relation

$$\nu = \kappa u \pm \kappa\sqrt{\kappa^2 - \kappa_0^2}, \tag{6}$$

where $\kappa_0^2 = A_0^2(A_0^2 - 2u)$. An Alfvén wave with magnetic field (5) may be subject to modulational instability when $A_0^2 - 2u > 0$ and the wavenumbers of the longitudinal perturbations are sufficiently small, $\kappa < \kappa_0$. In dimensional units, the latter condition indicates that the wavelength $\tilde{\lambda}$ of the longitudinal perturbations should be sufficiently long,

$$\tilde{\lambda} > \left(\frac{B_0}{\tilde{b}}\right)^2 r_i, \tag{7}$$

where $\tilde{b} \sim A_0$. Thus, for $\tilde{b}/B_0 \sim 10^{-2}$, we have $\tilde{\lambda} > 10^4 r_i$.

The growth rate of the modulational instability of Alfvén wave (5) has the form

$$\Gamma(\kappa) = \kappa\sqrt{\kappa_0^2 - \kappa^2} \tag{8}$$

and is maximum at $\kappa_m = \dfrac{\kappa_0}{\sqrt{2}}$ (Fig. 2).

We assume that the instability growth rate satisfies the conditions

$$\omega_{Bi} > \Gamma > \omega, \tag{9}$$

where ω is the frequency of the FMS wave. This frequency can be estimated as $\omega \approx c_\perp k$. The right-hand inequality in conditions (9) yields the following estimate

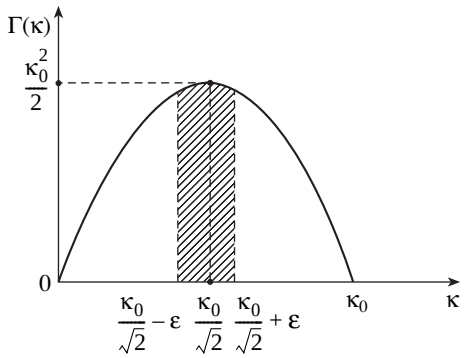

Fig. 2. Growth rate of the modulational instability of a longitudinal Alfvén mode vs. wavenumber κ. The interval of width 2ε, centered at the wavenumber κ_m, at which the instability growth rate Γ is maximum, is hatched.

for the wavelength λ of the FMS wave in terms of the characteristic scale $\tilde{\lambda}$ of the turbulence:

$$\lambda > \sqrt{3}\left(\frac{B_0}{\tilde{b}}\right)^2\tilde{\lambda}. \tag{10}$$

For $\tilde{b}/B_0 \sim 10^{-2}$, we have $\lambda > 1.7 \times 10^4\tilde{\lambda}$.

Using the left-hand inequality in conditions (9), we can estimate the smallest scale on which Alfvén turbulence develops. To do this, we assume that $\tilde{b}/B_0 \sim 10^{-2}$ and $\tilde{\lambda} > 10^4 r_i$. Then, we combine inequalities (7) and (10) to obtain the range of the characteristic scales of the modulationally unstable Alfvén modes:

$$\left(\frac{B_0}{\tilde{b}}\right)^2 r_i < \tilde{\lambda} < 0.6\left(\frac{\tilde{b}}{B_0}\right)\lambda. \tag{11}$$

The wavelength of the FMS wave satisfies the condition $\lambda \gg r_e, r_i$. The envelope of Alfvén wave (5) changes during the modulational instability. Consequently, in order to take into account all possible modes of the instability-driven longitudinal perturbations, it is necessary determine the correlation functions of these perturbations, $\langle\tilde{b}_1^2\rangle$, which are in turn required to calculate the coefficients in expressions (4). According to [2], we have $\langle b_1^2\rangle = A_{1\kappa}^2$, where $A_{1\kappa}$ is the Fourier component of the perturbation of wave amplitude (5). In what follows, we will assume that $A_1 \le A_0$; in other words, the modulational instability generates Alfvén structures with amplitudes no larger than A_0.

To simplify further calculations, we make the following two assumptions. First, Alfvén wave (5) is perturbed in such a way that the wavenumbers of the excited modes,

$$\frac{\kappa_0}{\sqrt{2}} - \Delta\kappa < \kappa < \frac{\kappa_0}{\sqrt{2}} + \Delta\kappa, \quad \Delta\kappa \ll 1,$$

lie within a narrow interval around the wavenumber κ_m, at which the growth rate of the modulational instability of an Alfvén wave is maximum (Fig. 2). Second, the Fourier components $A_{1\kappa} = A_1(\kappa)$ are weakly dependent on κ; hence, in expressions (4), they can all be replaced with $A_1(\kappa_m)$.

A more rigorous analysis of range (11) leads to the following range of characteristic scales on which Alfvén modes are excited under conditions such that $\tilde{b}/B_0 \sim 10^{-2}$ and $\lambda \sim 10^9 r_i$:

$$10^4 r_i < \tilde{\lambda} < 6 \times 10^4 r_i.$$

We see that the width of this range, $\sim 5 \times 10^4 r_i$, is comparable with the characteristic wavelength $\lambda_m \sim 2 \times 10^4 r_i$.

4. FORMATION OF STEADY-STATE STRUCTURES FROM AN ALFVÉN WAVE

The Alfvén turbulence described in the previous section is capable of changing the envelope of Alfvén wave (5) through the generation of steady-state structures of Alfvén modes on scales (11). In order to describe these structures, we convert Eq. (1) into the form [8]

$$\left(4A\frac{\partial A}{\partial \zeta}\right)^2 = (4AC + C_0 - A^4 + 2vA^2) \times (4AC - C_0 + A^4 - 2vA^2), \qquad (12)$$
$$\frac{\partial \alpha}{\partial \zeta} = \frac{3A^4 - 2vA^2 + C_0}{4A^2},$$

where $\zeta = \xi - vt$ with ξ and t defined in Eq. (1), v is the phase velocity of a steady-state structure, the quantities A and α in Eq. (1) are related to ζ by $q = A\exp(i\alpha)$, and C_0 and C are integration constants.

The relationship between the phase velocities of the structure and Alfvén wave (5), from which the structure is produced, is as follows:

$$v = u + \frac{a^2}{4}. \qquad (13)$$

According to this relationship, the structure produced moves faster than wave (5). Equations (12) have the obvious first integral

$$A^4 - 2vA^2 + 4AC\cos\alpha = C_0, \qquad (14)$$

which is actually the Hamiltonian of the equations. Since the constant C_0 has the meaning of the energy of dynamic system (12) and, according to relationship (13), the relative velocity of the sought steady-state structure is proportional to $\sim a^2$, we can assume that C_0 is related to a by

$$C_0 = A_0^4 - 2uA_0^2 - \frac{a^4}{4}. \qquad (15)$$

System (12) is conservative, which is consistent with the fact that the structure originates from wave (5) under the action of internal longitudinal perturbations driven by the modulational instability. Relationship (14) implies that the solutions to Eqs. (12) are symmetric under the transformation

$$a \longrightarrow a + \pi, \quad C \longrightarrow -C. \qquad (16)$$

Let us consider the case $C_0 = 0$. Using first integral (14), we reduce Eqs. (12) to the form

$$\frac{\partial A}{\partial \zeta} = C\sin\alpha,$$
$$\frac{\partial \alpha}{\partial \zeta} = \frac{3A^4 - 2vA^2}{4A^2}. \qquad (17)$$

The singular points of dynamic system (17) are those that lie in the plane (A, α) and at which we have

$$\alpha_1 = \pi n, \quad n = 0, \pm 1, \ldots, \quad A_1^2 = \frac{2v}{3}. \qquad (18)$$

Because of the modulational instability, which produces steady-state structures, the quantities $A(\zeta)$ and $\alpha(\zeta)$, as well as the constant $C(\zeta)$, become functions of ζ. With these functions $A(\zeta)$ and $\alpha(\zeta)$, the right-hand sides of Eqs. (12) vanish:

$$A^3 - 2vA + 4C = 0,$$
$$3A^4 - 2vA^2 = 0. \qquad (19)$$

The first of Eqs. (19) is satisfied by

$$A(\zeta) = \sqrt{\frac{8v}{3}}\cos\left(\frac{\zeta + \pi}{3}\right), \quad C = \frac{1}{4}\left(\frac{8v}{3}\right)^{3/2}\cos\zeta. \qquad (20)$$

Inserting functions (20) into the second of Eqs. (19), we obtain the singular points of the equations. In what follows, we will be interested in the singular points at which

$$\cos\left(\frac{\zeta + \pi}{3}\right) = \pm\frac{1}{2}.$$

We introduce the variable $(\zeta + \pi)/3 = \Sigma$, with which to write the solutions as

$$\Sigma_1 = \pi/3 + 2\pi m, \quad \Sigma_2 = 2\pi/3 + 2\pi p,$$

where $m, p = 0, \pm 1, \ldots$.

It is easy to show that these values of Σ_1 and Σ_2 determine the positions of the rotational discontinuities in the steady-state structure. For $A \longrightarrow A_1$, relationships (18) allow us to make the first of Eqs. (12) inte-

grable in the vicinity of these solutions ($\Sigma \longrightarrow \Sigma_1$, $\Sigma \longrightarrow \Sigma_2$):

$$\left(\frac{\partial A}{\partial \zeta}\right)^2 = \frac{1}{16}\left(A^2 - \frac{2\nu}{3}\right)^2\left(\frac{8\nu}{3} - A^2\right).$$

For $0 \le A^2 \le 2$, this equation is easy to integrate:

$$A^2 = \frac{4\nu}{3}\frac{\cosh\frac{\nu\zeta}{\sqrt{3}} - 1}{\cosh\frac{\nu\zeta}{\sqrt{3}} + 1}. \qquad (21)$$

We substitute solution (21) into the second of Eqs. (17) and integrate the resulting equation over ζ to obtain

$$\alpha = \alpha_0 - 3\arctan\frac{(2\exp(\nu\zeta/\sqrt{3}) - 1)}{\sqrt{3}}, \qquad (22)$$

where α_0 is an integration constant.

Expression (22) yields

$$\alpha(-\infty) = \pi + \alpha(+\infty),$$

which indicates that solutions (21) and (22) describe a rotational discontinuity in which the magnetic field of an Alfvén wave rotates in a counterclockwise direction and whose position in space is determined by the coordinates Σ_1 and Σ_2.

The definition of $C(\zeta)$ in solution (20) implies that, under the transformation $C \longrightarrow -C$, we have $\zeta \longrightarrow \pi + \zeta$; as a result, along with solution (20), we obtain the solution

$$A(\Sigma) = \sqrt{\frac{8\nu}{3}}\cos\left(\Sigma + \frac{\pi}{3}\right).$$

Combining this solution with solution (20) and using the inequality $A \ge 0$, which holds because $|\zeta| = A$, we can readily construct the steady-state structure shown in Fig. 3. Substituting solution (20) into the second of Eqs. (17) and integrating the resulting equation, we obtain

$$\alpha = \frac{3\nu\Sigma}{2} + \frac{3}{4}\nu\sin 2\Sigma + \delta_2, \qquad (23)$$

where δ_2 is an integration constant. Formula (23) describes how the phase changes in the structure. From Fig. 3, we can see that the characteristic spatial scale of the steady-state structure is about $\Delta\tilde{\lambda} \approx 20 r_i$.

Recall that Eq. (2) describes the evolution of an FMS wave in its interaction with certain structures of Alfvén turbulence. The above analysis shows that the role of these objects may well be played by the steady-state structures described by expressions (20) and (23) and, within the rotational discontinuities, by formulas (21) and (22). Even for $\tilde{b}/B_0 \sim 10^{-1}$, the lower limit of the range of scales (11) is about $10^2 r_i$. In this case, however, it is necessary to take into account the terms of higher orders in the nonlinearity parameter in Eq. (1); as a result, the shape of the structures in question and their characteristic scale length $\Delta\lambda$ can change. Note that, solving Eq. (12) in the region inside the discontinuities, we restricted ourselves to solutions (21) and (22), which have the form of wells of the magnetic field of an Alfvén wave [8]. The reason is that it is necessary to satisfy the assumptions used in [3] in obtaining the correlation functions $\langle\tilde{b}^2\rangle$ in formulas (4); specifically, the Fourier components $A_{1\kappa}$ in these formulas should be small in comparison with A_0.

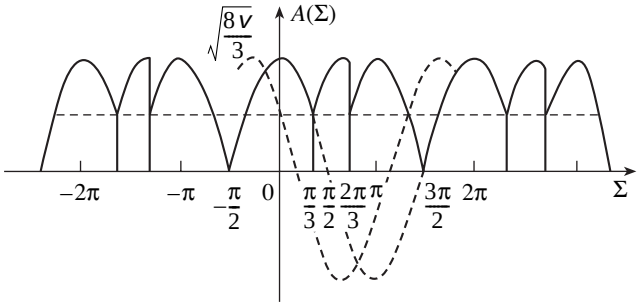

Fig. 3. Amplitude A of a steady-state Alfvén wave, calculated from expressions (16) and (20) as a function of the coordinate $\Sigma = (\zeta + \pi)/3$.

5. INTERACTION OF A FAST MAGNETOSONIC WAVE WITH STRONG ALFVÉN TURBULENCE

The evolution of a long FMS wave interacting with the steady-state structure analyzed in the previous section can be described by Eq. (2). Under the condition $\omega_{Bi} \gg \Gamma$, which corresponds to the condition $(\tilde{b}/B_0)^4 \ll 1$ and is well satisfied for $\tilde{b}/B_0 < 1$, the terms with imaginary coefficients in Eq. (2) can be neglected and the equation itself reduces to

$$\frac{\partial h}{\partial T} + \frac{\partial^3 h}{\partial \Sigma^3} + h\frac{\partial h}{\partial \Sigma} = k_2\frac{\partial^2 h}{\partial \Sigma^2} - k_3 h. \qquad (24)$$

Note that Eq. (24) has no steady solutions because of the presence of the last term on the right-hand side. The quantity h behaves as

$$h \sim \exp(-k_3 T).$$

For $k_3 > 0$, the solution to Eq. (24) is decreasing, and, for $k_3 < 0$, it increases exponentially.

Physically, a decrease in h indicates that the FMS wave is scattered by the steady-state structures of an Alfvén wave, whereas an increase in h corresponds to the conversion of the energy of Alfvén modes into the energy of the FMS wave.

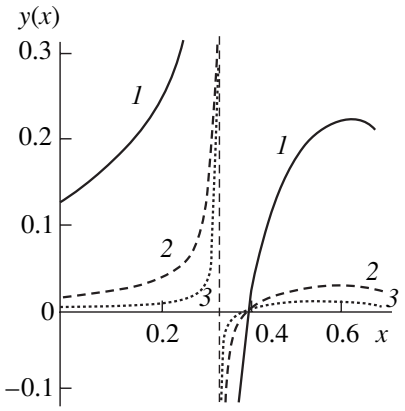

Fig. 4. Plots of the function $y(x)$ vs. parameter $x = 2u/A_0^2$ of the nonlinear Alfvén wave generating Alfvén structures used to model turbulence for different values of the parameter $\varepsilon = \frac{\Delta\kappa}{A_0^2}$ = (*1*) 0.001, (*2*) 0.005, and (*3*) 0.01.

Let us examine the relative roles played by these two processes. To do this, we assume that the steady-state structures described by expressions (20) and (23) are generated during the modulational instability of Alfvén wave (5). The mode numbers of the longitudinal perturbation of this wave are nonzero only in a narrow interval around the wavenumber κ_m, at which the growth rate (8) of the modulational instability of an Alfvén wave is maximum and the amplitudes of Alfvén modes possess the property described in Section 3.

In order to determine the conditions for the propagation of an FMS wave, we calculate k_3 from formulas (3) and (4) in which the Fourier components $A_{1\kappa}$ are independent of κ and the frequencies Ω_1 and Ω_2 in the coefficients A and B in formulas (4) are expressed as [2]

$$\Omega_1 = k_0 u - \kappa u - \omega_0, \quad \Omega_2 = k_0 u + \kappa u + \omega_0,$$

where, according to [2], $k_0 = A_0^2 - u$ and $\omega_0 = \kappa u$. The integration in formulas (4) is limited to a narrow interval of the wavenumber κ, from $\kappa_m - \Delta\kappa$ to $\kappa_m + \Delta\kappa$. Here, we present only the results calculated for k_3 (details of the calculations are given in the Appendix). The dependence of k_3 on the parameters of wave (5) can be represented in the form of the function $k_3 = k_3(x)$, where $x = 2u/A_0^2$ (Fig. 4).

It can be seen from Fig. 4 that an FMS wave with the parameter x lying within the interval $0 < x \le 0.33$ is scattered by Alfvén structures. An FMS wave with $x \approx 0.33$ can come into resonance with Alfvén structures. As an FMS wave interacts resonantly with the structures described above, the rate at which it is damped in the scattering process, first, increases rapidly and, then, decreases in a jumplike manner. An FMS wave with $x \approx 0.33$ extracts energy from Alfvén structures. At $x \approx 0.39$, the function $k_3(x)$ vanishes. Physically, this indicates that the FMS wave interacting with the Alfvén structures is not scattered by them. Or, more precisely, the FMS wave is, of course, scattered, but the energy lost during the scattering is exactly compensated for by the energy coming from the Alfvén modes. As the parameter x increases further, the scattering rate gradually increases (Fig. 4).

If we set $a^2 = 8u$ in relationships (13) and (15), then, at $C_0 = 0$, we obtain from relationship (15) the following equation:

$$A_0^4 - 2uA_0^2 - 16u^2 = 0.$$

This equation has a root at $x \approx 0.39$, in which case relationship (13) becomes

$$v = 3u. \tag{25}$$

As the width of the above interval of wavenumbers, $\Delta\kappa$, increases, the root of the equation $k_3(x) = 0$ is gradually displaced toward larger values of x. The structures originating from Alfvén wave (5) scatter an FMS wave with the parameter $x \approx 0.39$ in such a way that the damping of the FMS wave is balanced by the energy transfer from the Alfvén modes. In this case, we can set $k_3 = 0$ in Eq. (24). In this case, the evolution of an FMS wave is described by the KdVB equation, however, the coefficient k_2 in formulas (3) should be obtained by taking the integrals in formulas (4) over the wavelength range $\tilde{\lambda} \sim \lambda_m \sim 2 \times 10^4 r_i$ of Alfvén modes at $\tilde{b}/B_0 \sim 10^{-2}$ (rather than over the short-wavelength range of Alfvén turbulence, $\tilde{\lambda} \ll 10^4 r_i$, as was done in [2]).

6. CONCLUSION

Long-wavelength FMS waves whose field geometry is like that shown in Fig. 1 can propagate in a high-temperature plasma with $\beta_e \approx \beta_i \approx 1$ and $n_e \approx n_i \approx (1\text{–}5)$ cm^{-3} through steady-state structures originating from nonlinear Alfvén waves. If the characteristic scales of the steady-state Alfvén structures are about $20r_i$, then, for $\tilde{b}/B_0 \sim 10^{-2}$, they lie between the long-wavelength ($\tilde{\lambda} \sim 2 \times 10^4 r_i$) and short-wavelength ($\tilde{\lambda} \ll 10^4 r_i$) Alfvén modes generated on scales (11).

The interaction of an FMS wave with such structures can be described by the KdVB equation for Alfvén waves (5) with certain values of the parameters x.

In this paper, the effect of an FMS wave on the magnetic field of an Alfvén wave was neglected. Although the amplitudes of the Alfvén structures can be comparable with the amplitude of FMS wave (5), their wavelengths are very different, $\tilde{\lambda} \ll \lambda$; hence, the field of the FMS wave may be considered constant on the characteristic scales of these structures.

The anomalous dissipation mechanism considered above (namely, the mechanism that is responsible for the anomalous dissipation of a long-wavelength FMS wave with the field geometry shown in Fig. 1 and that involves Alfvén structures) can play an important part in the dissipation of FMS waves in space plasmas, in particular, solar-wind plasma, solar-corona plasma, and intergalactic plasmas.

Physically, the existence of the lower limit on the wavelengths of Alfvén structures, $\tilde{\lambda} \sim 20r_i$ (which plays the role of a boundary between the long- and short-wavelength modes of Alfvén turbulence), and the fact that, at this limit, the evolutionary equation for a long-wavelength FMS wave transforms into the KdVB equation (as does the equation for short-wavelength Alfvén modes [2]) may indicate that we are dealing with the so-called "soliton-like turbulence."

APPENDIX

The functional dependence of the coefficient $k_3(x)$ with $x = 2u/A_0^2$ in the evolutionary equation (2) for an FMS wave can be determined from formulas (3) and (4). The quantities A and B are calculated by integrating from $\kappa = \kappa_m - \Delta\kappa$ to $\kappa = \kappa_m + \Delta\kappa$ under the assumption that the Fourier components are independent of κ and are equal to $A_{1\kappa}^2 = A_{1m}^2$. We insert $\kappa = \kappa_m + \varepsilon$ into expression (8) and neglect small terms of higher orders to get

$$\Gamma(\kappa) \approx \frac{\kappa_0^2}{2} - \varepsilon^2, \quad \text{where} \quad -\Delta\kappa < \varepsilon < \Delta\kappa.$$

In formulas (4) for A and B, we switch to the variable ε and obtain the following expression for the coefficient B:

$$B = A_{1m}^2 \left[\frac{1}{u^2 - \kappa_0^2} \int_{-\Delta\kappa}^{\Delta\kappa} \frac{a - u\varepsilon}{\left(\varepsilon - \frac{ua}{u^2 - \kappa_0^2}\right)^2 + \frac{\kappa_0^2(\kappa_0^2 u^2 - \kappa_0^4 - 4a^2)}{4(u^2 - \kappa_0^2)^2}} d\varepsilon \right.$$
$$\left. + \frac{1}{u^2 - \kappa_0^2} \int_{-\Delta\kappa}^{\Delta\kappa} \frac{b + n\varepsilon}{\left(\varepsilon + \frac{ua}{u^2 - \kappa_0^2}\right) + \frac{\kappa_0^2(\kappa_0^2 u^2 - \kappa_0^4 - 4b^2)}{4(u^2 - \kappa_0^2)^2}} d\varepsilon \right], \tag{26}$$

where

$$a = k_0 u - \frac{\kappa_0 u}{\sqrt{2}}, \quad b = k_0 u + \frac{\kappa_0 u}{\sqrt{2}}, \quad k_0 = A_0^2 - u.$$

The other coefficient is expressed in a similar manner.

The quantity $u^2 - \kappa_0^2 = A_0^4(x - 2(\sqrt{2} - 1))(x + 2(\sqrt{2} + 1))$ with $x = 2u/A_0^2$ is negative in the range $x < 2(\sqrt{2} - 1)$ or, equivalently, $x < 0.828$. In this range, the second terms in the denominators of the integrands are negative, and the integrals are expressed in terms of the natural logarithms. When conditions (9) are satisfied, we can assume that $a_* \simeq a_D$. The coefficient $k_3(x)$ can now be represented as

$$k_3(x) = \frac{2m_i\omega_{Bi}a_D A_{1m}^2}{m_e c_\perp}(B - A) = \frac{2m_i\omega_{Bi}a_D A_{1m}^2}{m_e c_\perp} y(x).$$

Here,

$$y(x) = [x(g + 2f) - F]\ln\left[1 + \frac{\varepsilon}{\sqrt{\frac{1-x}{2}} - \frac{\varepsilon}{2} + \frac{xf}{2g} - \frac{p}{2g}}\right]$$
$$+ [x(g + 2f) + F]\ln\left[1 + \frac{\varepsilon}{\sqrt{\frac{1-x}{2}} - \frac{\varepsilon}{2} + \frac{xf}{2g} + \frac{p}{2g}}\right]$$
$$- [x(g + 2\varphi) + \Phi]\ln\left[1 + \frac{\varepsilon}{\sqrt{\frac{1-x}{2}} - \frac{\varepsilon}{2} + \frac{x\varphi}{2g} - \frac{q}{2g}}\right] \tag{27}$$
$$- [x(g + 2\varphi) - \Phi]\ln\left[1 + \frac{\varepsilon}{\sqrt{\frac{1-x}{2}} - \frac{\varepsilon}{2} + \frac{x\varphi}{2g} + \frac{q}{2g}}\right] - 8\varepsilon g,$$

where the functions g, φ, p, q, f, F, and Φ have the form

$$g(x) = 1 - x - \frac{1}{4}x^2, \quad \varphi(x) = \frac{x}{2}\left(1 - \frac{x}{2} + \sqrt{\frac{1-x}{2}}\right),$$

$$f(x) = \frac{x}{2}\left(1 - \frac{x}{2} - \sqrt{\frac{1-x}{2}}\right),$$

$$p(x) = \sqrt{[(1-x)^2 + 4f^2]g + x^2 f^2},$$

$$q(x) = \sqrt{[(1-x)^2 + 4\varphi^2]g + x^2\varphi^2},$$

$$F(x) = \frac{g(1-x+2f)^2 - 2g(1-x) + 2x^2f^2}{\sqrt{1-x}\sqrt{(1-x)g + 4f^2}},$$

$$\Phi(x) = \frac{g(1-x+2\varphi)^2 - 2g(1-x) + 2x^2\varphi^2}{\sqrt{1-x}\sqrt{(1-x)g + 4f^2}},$$

$$\varepsilon = \frac{\Delta\kappa}{A_0^2}.$$

The plots of the function $y(x)$ for different values of the parameter ε are given in Fig. 4. The function $y(x)$ is discontinuous at the point $x \approx 0.33$; the discontinuity corresponds to resonance between the FMS wave and the Alfvén mode.

REFERENCES

1. A. B. Mikhailovskiĭ and A. I. Smolyakov, Zh. Éksp. Teor. Fiz. **88**, 189 (1985) [Sov. Phys. JETP **61**, 109 (1985)].
2. V. R. Zemskov, Fiz. Plazmy **28**, 208 (2002) [Plasma Phys. Rep. **28**, 183 (2002)].
3. V. R. Zemskov, Izv. Vyssh. Uchebn. Zaved., Radiofiz. **35**, 663 (1992).
4. Ch. F. Kennel, M. A. Mal'kov, and R. Z. Sagdeev, Pis'ma Zh. Éksp. Teor. Fiz. **48**, 75 (1988) [JETP Lett. **48**, 79 (1988)].
5. E. Mjolhus and J. Wyller, J. Plasma Phys. **40**, 229 (1998).
6. M. V. Medvedev and P. H. Diamond, Phys. Plasmas **3**, 863 (1996).
7. M. V. Medvedev, Phys. Rev. Lett. **78**, 4934 (1997).
8. S. I. Vaĭnshteĭn, I. N. Toptygin, and A. M. Bykov, *Turbulence, Current Sheets, and Shock Waves in Space Plasma* (Nauka, Moscow, 1989), Chap. 8.
9. L. Nocera and B. Buti, in *Proceedings of the 25th ICPP Conference on Controlled Fusion and Plasma Physics, 1998*, Vol. 22, p. 2295.
10. A. V. Gurevich and L. P. Pitaevskii, Zh. Éksp. Teor. Fiz. **92**, 168 (1987) [Sov. Phys. JETP **66**, 490 (1987)].

Translated by O.E. Khadin

Plasma Physics Reports, Vol. 29, No. 8, 2003, pp. 683–687. Translated from Fizika Plazmy, Vol. 29, No. 8, 2003, pp. 742–746.

PLASMA OSCILLATIONS AND WAVES

Evolution of the Electron Langmuir Oscillations in an Inhomogeneous Magnetized Plasma

A. V. Timofeev

Russian Research Centre Kurchatov Institute, pl. Kurchatova 1, Moscow, 123182 Russia

Received December 5, 2002

Abstract—The conditions under which the energy of the electron Langmuir oscillations can escape from the plasma into vacuum are determined in the simplest model of a plane slab of an inhomogeneous cold magnetized plasma in a uniform magnetic field. © *2003 MAIK "Nauka/Interperiodica".*

1. For oscillations of an inhomogeneous plasma in a magnetic field, the surface at which the oscillation frequency ω is equal to the electron Langmuir frequency ω_{pe} plays an especially important role: at this surface, whose vicinity is an opaque region, the polarization of oscillations changes and the ray trajectories have singularities. In what follows, such a surface will be referred to as a critical surface. Although the phenomena occurring close to the critical surface have been investigated primarily in connection with the problem of launching microwave energy into a dense plasma, they are also of interest from some other viewpoints. In particular, they provide new insight into the problem of the escape of microwave energy from a turbulent plasma. Thus, in [1], it was established that, when electromagnetic oscillations approach the critical surface, they can transform into electron Langmuir oscillations. (In a cold plasma, the frequency of the electron Langmuir oscillations is equal to ω_{pe}; hence, they should be localized at the critical surface.) Of course, the opposite is also true: electron Langmuir oscillations propagating away from the critical surface change their nature and transform into electromagnetic oscillations. In [2], in studying the plasma in an open confinement system, it was shown that the energy of electron Langmuir oscillations can escape into vacuum as a result of this conversion process.

In the present paper, the question about the evolution of the electron Langmuir oscillations in an inhomogeneous plasma is treated by using the simplest model of a plane plasma slab in a uniform magnetic field. It is shown that, when the refractive index $N = \dfrac{kc}{\omega}$ is less than a certain value $N_{\max}$, the electromagnetic oscillations into which the electron Langmuir oscillations are converted when moving away from the critical surface escape into vacuum. For $N > N_{\max}$, electromagnetic oscillations propagating in an inhomogeneous plasma eventually reach the plasma resonance surface (the upper hybrid resonance), at which they are absorbed. Here, $N_{\max} = \sqrt{\dfrac{\omega_e}{\omega_e + \omega}}$ when the plasma oscillation frequency is higher than the electron cyclotron frequency ω_e, and $N_{\max} = \sqrt{\dfrac{\omega_e}{\omega_e - \omega}}$ when $\omega < \omega_e$.

These results may be useful in interpreting the data from experiments aimed at investigating the oscillations of nonequilibrium plasmas, in particular, plasma penetrated by an electron beam. Theoretically, the beam is expected to preferentially excite potential electron Langmuir oscillations. In experiments, however, nonpotential plasma oscillations, in particular, helicons (whistlers), were observed both inside and outside the plasma [3–6]. The results obtained in the present paper show that, when the electron Langmuir oscillations excited by an electron beam propagate away from the critical surface, they should transform into electromagnetic oscillations. In turn, electromagnetic oscillations may or may not escape from the plasma, depending on the plasma parameters and the value of the refractive index. Previously, both nonlinear (see, e.g., [4, 7]) and linear [8, 9] mechanisms for the conversion of potential oscillations into electromagnetic ones were invoked to explain the energy emission from a nonequilibrium plasma. The linear mechanism is associated with the penetration of oscillations through an opaque region that separates the region from which the oscillations escape into vacuum from the region that is adjacent to the plasma (upper hybrid) resonance surface and in which the oscillations become potential.

2. It is convenient to analyze plasma oscillations in a magnetic field by using the following dispersion relation and the following expression for the polarization of oscillations (see, e.g., [10]):

$$D = 1 + \frac{N_\perp^2}{2}\left(\frac{1}{\varepsilon_+ - N^2} + \frac{1}{\varepsilon_- - N^2}\right) + \frac{N_\parallel^2}{\varepsilon_\parallel - N^2} = 0, \quad (1)$$

1063-780X/03/2908-0683$24.00 © 2003 MAIK "Nauka/Interperiodica"

$$\mathbf{E} = (E_+, E_-, E_\parallel) = \text{const}\left(\frac{N_+}{\varepsilon_+ - N^2}, \frac{N_-}{\varepsilon_- - N^2}, \frac{N_\parallel}{\varepsilon_\parallel - N^2}\right). \quad (2)$$

Here, $N_\pm = \frac{1}{\sqrt{2}}(N_x \pm iN_y)$, $N_\perp^2 = N_x^2 + N_y^2$, $N_\parallel = \frac{k_z c}{\omega}$, $E_\pm = \frac{1}{\sqrt{2}}(E_x \pm iE_y)$, and $E_\parallel = E_z$, where the subscripts $\parallel$ and $\perp$ signify the direction with respect to the main magnetic field. Dispersion relation (1) and expression (2) are written in Cartesian coordinates with the z-axis directed along the main magnetic field. The electric field components E_+ and E_- are perpendicular to the magnetic field and gyrate in the same direction as the ions (left-hand polarization) and electrons (right-hand polarization), respectively. The refractive index is represented in an analogous manner. The rest of the notation in these two formulas is as follows: $\varepsilon_\pm = 1 - \frac{\omega_{pe}^2}{\omega(\omega \pm \omega_e)}$ and $\varepsilon_\parallel = 1 - \left(\frac{\omega_{pe}}{\omega}\right)^2$. The plasma is assumed to be cold, and the ions are assumed to be immobile (by virtue of the high frequency of oscillations).

Near the critical surface, dispersion relation (1) has the form

$$D \approx \frac{1}{N^2}\left(\frac{N_\perp^2(N^2-1)}{(\varepsilon_{+,c} - N^2)(\varepsilon_{-,c} - N^2)}\varepsilon_{\perp,c} + \varepsilon_\parallel\right) = 0, \quad (3)$$

where $\varepsilon_{\pm,c} = \frac{\omega_e}{\omega_e \pm \omega}$ are the values of $\varepsilon_\pm$ at the critical surface and $\varepsilon_{\perp,c} = \frac{1}{2}(\varepsilon_{+,c} + \varepsilon_{-,c}) = \varepsilon_{+,c}\varepsilon_{-,c}$. For a weakly inhomogeneous plasma in which the density varies on a spatial scale much longer than the oscillation wavelength, dispersion relation (1) should be regarded as an eikonal equation that relates the local value of the refractive index to the frequency.

Generally, dispersion relation (3) implies that, regardless of the value of $N_\parallel$, the transverse components of the refractive index should vanish at the critical surface. Along with $N_\perp$, the transverse components of the electric field also vanish at this surface, in accordance with expression (2). Consequently, the oscillations that approach the critical surface should transform into electron Langmuir oscillations. In fact, in a cold magnetized plasma, the latter are the only oscillations whose frequency is equal to ω_{pe} regardless of the value of the refractive index and whose electric field is parallel to the main magnetic field. The only exceptions are oscillations with $N^2 = \varepsilon_{\pm,c}$ and $N = 1$. Oscillations with $N^2 = \varepsilon_{\pm,c}$ are a superposition of the electron Langmuir oscillations and circularly polarized ones. At the critical surface, the transverse component of their refractive index vanishes, as is the case with electron Langmuir oscillations. However, in contrast to electron Langmuir oscillations, they freely cross the critical surface at a certain angle with respect to the normal of the surface. Such oscillations hold promise for launching microwave power into a dense plasma (see, e.g., [1]). Oscillations with $N = 1$ also can pass through the critical surface. Their wave vector can point in an arbitrary direction, as is the case with electromagnetic oscillations in vacuum, but their group and phase velocities are different. In addition, their polarization also differs from that of electromagnetic oscillations in vacuum [see expression (2)].

3. Let us consider the evolution of the electron Langmuir oscillations. As was shown above, they should be localized at the critical surface and their refractive index is parallel to the magnetic field. When the plasma density changes in the direction transverse to the magnetic field, refraction gives rise to the transverse component of the refractive index. As a result, electron Langmuir oscillations propagate from the critical surface; simultaneously, the transverse component of the electric field becomes nonzero.

The question naturally arises as to whether this process can serve as a mechanism for the escape of the energy of electron Langmuir oscillations into vacuum. This question can be answered by appealing to the simplest model of a plane plasma slab in which the density gradient is directed at a certain angle χ to the magnetic field. Together with the Cartesian coordinates introduced above, it is convenient to use a coordinate system (ξ, y, ζ) with the ξ-axis directed along the density gradient, so that $\xi = x\sin\chi + z\cos\chi$ and $\zeta = -x\cos\chi + z\sin\chi$. In these coordinates, $\varepsilon_\parallel \approx -\xi/L$ near the critical surface. As the electron Langmuir oscillations propagate in a plane-stratified plasma, the components of the refractive index N_y and N_ζ remain constant and only the component N_ξ varies. The dependence of N_ξ on the plasma density (the ξ coordinate) provides insight into the regions that are transparent to oscillations. At fixed values of N_y and N_ζ, this dependence is topologically equivalent to the dependence $N(q_e)$ for oscillations in a homogeneous plasma at a fixed angle θ between the vector of the refractive index and the magnetic field. That is why the most usual practice is to present the dependence $N^2(q_e)$ with $q_e = \left(\frac{\omega_{pe}}{\omega}\right)^2$ (see Figs. 1, 2). In a homogeneous plasma, the waves propagating toward one another have the same value of $N_\xi(q_e)$. For a plane-stratified plasma, the dispersion curve $N_\xi(q_e)$ in the (q_e, N_ξ) plane is generally asymmetric about the abscissa axis because ∇n_0 is not parallel to $\mathbf{B}_0$.

Near the critical surface, the squared transverse refractive index of the oscillations that transform into electron Langmuir oscillations at this surface is approximately equal to $N_\perp^2 \approx (N_\xi\sin\chi - N_\zeta\cos\chi)^2 \approx \text{const}\,\xi$. Consequently, the point of tangency between the dis-

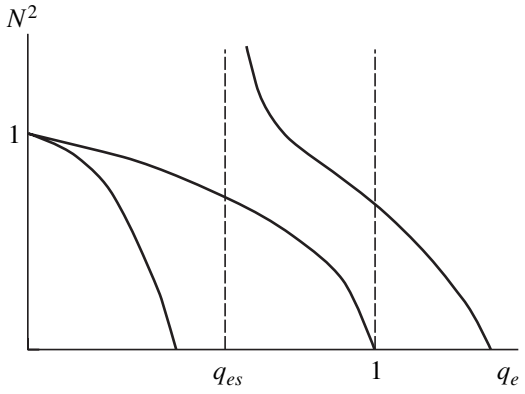

Fig. 1. N^2 as a function of the density of a homogeneous plasma for $\omega > \omega_e$ and $\pi/2 > \theta > 0$.

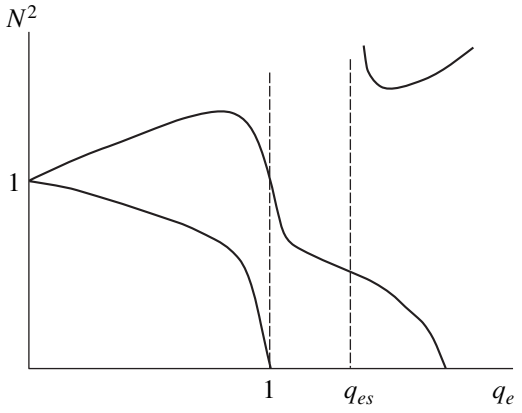

Fig. 2. Same as in Fig. 1, but for $\omega < \omega_e$.

persion curve and the vertical line $q_e = 1$ corresponds to the electron Langmuir oscillations. The energy of these oscillations will escape into vacuum if the dispersion curve that is tangent to the straight line $q_e = 1$ ends at the ordinate axis, at which $q_e = 0$. For $N_y = 0$, there will always be points of tangency, regardless of the value of N_ζ.

Let us analyze a simpler case of oscillations with $\omega > \omega_e$. The dispersion curves $N_\xi(q_e)$ for $N_y = 0$ and for different values of N_ζ are shown in Fig. 3. The distinctive features of the curves are as follows. Regardless of the N_ζ value, one of the dispersion curves in the (q_e, N_ξ) plane crosses the vertical line $q_e = 1$ at $N_\xi = (1 - N_\zeta^2)^{1/2}$. At the intersection point, the refractive index is equal to one. For $N_\zeta = \sqrt{\varepsilon_{+,c}}\sin\chi$, there is no point of tangency and the two dispersion curves become straight lines, also crossing the critical surface. These cases have already been mentioned above.

According to Fig. 3, the only oscillations that can escape from the plasma into vacuum are those with $N_\zeta < \varepsilon_{+,c}^{1/2}\sin\chi$. At the critical surface, these oscillations are such that $N_\xi < \varepsilon_{+,c}^{1/2}\cos\chi$ ($N < \varepsilon_{+,c}^{1/2}$). Oscillations with large N_ζ values belong to the branch of oscillations that reach the plasma resonance surface, in whose vicinity they are absorbed because of a sharp increase in the refractive index. In a plane-stratified plasma, the plasma resonance surface occurs at $q_{es} = \dfrac{\omega^2 - \omega_e^2}{\omega^2 - \omega_e^2\cos^2\chi}$.

For oscillations with $\omega < \omega_e$, the pattern of dispersion curves in the (q_e, N_ξ) plane is far more complicated, because both ordinary and extraordinary oscillations can reach the critical surface from the side of the lower plasma density. When propagating along the magnetic field, extraordinary oscillations become right-polarized (the electric vector rotates in the same direction as the electrons). Note, however, that, for $\chi > \arccos(2\omega_e/\omega - 1)^{-1/2}$, extraordinary oscillations cannot escape into vacuum, because in the vicinity of the critical surface there is only a waveguide channel bounded along the direction of the density gradient [1].

The dispersion curves $N_\xi(q_e)$ for $\omega < \omega_e$ and for $\omega > \omega_e$ are not plotted here because, in both cases, they can be obtained by deforming the corresponding curves in Fig. 2. Note only that electron Langmuir oscillations with $N_\zeta < \varepsilon_{+,c}^{1/2}\sin\chi$ escape into vacuum after their conversion into an ordinary wave. Analogously, electron Langmuir oscillations with $\varepsilon_{+,c}^{1/2}\sin\chi < N_\zeta < \varepsilon_{-,c}^{1/2}\sin\chi$ convert into an extraordinary wave and also escape into vacuum. Oscillations with $N_\zeta > \varepsilon_{-,c}^{1/2}\sin\chi$ do not escape: they are eventually absorbed near the plasma resonance surface. For $\omega \longrightarrow \omega_e$, the maximum value of N_ζ at which the energy of electron Langmuir oscillations can escape into vacuum increases abruptly. Note, however, that, since $N = 1$ in vacuum and the component N_ζ of the refractive index of oscillations propagating in a plane-stratified plasma is conserved, the only oscillations of interest are those with $N_\zeta < 1$.

4. Whether the energy of the electron Langmuir oscillations escapes into vacuum or is absorbed near the plasma resonance surface depends on the relationship between N_ζ and $N_{\zeta,\max} = \varepsilon_{\pm,c}^{1/2}\sin\chi$. Because of the effect of electron thermal motion, these quantities change by an amount on the order of β^2, where $\beta = v_{Te}/c$ and v_{Te} is the electron thermal velocity. The critical density changes by the same amount. For a nonrelativistic plasma, these changes are insignificant. The influence of the thermal effects on the shape of the ray trajectories near the critical surface is more important.

This influence can be analyzed by incorporating the electron thermal motion into dispersion relation (3) and

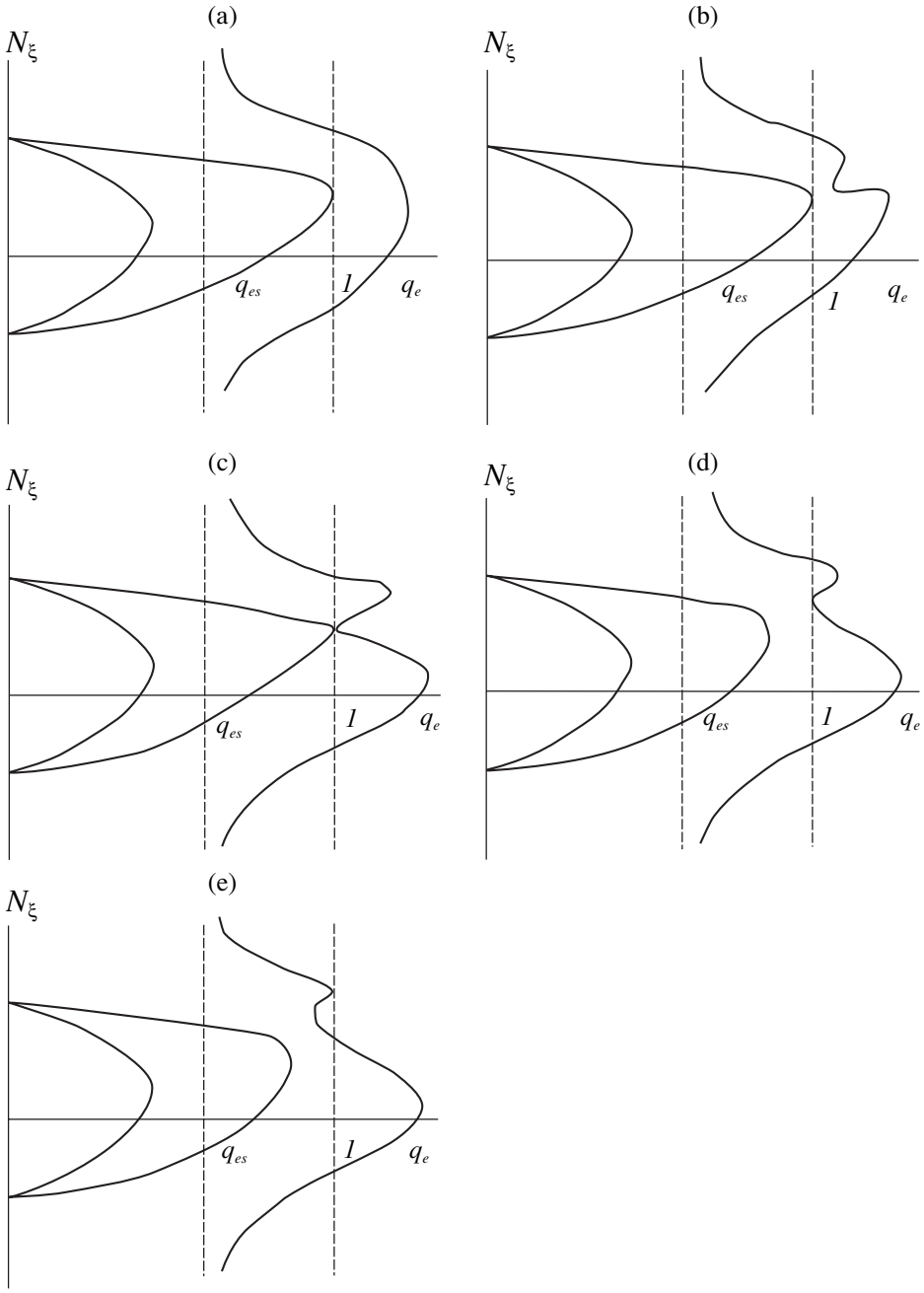

Fig. 3. N_ξ as a function of the density of a plane plasma slab for $N_y = 0$ and (a) $0 < N_\zeta < \sqrt{\varepsilon_{+,c}}\sin\chi$, (b) $N_\zeta < \sqrt{\varepsilon_{+,c}}\sin\chi$, $|N_\zeta - \sqrt{\varepsilon_{+,c}}\sin\chi| \ll \sqrt{\varepsilon_{+,c}}\sin\chi$, (c) $N_\zeta = \sqrt{\varepsilon_{+,c}}\sin\chi$, (d) $\sqrt{\varepsilon_{+,c}}\sin\chi < N_\zeta < \sin\chi$, and (e) $\sin\chi < N_\zeta$.

resolving the resulting equation in terms of the frequency:

$$\omega \approx \omega_{pe} - \frac{\omega_{pe0}\varepsilon_{\perp,c}}{2}\frac{N_\perp^2(N_\parallel^2-1)}{(N_\parallel^2-\varepsilon_{+,c})(N_\parallel^2-\varepsilon_{-,c})} + 3\frac{\omega_{pe0}}{2}N_\parallel^2\beta^2, \tag{4}$$

where $\omega_{pe} \approx \omega_{pe0}(1 + \xi/L)$ and ω_{pe0} is the value of ω_{pe} at the critical surface.

The ray trajectories are described by the following standard equations of the geometrical-optics approximation:

$$\dot{N}_x = A, \quad \dot{x} = BN_x, \quad \dot{z} = C_1N_x^2 + C_2, \tag{5}$$

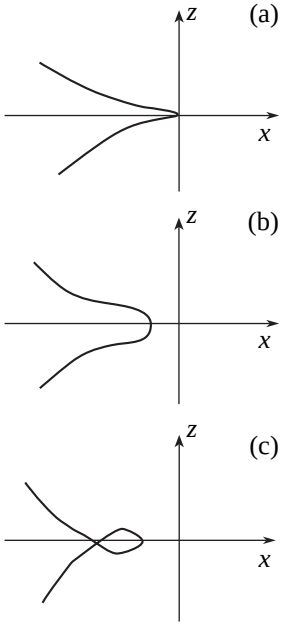

Fig. 4. Ray trajectories of oscillations with $N_y = 0$ near the critical surface for (a) $C_2 = 0$, (b) $C_1C_2 > 0$, and (c) $C_1C_2 < 0$.

where $A = -\frac{\omega\sin\chi}{L}$, $B = \frac{(N_\parallel^2 - 1)\omega\varepsilon_{\perp,c}}{(N_\parallel^2 - \varepsilon_{+,c})(N_\parallel^2 - \varepsilon_{+,c})}$, $C_1 = \frac{N_\parallel}{(N_\parallel^2 - \varepsilon_{+,c})^2(N_\parallel^2 - \varepsilon_{+,c})^2}\left((N_\parallel^2 - 1)^2 + \frac{\omega^2}{\omega_e^2 - \omega^2}\right)\omega\varepsilon_{\perp,c}$, $C_2 = 3\omega N_\parallel\beta^2$. The variations in the longitudinal component of the refractive index are neglected (which is valid at short distances from the critical surface). All quantities that have the dimension of length are normalized to c/ω.

Equations (5) yield

$$N_x = At,$$

$$x = Bt^2/2,$$

$$z = C_1t^3/3 + C_2t.$$

In the (x, z) plane, the ray trajectories have the form (see Fig. 4)

$$z = \pm\frac{C_1}{3}\left(\frac{2x}{B}\right)^{3/2} \pm C_2\left(\frac{2x}{B}\right)^{1/2}.$$

For $C_2 = 0$ (which corresponds to a cold plasma), the ray trajectories are semicubical parabolas [1]. Hence, near the critical surface, electron Langmuir oscillations propagate across the magnetic field; i.e., their group velocity and wave vector are mutually perpendicular. This property is characteristic of the potential oscillations of a cold plasma. Piliya and Fedorov [11] established that this is also true of oscillations near the plasma resonance surface, at which $N \longrightarrow \infty$. The effect of the electron thermal motion is that the group velocity of the electron Langmuir oscillations becomes nonzero. As a result, the cusps of the ray trajectories are smoothed, in which case the trajectories in the vicinity of the critical surface form loops, provided that the constants C_1 and C_2 have opposite signs.

In conclusion, note that the energy of the electron Langmuir oscillations can escape into vacuum via this mechanism only from a magnetized plasma. In fact, a decrease in the magnetic field has two consequences. First, the resonance surface whose position is given by $q_{es} = \frac{\omega^2 - \omega_e^2}{\omega^2 - \omega_e^2\cos^2\chi}$ approaches the critical surface. This should result in the absorption of Langmuir oscillations. Second, as the magnetic field decreases to zero, $\varepsilon_{\pm,c} = \sqrt{\frac{\omega_e}{\omega_e \pm \omega}}$ also tends to zero and the range of values (at the critical surface) of the refractive index for oscillations that can escape into vacuum shrinks to a point.

REFERENCES

1. A. V. Timofeev, Fiz. Plazmy **27**, 978 (2001) [Plasma Phys. Rep. **27**, 922 (2001)].
2. A. V. Timofeev, Fiz. Plasmy **27**, 1046 (2001) [Plasma Phys. Rep. **27**, 990 (2001)].
3. A. K. Berezin, G. P. Berezin, L. I. Bolotin, and Ya. B. Faĭnberg, At. Énerg. **14**, 249 (1963).
4. B. A. Demidov, N. I. Elagin, D. D. Ryutov, and S. D. Fanchenko, Zh. Éksp. Teor. Fiz. **48**, 454 (1965) [Sov. Phys. JETP **21**, 302 (1965)].
5. V. E. Golant, A. P. Zhilinskiĭ, I. F. Liventsova, and I. E. Sakharov, Zh. Tekh. Fiz. **35**, 2034 (1965) [Sov. Phys. Tech. Phys. **10**, 1559 (1966)].
6. A. N. Karkhov, Zh. Éksp. Teor. Fiz. **59**, 356 (1970) [Sov. Phys. JETP **32**, 192 (1971)].
7. V. N. Tsytovich, *Nonlinear Effects in Plasmas* (Nauka, Moscow, 1967; Plenum, New York, 1970).
8. V. L. Ginzburg, *The Propagation of Electromagnetic Waves in Plasmas* (Nauka, Moscow, 1967; Pergamon, Oxford, 1970).
9. V. V. Zheleznyakov, *Electromagnetic Waves in Space Plasma* (Nauka, Moscow, 1977).
10. A. V. Timofeev, *Resonance Phenomena in Plasma Oscillations* (Fizmatlit, Moscow, 2000).
11. A. D. Piliya and V. I. Fedorov, in *High-Frequency Plasma Heating*, Ed. by A. G. Litvak (Inst. Prikl. Fiz., Gorkii, 1983), p. 281.

Translated by O.E. Khadin

Plasma Physics Reports, Vol. 29, No. 8, 2003, pp. 688–694. Translated from Fizika Plazmy, Vol. 29, No. 8, 2003, pp. 747–753.

BEAMS IN PLASMA

Effect of the Microwave Ponderomotive Force on the Development of the Beam Instability at Different Plasma and Beam Parameters

Yu. P. Bliokh*, V. O. Podobinskiĭ, and G. V. Sotnikov****

**Technion, Haifa, 3200 Israel*

***Institute of Plasma Electronics and New Acceleration Methods, National Science Center Kharkov Institute of Physics and Technology, ul. Akademicheskaya 1, Kharkov, 61108 Ukraine*

Received August 12, 2002; in final form, October 16, 2002

Abstract—A study is made of the effect of the parameters of a beam and a plasma-filled waveguide in a traveling-wave tube amplifier on the stability of the amplification regime against the excitation of ion acoustic waves by the microwave ponderomotive force. It is shown that, in such an amplifier, the stability of the amplification of a microwave can be achieved by simultaneously increasing the density and energy of the electron beam. © *2003 MAIK "Nauka/Interperiodica".*

1. INTRODUCTION

A number of experiments on microwave generation and amplification by electron beams propagating in plasma-filled waveguide structures revealed a deep low-frequency self-modulation of the output microwave signal [1–3]. In [3–5], this self-modulation was attributed to the plasma nonlinearity, which manifests itself in the interrelation between the conditions for the generation of microwave fields in the plasma and the plasma parameters. Thus, a microwave ponderomotive force arising from the spatial variations of the amplitude of the microwave that is synchronized with the beam can substantially distort an originally uniform longitudinal plasma density profile. Because of the resonant nature of the beam instability, this effect changes the amplitude of the amplified wave. Moreover, a microwave ponderomotive force whose strength exceeds a certain threshold gives rise to ion acoustic waves in the plasma. The ion acoustic waves so generated propagate in the direction opposite to the propagation direction of the beam, thereby giving rise to distributed feedback and changing the microwave amplifier into a generator of low-frequency waves.

The simplest version of the mathematical model proposed in [3–5] contains a single parameter, whose value characterizes the degree to which the plasma nonlinearity influences the development of the beam instability. When the parameter is large, propagating intense ion acoustic waves induce a deep (up to 100%) modulation of the amplitude of the amplified microwave. One of the consequences of this modulation is a significant decrease in the time-averaged amplitude of the output signal from a traveling-wave tube (TWT) amplifier. The value of the parameter depends on the parameters of the beam and plasma-filled waveguide structure. That is why knowledge of this dependence is important for the development and creation of particular devices with the desired output parameters. In other words, the problem is to determine the parameter ranges of the beam and plasma-filled waveguide structure within which the plasma nonlinearity plays an essential role. Here, this problem is solved for a TWT amplifier with a slow wave structure in the form of a cylindrical magnetized waveguide partially filled with a magnetized plasma.

2. ANALYTICAL CALCULATIONS

First, we briefly outline the mathematical model proposed in [3–5].

For $n_b \ll n_p$ (where n_b and n_p are the beam and plasma densities, respectively), the growth rate δk of the beam instability is slow ($\delta k \ll k$, where k is the wave vector of a microwave) and the longitudinal component of the electric field of the amplified wave can be represented as

$$E(\mathbf{r}, z, t) = E_0(z, t)G(\mathbf{r})\exp(ikz - i\omega t) + \text{c.c.}$$

Here, $E_0(z, t)$ is a slowly varying complex amplitude and the function $G(\mathbf{r})$ describes the dependence of the field of the eigenmode of the waveguide structure on the radial coordinate $\mathbf{r}$. The frequency ω of the wave and its wave vector are related by the resonance condition $\omega = kv_b$, where v_b is the initial velocity of the electron beam.

1063-780X/03/2908-0688$24.00

The mathematical model is based on the equations for the excitation of a microwave by an electron beam in an unsteady inhomogeneous plasma,

$$\frac{\partial \varepsilon}{\partial \zeta} + i\left(\eta - \frac{1}{\zeta_0}\int_0^{\zeta_0} \eta\, d\zeta\right)\varepsilon = -\frac{1}{2\pi}\int_0^{2\pi} e^{-i\varphi(\varphi_0,\zeta)}\, d\varphi_0,$$

$$\frac{\partial^2 \varphi}{\partial \zeta^2} = \mathrm{Re}(\varepsilon e^{i\varphi}),$$

and the equations describing the behavior of the slow, small perturbations of the plasma density and velocity under the action of the microwave ponderomotive force,

$$\frac{\partial \eta}{\partial \tau} + \frac{\partial u}{\partial \zeta} = 0, \quad \frac{\partial u}{\partial \tau} + \frac{\partial \eta}{\partial \zeta} = -\Lambda \frac{\partial |\varepsilon|^2}{\partial \zeta}.$$

Here, $\zeta = \delta k \cdot z$ is the dimensionless longitudinal coordinate; $\varepsilon = \dfrac{ekE_0 G(0)}{m v_b^2 \delta k^2}$ is the dimensionless wave amplitude; $\varphi = \omega(z/v_b - t)$ is the phase of a beam electron in the wave; φ_0 is the initial phase in the injection plane $z = 0$ for the beam; $(\eta(\zeta, \tau), u(\zeta, \tau)) = \dfrac{k}{2\delta k}\dfrac{\omega_p}{v_{ph}}\dfrac{\partial v_{ph}}{\partial \omega_p}\left(\dfrac{\delta \bar{n}_p}{n_0}, \dfrac{\bar{V}}{c_s}\right)$ are the changes in the dimensionless density and velocity of the plasma under the action of the microwave ponderomotive force, where the superior bar stands for averaging over the plasma cross-sectional area S_p ($\bar{f} \equiv (\int_{S_p} G^2 f\, dS)(\int_{S_p} G^2 dS)^{-1}$ with the corresponding normalization indicated; v_{ph} is the phase velocity of the microwave; and ζ_0 is the distance corresponding to the linear amplification stage. The expression for the spatial growth rate of the beam instability in a homogeneous plasma has the form

$$\delta k = -k\left(\frac{\omega_b^2}{\omega^2}\frac{S_b G^2(0)/\int_{S_w} G^2 dS}{k(\partial D/\partial k)}\right)^{1/3}, \qquad (1)$$

where S_w and S_b are the cross-sectional areas of the waveguide and beam, respectively; $\omega_b = \left(\dfrac{4\pi e^2 n_b}{m_e \gamma_b^3}\right)^{1/2}$ is the beam plasma frequency; $D \equiv D(\omega, k, n_p)$ is a function whose zeros determine the dispersion of the eigenmodes of the system; and $\gamma_b = (1 - v_b^2/c^2)^{-1/2}$ is the relativistic factor of the beam.

The conditions under which the above equations are valid were described in detail in [3–5]. Here, note only that, in the cases that may be of interest for microwave electronics, the inequality $v_g \gg c_s$ (where v_g is the group velocity of the microwave, $c_s = \sqrt{T_e/M}$ is the ion acoustic speed, T_e is the plasma electron temperature, and M is the mass of a plasma ion) is satisfied by a large margin. This allows us to describe the wave excitation by time-independent equations, in which case the unsteady nature of the plasma in the structure can be accounted for through the parametric dependence of the plasma density perturbations δn_p on the dimensionless time $\tau = \delta k \cdot c_s t$.

In the case in which the beam velocity and density at the entrance to the system ($\zeta = 0$) are constant and the field amplitude $|\varepsilon|_0$ is prescribed, the initial conditions for the equations describing the excitation of a microwave have the form

$$\varepsilon(0, \tau) = |\varepsilon|_0, \quad \varphi(0, \tau) = \varphi_0,$$

$$\frac{\partial \varphi}{\partial \zeta}(0, \tau) = 0, \quad 0 \le \varphi_0 \le 2\pi.$$

The set of plasma transport equations is supplemented by the following boundary conditions at the entrance (left) end of the waveguide structure ($\zeta = 0$) and at its exit (right) end ($\zeta = l = \delta k \cdot L$, where L is the dimensional length of the system):

$$(1 + \gamma)\eta(0, \tau) + (1 - \gamma)u(0, \tau) = 0,$$
$$(1 + \gamma)\eta(l, \tau) - (1 - \gamma)u(l, \tau) = 0,$$

with γ being the reflection coefficient of the ends of the system for an ion acoustic wave.

The parameter

$$\Lambda = \frac{m v_b^2}{2T_e}\left(\frac{\delta k}{k}\right)^3 \frac{\omega_p}{v_{ph}}\frac{\partial v_{ph}}{\partial \omega_p} \times \int_{S_p} G^4(\mathbf{r})\, dS \left(G^2(0)\int_{S_p} G^2(\mathbf{r})\, dS\right)^{-1} \qquad (2)$$

is the main parameter of the model. At a certain critical value of this parameter, $\Lambda = \Lambda_c$, the steady-state operating regime of a TWT amplifier becomes unstable and the amplifier begins to operate in a self-modulation regime. Numerical simulations show that, for a TWT amplifier operating in a nonlinear regime, the critical value of the main parameter is essentially independent of the boundary conditions and is approximately equal to $\Lambda_c \approx 1$.

Now, we proceed to the solution of the problem in question—determination of the dependence of the parameter Λ on parameters of the beam and a waveguide partially filled with a magnetized plasma.

Using the resonance condition $\omega = k v_b$, we write the following expressions for the function $G(r)$:

$$G(r) = J_0(k_p r), \quad 0 \le r \le R_p;$$

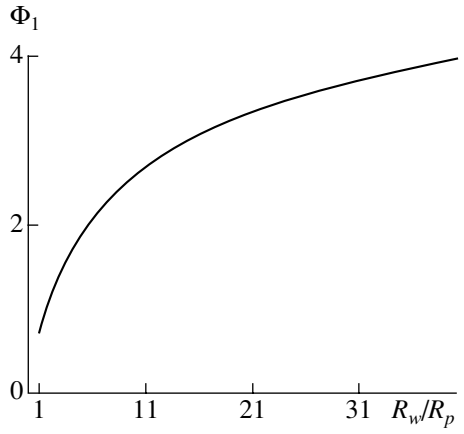

Fig. 1. Plot of the function $\Phi_1(R_w/R_p)$.

$$G(r) = \frac{I_0(k_\nu r)K_0(k_\nu R_w) - I_0(k_\nu R_w)K_0(k_\nu r)}{I_0(k_\nu R_p)K_0(k_\nu R_w) - I_0(k_\nu R_w)K_0(k_\nu R_p)} J_0(k_p R_p),$$
$$R_p \le r \le R_w.$$

Here, J_0, I_0, and K_0 are Bessel functions; $k_\nu = k/\gamma_b$; $k_p = (-\varepsilon_0)^{1/2}k/\gamma_b$; and $\varepsilon_0 = 1 - \omega_p^2/\omega^2$ is the plasma permittivity. The dispersion relation of the eigenmodes of a magnetized plasma waveguide has the form (see, e.g., [6])

$$k_p \frac{J_1(k_p R_p)}{J_0(k_p R_p)} = k_\nu \frac{I_1(k_\nu R_p)K_0(k_\nu R_w) + I_0(k_\nu R_w)K_1(k_\nu R_p)}{I_0(k_\nu R_p)K_0(k_\nu R_w) - I_0(k_\nu R_w)K_0(k_\nu R_p)}, \quad (3)$$

where J_1, I_1, and K_1 are Bessel functions.

From formulas (1)–(3) we obtain the following expression for the parameter Λ in the case of a magnetized plasma waveguide:

$$\Lambda = \frac{c^2 n_b R_b^2}{\nu_T^2 n_p R_p^2} \frac{\gamma_b^2 - 1}{\gamma_b^6} \frac{\int_0^1 J_0^4(k_p R_p x) x dx}{J_0^4(k_p R_p)(1 + F^2)^2}, \quad (4)$$

where

$$F = \frac{c(\gamma_b^2 - 1)^{1/2}/R_p\omega_p}{I_0(k_\nu R_p)K_0(k_\nu R_w) - I_0(k_\nu R_w)K_0(k_\nu R_p)}$$

with $\nu_T = (2T_e/m)^{1/2}$ being the thermal velocity of the plasma electrons.

Note that the explicit dependence of the parameter Λ on the beam density, beam radius, and plasma temperature is given by expression (4). The dependence on the plasma density, plasma radius, waveguide radius, and the energy of a relativistic beam is more difficult to obtain. The corresponding expressions derived analytically and calculated numerically will be presented below.

Dispersion relation (3) has n solutions ($n = 1, 2, 3, \ldots$) describing eigenmodes with different radial numbers. The solution $\omega_n = \omega_n(k)$ lies in the interval between the roots with the same number of the functions $J_1(k_p R_p)$ and $J_0(k_p R_p)$.

An electron beam can excite an eigenmode with the frequency $\omega_n(k)$ when the Langmuir frequency of the plasma electrons is higher than the threshold frequency ω_{pn},

$$\omega_{pn}(\lambda_n) \equiv \sqrt{4\pi e^2 n_n(\lambda_n)/m} = \lambda_n c(\gamma_b^2 - 1)^{1/2}/R_p, \quad (5)$$

where the numbers λ_n are solutions to the equation

$$\frac{J_0(\lambda_n)}{J_1(\lambda_n)} = \lambda_n \ln\frac{R_w}{R_p}. \quad (6)$$

Expression (5) and Eq. (6) imply that the threshold plasma density decreases as the ratio of the waveguide radius to the radius of the plasma increases.

From formulas (3) and (4) we can easily deduce the critical value of the parameter Λ:

$$\Lambda_n(\lambda_n) = \left(\frac{\omega_b R_b}{2\nu_T\gamma_b^3}\right)^2 \Phi_n(\lambda_n), \quad (7)$$

where Φ_n, being a function of the ratio of the radii, is defined by the expression

$$\Phi_n(\lambda_n) = \frac{\int_0^{\lambda_n} J_0^4(x) x dx}{\left[\int_0^{\lambda_n} J_0^2(x) x dx\right]^2}. \quad (8)$$

The range of changes of the function Φ_n for the $n = 1$ radial mode differs fundamentally from that for the remaining modes. Thus, the function for the first radial mode increases from $\Phi_1(\gamma_{0,1})$ at $R_w = R_p$ to infinity for large values of the ratio of the radii (with the asymptotics $\Phi_1 = \ln(R_w/R_p)$). Here, $\gamma_{0,1}$ is the first root of the function $J_0(x)$. The plot of this function is shown in Fig. 1. For modes with the radial numbers $n = 2, 3, \ldots$, the functions Φ_n vary within fairly narrow intervals, from $\Phi_n(\gamma_{0,n})$ at $R_w = R_p$ to $\Phi_n(\gamma_{1,n})$ at $R_w \gg R_p$. Here, $\gamma_{1,n}$ is the nth root of the function $J_1(x)$.

This analysis shows that, at a fixed plasma radius, the critical value of the parameter Λ for all radial modes increases with waveguide radius. The range of Λ_n values narrows with increasing mode number.

For a waveguide fully filled with plasma ($R_w = R_p$), the expression for the parameter Λ that is valid over the

entire wavelength range can be derived from definition (4) and Eq. (3):

$$\Lambda = \Lambda_f = \Lambda_n(\gamma_{0,n})\frac{n_p}{n_n(\gamma_{0,n})}. \quad (9)$$

As can be seen from expressions (5), (7), and (8), the critical value Λ_f is independent of the plasma radius. The parameter Λ increases linearly with the plasma density; the rate of increase $\partial\Lambda/\partial n_p$ is proportional to the cross-sectional area of the plasma and decreases for modes with larger radial numbers.

For a waveguide partially filled with a plasma, an explicit dependence of Λ on the parameters of the waveguide structure can be obtained analytically only for long- and short-wavelength modes.

2.1. Long-Wavelength Modes

The term "long-wavelength mode" can be introduced through a comparison with the characteristic radial scale in the waveguide. When the plasma radius R_p and the waveguide radius R_w are of the same order of magnitude, the condition for the wavelength to be long is $k_\nu R_w \ll 1$. When the radii are markedly different, the wavelength can be regarded as being long under the conditions $k_\nu R_p \ll 1$ and $k_\nu R_w \gg 1$, which indicate that the wavelength is large in comparison with the plasma radius but is short in comparison with the waveguide radius. When the plasma and waveguide radii are close to each other, the characteristic transverse dimension is the width of the vacuum gap; in this case, the condition in question has the form $k_\nu(R_w - R_p) \ll 1$.

We will work under the condition $k_\nu R_w \ll 1$. Using the solution to dispersion relation (3) in this approximation, we obtain the following expression for the parameter Λ:

$$\Lambda = \Lambda_n(\lambda_n)\left(1 + \left(\frac{n_p}{n_n(\lambda_n)} - 1\right)(1 + \Psi_1(\lambda_n))\right). \quad (10)$$

Since the expression for the function Ψ_1 is fairly involved, we will not write it out here and restrict ourselves to a graphic representation of this function for the first radial mode (see Fig. 2). As can be inferred from this figure, the condition $\Psi_1 \ll 1$ is satisfied for all possible ratios of the waveguide radius to the plasma radius. Analogous conditions hold for the remaining modes. Consequently, with a high degree of accuracy, we can set

$$\Lambda = \Lambda_n(\lambda_n)\frac{n_p}{n_n(\lambda_n)}. \quad (11)$$

It is easy to see that this expression is a generalization of expression (9) to an arbitrary ratio of the waveguide and plasma radii. Formulas (5), (9), and (11) show that the larger the ratio of these radii, the higher the rate at which the parameter Λ increases with plasma density.

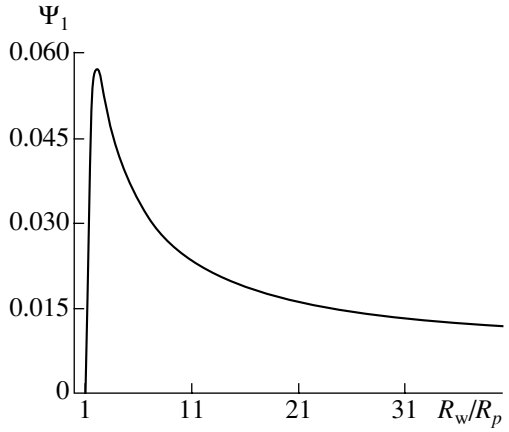

Fig. 2. Plot of the function $\Psi_1(R_w/R_p)$.

On the contrary, the larger the mode number, the lower the rate.

We consider a plasma waveguide structure with very different waveguide and plasma radii, $R_w \gg R_p$. Recall that this case can be described by the conditions $k_\nu R_p \ll 1$ and $k_\nu R_w \gg 1$. According to the dispersion relation, these two conditions are equivalent to

$$\lambda_n^2 \ll \frac{n_n(\lambda_n)}{n_p} \ll \lambda_n^2 \ln\frac{R_w}{R_p}. \quad (12)$$

For the plasma density range determined by conditions (12), we substitute the solution to dispersion relation (3) into formula (4) to obtain the following expression for the parameter Λ:

$$\Lambda = \Lambda_n(\lambda_n)\left(\frac{n_n(\lambda_n)}{n_p}(1 - \Psi_2(\lambda_n)) + \Psi_2(\lambda_n)\right) \times\left(1 + \frac{J_1^2(\lambda_n)}{J_0^2(\lambda_n)}\right)^2, \quad (13)$$

where

$$\Psi_2(\lambda_n) = \lambda_n^2 - 1 + \frac{\lambda_n^2 J_0^4(\lambda_n)}{2\int_0^{\lambda_n} J_0^4(x)x\,dx}.$$

Expression (13) can be simplified by using the relationship $\lambda_n^2 \approx 2(\ln R_w/R_p)^{-1} \ll 1$, which follows from Eq. (6), and by taking into account formulas (5), (7), and (8). As a result, to zero order in the small quantity λ_n, expression (13) reduces to $\Lambda = \frac{1}{2\gamma_b^4}\frac{n_b}{n_p}\left(\frac{v_b R_b}{v_T R_p}\right)^2$. We can see that the parameter Λ is independent of the waveguide radius and decreases as the plasma density increases.

For a waveguide of large radius, the local maximum Λ_{max} can be estimated by equating expressions (11) and (13):

$$\Lambda_{max} = \Lambda_n(\lambda_n)\left(1 + \frac{J_1^2(\lambda_n)}{J_0^2(\lambda_n)}\right). \quad (14)$$

This formula implies that, in the limit $\ln(R_w/R_p) \longrightarrow \infty$, the maximum value is $\Lambda_{max} = \Lambda_n(\lambda_n)$.

Now, we consider a waveguide structure in which the plasma and waveguide radii differ only slightly, $\delta = R_w/R_p - 1 \ll 1$. This condition allows us to consider a wider range of wavelengths in comparison with that in the case analyzed at the beginning of this section ($k_v R_w \ll 1$). The reason is that, for such a waveguide structure, the condition for the wavelength to be long has the form $k_v R_p \delta \ll 1$. As follows from dispersion relation (3), this is equivalent to the condition

$$1 - 2\delta \le \frac{n_p}{n_n(\gamma_{0,n})} \ll \frac{1}{\gamma_{0,n}^2 \delta^2}. \quad (15)$$

For plasma densities satisfying condition (15), we obtain

$$\Lambda = \Lambda_f(1 + 2\delta). \quad (16)$$

A comparison of this expression with that for a waveguide fully filled with a plasma shows that, for long-wavelength modes excited in the waveguide at hand, the parameter Λ again increases linearly with the plasma density but at a higher rate.

2.2. Short-Wavelength Modes

Here, we will assume that the condition $k_v R_p \min\{1, \delta\} \gg 1$ is satisfied, which, according to dispersion relation (3), is equivalent to

$$\frac{n_p}{n_n(\gamma_{0,n})} \gg \frac{1}{\gamma_{0,n}^2 \min\{1, \delta^2\}}. \quad (17)$$

From formula (4) and dispersion relation (3), we obtain

$$\Lambda = \Lambda_f\left(1 + \frac{4}{\gamma_{0,n}}\sqrt{\frac{n_n(\gamma_{0,n})}{n_p}} + \frac{8}{\gamma_{0,n}^2}\frac{n_n(\gamma_{0,n})}{n_p}\right). \quad (18)$$

This expression shows that, for short-wavelength modes, the parameter Λ is independent of the waveguide radius. Since, in the limit $n_p \longrightarrow \infty$, the wave field is nonzero only inside the plasma and, to zero order in the small parameter $1/n_p$, the dispersion relations for a waveguide fully filled with a plasma and for an open system (without a waveguide wall) are the same, it might be expected that the straight line Λ_f described by formula (9) would be the asymptote of dependence (18). This is not the case, however. In fact, the contribution to Λ_f from the second term on the right-hand side of formula (18) increases with the plasma density, so that the difference $\Lambda - \Lambda_f$ increases in absolute value. Nevertheless, dependence (18) and straight line (9) are asymptotically close to each other, because the relative difference $(\Lambda - \Lambda_f)/\Lambda_f$ decreases as the plasma density increases.

For a waveguide of large radius ($R_w \gg R_p$), the local minimum Λ_{min} can be estimated from expressions (13) and (18):

$$\Lambda_{min} \approx 4\Lambda_n(\gamma_{0,n})\left(1 + \frac{J_1^2(\lambda_n)}{J_0^2(\lambda_n)}\right)\frac{\lambda_n}{\gamma_{0,n}}\left[\frac{\Phi_n(\lambda_n)}{\Phi_n(\gamma_{0,n})}\right]^{1/2}. \quad (19)$$

In the limit $\ln(R_w/R_p) \longrightarrow \infty$, we can estimate this quantity for the first radial mode as $\Lambda_{min} \approx 3\Lambda_n(\gamma_{0,1})$.

Summarizing the results obtained in this section in investigating the dependence of the parameter Λ on the plasma density for different values of the ratio of the plasma radius to the waveguide radius, we can draw the following conclusions. The critical value Λ_n increases as this ratio becomes larger and decreases as the radial mode number increases. The larger the ratio of the radii, the larger the amount by which Λ_n decreases. The rate $\partial\Lambda/\partial n_p$ at which the parameter Λ increases with the plasma density also becomes lower as the mode number increases. For a waveguide structure with a large value of the ratio of the waveguide radius to the radius of the plasma, the rate at which the parameter Λ decreases in a narrow range of plasma densities is essentially independent of the radial mode number.

Now we address the question of how the parameter Λ depends on the beam energy. The above formulas show that the critical value of this parameter and (to an even greater extent) the rate at which it changes with increasing plasma density depend on the beam energy in an extremely nonlinear fashion. As the beam energy increases, the parameter Λ decreases abruptly. It might seem that this provides an efficient way of stabilizing the amplification of a microwave in a TWT amplifier. However, it is impossible to achieve the desired stabilization effect merely by increasing the energy, because doing so will reduce the amplification coefficient. In fact, the maximum amplitude of the wave excited by a beam in a plasma waveguide is known to be determined by the trapping of the beam electrons by the field of the excited wave and, to within a numerical factor on the order of unity, is approximately equal to $E_{max} \approx \frac{m v_b^3 \delta k^2}{e\omega}$. Using expression (1) and dispersion relation (3), we can readily show that the maximum amplitude of the wave excited at a given frequency ω depends on the beam parameters as $E_{max} \sim (\omega_b^2/\gamma_b^4)^{2/3}$. Here and below, to simplify the formulas, we assume that $\gamma_b^2 \gg 1$.

Hence, the requirement that the amplification coefficient, at least, should not decrease as the beam energy increases is equivalent to the conservation of the quan-

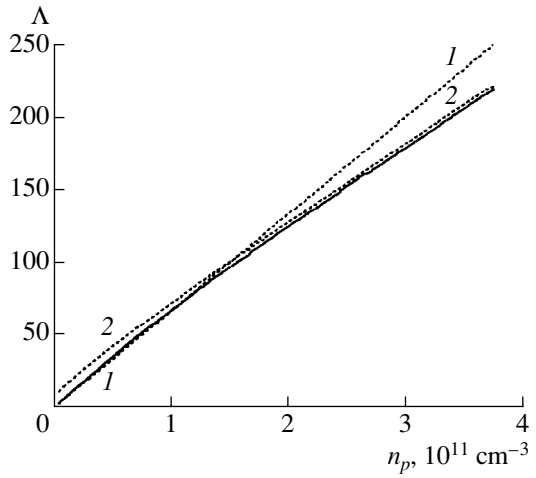

Fig. 3. Dependence $\Lambda(n_p)$ for $R_w/R_p = 1.2$. The solid curve was computed numerically, and dashed curves *1* and *2* were calculated from formulas (16) and (18), respectively.

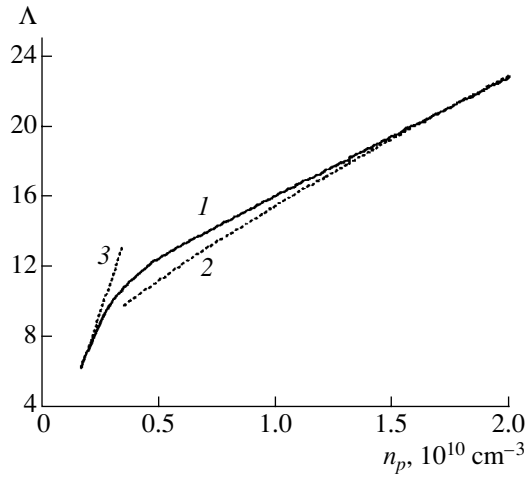

Fig. 4. Dependence $\Lambda(n_p)$ for $R_w/R_p = 3.0$. Solid curve *1* was computed numerically, and dashed curves *2* and *3* were calculated from formulas (18) and (11), respectively.

tity ω_b^2/γ_b^4. This indicates that the energy of the beam should be increased simultaneously with its density. Hence, according to the above formulas, the behavior of the parameter Λ can be described as follows. The critical value of this parameter decreases in proportion to $\sim\gamma_b^{-2}$ and the rate at which it increases with plasma density is proportional to $-\partial\Lambda/\partial n_p \sim 1/\gamma_b^4$. For a waveguide with $\ln R_w/R_p \gg 1$, the rate at which the parameter Λ decreases in a narrow range of plasma densities remains essentially the same.

3. NUMERICAL RESULTS

Numerical calculations were carried out for the parameters of the experimental device used in [3] to investigate the self-consistent dynamics of the plasma and the microwaves generated in it by an electron beam. The device was a 12.5-cm-radius metal waveguide placed in a uniform guiding magnetic field with an induction of 1.5 kG. An electron beam with a current of 50 mA, an electron energy of 1 keV, and a radius of 1 cm was injected into the neutral gas filling the waveguide. The plasma was produced by the impact ionization of a neutral gas by the beam electrons and, in a sufficiently strong microwave field, by the conventional ionization processes occurring in a beam–plasma discharge. The plasma radius essentially coincided with the beam radius. The only parameter that was varied in the experiments was the neutral gas pressure, and, consequently, the plasma density.

For numerical calculations, we chose the first radial mode because this mode is the first to be excited by the beam as the plasma density increases. Figures 3–5 show the parameter Λ calculated numerically from formula (2) as a function of the plasma density for three different values of the ratio of the waveguide radius to the plasma radius: $R_w/R_p = 1.2$, 3.0, and 12.5. Note that the last value coincides with that in the experimental device. The dashed curves in the figures show the function $\Lambda(n_p)$ calculated analytically from formulas (11), (13), (16), and (18).

As can be seen from Figs. 3–5, the above analytic expressions provide a qualitatively and even quantitatively (in the plasma regions for which they are valid) good description of the behavior of the parameter Λ. Note that, in Fig. 5, the agreement between dashed curve *4*, which is calculated from formula (13), and the computed solid curve is quantitatively unsatisfactory. This disagreement stems from the fact that formula (13) was derived under the condition $\ln(R_w/R_p) \gg 1$,

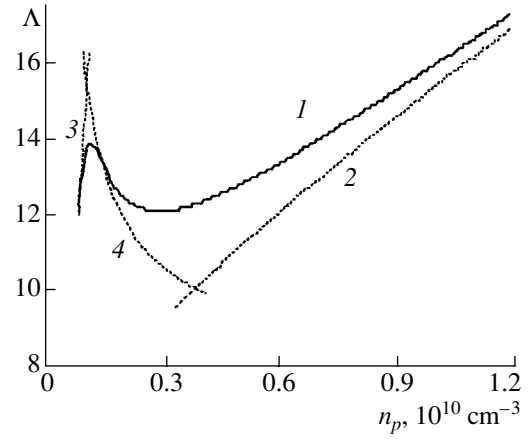

Fig. 5. Dependence $\Lambda(n_p)$ for $R_w/R_p = 12.5$. Solid curve *1* was computed numerically, and dashed curves *2*, *3*, and *4* were calculated from formulas (18), (11), and (13), respectively.

whereas, in the case at hand, we have $\ln(R_w/R_p) \approx 2.5$. Nevertheless, it is evident from Fig. 5 that formula (13) can serve to estimate the values of the parameter Λ.

The results of our numerical simulations confirm the conclusion that the parameter Λ increases with the plasma density and the ratio of the waveguide radius to the radius of the plasma. Computations carried out over the entire range of plasma densities and for all possible degrees of the filling of the waveguide with plasma show that the minimum value of Λ is approximately equal to the critical value of this parameter for a waveguide completely filled with plasma, $\Lambda_n(\gamma_{0,1}) \approx 3$. Hence, even in the case under consideration—that of a low-power beam—the values of this parameter substantially exceed the critical value $\Lambda_c \approx 1$, at which the steady-state operating regime becomes unstable.

4. CONCLUSIONS

Our analytical and numerical calculations show that a TWT amplifier based on a magnetized plasma-filled waveguide is highly sensitive to the action of the microwave ponderomotive force. Even with a low-power beam, it is impossible to achieve a steady-state amplification regime by choosing a certain value of the ratio of the waveguide radius to the plasma radius. In such an amplifier, the process of amplification of a microwave can only be stabilized by simultaneously increasing the density and energy of the electron beam.

Note that it is incorrect to directly apply the results obtained above to TWT amplifiers based on other types of plasma-filled waveguide structures. In general, however, the behavior of plasma under the action of the microwave ponderomotive force should be the same for all TWT amplifiers in which the plasma plays an essential role. In contrast to a TWT amplifier based on a plasma-filled waveguide, the phase velocity of a microwave excited in a TWT amplifier based on a hybrid slow wave structure [2] is determined primarily by the vacuum slow wave structure. Consequently, the parameter $\frac{\omega_p}{v_{ph}}\frac{\partial v_{ph}}{\partial \omega_p}$ in formula (2) will change only slightly as the plasma density changes. On the other hand, for a hybrid waveguide, the function $G(r)$, which describes the radial structure of the wave, is very sensitive to the plasma density variations. Hence, for a TWT amplifier based on a hybrid waveguide structure, the value of the parameter Λ should also depend strongly on both the beam parameters and the parameters of the waveguide structure [see formula (2)].

ACKNOWLEDGMENTS

We are grateful to I.N. Onishchenko for discussing the results obtained.

REFERENCES

1. E. A. Kornilov and S. M. Krivoruchko, Pis'ma Zh. Éksp. Teor. Fiz. **10**, 465 (1969) [JETP Lett. **10**, 299 (1969)].
2. A. N. Antonov, Yu. P. Bliokh, E. A. Kornilov, *et al.*, Fiz. Plazmy **27**, 268 (2001) [Plasma Phys. Rep. **27**, 251 (2001)].
3. Yu. P. Bliokh, N. M. Zemlyanskiĭ, M. G. Lyubarskiĭ, *et al.*, *Scientific-Technical Report on the UNTTs Project No. 277, 1997*, p. 81.
4. Yu. P. Bliokh, Ya. B. Fainberg, M. G. Lyubarskii, and V. O. Podobinskii, *SPIE on Intense Microwave Pulses, San Diego, CA, 1997*, Vol. 3158, p. 182.
5. K. Yu. Bliokh, Yu. P. Bliokh, M. G. Lyubarskiĭ, and V. O. Podobinskiĭ, Izv. Vyssh. Uchebn. Zaved., Prikl. Nelin. Dinam. **7** (1), 29 (1999).
6. A. N. Kondratenko, *Plasma Waveguides* (Atomizdat, Moscow, 1976).

Translated by I.A. Kalabalyk

Plasma Physics Reports, Vol. 29, No. 8, 2003, pp. 695–708. Translated from Fizika Plazmy, Vol. 29, No. 8, 2003, pp. 754–767.

LOW-TEMPERATURE PLASMA

Formation and Development of a Leader Channel in Air

N. A. Popov

Skobeltsyn Institute of Nuclear Physics, Moscow State University, Vorob'evy gory, Moscow, 119899 Russia

Received December 26, 2002

Abstract—A self-consistent model is constructed that makes it possible to investigate the formation of a leader channel in air and the evolution of the channel parameters in the developed stage, when the leader is as long as several meters or more. The initial stage of the formation of the channel is characterized by a rapid increase in the electron density and gas temperature, which is a consequence of the onset of thermal–ionizational instability. The radius of a fully developed plasma column at the current $I = 1$ A in air at atmospheric pressure is $R_h \cong 10^{-2}$ cm. Then, because of the gas-dynamic and thermal expansion, the plasma radius R_h increases considerably; as a result, the electric field and the reduced field E/N in the corresponding parts of the channel decrease. In the case under consideration, the field in the "oldest" parts of the leader drops to 200 V/cm and even lower and the reduced field becomes as weak as $E/N \leq 10$ Td. In this case, the densities of the main species of neutral and charged particles at the center of the channel remain close to their thermodynamically equilibrium values. The results of calculations are compared with the available experimental data. © *2003 MAIK "Nauka/Interperiodica".*

1. INTRODUCTION

The onset of a leader (or the streamer–leader transition), which is one of the most important stages of the leader process, is apparently among the least studied ones [1]. The leader originates near an electrode in the main channel of the initial burst of a pulsed corona, where the gas is sufficiently heated by the total current of the streamers starting from a common base (main channel). A necessary condition for the onset of each subsequent element of the leader channel in air is the heating of the air within the channel head to temperatures of about 1500–2000 K [2, 3]. For a leader channel propagating in air with a typical velocity of $(1–3) \times 10^6$ cm/s, the duration of such a heating process is no longer than 3×10^{-7} s [1]. Hence, the gas in the leader head should be heated at least at a rate of 3×10^9 K/s.

At $T \geq 1500$ K, the negative ions are actively destroyed and the attachment of electrons is balanced by their detachment at a progressively increasing rate. This makes it possible to significantly increase the lifetime of the plasma produced [2, 3]. Later, however, it was shown that the fraction of negative ions in the balance of charged particles in the main channel of the corona is relatively small; hence, an increase in the detachment rate does not have any important effect on the channel conductivity [4, 5]. Charged particles in the main channel of a pulsed corona are lost mainly through electron–ion recombination [1, 4, 5], whose rate depends substantially on which of the species of positive ions dominates. As the gas temperature increases, the complex ions (recombining as a relatively high rate) are destroyed and the loss rate of the charged particles slows down. Hence, it is generally accepted that, in order for the streamer–leader transition to occur, it is necessary to heat the cold air in the streamer channels to temperatures $T \geq 1500$–2000 K [1–3].

The leader can originate immediately after the initial burst of a pulsed corona and also after the dark pause, which can last several microseconds [1, 6, 7]. The onset of the dark pause is associated with the weakening of the electric field by the space charge of the initial burst and with the termination of the ionization processes. The absence of a dark pause indicates that the weakening of the electric field is partially balanced by both a decrease in the gas density (i.e., the reduced field E/N is conserved) and the onset of additional ionization processes in a highly excited hot gas.

The first data on the leader diameter were obtained with a streak camera [8]. The radius of the initial visible channel was found to be $R_v = 0.1 \pm 0.05$ mm. The dependence of the gas-dynamic expansion of the channel on the growth rate of the leader current was investigated by Gorin and Inkov [9]. It was found that, when the current increased linearly, the channel also expanded according to a linear law, in which case the initial radius of the leader was again $R_v = 0.1 \pm 0.05$ mm.

In [6, 10], the thermal diameter of a leader channel in a 1.5-m-long gap was measured by shadowgraphy. The measured diameter increased from the initial value $2R_h = 0.03$ mm to values of 1.6–3.8 mm at a time corresponding to a transition to the main stage of a spark discharge. These values characterize the transverse size of the main energy deposition region. The measurement error was estimated to be ±0.1 mm. At a fixed leader current, the cross-sectional area of the hot part of the channel increased linearly with time [10].

1063-780X/03/2908-0695$24.00

The mean electric field E_L is one of the most important parameters of the already formed part of the leader channel. However, the electric field distribution along the leader has not yet been measured directly, and the estimates obtained for the mean field E_L from indirect measurements differ by more than one order of magnitude [1]. In the parts of the channel that have just been formed in air at atmospheric pressure, the electric field (at $T = 1500$–2000 K) is as strong as several kV/cm [1]. On the other hand, according to the data of [11], leaders can bridge a gap of length 150–200 m at an applied voltage of $U_0 \leq 4 \times 10^6$ V, which corresponds to a mean electric field of $E_L \leq 200$–250 V/cm. It follows from here that, as time elapses, the electric field in the corresponding cross section of the leader channel can be greatly weakened.

In early papers [12, 13], the leader parameters were calculated under the assumption that the plasma is in local thermodynamic equilibrium. The models developed in those papers make it possible to investigate the evolution of long-lived parts of the leader channel, but they are incapable of describing the initial nonequilibrium stage of the channel formation and the transition to the final quasi-equilibrium stage. In more recent works (see, e.g., [2, 3, 14] and other related papers), the formation of a leader was mostly investigated under the assumption that charged particles are produced mainly by electron-impact ionization of molecules. In this case, the reduced field E/N approaches a quasi-steady value of about 70–80 Td (1 Td = 10^{-17} V cm^2), and the electric field is weakened because the density of the gas decreases during its heating and gas-dynamic expansion. In [1, 6], it was found that the radius of the leader channel at a mean current of about $I_L \cong 1$ A amounted to $R_h \cong 0.1$ cm and the gas temperature increased to $T = 5000$–6000 K. In this case, the electron density at $E/N = 80$ Td was $N_e = I_L/(\pi R_h^2 eV_{dr}) \cong 2 \times 10^{13}$ cm^{-3}, which was markedly lower than the corresponding equilibrium densities (in air at atmospheric pressure, the electron density at $T = 5000$ K is 4.9×10^{13} cm^{-3}, and, at $T = 6000$ K, it is equal to 2.14×10^{14} cm^{-3} [15]). This circumstance indicates that the kinetic model in question must include the processes that make it possible to adequately describe a transition to the equilibrium stage of the channel evolution, in particular, the associative ionization reactions

$$N(^4S) + O(^3P) \longrightarrow NO^+ + e, \qquad (1)$$

which ensure the production of the bulk of charged particles in air at temperatures $T \geq 3000$–4000 K.

In modeling the formation of a leader channel and its subsequent evolution, Aleksandrov *et al.* [16] used the following approach. They described the initial stage of the channel evolution by a zero-dimensional kinetic model [17] with a simplified description of the gas-dynamic processes. They showed that, by the end of this stage, the densities of the main species of charged particles approach their thermodynamically equilibrium values and that charged particles are mainly produced in reactions (1). The parameters of the leader channel in the developed stage were described by a one-dimensional non-steady-state model for the gas temperature under the assumption that the densities of neutral particles are equal to their thermodynamically equilibrium values and the gas pressure is constant. An important conclusion obtained in [16] is that the calculated results are weakly sensitive to the initial conditions, the available information on which is scanty. Taking into account reactions (1) made it possible to adequately describe the experimental data obtained by Baselyan and Razhanskiĭ [18] for electric field dynamics on time scales longer than 100 μs.

The initial stage of the formation of a leader channel was studied by Temnikov [19], who considered the heating and gas-dynamic expansion of the main channel of a streamer corona. He assumed that the time dependence of the power deposited in the discharge is prescribed, but did not calculate the discharge parameters. He calculated the maximum initial radius of the current channel at which the leader can form under the experimental conditions of [6, 7] and found that it is no larger than $R_0 \leq 50$–60 μm. Note that, in [19], the gas heating in the reactions of quenching of the electronically excited atoms and molecules was not taken into account. In what follows, however, it will be shown that, under the conditions in question, such gas heating predominates. Presumably, it is for this reason that the obtained values of the radius R_0 are so small.

Hence, the problem of describing the initial stage of the evolution of a leader channel has not yet been completely solved. The model designed to solve this problem should be based on the gas-dynamic equations and should incorporate a sufficiently complete set of kinetic reactions, as well as the main processes responsible for gas heating. Such a model should also be capable of adequately describing a transition from the equilibrium plasma state to the final quasi-equilibrium state.

The objective of this paper is to construct a self-consistent model that would make it possible to investigate the parameters of the leader channel in both the stage of its formation and the developed stage. Another objective is to test the model by comparing the calculated results with the experimental data.

2. DESCRIPTION OF THE MODEL

The problem of describing the evolution of the parameters of a solitary plasma channel is treated in a one-dimensional axisymmetric geometry. The time dependence of the conduction current in the channel cross section under consideration is assumed to be known. The density of charged particles and the channel radius R_0 are assumed to be specified at the initial time, at which the gas is assumed to be in an unexcited state.

In a number of works (see, e.g., [20, 21] and other related papers), it was shown that the radial profile of the electron density in a streamer channel is close to a Gaussian one. The radial distributions of the radiation intensity and gas density in the main channel and the "young" leader are also close to Gaussian [10, 22]. On this basis, the initial radial profile of the electron density can be chosen in the form

$$N_e(r) = N_e^0 \exp\left[-\left(\frac{r}{R_0}\right)^2\right]. \quad (2)$$

The initial radius R_0 is the parameter of the problem.

For a given discharge current, the electric field at each instant of time is described by the equation

$$E = \frac{I}{2\pi e\int_0^\infty N_e(r)\mu(r)r\,dr}, \quad (3)$$

where $N_e(r)$ is the radial electron density profile and $\mu(r)$ is the electron mobility, which is determined by the radial profiles of the gas density and reduced field $E/N(r)$.

The kinetic block of the model includes the processes responsible for changes in the densities of the main species of the neutral and charged components, vibrational excitation, and gas heating in the discharge. The dependences of the rates of ionization and excitation of the particles in the discharge on both the reduced field E/N and the degree of vibrational excitation of molecules were taken from [23, 24].

The electron density was determined by solving the balance equation

$$\frac{\partial N_e}{\partial t} + \frac{1}{r}\frac{\partial(uN_e)}{\partial r} = \frac{1}{r}\frac{\partial}{\partial r}\left(rD_a\frac{\partial N_e}{\partial r}\right) + N_e(\nu_{\text{ion}} - \nu_{\text{att}}) + Q_{\text{ass}} - Q_{\text{rec}} + Q_{\text{det}}. \quad (4)$$

Here, D_a is the ambipolar diffusion coefficient; ν_{ion} is the ionization rate; ν_{att} is the electron attachment rate; Q_{rec} is the electron–ion recombination rate; Q_{det} is the rate of detachment of the electrons from all negative ion species, such as $O(^3P)$ atoms, $O_2(a^1\Delta_g)$ molecules, etc. [25]; and Q_{ass} is the rate of production of charged particles in the associative ionization reactions [26]

$$\begin{aligned} &N_2(A^3\Sigma_u^+) + N_2(a'^1\Sigma_u^-) \longrightarrow e + N_4^+, \\ &\quad 5\times10^{-11}\ \text{cm}^3/\text{s}, \\ &N_2(a'^1\Sigma_u^-) + N_2(a'^1\Sigma_u^-) \longrightarrow e + N_4^+, \\ &\quad 2\times10^{-10}\ \text{cm}^3/\text{s}. \end{aligned} \quad (5)$$

The densities of all other species of charged particles were determined from analogous balance equations. Ten species of positive and negative ions were taken into account: O_2^+, O_4^+, $O_2^+\cdot N_2$, N_2^+, N_4^+, NO^+, O^-, O_2^-, O_3^-, and O_4^-. The model set of reactions was based on the set of ion–molecular reactions [25] and also included the reactions involving the neutral particles $N_2(X^1\Sigma_g)$, $N_2(A^3\Sigma_u^+)$, $N_2(B^3\Pi_g)$, $N_2(C^3\Pi_u)$, $N_2(a'^1\Sigma_u^-)$, $N(^4S)$, $N(^2D)$, $N(^2P)$, $O_2(X^3\Sigma_g)$, $O_2(a^1\Delta_g)$, $O(^3P)$, $O(^1D)$, and $O(^1S)$. The main reactions and their rate constants are presented in [25, 27, 28].

Experimental investigations (see [29–31] and other related papers) made it clear that the gases (nitrogen, air) are rapidly heated by high-power discharges, in which case a significant fraction of the discharge power is expended on the excitation of the electronic degrees of freedom of the molecules [28]. The specific heat release power W_T has the form

$$W_T = W_E + \frac{\varepsilon_V - \varepsilon_0(T)}{\tau_{VT}},$$

where W_E is the specific power of the rapid gas heating due to the relaxation of the energy of electronic states, ε_V is the energy density of the vibrational excitation of N_2 molecules, and τ_{VT} is the characteristic VT relaxation time. Rapid gas heating was described by the model developed in [28] with allowance for the reactions of predissociation of highly excited electronic states of oxygen molecules (which are populated via electron impact or the quenching of the excited states of N_2 molecules), the reactions of the quenching of the metastable atoms $O(^1D)$ by N_2 molecules, etc. Account was also taken of the reactions of the VT relaxation of the vibrationally excited nitrogen molecules by $O(^3P)$ atoms and O_2 molecules [32].

According to the data from spectroscopy measurements [1, 6], the gas temperature in the leader channel can be higher than 5000–6000 K. In order to describe the kinetic processes occurring in air at such high temperatures, the model was supplemented with the reactions of thermal dissociation of N_2, O_2, and NO molecules, the rate constants of which were taken from review [33], and associative ionization reactions (1),

$$N(^4S) + O(^3P) \longrightarrow NO^+ + e,$$

$$k_1 = 1.5\times10^{-15}T\exp\left(-\frac{32000}{T}\right)\ \text{cm}^3/\text{s},$$

whose rate constant was taken from [34].

The radial expansion of a hot gas channel was modeled by the following set of one-dimensional time-dependent equations:

$$\frac{\partial\rho}{\partial t} + \frac{1}{r}\frac{\partial\rho ur}{\partial r} = 0, \quad (6)$$

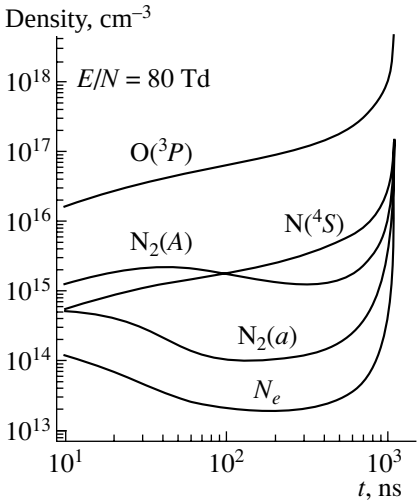

Fig. 1. Dynamics of the main air components excited by a discharge at E/N = 80 Td ($U \cong 19.5$ kV) and P = 760 torr.

$$\frac{\partial \rho u}{\partial t} + \frac{1}{r}\frac{\partial \rho u^2 r}{\partial r} + \frac{\partial P}{\partial r} = 0, \quad (7)$$

$$\frac{\partial \rho E_g}{\partial t} + \frac{1}{r}\frac{\partial \rho u r (E_g + P)}{\partial r} = \frac{1}{r}\frac{\partial}{\partial r}\left(r\lambda\frac{\partial T}{\partial r}\right) + W_T, \quad (8)$$

where ρ, u, and P are the density, velocity, and pressure of the gas, respectively, and $E_g = \varepsilon + u^2/2$ with ε being the internal energy per unit gas volume. The dependences $\varepsilon = \varepsilon(\rho, T)$ for air over wide density and temperature ranges are given in [15]. The first term on the right-hand side of Eq. (8) describes the change in the internal gas energy due to thermal conduction. The thermal conductivity of air was taken from [35].

The boundary conditions for Eqs. (3) and (6)–(8) were chosen in accordance with the assumptions that the central discharge region is axisymmetric and the gas parameters at the outer boundary of the computation region, $r = R$, are unperturbed,

$$\left.\frac{\partial N}{\partial r}\right|_{r=0} = 0, \quad \left.\frac{\partial T}{\partial r}\right|_{r=0} = 0, \quad N|_{r=R} = N_0,$$

$$T|_{r=R} = 300 \text{ K}.$$

The set of Eqs. (6)–(8) was solved numerically on a radially uniform grid by using a modified MacCormack method of second-order accuracy in space and time [36]. It is worth noting that the numerical scheme used to solve the equation should, on the one hand, ensure a sufficiently high accuracy in approximating the solution and, on the other, not produce any oscillating solutions near the discontinuities in the gas-dynamic parameters (the property of high-accuracy difference schemes [37]). Under the conditions in question, the onset of oscillations in the gas density led to oscillations in the reduced field E/N and the development of thermal–ionizational instability.

3. CALCULATED RESULTS

3.1. Testing of the Model

The kinetic block of the model described above was tested by calculating the time of breakdown in air, τ_{br}, as a function of the reduced field E/N. The calculated results were compared with the experimental data obtained by Larsson [38] in studying the development of streamer breakdown in a 1-cm-long air gap between a rod and a plane at pressures P = 0.75 and 1 atm, the applied voltage being U = 17–25 kV. The electric circuit used in [38] was capable of maintaining a constant voltage across the discharge gap during the total time of breakdown. In the model developed here, the electric field in the discharge gap was calculated by the formula $E = (U - U_c)/d$, where U is the applied voltage and U_c is the voltage drop at the cathode. According to the calculations of [39], the latter parameter under the conditions of [38] is approximately equal to $U_c \cong 0.2$ kV.

The initial (streamer) stage of the formation of a plasma channel and the final stage of breakdown of the discharge gap were investigated numerically by Naidis [39]. The results obtained in that paper show that the problem of determining the breakdown time τ_{br} under the conditions of [38] can be treated in terms of a uniform model with a given initial electron density ($N_e^0 \cong 2 \times 10^{14}$ cm^{-3}).

As an example, Fig. 1 illustrates the results obtained from the above model of the evolution of the air components excited by a discharge with the electric field E/N = 80 Td (under the conditions of [38] and for P = 760 torr, this corresponds to an applied voltage of $U \cong$ 19.5 kV). For other magnitudes of the reduced field E/N, the calculated time evolutions are analogous to those shown in Fig. 1.

The main processes that govern an explosive increase in the electron density are associative ionization reactions (5). It is also important to take into account the effect of the vibrationally excited nitrogen molecules on the rates of the electron processes whose thresholds are higher than the mean electron energy [24]. Thus, as the degree of vibrational excitation of N_2 increases, the rates of population of the $N_2(A^3\Sigma_u^+)$, $N_2(a'^1\Sigma_u^-)$, and other states by electron impact become markedly higher and, consequently, associative ionization reactions (5) proceed faster. Analogous conclusions were reached by Naidis [39] based on the results of the corresponding calculations.

Figure 2 shows the breakdown time τ_{br} measured experimentally [38] and calculated numerically as a function of the reduced field E/N. (In calculations, the breakdown time τ_{br} was defined as the time during which the electron density becomes ten times higher than its initial value N_e^0.) It can be seen that the kinetic model developed here provides an adequate description

of the experimental data from [38] over a fairly wide range of reduced fields, E/N = 75–105 Td. The model proposed in [39] also agrees well with the experiment. The dashed curve in Fig. 2 shows the results calculated without allowance for the effect of the vibrational excitation of N_2 molecules on the rates of the electron processes. As expected, this effect is most pronounced in the range of low values of the reduced field, E/N < 80–85 Td.

Recall that, in order to calculate the parameters of the leader channel at high temperatures, the model also incorporates additional processes that are responsible for a transition to the final quasi-equilibrium plasma state. Figure 3 displays the equilibrium densities of the neutral and charged particles as functions of the air temperature at the pressure P = 1 atm. The symbols show the experimental data of [15], and the curves show the calculated results. The model proposed here is seen to well describe the data of [15] in the temperature range T = 4000–7000 K.

The gas-dynamic part of the model was tested against the results of solving the problem of the evolution of a plane discontinuity [40]. At the initial instant, the coordinate of the discontinuity was x_0 = 80. To the left of the discontinuity, the initial normalized pressure, velocity, and density of the gas were: P_1 = 480, u_1 = 0, and ρ_1 = 8, respectively, and, to the right of x_0, these parameters were equal to P_2 = 1, u_2 = 0, and ρ_2 = 1. The decay of the discontinuity results in the formation of all structures typical of a gas-dynamic flow: a shock wave, a contact discontinuity, and a rarefaction wave [40]. The results of calculations of the gas density profile formed at the time t = 4 are illustrated in Fig. 4, in which the solid curve shows an analytic solution. We can see that the analytic solution adequately reflects all of the structures of the flow. The shock wave spreads out over two grid step sizes, and the contact discontinuity (at x = 113.3) spreads out over five to seven grid step sizes. It is important to note that the numerical solution does not oscillate near the discontinuities in the gas-dynamic parameters.

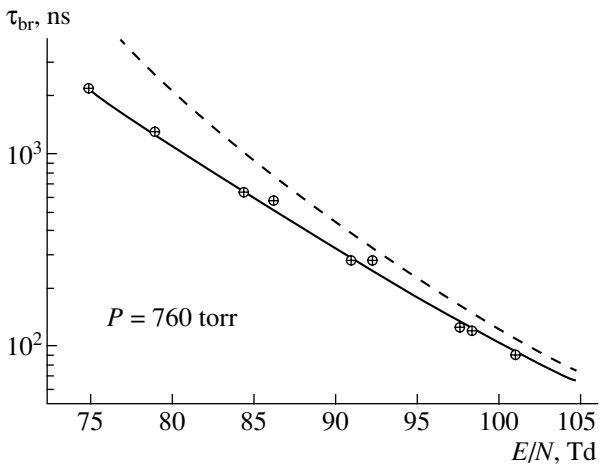

Fig. 2. Dependence of the breakdown time τ_{br} in air on E/N. The symbols show the experimental data from [38], the solid curve is calculated from the complete model, and the dashed curve is calculated without allowance for the effect of the vibrational excitation of N_2 molecules on the rates of electron processes.

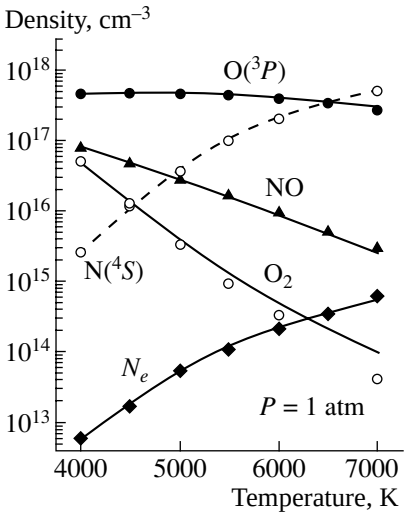

Fig. 3. Equilibrium densities of neutral and charged particles vs. air temperature at P = 1 atm. The symbols show the data from [15], and the curves show the calculated results.

3.2. Modeling of the Initial Stage of the Formation of a Leader Channel

The results presented in this section were obtained from numerical calculations of the parameters of the channel that forms in an air at atmospheric pressure under the action of a pulsed corona discharge ignited between a sphere and a plane [6]. Figure 5 shows the measured waveform of the current near a spherical anode with a diameter of 12.5 cm for the case in which the leader channel originates from the main channel of a pulsed corona without a dark pause [6]. In [2, 19, 41], the maximum initial radius R_0 of the current channel under the experimental conditions of [6] was determined by assuming that, for $t \geq 120$ ns, the gas temperature is lower than 1500–2000 K. According to [2, 19], these conditions are favorable for the formation of the leader channel immediately after the initial burst of a pulsed corona (without any significant dark pause). In [2, 41], the maximum initial channel radius was found to be $R_0 \cong 100$ μm, and, in [19], it was found to be $R_0 \leq$ 50–60 μm. In the present paper, the gas-heating dynamics at the discharge axis was calculated for the discharge-current evolution observed in [6]. The results calculated for different initial radii R_0 of the channel are presented in Fig. 5. On time scales of $t \geq 120$ ns, the

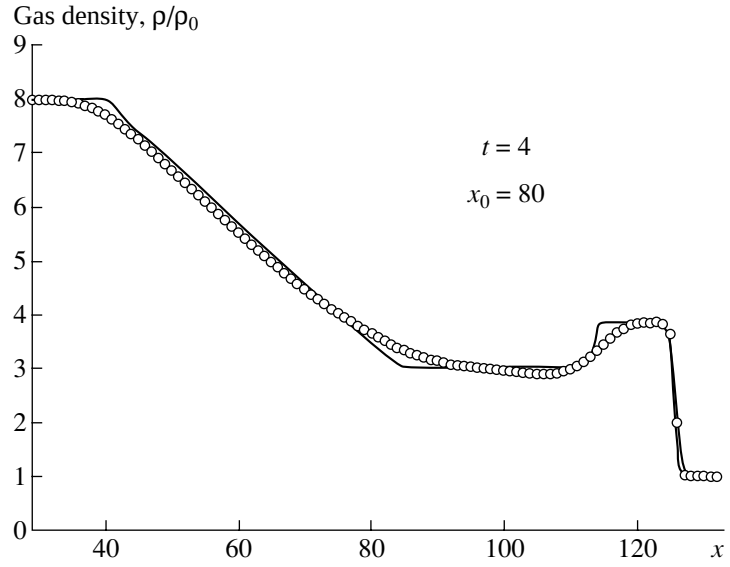

Fig. 4. Decay of a discontinuity with the parameters $x_0 = 80$, $\gamma = 5/3$, $u_1 = u_2 = 0$, $\rho_1 = 8$, $\rho_2 = 1$, $P_1 = 480$, and $P_2 = 1$. The solid curve is an exact solution [40] at $t = 4$, and the circles show the results of our calculations.

condition $T \geq 2000$ K is satisfied for $R_0^{\max} \cong 0.4$ mm. Since the gas-heating rate depends strongly on R_0 (Fig. 5), the value $R_0^{\max}$ can be determined with a fairly high accuracy.

Figure 6 demonstrates the results of calculations of the dynamics of the reduced field E/N and the energy deposited in the axial region of the plasma channel for the condition of [6]. One can see that, near the axis, the energy is deposited mainly at reduced electric fields of $E/N = 65$–75 Td and the energy input amounts to $W \cong 3$ eV/mol.

The formation of the main channel of a pulsed corona in air under the conditions of [6] was simulated numerically by Aleksandrov and Bazelyan [42]. They used a quasi-two-dimensional model that includes a fairly complete set of plasmochemical processes and takes into account the ionization expansion of the channel; the heating and gas-dynamic expansion of the channel were neglected. The model developed in [42]

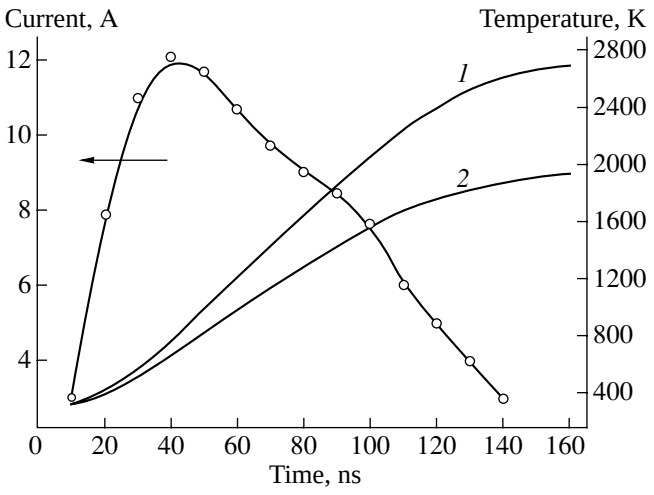

Fig. 5. Dynamics of the current in the main channel of a pulsed corona [6] and results from calculations of gas heating at the discharge axis for $R_0 = (1)$ 0.4 and (2) 0.45 mm.

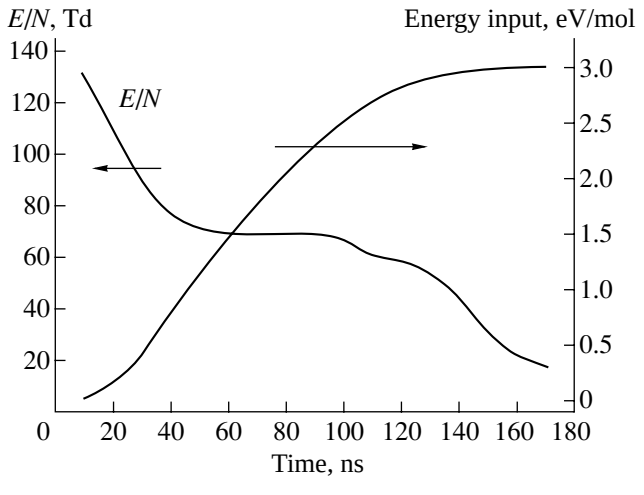

Fig. 6. Time evolutions of the reduced field E/N and the energy deposited at the discharge axis for the conditions of Fig. 5 and $R_0 = 0.4$ mm.

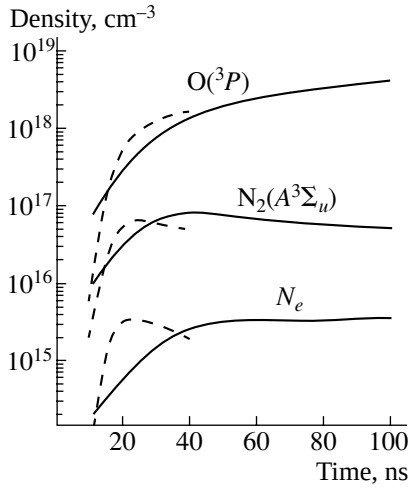

Fig. 7. Dynamics of the air components for the conditions of Fig. 5. The dashed curves show the results of calculations from a quasi-two-dimensional model with allowance for the ionization expansion of the channel [42].

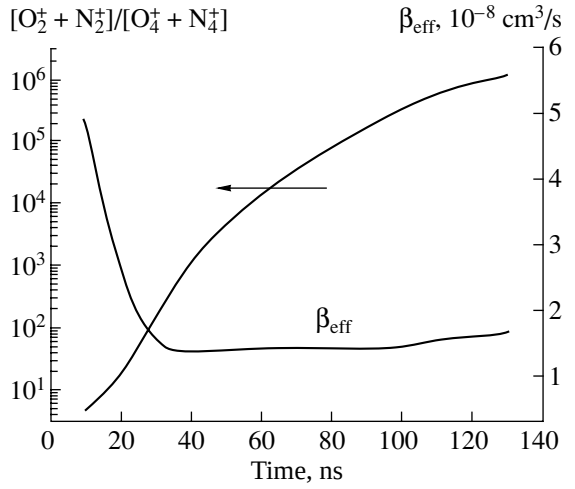

Fig. 8. Time evolutions of the relative content of complex ions and the effective recombination coefficient β_{eff} at the discharge axis for P = 760 torr and R_0 = 0.4 mm.

provides both an adequate description of the discharge-current evolution observed in [6] and a qualitatively correct picture of the propagation of the front of the secondary ionization wave, which forms the main channel of the corona (the corresponding experimental data were obtained in [43] for conditions analogous to those of [6]).

The time behavior of three air components at the discharge axis is illustrated in Fig. 7, in which the dashed curves show the results obtained in [42] and the solid curves show the results of the present calculations. The results are seen to agree fairly well. The densities of the $N_2(A^3\Sigma_u^+)$ and $N_2(a'^1\Sigma_u^-)$ molecules amount to (3–5) $\times$ 10^{16} cm^{-3}; as a result, the role of associative ionization reactions (5) involving these molecules substantially increases. It should also be noted that the degree of dissociation of oxygen molecules near the discharge axis is high: the density of $O(^3P)$ atoms is higher than 4×10^{18} cm^{-3}. As a consequence, the negative and complex positive ions are rapidly decomposed in the reactions [25]

$$N_4^+ + O(^3P) \longrightarrow O^+ + 2N_2, \quad 2.5 \times 10^{-10}\ \text{cm}^3/\text{s},$$

$$O_4^+ + O(^3P) \longrightarrow O_2^+ + O_3, \quad 3 \times 10^{-10}\ \text{cm}^3/\text{s}.$$

Figure 8 shows the results of calculations of the dynamics of the relative densities of complex ions, $[O_2^+ + N_2^+]/[O_4^+ + N_4^+]$, and the effective electron–ion dissociative recombination coefficient β_{eff},

$$\beta_{eff} = \frac{\sum \beta_{ion} N_{ion}^+}{\sum N_{ion}^+}.$$

We can see that, for $t \geq 30$ ns, the relative densities of the complex ions are such that $[O_2^+ + N_2^+] \gg [O_4^+ + N_4^+]$ and the recombination coefficient is almost constant, $\beta_{eff} \cong$ const; a slight increase in β_{eff} after 100 ns is associated with a decrease in both the reduced field E/N (Fig. 6) and the electron temperature. Complex ions are decomposed mainly by the $O(^3P)$ atoms rather than as a result of gas heating, as was assumed in [4, 5]. Hence, the criterion for the onset of the leader channel, $T \geq$ 2000 K, cannot be associated with a change in the ion

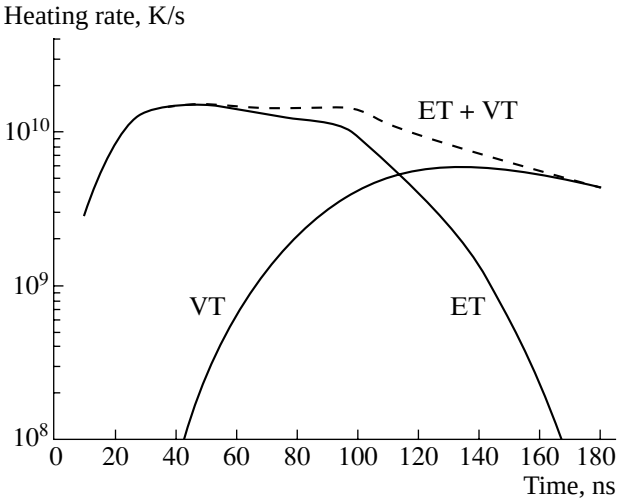

Fig. 9. Time evolution of the gas-heating rate at the discharge axis in the processes of rapid heating (curve ET) and in reactions of the vibrational relaxation of nitrogen molecules (curve VT) for P = 760 torr and R_0 = 0.45 mm.

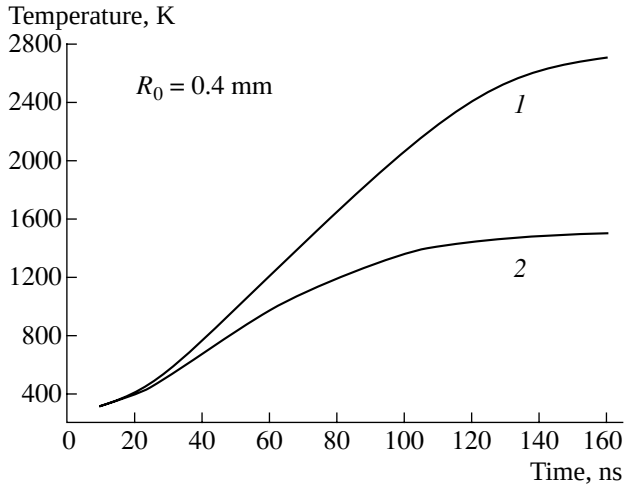

Fig. 10. Calculated dynamics of the gas temperature at the discharge axis for R_0 = 0.4 mm (*1*) with and (*2*) without allowance for associative ionization reactions (5).

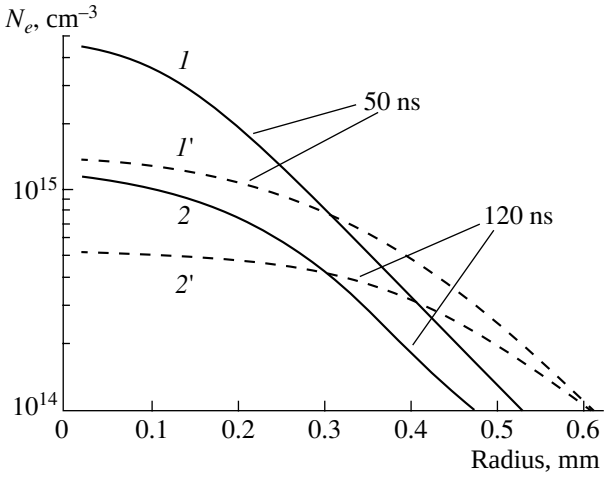

Fig. 11. Radial profiles of the electron density at two different times, calculated with (curves *1*, *2*) and without (curves *1*', *2*') allowance for associative ionization reactions.

composition or a decrease in the effective recombination coefficient.

Recall that, in order to achieve the streamer–leader transition, it is necessary to heat cold air in the streamer channels to 1500–2000 K. Then, in the processes of VT relaxation of the vibrationally excited nitrogen molecules, the gas temperature in the plasma channel increases to final values of 5000–6000 K, recorded in experiments in air at atmospheric pressure. Figure 9 displays the results of calculations of the gas heating rates in the processes of VT relaxation of nitrogen molecules by O(^3P) atoms and in the processes of rapid heating (ET processes). During the current pulse, the gas temperature increases almost exclusively in the rapid heating processes, whereas the effect of VT relaxation is relatively small. In this stage ($t \le 100$ ns), the gas is heated at a rate higher than 10^{10} K/s. Then, as the reduced field E/N decreases (Fig. 6), the rate of rapid heating becomes substantially lower, and the processes of VT relaxation become dominant. The gas heating rate in the VT relaxation reactions is about (4–5) $\times$ 10^9 K/s, which is associated with the high density of O(^3P) atoms (by which the vibrationally excited nitrogen molecules are relaxed) and the high rate constant of VT relaxation (for $T > 2000$ K, it is higher than 3×10^{-13} cm^3/s [32]).

In the model developed here, associative ionization reactions are an important part of the kinetic block. It is thus interesting to study how they affect the gas-heating rate and other parameters of the plasma channel. Figure 10 presents the results of calculations of the dynamics of the gas temperature at the discharge axis with and without allowance for reactions (5). The calculated results show a significant effect of the associative ionization reactions, which substantially increase the gas-heating rate in the axial region of the discharge. The reason for this is the following. Because of a nonuniform power deposition over the channel radius, chemically active particles (such as O(^3P), $N_2(A^3\Sigma_u^+)$, $N_2(a'^1\Sigma_u^-)$, etc.) are primarily accumulated near the channel axis, thereby substantially intensifying the ionization processes in the axial region, which leads in turn to an additional redistribution of the energy input and a further discharge contraction toward the axis. The latter phenomenon is clearly seen in Fig. 11, which depicts the radial electron density profiles calculated with (curves *1*, *2*) and without (curves *1*', *2*') allowance for associative ionization reactions.

Hence, the reactions responsible for rapid gas heating and associative ionization reactions are the most important part of the kinetic block of the model, because they largely govern the parameters of the forming leader channel.

As the discharge contracts toward its axis, the effective radius of the plasma channel decreases. According to calculations, the thermal radius R_h of the channel, defined as the radius of the surface at which the temperature is equal to $T_{max}/1.5$, approaches its steady-state value on time scales of $t \ge 90$–100 ns. This value is calculated to be $R_h \cong 0.1$ mm, which agrees with the measurement results [6, 9].

3.3. Evolution of the Parameters of the Leader Channel in the Developed Stage

Far from the electrodes, the next part of the leader channel originates from the streamer zone, which, in the case at hand, is an analogue of a pulsed corona. In this situation, the leader channel plays the role of the electrode. The leader current is determined by ionization processes in the streamer zone and is weakly sen-

sitive to the channel parameters [1–3, 6]. Under laboratory conditions, the typical magnitudes of the leader current are I_L = 0.5–4 A. Most of the calculations described in this paper were carried out for I_L = 1 A. The initial radial profile of the electron density was described by formula (2), and the initial radial profile of the gas temperature was also specified. The remaining parameters in the initial state were set equal to their unperturbed values.

Figure 12 illustrates the results of calculations of the dynamics of the electron density and gas temperature at the discharge axis for I_L = 1 A, P_0 = 760 torr, and T_0 = 400 K. We can see that, for a time shorter than 300 ns, the electron density increases to about $N_e^{\max} = (1–2) \times 10^{16}$ cm^{-3} and the gas temperature becomes as high as 5500–6000 K. This is a consequence of the development of thermal–ionizational instability, which leads to discharge contraction. In the hot region with a lower gas density, the reduced electric field E/N is stronger and the ionization rate is higher than those in the cold regions, and the effective electron loss rate is somewhat lower. As a result, the electric conductivity of the plasma in the heated region and the specific heat power released there both become higher, which leads to an increase in the temperature and the reduced field E/N, and so on. The results of the corresponding calculations of the evolution of the normalized gas density ρ/ρ_0 under such conditions are illustrated in Figs. 13 and 14a. From Fig. 13, we clearly see that a narrow hot low-density channel with a characteristic radius $R_h \cong 0.1$ mm has already formed at about 300 ns. From this time on, the values of the reduced electric field at the center of the discharge and at its periphery differ by a factor of more than 10.

The gas-dynamic processes in different stages of the evolution of a leader channel were investigated by Brago and Stekol'nikov [44] by means of schlieren photography. They observed that, in the stage of leader formation, an axisymmetric shock wave developed and rapidly evolved into an acoustic wave. An analogous phenomenon was captured in the calculations illustrated in Fig. 13. The onset of shock waves provides evidence of a rapid gas heating during the formation of a leader channel.

The effect of discharge contraction (over the time τ_c) is that, on the time scales $t \gg \tau_c$, the channel parameters are essentially independent of their initial values. As an example, Fig. 15 demonstrates the results of calculations of the electric field dynamics for the same initial profile $N_e(r)$ and for different profiles of the gas temperature and density: curve *1* was obtained for T_0 = 300 K and $\rho(r) = \rho_0$, and curve *2* was obtained for $T_0(r) = 300 + 100\exp(-r/R_0)^2$ and $\rho(r)/\rho_0 = 300/T_0(r)$. It can be seen that the initial conditions play a significant role on the time scales τ_c, on which the discharge contracts, and do not influence the channel parameters on longer time scales ($t \gg \tau_c$). Varying the initial radial profiles of the electron density and gas pressure, as well as the initial channel radius R_0, yielded a similar result. Hence, the calculated results are devoid of uncertainties associated with the initial conditions.

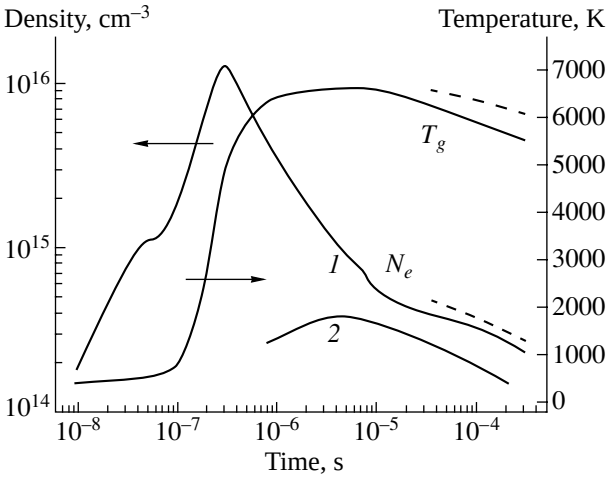

Fig. 12. Dynamics of the electron density (curves *1*, *2*) and gas temperature at the channel axis. The solid curves are calculated from the proposed model, and the dashed curves are calculated from the equilibrium model developed in [16]. Curve *2* shows the equilibrium electron density N_e at the gas temperature calculated here. The calculations were carried out for I_L = 1 A, P_0 = 760 torr, R_0 = 0.3 mm, and T_0 = 400 K.

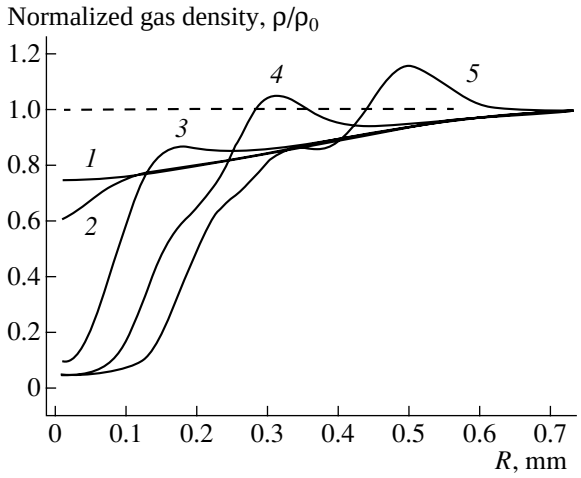

Fig. 13. Radial profiles of the gas density at different times: (*1*) 0, (*2*) 0.15, (*3*) 0.3, (*4*) 0.6, and (*5*) 1.0 μs. The calculations were carried out for the conditions of Fig. 12.

Among the main reasons why the electric field in a fixed cross section of the plasma channel decreases on time scales of 0.1–10 μs (Fig. 15) are an increase in the gas temperature and a decrease in the gas density in this cross section. The time τ_f during which the electric field

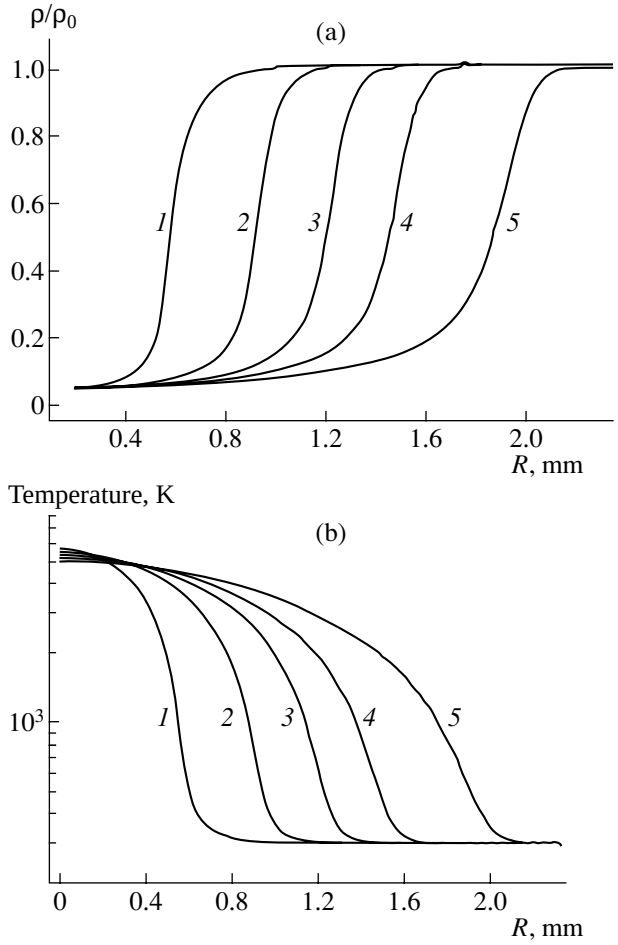

Fig. 14. Radial profiles of the (a) relative gas density and (b) gas temperature at different times: (*1*) 10, (*2*) 30, (*3*) 60, (*4*) 100, and (*5*) 200 μs. The calculations were carried out for the conditions of Fig. 12.

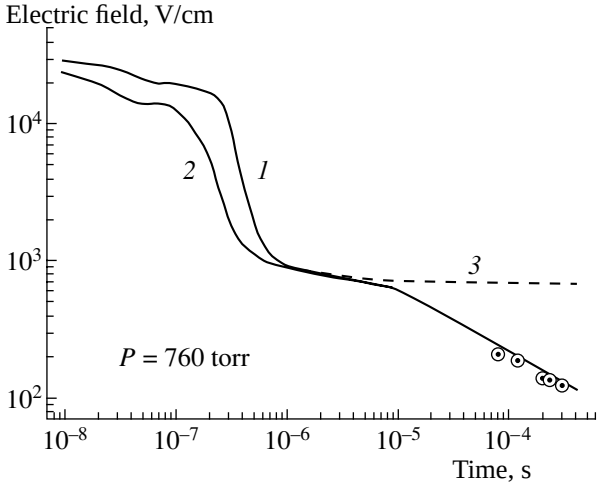

Fig. 15. Dynamics of the electric field in a plasma channel in air at P_0 = 760 torr. The symbols show the experimental data from [18]. The curves were calculated for R_0 = 0.3 mm and T_0 = 300 K (curve *1*) and for T_0 = 400 K with (curve *2*) and without (curve *3*) allowance for reactions (1).

rapidly decreases is very sensitive to the initial conditions (primarily, the initial gas temperature and the initial channel radius R_0). An analysis of the experimental data on the electric field dynamics at times $t \geq \tau_f$ makes it possible to draw conclusions about the heating rate of the leader channel and its gas-dynamic expansion. Recall that no direct measurements exist for the evolution of the electric field, and the available experimental data were obtained from indirect estimates. Bazelyan and Ponizovskiĭ [45] measured the parameters of the leader channel in a 1-m-long gap between a rod and a plane at a fixed current of $I_L \cong 1$ A. They estimated the mean electric field in the channel from the formula

$$E_L(t) = \frac{U(t) - E_s L_s(t)}{L(t)}, \qquad (9)$$

where $U(t)$ is the voltage across the gap, $L_s(t)$ is the length of the streamer zone, $E_s \cong 4.65$ kV/cm is the mean electric field in the streamer zone, and $L(t)$ is the length of the projection of the leader channel onto the discharge axis. The actual length of the channel is larger than $L(t)$ by approximately 30% because the channel is curved [1, 6]. For this reason, in [45], the values obtained for E_L were reduced by the same amount (30%). These new data are presented in Fig. 16, which also shows the results of calculations of $E_L(t)$ for R_0 = 0.4 mm and T_0 = 300 K. In calculations, as well as in experiments, the mean electric field in the leader channel was found to decrease to 1.2–1.3 kV/cm on time scales of $t > 20$ μs. These values are about a factor of 7 smaller than those obtained in [6] for the same time scales of the development of a leader. In [1], this difference was attributed to the large errors in calculating the channel head potential U_H, which was used in [6] to determine $E_L(t)$. The dashed curve in Fig. 16 shows the calculated time evolution of the mean (averaged over the channel length) gas density in the axial region. The mean electric field $E_L(t)$ and the gas density are seen to decrease almost synchronously; as a result, the corresponding average value $(E/N)_{av}$ changes insignificantly (by less than 25%).

The parameters of the leader channel are often described in the isobaric approximation [2, 3, 16]. Figure 17 illustrates how the normalized gas pressure P/P_0 evolves at different distances from the discharge axis. Despite intense heat release, the gas pressure in the channel cross section under consideration is equalized over a time of $t \geq 1$ μs. Thereafter, the normalized gas pressure can be assumed to be about unity, $P/P_0 \cong 1$.

On longer time scales, the plasma channel expands primarily due to heat conduction. As a result, the effective channel radius increases, the specific heat release power decreases, and the gas in the central region begins to slowly cool down (Figs. 12, 14b). Analogous results were obtained in [2, 16].

The radial profiles of the reduced electric field that are shown in Fig. 18 were calculated with (solid curves)

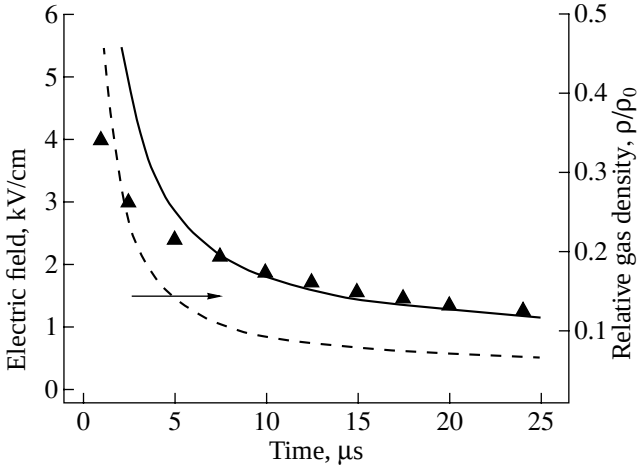

Fig. 16. Time evolution of the electric field averaged over the channel length. The symbols show the experimental data from [45] (see text for details); the solid curve is calculated for I_L = 1 A, R_0 = 0.4 mm, and T_0 = 300 K; and the dashed curve shows the on-axis gas density averaged over the channel length.

and without (dashed curves) allowance for ionization reactions (1). In the latter case, the reduced electric field E/N near the discharge axis is essentially constant in time, which agrees with the results of calculations carried out in [2]. The quasi-steady value of the reduced field calculated here, $(E/N)_{st} \cong$ 65–70 Td (Fig. 18), is somewhat lower than that obtained in [2], $(E/N)_{st} \cong$ 80 Td. This difference is attributed to the effect of associative ionization reactions (5).

When ionization reactions (1) are taken into account, the reduced field E/N near the channel axis decreases with time. As a result, the role of the electron impact ionization processes also decreases; i.e., the charged particles are mainly produced in reactions (1). Under the conditions in question, the dominant ionization mechanism changes on time scales of $t \geq 20$ μs. This can be seen, e.g., from Fig. 15, which illustrates the results on the electric field dynamics in a fixed cross section of the leader channel (see above). When reactions (1) are taken into account (Fig. 15, curve *2*), the electric field decreases with time and, at t = 100–300 μs, becomes as weak as 100–200 V/cm, which agrees with the measurement results of [18]. If reactions (1) are neglected (Fig. 15, curve *3*), then, under the conditions adopted here, the field E_L approaches a quasisteady value of about 670 V/cm. Figure 15 also shows that, for a leader velocity of 2×10^6 cm/s [1–3], the length of the channel region where the mean electric field is strong ($E_L \geq 1$ kV/cm) is smaller than 2 cm. In the remaining regions of the channel, the field E_L is substantially weaker; as a result, for leaders longer than 2 m, the mean electric field can be as low as 200–300 V/cm.

One of the main arguments in support of the hypothesis that thermal ionization has no influence on the processes in the leader channel is the fact established in [46]: the current in the leader and its brightness change nearly proportionally to time. Actually, if the main ionization mechanism is electron impact ionization, then the change in the current will primarily influence the electron density N_e, while the reduced field will remain nearly constant, $E/N \cong$ const [2, 3]. In this case, the brightness of the leader, $Q(t) \sim N_e(t)k_R(E/N)$ (where k_R is the rate constant of the excitation of radiating states) should change in almost direct proportion to $I_L(t)$. If more intense ionization mechanisms [e.g., reactions (1)]

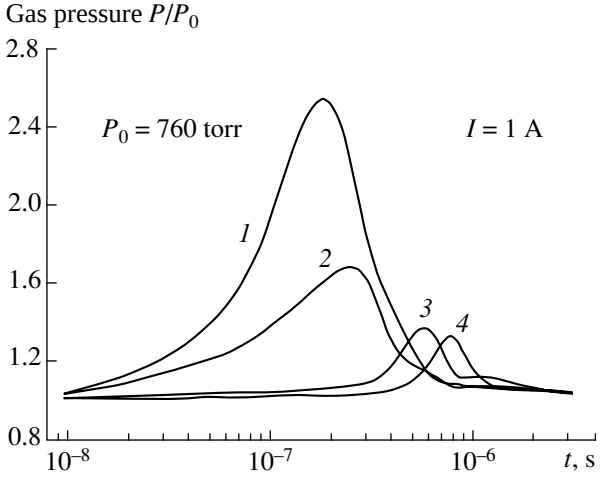

Fig. 17. Time evolution of the normalized gas pressure P/P_0 at different distances from the discharge axis: r = (*1*) 0, (*2*) 0.1, (*3*) 0.3, and (*4*) 0.4 mm.

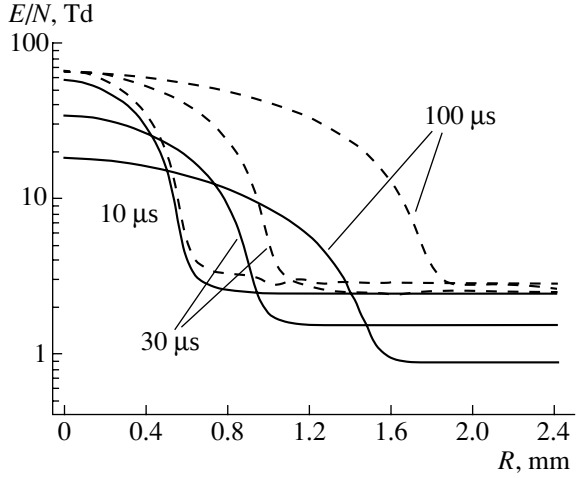

Fig. 18. Radial profiles of the reduced electric field E/N at three different times, calculated with (solid curves) and without (dashed curves) allowance for reactions (1).

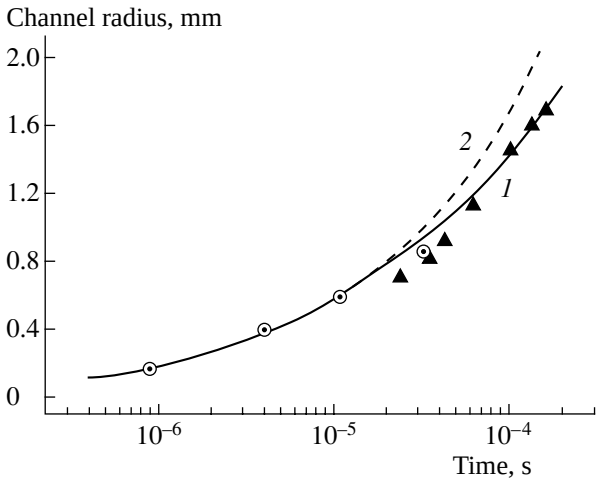

Fig. 19. Dynamics of the thermal radius of the plasma channel, determined by the surface at which the relative gas density is equal to $\rho/\rho_0 = 0.4$. The circles and triangles show the experimental data from [2] and [10], respectively, and the curves present the results of calculations with (curve *1*) and without (curve *2*) allowance for reactions (1).

operate, then the electron density will be nearly constant, $N_e \cong \text{const}$, and the change in the current will primarily influence the electric field strength $E(t)$. Since for $E/N \leq 200$ Td the rate constant of the excitation of radiating states depends rather strongly on the reduced field ($k_R(E/N) \sim (E/N)^\alpha$ with $\alpha \geq 5$ [23]), the dependence of the brightness on the current should also be strong, $Q(t) \sim I_L(t)^\alpha$.

All these considerations apply to the emission from a certain cross section of the leader channel. It should be noted that, in [46], the emission from the entire discharge gap was measured. However, this emission is dominated by the leader head [47], in which the main ionization mechanism is, of course, electron impact ionization. Consequently, the results obtained in [46] give no information about the dominant ionization mechanism in the cross sections of the discharge channel that are sufficiently remote from the leader head.

Due to a decrease in the electric field in the channel at a gas temperature of $T \geq 5500$–6000 K, the on-axis densities of the main neutral components (such as $O(^3P)$ and $N(^4S)$ atoms, NO and O_2 molecules, etc.) approach their thermodynamically equilibrium values. The densities of the charged particles of different species somewhat exceed their equilibrium densities (Fig. 12; curves *1*, *2*), because the electron temperature is nevertheless higher than the gas temperature and the electron–ion recombination reactions proceed at a slower rate than they do at $T_e = T$. At the channel periphery, where the gas temperature is lower than 3000–4000 K, the densities of nitrogen atoms and most species of charged particles can markedly exceed their equilibrium densities.

In Fig. 12, the dashed curves show the results obtained in [16] from numerical calculations of the dynamics of the gas temperature and electron density at the axis of the leader channel. The calculations were carried out for $I_L = 1$ A and $P_0 = 760$ torr on the basis of a thermodynamically equilibrium model. The values of T and N_e that were obtained in [16] are somewhat higher than those calculated from the model proposed here. However, for $t \geq 30$ μs, both models yield essentially the same evolution of the electric field in the channel.

Recall that the thermal radius of the leader channel, which characterizes the transverse dimension of the main energy deposition region, was measured in some experimental papers. The channel boundary was regarded as the surface at which the gas density gradient is maximum. According to Fig. 14a, the gradients are maximum at $\rho/\rho_0 = 0.4$–0.6. In the present calculations, the thermal radius R_h was determined from the relative density level $\rho/\rho_0 = 0.4$. Figure 19 shows the experimental data obtained in [2, 10] and the calculated time evolution of the channel radius R_h with (curve *1*) and without (curve *2*) allowance for reactions (1). In the second case, the channel expands at a higher rate because of the stronger electric field and higher power input into the discharge. Note that, for $t \geq 20$ μs, the cross-sectional area of the channel, $S_h = \pi R_h^2$, increases almost linearly, the expansion rate being $dS_h/dt \cong 0.05$ m^2/s.

4. CONCLUSIONS

In this paper, a self-consistent model has been constructed that makes it possible to investigate the formation of a leader channel in air and the evolution of the channel parameters in the developed stage, when the leader is as long as several meters or more. It is shown that, in the initial stage of the channel formation, an important role is played by both the reactions responsible for rapid gas heating and associative ionization reactions (5), which largely govern the parameters of this stage of the leader process.

A rapid increase in the electron density and gas pressure near the axis of the plasma channel initiates the gas-dynamic processes that lead to a decrease in the gas density and give rise to thermal–ionizational instability. As a result, the discharge contracts toward the channel axis and evolves into a highly conducting thin column. The radius of the column that has been formed at the current $I = 1$ A in air at atmospheric pressure is about $R_h \cong 10^{-2}$ cm, which agrees with the experimental data. Then, because of the gas-dynamic and thermal expansion, the radius R_h increases considerably; as a result, both the electric field and E/N decrease in the corresponding parts of the channel.

Another consequence of the discharge contraction is that, in the developed stage, the parameters of the

leader channel depend weakly on their initial values. Hence, the calculated results are free of uncertainties associated with the initial conditions. Recall that an analogous conclusion was reached by Aleksandrov *et al.* [16] based on the results of the numerical calculations.

When the gas temperature in the channel is higher than 5000–6000 K, a significant contribution to the production of charged particles, together with the electron impact ionization, comes from associative ionization reactions (1), involving the excited atoms $N(^4S)$ and $O(^3P)$. As a result, the electric field and the reduced field E/N further decrease. In the case under consideration, the electric field in the oldest parts of the leader channel drops to 200 V/cm or lower (which agrees with both the experimental data of [18] and the calculations of [16]) and the reduced field becomes as weak as $E/N \leq 10$ Td. The densities of the main species of neutral and charged particles in the axial region turn out to be close to their thermodynamically equilibrium values. At the channel periphery, the densities of nitrogen atoms and most species of charged particles can differ markedly from their equilibrium densities.

ACKNOWLEDGMENTS

I am grateful to N.L. Aleksandrov and É.M. Bazelyan for fruitful discussions of the results obtained. This study was supported by the Russian Foundation for Basic Research (project no. 02-02-17373) and the Council on the Grants of the President of the Russian Federation (grant no. NSh-1713.2003.2).

REFERENCES

1. E. M. Bazelyan and Yu. P. Raĭzer, *Spark Discharge* (Mosk. Fiz. Tekh. Inst., Moscow, 1997).
2. I. Gallimberti, J. Phys. Colloq. **40** (7), 193 (1979).
3. A. Bondiou and I. Gallimberti, J. Phys. D **27**, 1252 (1994).
4. N. L. Aleksandrov and E. M. Bazelyan, J. Phys. D **29**, 2873 (1996).
5. N. L. Aleksandrov and E. M. Bazelyan, Plasma Sources Sci. Technol. **8**, 285 (1999).
6. *Positive Discharges in Long Air Gaps at Les Renardieres Group*, Electra, No. 53, 31 (1977).
7. I. Gallimberti and M. Rea, Alta Friequenza **42** (6), 264 (1973).
8. V. S. Komel'kov, Izv. Akad. Nauk SSSR, Otd. Tekh. Nauk, No. 8, 955 (1947).
9. B. N. Gorin and A. Ya. Inkov, Zh. Tekh. Fiz. **32**, 329 (1962) [Sov. Phys. Tech. Phys. **7**, 235 (1962)].
10. P. Domens, J. Dupuy, A. Gibert, *et al.*, IEE Proc. A **133**, 457 (1986).
11. A. S. Gayvoronskii and A. G. Ovsjannikov, in *Proceedings of the 9th International Conference on Atmospheric Electricity, St. Petersburg, 1992*, p. 792.
12. G. N. Aleksandrov, Sov. Fiz. **10**, 949 (1966).
13. I. M. Razhanskiĭ, Izv. Sib. Otd. Akad. Nauk SSSR, Ser. Tekh. Nauk, No. 3, 41 (1976).
14. F. Bastien and E. Marode, J. Phys. D **18**, 377 (1985).
15. A. S. Predvoditelev, E. V. Stupochenko, A. S. Pleshanov, *et al.*, *The Tables of Thermodynamical Functions of Air* (Vychisl. Tsentr Akad. Nauk SSSR, Moscow, 1962).
16. N. L. Aleksandrov, E. M. Bazelyan, and A. M. Konchakov, Fiz. Plazmy **27**, 928 (2001) [Plasma Phys. Rep. **27**, 875 (2001)].
17. N. L. Aleksandrov and E. M. Bazelyan, J. Phys. D **30**, 1616 (1997).
18. E. M. Bazelyan and I. M. Razhanskiĭ, *Spark Discharge in Air* (Nauka, Moscow, 1988).
19. A. G. Temnikov, *Theory and Practice of Electrical Discharges in Power Engineering*, Ed. by A. F. D'yakov (Mosk. Énerg. Inst., Moscow, 1997), p. 147.
20. H. A. Vitello, B. M. Penetrante, and J. N. Bardsley, Phys. Rev. E **49**, 5574 (1994).
21. N. Yu. Babaeva and G. V. Naidis, J. Phys. D **29**, 2423 (1996).
22. F. Ruhling, IEE Proc. A **133**, 455 (1986).
23. N. L. Aleksandrov, F. I. Vysikailo, R. Sh. Islamov, *et al.*, Teplofiz. Vys. Temp. **19**, 22 (1981).
24. A. Kh. Mnatsakanyan and G. V. Naĭdis, *Plasma Chemistry* (Énergoatomizdat, Moscow, 1987), Vol. 14, p. 227.
25. I. A. Kossyi, A. Y. Kostinsky, A. A. Matveev, and V. P. Silakov, Plasma Sources Sci. Technol. **1**, 207 (1992).
26. H. Brunet and J. Rocca-Serra, J. Appl. Phys. **57**, 1574 (1985).
27. N. A. Popov, Fiz. Plazmy **20**, 335 (1994) [Plasma Phys. Rep. **20**, 303 (1994)].
28. N. A. Popov, Fiz. Plazmy **27**, 940 (2001) [Plasma Phys. Rep. **27**, 886 (2001)].
29. V. Yu. Baranov, F. I. Vysikaĭlo, A. P. Napartovich, *et al.*, Fiz. Plazmy **4**, 358 (1978) [Sov. J. Plasma Phys. **4**, 201 (1978)].
30. I. L. Kamardin, A. A. Kuchinskiĭ, V. A. Rodichkin, *et al.*, Teplofiz. Vys. Temp. **23**, 653 (1985).
31. F. S. Zarin, A. A. Kuzovnikov, and V. M. Shibkov, *Freely Localized Microwave Discharge in Air* (Neft' i Gaz, Moscow, 1996).
32. A. Kh. Mnatsakanyan and G. V. Naĭdis, Teplofiz. Vys. Temp. **23**, 640 (1985).
33. O. E. Krivonosova, S. A. Losev, V. P. Nalivaĭko, *et al.*, *Plasma Chemistry* (Énergoatomizdat, Moscow, 1987), Vol. 14, p. 3.
34. C. Park, AIAA Rep. No. 89-1740 (1989).
35. *Physics and Technology of Low-Temperature Plasma*, Ed. by S. V. Dresvin (Atomizdat, Moscow, 1972).
36. D. A. Anderson, J. C. Tannehill, and R. H. Pletcher, *Computational Fluid Mechanics and Heat Transfer* (Hemisphere, New York, 1984; Mir, Moscow, 1990).

37. S. K. Godunov, A. V. Zabrodin, M. Ya. Ivanov, A. N. Kraiko, and G. P. Prokopov, *Numerical Solution of Multidimensional Problems of Gas Dynamics* (Nauka, Moscow, 1976).
38. A. Larsson, J. Phys. D **31**, 1100 (1998).
39. G. V. Naidis, J. Phys. D **32**, 2649 (1999).
40. J. P. Boris and D. L. Book, J. Comput. Phys. **11**, 38 (1973).
41. L. Ullrich and I. Gallimberti, in *Proceedings of IX International Conference on Gas Discharges and Their Applications, Venice, 1989*, p. 419.
42. N. L. Aleksandrov and E. M. Bazelyan, Fiz. Plazmy **22**, 458 (1996) [Plasma Phys. Rep. **22**, 417 (1996)].
43. E. N. Brago and I. S. Stekol'nikov, Izv. Akad. Nauk SSSR, Otd. Tekh. Nauk, No. 11, 50 (1958).
44. P. Domens, J. Dupuy, A. Gibert, *et al.*, J. Phys. D **21**, 1613 (1988).
45. E. M. Bazelyan and A. Z. Ponizovskiĭ, Izv. Akad. Nauk SSSR, Énerg. Transp., No. 6, 329 (1980).
46. *Research on Long Air Gap Discharges at Les Renardieres*, Electra, No. 23, 53 (1972).
47. A. P. Baĭkov, O. V. Bogdanov, A. S. Gaĭvoronskiĭ, *et al.*, Élektrichestvo, No. 9, 60 (1988).

Translated by O.E. Khadin

Plasma Physics Reports, Vol. 29, No. 8, 2003, pp. 709–716. Translated from Fizika Plazmy, Vol. 29, No. 8, 2003, pp. 768–774.

LOW-TEMPERATURE PLASMA

New Mechanism for the Influence of Xe on the Concentration of CO_2 Molecules in Self-Sustained CO-Laser Discharges

G. M. Grigorian*, N. A. Dyatko, and I. V. Kochetov****

**Fok Research Institute of Physics, St. Petersburg State University, Ul'yanovskaya ul. 1, Petrodvorets, St. Petersburg, 198504 Russia*

***Troitsk Institute for Innovation and Fusion Research, Troitsk, Moscow oblast, 142190 Russia*

Received December 20, 2002

Abstract—The dependence of the CO_2 concentration on the discharge conditions and the mixture composition in a CO laser is studied experimentally. The experimental data are compared with the calculated results. A scheme of the reactions that govern the concentration of CO_2 molecules under the experimental conditions in question is constructed. It is shown that, in a gas-discharge plasma, an admixture of Xe in a mixture containing CO molecules gives rise to a new mechanism for the dissociation of CO_2 molecules by metastable xenon atoms. Under conditions close to the operating conditions of sealed-off CO lasers, the dissociation of CO_2 molecules in collisions with metastable $Xe(^3P_2)$ atoms becomes the dominant dissociation mechanism in a He : CO mixture because it proceeds at a fast rate. This explains the observed decrease in the CO_2 concentration in a xenon-containing He : CO mixture. © *2003 MAIK "Nauka/Interperiodica".*

1. INTRODUCTION

Since mixtures containing carbon oxide molecules are used as active working media in electric-discharge CO lasers, interest in the processes occurring in the low-temperature plasmas in discharges in such mixtures has persisted for many years. It is well known that, under the action of electric discharges, the composition of working gas mixtures can change substantially, thereby worsening the parameters of the active medium, primarily due to the quenching of vibrationally excited CO molecules by the products of plasmochemical reactions. Such degradation of the original mixture has an especially strong effect on the operation of sealed-off devices, which work without pumping a gas mixture through the discharge region. A distinctive feature of sealed-off CO lasers is that their high energy efficiency can be achieved only with xenon-containing working mixtures [1, 2]. Although opinion in the literature is divided on this issue, the prevailing view is that, in this case, a key role is played by the decrease in both the mean electron energy and the reduced electric field E/N in the discharge, which provides more efficient excitation of the vibrational levels of CO molecules [3, 4]. In a number of papers [5–8], it was revealed that adding xenon to such mixtures as He : CO and He : CO : N_2 leads to a substantial decrease in the concentration of CO_2 molecules produced in plasmochemical reactions during the discharge. Although this effect has long been known, its causes have not yet been investigated systematically. The observed decrease in the CO_2 concentration is usually assumed to result from a decrease in the quantity E/N in the discharge in a xenon-containing working mixture (see, e.g., [8]). Moreover, in [8], a decrease in the concentration of CO_2 molecules followed by the slowing of the rate at which the vibrationally excited CO molecules are quenched by them is asserted to be the main cause of the improvement of the energy characteristics of a sealed-off laser operating with a xenon-containing gas mixture. In this connection, it is relevant to investigate the processes that affect the CO_2 concentration in a gas-discharge plasma and to construct a scheme of reactions that would make it possible to model the dependence of the CO_2 concentration on the experimental conditions.

This paper is devoted to the experimental and theoretical investigation of the effect of adding Xe to a He : CO mixture on the concentration of CO_2 molecules produced in a gas-discharge plasma. A brief description of the results obtained has been given in our earlier paper [9].

2. DESCRIPTION OF THE EXPERIMENT

The experiments were carried out with discharge tubes 15–20 mm in diameter made of molybdenum glass and cooled with running water. The length of the discharge region was varied from 20 to 50 cm. Hollow cylindrical tantalum electrodes were arranged within the vertical taps of the discharge tube. The discharges were initiated by a direct current. The experimental device operated either with sealed-off discharge tubes or with tubes through which gas mixtures were pumped at a slow rate (about 1 m/s). Before the working mixture was pumped into the tube, it was passed through a system of silica gel and zeolite traps. The mixture composition in the discharge tube was analyzed by an MSC-6 time-of-flight mass spectrometer. The gas samples were

1063-780X/03/2908-0709$24.00 © 2003 MAIK "Nauka/Interperiodica"

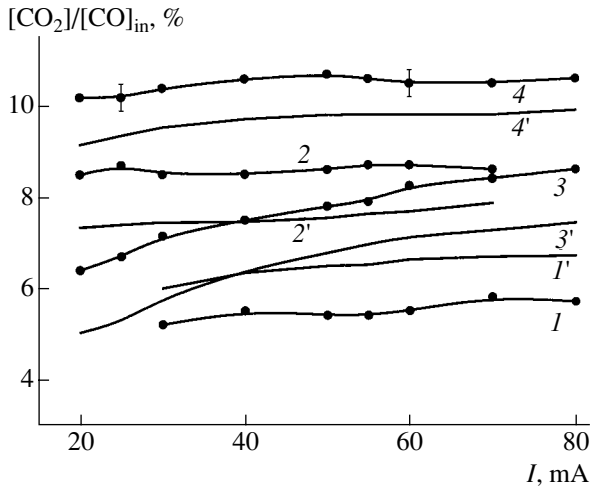

Fig. 1. Concentration of CO_2 molecules in the discharge vs. discharge current in experiments with the (*1*) He + 6% CO mixture at p = 10 torr and d = 20 mm, (*2*) He + 3% CO mixture at p = 10 torr and d = 15 mm, (*3*) He + 9% CO mixture at p = 12 torr and d = 20 mm (the gas pumping rate is $v \sim$ 1 m/s), and (*4*) He + 3% CO mixture at p = 16 torr and d = 15 mm. Curves *1*', *2*', *3*', and *4*' show the results of numerical calculations.

examined in two ways. First, the samples were analyzed in the course of the experiment, just after they were taken from the discharge tube. Second, the gas was drawn into a special balloon, and then the gas composition was examined by mass spectrometry and chromatography. The results of mass-spectrometric and chromatographic analyses differed by no more than ~10% (the level of the reproducibility of experiments). The mass spectrometer was calibrated with specially prepared standard gas mixtures. The gas temperature at the axis of the discharge tube and the radial temperature profile were determined spectroscopically by analyzing the rotational structure of the bands of CO molecules in the discharge emission spectrum. The electric field in the discharge region was found from measurements of the voltage drops across the discharge gap and the electrode sheaths. The voltage drops at the electrodes were determined from measurements of the voltage in experiments with discharges initiated in regions of different lengths. Typical voltage drops at the electrodes were found to be 350–400 V. Depending on the experimental conditions, the reduced electric field E/N varied in the range $(1.8–2.7) \times 10^{-16}$ V cm^2 in discharges in He : CO mixtures and in the range $(1–1.5) \times 10^{-16}$ V cm^2 in discharges in He : CO : Xe mixtures.

The distribution function of CO molecules over vibrational levels (up to the $v = 29$ level) was determined by detecting infrared radiation from transitions within the first and second vibrational overtones of CO molecules (the transitions $v \longrightarrow v-2$ and $v \longrightarrow v-3$, respectively). The distribution function of CO molecules over vibrational levels was determined by a method similar to that described in [10].

3. THEORETICAL MODEL

The rate constants of the processes involving electrons were found by numerically solving the Boltzmann kinetic equation for the electron energy distribution function (EEDF) in terms of the reduced electric field E/N (where E is the electric field strength and N is the concentration of neutral particles) and the vibrational temperature. The radial profile of the electron density in the discharge tube was described by a Bessel function. The vibrational temperature was determined from experimental data.

The cross sections for electron scattering by He atoms were taken from [11], the transport cross section for electron scattering by Xe atoms was taken from [12], the cross section for the excitation of the lowest electronic level was taken from [13], and the cross sections for the excitation of other electronic levels and the ionization of Xe atoms were taken from [14]. The set of cross sections for CO_2 molecules was taken from [15]. The cross sections for electron scattering by CO molecules in the ground state generally corresponded to those presented in [16, 17]. In accordance with the recommendations of [18, 19], the resonant component of the cross sections for vibrational excitation from the ground state was increased by a factor of 1.3 in comparison with that in [17]. The cross sections for electron impact–induced transitions between the vibrational levels were calculated in a way analogous to that in [20].

The method used to solve the Boltzmann equation numerically was described in detail in [21].

The concentration of CO_2 molecules produced in a gas-discharge plasma was calculated by solving a set of balance equations for the concentrations of $CO(a^3\Pi)$ and CO_2 molecules and $Xe(^3P_2)$ atoms. Since mass-spectrometry measurements provided data on the averaged (over the cross section of the discharge tube) concentrations of these molecules, the CO_2 concentration was calculated from the radius-averaged value of the reduced electric field, $(E/N)_{av} = EkT_{av}/p$, where T_{av} is the radius-averaged temperature obtained from the experimentally measured profile of the gas temperature and p is the gas pressure in the discharge tube.

4. RESULTS AND DISCUSSION

The experimental dependence of the relative concentration of CO_2 molecules on the discharge current in discharges in He : CO mixtures is illustrated by the closed circles in Fig. 1 (in which the vertical bars show the experimental errors). The points on curves *1*, *2*, and *4* were obtained from experiments without pumping a gas mixture through the discharge tube, and the points on curve *3* were obtained from experiments with tubes through which the working gas mixtures were pumped at a slow rate (in this case, the gas to be analyzed was sampled at the exit from the discharge tube). In experiments without gas pumping, the concentration of CO_2

molecules was measured ten minutes after the discharge was switched on. The measured concentrations are close to those obtained in other experiments under similar conditions [6–8].

The processes of the production of CO_2 molecules in gas discharges in He : CO mixtures have been studied fairly well [22–24]. An analysis of the possible mechanisms for producing CO_2 molecules in a discharge plasma under the conditions of our experiments shows that the main process is a reaction in which a metastable molecule $CO(a^3\Pi)$ collides with a CO molecule in the ground state:

$$CO(a^3\Pi) + CO \longrightarrow CO_2 + C. \quad (1)$$

The excitation energy of this metastable state is 6 eV; the excitation rate constant was measured to be $K_1 = 1.4 \times 10^{-12}$ cm^3/s [23] and 1.2×10^{-12} cm^3/s [25].

The production of CO_2 molecules in volume and heterogeneous recombination reactions can be neglected because, in our experiments, the concentration of oxygen atoms was low [26] and the corresponding rate constants are small [22, 27, 28].

In some papers (see, e.g., [29–31]), it was proposed that CO_2 molecules can be efficiently produced in collisions between two vibrationally excited CO molecules. The rate constant of this collision process is unknown. In total, there should be more than 20 excited levels of the two CO molecules involved. Measurements of the populations of the vibrational levels of CO molecules in our experiments showed that, in order for this reaction to play an appreciable role in the production of CO_2 molecules, its rate should be faster than the gas-kinetic rate, which, however, seems very unlikely. Note also that, over the entire range of conditions investigated in our experiments, we failed to observe a correlation between the concentration of CO_2 molecules in the discharge and the populations of the vibrational levels of CO molecules that can take part in this reaction. In particular, the CO_2 concentration was found to be independent of whether or not the generation occurs, which changes the populations of the upper vibrational levels $CO(v)$ by more than one order of magnitude. We can thus conclude that, under the conditions of our experiments, this reaction does not have any significant influence on the concentration of CO_2 molecules. An analogous conclusion about the role of this reaction in the production of CO_2 molecules in a gas-discharge plasma was made earlier in [22–24].

Estimates of the rates of the energetically possible processes in which the CO_2 molecules are lost show that the main loss mechanism is electron-impact dissociation. All the remaining reactions that lead to the loss of CO_2 molecules in our experiments can be ignored.

The dissociation of a CO_2 molecule in collisions with electrons proceeds through the production of its electronically excited states:

$$CO_2 + e \longrightarrow CO_2^* (E \geq 7 \text{ eV}) + e \longrightarrow CO + O + e. \quad (2)$$

The cross sections for the excitation of these states are presented in [15]. The rate constants calculated for the electron-impact dissociation of CO_2 molecules with the help of these cross sections [15] agree well with those obtained experimentally in [32].

Recall that reaction (2) is the main loss mechanism for CO_2 molecules in a discharge plasma in our experiments. Estimates show that, under our experimental conditions, the vibrational excitation of CO_2 molecules does not significantly influence the rate of their dissociation by electron impact.

An important question is how much the processes of the production and loss of CO_2 molecules at the electrodes and in the regions adjacent to them affect the total CO_2 concentration in discharge tubes, especially in sealed-off ones. For a flow-type discharge in a He : CO mixture, the effect of the electrodes was investigated by Ivanov *et al.* [33]. They compared the CO_2 concentrations measured under similar plasma conditions in an electrodeless rf discharge and in a conventional dc discharge with internal tantalum electrodes and showed that the electrodes have essentially no effect on the concentration of CO_2 molecules in a discharge plasma. In our experiments with sealed-off discharge tubes, the electrodes should play a more important role in plasmochemical processes, especially in long-lived discharges. That is why we carried out a special series of experiments aimed at estimating the effect of the electrodes on the CO_2 concentration by the same method as in [33]. We initiated electrodeless rf discharges in a discharge tube and adjusted the discharge parameters so that the position of the positive column of the discharge and its brightness in a He : CO mixture coincided with those of dc discharges with internal electrodes in our experiments. Measurements did not reveal any significant difference between the CO_2 concentrations in these two types of discharge, thereby indicating that the electrodes (and the regions near the electrodes) have little influence on the processes of production and loss of CO_2 molecules.

An analysis of the processes involving CO_2 molecules shows that their concentration in the plasma of gas discharges in He : CO mixtures in our experiments is governed by reactions (1) and (2). This agrees with the results obtained in [22, 24]. In particular, in [24], a good agreement was achieved between the CO_2 concentrations calculated numerically from the model used here and those measured experimentally in flow-type discharges in He : CO mixtures in a tube cooled with liquid nitrogen. The CO_2 concentrations calculated numerically as functions of the discharge current with allowance for these two reactions under different con-

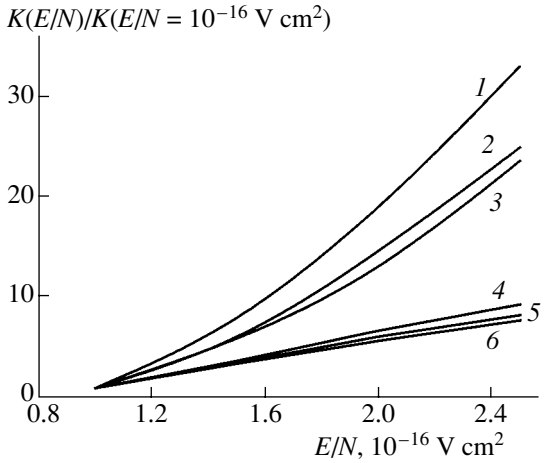

Fig. 2. Relative values of the rate constants of the electron-impact dissociation of CO_2 molecules (curves *1*, *2*, and *3*) and the electron-impact excitation of the state $CO(a^3\Pi)$ (curves *4*, *5*, and *6*) in experiments with the (*1*, *4*) He : CO : Xe = 96 : 3 : 1 mixture, (*2*, *5*) He : CO : Xe = 90 : 3 : 7 mixture, and (*3*, *6*) He : CO : Xe = 85 : 3 : 12 mixture.

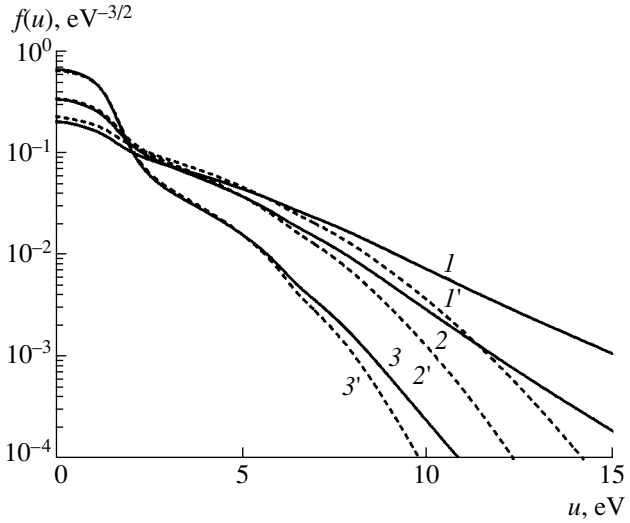

Fig. 3. EEDF calculated for different values of E/N: (*1*) 2×10^{-16}, (*2*) 1.7×10^{-16}, and (*3*) 10^{-16} V cm^2. Curves *1*, *2*, and *3* refer to experiments with a He : CO = 97 : 3 mixture, and curves *1*', *2*', and *3*' refer to experiments with a He : CO : Xe = 85 : 3 : 12 mixture.

ditions are illustrated by the solid curves in Fig. 1. A comparison of the numerical results with the experimental data shows that the model provides a good description of the concentrations measured in discharges in a sealed-off tube (see the pairs of curves *1* and *1*', *2* and *2*', and *4* and *4*') or with a tube through which a gas mixture was pumped at a slow rate (curves *3* and *3*'). The weak dependence of the concentration of CO_2 molecules on the discharge current is explained the fact that the rates of their production and loss in the discharge plasma depend on the electron density in the same manner.

Analyzing the processes that govern the concentration of CO_2 molecules in our experiments, we can conclude that the CO_2 concentration in the discharge plasma cannot be lowered by decreasing the quantity E/N, in particular, by adding Xe to a He : CO mixture. In contrast, as the reduced electric field E/N in the discharge decreases, the CO_2 concentration should increase, because, on the one hand, the dissociation energy of CO_2 molecules is markedly higher than the excitation energy of the metastable state $CO(a^3\Pi)$ and, on the other, as E/N increases, the excitation rate constants for the state $CO(a^3\Pi)$ increase more gradually than the dissociation rate constants for CO_2 molecules (Fig. 2), especially in xenon-containing gas mixtures, in which the high-energy tail of the EEDF decreases more abruptly (see the dashed curves in Fig. 3).

As an example, Fig. 4 illustrates the calculated dependence of the CO_2 concentration on E/N. We can see that the concentration of CO_2 molecules cannot be lowered by decreasing the quantity E/N. Moreover, the behavior of curve *1* in Fig. 4 implies that, in xenon-containing mixtures, a decrease in E/N should result in an even greater increase in the CO_2 concentration in comparison with that in He : CO mixtures, because, as was explained above, in discharges in a xenon-containing gas mixture, the density of high-energy electrons decreases more rapidly. Nevertheless, our experiments revealed that adding Xe to a He : CO mixture leads to a sharp decrease in the concentration of CO_2 molecules (by a factor of 3 to 30, depending on the Xe concentration in the mixture).

The closed circles in Fig. 5 show the results of measurements of the dependence of the CO_2 concentration

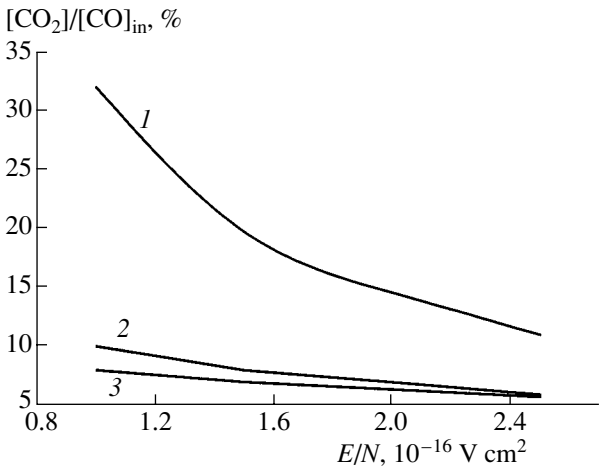

Fig. 4. Concentration of CO_2 molecules vs. E/N in experiments with the (*1*) He : CO : Xe = 85 : 3 : 12 mixture, (*2*) He : CO = 94 : 6 mixture, and (*3*) He : CO = 97 : 3 mixture.

on the discharge current in different gas mixtures (the vertical bars reflect the experimental errors). This figure also displays the CO_2 concentrations (solid curves) calculated using the previous model, based on reactions (1) and (2), in which carbon dioxide is produced and lost, respectively. We can see that CO_2 concentrations calculated for gas mixtures with a large amount of Xe are one order of magnitude higher than those measured experimentally (curves *1*, *2*). In mixtures in which the Xe concentration is low, the concentration of carbon dioxide differs by only several times (curves *3*, *4*). An analysis of the possible reactions in which CO_2 molecules are lost in discharges in He : CO : Xe mixtures shows that the main loss mechanism may be the dissociation of CO_2 molecules in collisions with the electronically excited xenon atoms:

$$CO_2 + Xe(^3P_2) \longrightarrow CO + O + Xe. \quad (3)$$

The excitation energy of this state of xenon atoms is 8.31 eV. The excitation rate constant is known to be close to the gas-kinetic rate constant, $K_3 = 4 \times 10^{-10}$ cm^3/s [34, 35]. This is about 90% of the rate constant for the reaction of quenching of the electronically excited state $Xe(^3P_2)$ by CO_2 molecules:

$$CO_2 + Xe(^3P_2) \longrightarrow Xe + \text{products}, \quad (4)$$

the corresponding rate constant being $K_4 = 4.5 \times 10^{-10}$ cm^3/s [35].

Figure 6 demonstrates the calculated dependence of the ratio of the rate of dissociation of CO_2 molecules in reaction (3) to the rate of electron-impact dissociation in reaction (2) on the reduced electric field E/N ($\nu_{Xe*}/\nu_e = [Xe(^3P_2)]K_3/n_eK_{dis}$), in gas mixtures with different amounts of Xe. As the Xe concentration in the mixture increases (curves *3*, *2*, and *1*, respectively), the relative role of the dissociation of CO_2 molecules in collisions with excited Xe atoms increases in comparison with the electron-impact dissociation.

The dashed curves in Fig. 5 illustrate the concentration of CO_2 molecules calculated with allowance for their dissociation in collisions with excited Xe atoms. The calculated results are seen to agree well with the experimental data.

In the discharge plasma under investigation, the concentration of metastable $Xe(^3P_2)$ atoms is governed by the electron excitation processes and the quenching processes in collisions with CO and CO_2 molecules, the corresponding rate constants being equal to 3.6×10^{-11} and 4.5×10^{-10} cm^3/s, respectively [35]. Consequently, even when the CO_2 concentration is about 10% [CO], the these processes can appreciably affect the population of the metastable state of xenon atoms. Figure 7 illustrates the effect of an admixture of CO_2 molecules on the relative rate of their dissociation in collisions with the excited $Xe(^3P_2)$ atoms. In a gas mixture in which the amount of CO_2 molecules relative to CO

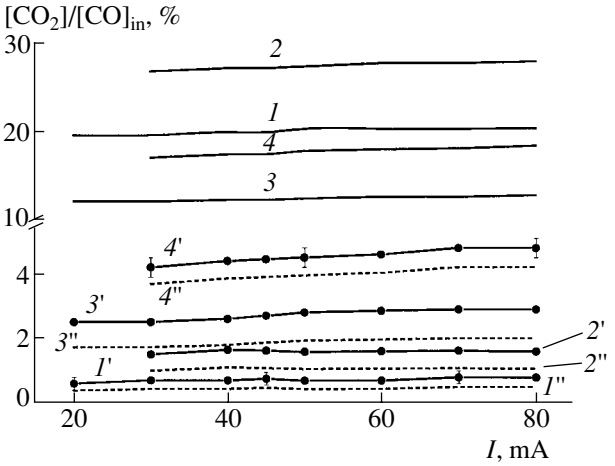

Fig. 5. Concentration of CO_2 molecules vs. discharge current in experiments with the (*1*) He : CO : Xe = 85 : 3 : 12 mixture at p = 10 torr, (*2*) He : CO : Xe = 85 : 3 : 12 at p = 16 torr, (*3*) He : CO : Xe = 96 : 3 : 1 mixture at p = 12 torr, and (*4*) He : CO : Xe = 96 : 3 : 1 mixture at p = 18 torr. Curves *1*, *2*, *3*, and *4* refer to the results of numerical calculations in which the dissociation of the CO_2 molecules in collisions with the excited $Xe(^3P_2)$ atoms was neglected. Curves *1*', *2*', *3*', and *4*' show the experimental results. Curves *1*", *2*", *3*", and *4*" were calculated with allowance for the dissociation of the excited CO_2 molecules in the reactions of quenching of the excited $Xe(^3P_2)$ atoms.

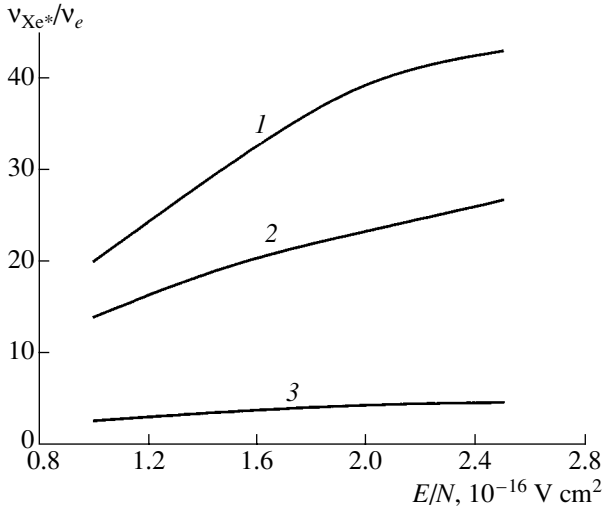

Fig. 6. Calculated dependence of the ratio of the dissociation rate ν_{Xe*} of the excited CO_2 molecules in collisions with the excited $Xe(^3P_2)$ atoms to the rate ν_e of electron-impact dissociation on the parameter E/N for experiments with the (*1*) He : CO : Xe = 85 : 3 : 12 mixture, (*2*) He : CO : Xe = 90 : 3 : 7 mixture, and (*3*) He : CO : Xe = 96 : 3 : 1 mixture.

molecules is 30%, the ratio of the rate of dissociation of CO_2 molecules in collisions with the excited $Xe(^3P_2)$ atoms to the rate of their dissociation by electron

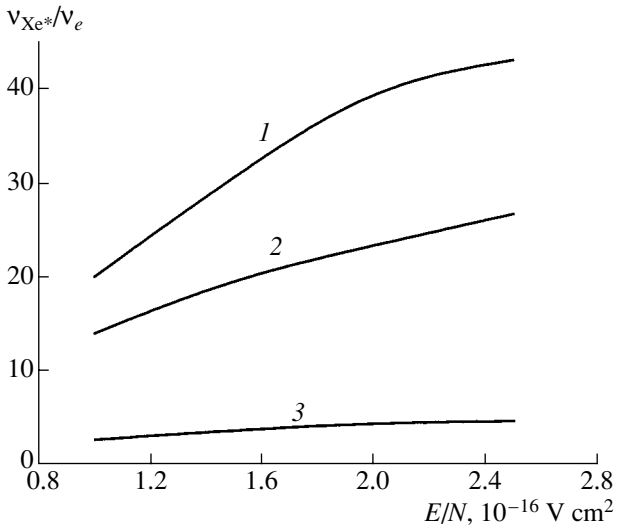

Fig. 7. Ratio of the dissociation rates vs. *E*/*N* at the discharge current *I* = 40 mA for mixtures with different contents of CO_2: (*1*) He : CO : Xe : CO_2 = 90 : 3 : 7 : 0.03, (*2*) He : CO : Xe : CO_2 = 90 : 3 : 7 : 0.3, and (*3*) He : CO : Xe : CO_2 = 90 : 3 : 7 : 0.9.

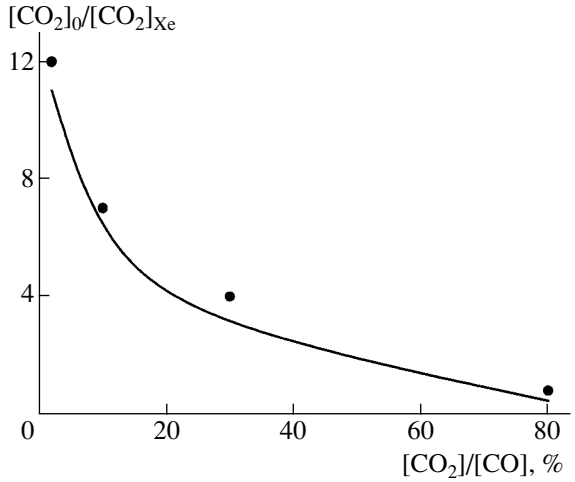

Fig. 8. Concentration of CO_2 molecules vs. CO_2 content in the original mixture at the current *I* = 40 mA in a He : CO : CO_2 = 97 : 3 : *X* mixture with an addition of xenon (in the amount [Xe] = 2.33[CO]). The closed circles show the experimental data, and the curve is the result of numerical calculations.

impact is five times lower than that in a mixture in which the relative amount of CO_2 is 1%.

Since CO_2 molecules and metastable xenon atoms are both lost in collisions with each other, their relative roles are governed by their initial concentrations. It is well known that Xe atoms are added to the working media of CO_2 lasers in order for the dissociation of CO_2 molecules (due to a decrease in *E*/*N*) to be less intense (see, e.g., [36, 37]). Since, in this case, the initial CO_2 concentration is high, the $Xe(^3P_2)$ states are poorly populated. Under such conditions, reaction (3) plays an insignificant role and the main dissociation mechanism is electron-impact dissociation. The situation with CO lasers is opposite: the initial working medium is free of carbon dioxide. The CO_2 molecules are produced in the plasma at a fairly slow rate (in our experiments, on characteristic time scales of about 0.1 s), while the rate at which the metastable state of Xe atoms is populated is faster by several orders of magnitude; as a result, the excited state $Xe(^3P_2)$ affects the CO_2 concentration through reaction (3).

In order to investigate the effect of a Xe admixture, we carried out experiments with gas mixtures that originally contained CO_2. The dependence of the concentration of CO_2 molecules in a Xe-containing He : CO : CO_2 mixture on the content of CO_2 in the original mixture is demonstrated in Fig. 8, in which the closed circles show the experimental data and the solid curves are the results of numerical calculations. We can see that the lower the concentration of CO_2 molecules, the larger the extent to which this concentration decreases in Xe-containing mixtures. When the concentration of CO_2 molecules is high, an addition of Xe leads to an increase (rather than a decrease) in the CO_2 concentration in the plasma. In this case, the $Xe(^3P_2)$ concentration is not high enough to affect the CO_2 concentration through reaction (3); as a result, the CO_2 concentration increases solely due to a decrease in *E*/*N* in the plasma and a reduction in the electron-impact dissociation rate. As can be seen, the results of modeling agree well with experiment.

Recall that, under the conditions of our experiments, the CO_2 molecules are produced primarily from the metastable $CO(a^3\Pi)$ molecules. In the plasma of a discharge in a He : CO mixture, these metastable molecules are generated in the reaction of the electron-impact excitation of CO molecules:

$$CO(X^1\Sigma) + e \longrightarrow CO(a^3\Pi) + e. \quad (5)$$

In Xe-containing mixtures, metastable $CO(a^3\Pi)$ molecules can be produced not only by direct electron impact but also by excitation transfer from the metastable state of xenon atoms [38, 39]:

$$CO(X^1\Sigma) + Xe(^3P_2) \longrightarrow CO^* + Xe, \quad (6)$$

$$CO^* \longrightarrow CO(a^3\Pi) + h\nu. \quad (7)$$

In this situation, the production of the excited $Xe(^3P_2)$ atoms can eventually increase the production rate of CO_2 molecules. The rate constant of reactions (6) is unknown. Even assuming an extreme situation, specifically, each of the excited $Xe(^3P_2)$ atoms produces an excited $CO(a^3\Pi)$ molecule in quenching reaction (6), we would see that, under the condition of our experiments, this quenching processes is incapable of

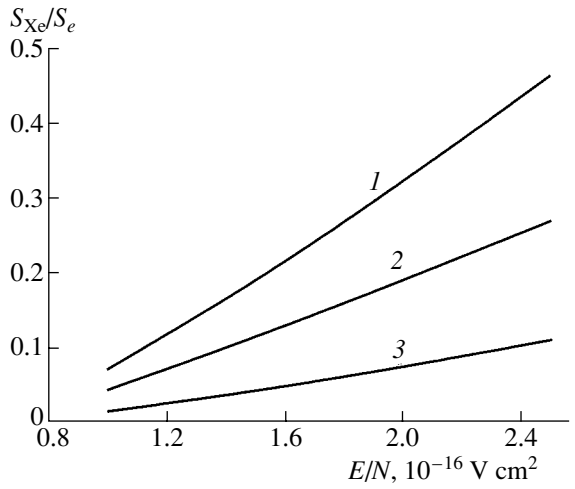

Fig. 9. Ratio of the excitation rates of the CO($a^3\Pi$) S_{Xe} states vs. E/N in experiments with the (*1*) He : CO : Xe = 85 : 3 : 12 mixture, (*2*) He : CO : Xe = 90 : 3 : 7 mixture, and (*3*) He : CO : Xe = 96 : 3 : 1 mixture. S_{Xe} is the rate of excitation transfer from the excited Xe($^3P_2$) atoms and S_e is the excitation rate of the state $a^3\Pi$ by direct electron impact.

competing with the process of the excitation to the state CO($a^3\Pi$) by direct electron impact. Figure 9 shows how the ratio of the rates of population of the CO($a^3\Pi$) states in reactions (5) and (6) depends on E/N for different gas mixtures. We can see that the excitation of the states CO($a^3\Pi$) in the reactions of quenching of the excited Xe($^3P_2$) atoms can be neglected.

5. CONCLUSIONS

We have discussed the main processes that govern the concentration of CO_2 molecules in discharges in a He : CO mixture, which is used in sealed-off CO lasers. We have shown that adding xenon to a mixture containing CO molecules gives rise to a new mechanism for the dissociation of CO_2 molecules in reactions involving metastable Xe atoms. Under the conditions of our experiments, the dissociation of CO_2 molecules in collisions with metastable Xe($^3P_2$) atoms becomes the dominant dissociation mechanism in a He : CO mixture because it proceeds at a fast rate. This explains the observed decrease in the CO_2 concentration in a He : CO mixture with an addition of xenon.

ACKNOWLEDGMENTS

We are grateful to A.P. Napartovich for supporting this work and fruitful discussions of the results obtained.

REFERENCES

1. P. G. Brawn and A. L. S. Smith, J. Phys. E **8**, 870 (1975).
2. I. L. Dubrovina, V. N. Ochkin, and N. N. Sobolev, Kvantovaya Élektron. (Moscow) **4**, 1038 (1975).
3. E. N. Lotkova, S. G. Goncharova, and V. V. Pisarenko, Kvantovaya Élektron. (Moscow) **1**, 542 (1974).
4. M. L. Bhaumik, *High Power Lasers* (New York, 1975).
5. G. B. Hocker, IEEE J. Quantum Electron. **7**, 573 (1974).
6. E. A. Trubacheev, Tr. Fiz. Inst. im. P. N. Lebedeva, Akad. Nauk. SSSR **102**, 1 (1977).
7. D. S. Murray and A. L. S. Smith, J. Phys. D **1**, 2478 (1978).
8. V. S. Aleinikov and V. I. Masychev, *Carbon-Oxide Lasers* (Radio i Svyaz', Moscow, 1980).
9. G. M. Grigorian, I. V. Kochetov, and N. A. Dyatko, in *Proceedings of the 6th International Science Seminar on Nonequlibrium Processes and Applications, Minsk, 2002*, p. 15.
10. G. M. Grigorian, B. M. Dymshits, and Yu. Z. Ionikh, Opt. Spektrosk. **65**, 766 (1988) [Opt. Spectrosc. **65**, 452 (1988)].
11. N. A. Dyatko, I. V. Kochetov, A. P. Napartovich, *et al.*, Teplofiz. Vys. Temp. **22**, 1048 (1984).
12. J. L. Pack, R. E. Voshall, A. V. Phelps, and L. E. Kline, J. Appl. Phys. **71**, 5363 (1992).
13. A. A. Mityureva and V. V. Smirnov, J. Phys. B **27**, 1869 (1994).
14. V. Yu. Baranov, V. M. Borisov, F. I. Fysikaĭlo, *et al.*, Preprint No. 3080 (Kurchatov Inst. Atomic Energy, Moscow, 1979).
15. I. V. Kochetov, V. G. Pevgov, L. S. Polak, and D. I. Slovetskiĭ, *Plasmochemical Reactions*, Ed. by L. S. Polak (Inst. Neftekhim. Sint., Akad. Nauk SSSR, Moscow, 1979), p. 28.
16. J. E. Land, J. Appl. Phys. **49**, 5716 (1978).
17. H. Ehrhardt, L. Langhans, F. Linder, and H. S. Taylor, Phys. Rev. **173**, 222 (1968).
18. G. N. Haddad and H. B. Milloy, Aust. J. Phys. **36**, 473 (1983).
19. N. L. Aleksandrov, I. V. Kochetov, and A. P. Napartovich, Khim. Vys. Energ. **20**, 291 (1986).
20. N. L. Aleksandrov, A. M. Konchakov, and E. E. Son, Zh. Tekh. Fiz. **49**, 1200 (1979) [Sov. Phys. Tech. Phys. **24**, 664 (1979)].
21. N. A. Dyatko, I. V. Kochetov, A. P. Napartovich, and M. D. Taran, Preprint No. 3842/12 (Kurchatov Inst. Atomic Energy, Moscow, 1983).
22. D. I. Slovetskiĭ, in *Plasma Chemistry*, Ed. by B. M. Smirnov (Énergoatomizdat, Moscow, 1984), Vol. 11, p. 213.
23. E. E. Ivanov, Yu. Z. Ionikh, N. P. Penkin, *et al.*, Khim. Fiz. **7**, 1694 (1982).
24. G. M. Grigorian and Yu. Z. Ionikh, Khim. Vys. Energ. **23**, 548 (1989).
25. A. I. Maksimov, L. S. Polak, D. I. Slovetskiĭ, *et al.*, Khim. Vys. Energ. **13**, 358 (1973).
26. G. M. Grigorian, in *Proceedings of the All-Russian Conference on Physics of Low-Temperature Plasma, Petrozavodsk, 2002*, p. 86.
27. S. Toby, Int. J. Chem. Kinet. **16**, 149 (1984).
28. F. Slanger and G. Black, J. Chem. Phys. **53**, 3722 (1970).
29. S. De Benedictis, M. Capitelli, F. Gramarossa, *et al.*, Opt. Comm. **47**, 107 (1983).

30. S. De Benedictis, C. Gorse, M. Cachiatori, *et al.*, Chem. Phys. Lett. **96**, 674 (1983).
31. S. De Benedictis, F. Gramarossa, R. D'Agostino, *et al.*, J. Phys. D **18**, 413 (1985).
32. L. S. Polak and D. I. Slovetsky, Int. J. Radiat. Phys. Chem. **8**, 2577 (1975).
33. E. E. Ivanov, Yu. Z. Ionikh, N. P. Penkin, *et al.*, Khim. Fiz. **7**, 1684 (1988).
34. J. E. Velzco, J. H. Kolts, and D. W. Setser, J. Chem. Phys. **69**, 4357 (1978).
35. J. Balamuta and M. F. Golde, J. Chem. Phys. **79**, 2430 (1982).
36. P. O. Clark and J. J. Wada, J. Quant. Electron. **4**, 267 (1968).
37. B. A. McArthur and J. Tulip, Rev. Sci. Instrum. **88**, 722 (1980).
38. D. Stedman and D. Setser, J. Chem. Phys. **52**, 3957 (1970).
39. M. Tsuji, K. Yamaguchi, and Y. Nishimura, Chem. Phys. **125**, 337 (1988).

Translated by G.V. Shepekina

Plasma Physics Reports, Vol. 29, No. 8, 2003, pp. 717–726. Translated from Fizika Plazmy, Vol. 29, No. 8, 2003, pp. 775–784.

LOW-TEMPERATURE PLASMA

Shape of the Current Tube of a Negative Point-to-Plane Corona in Air

Yu. S. Akishev, M. E. Grushin, V. B. Karal'nik, A. E. Monich, and N. I. Trushkin

Troitsk Institute for Innovation and Fusion Research, State Scientific Center of the Russian Federation, Troitsk, Moscow oblast, 142190 Russia

Received November 4, 2002; in final form, January 13, 2003

Abstract—Results are presented from the experimental studies of a negative point-to-plane air corona discharge with controlled geometry. It is shown that, in a certain range of parameters, the steady-state current–voltage characteristic of the corona can be fitted by a parabola. The results obtained are used to determine the time-averaged shape of the current tube of a negative corona. *© 2003 MAIK "Nauka/Interperiodica".*

1. INTRODUCTION

Point–plane electrode geometry is often used to produce a negative corona in atmospheric-pressure air. A quantitative description of such a corona is rather difficult because of the three-dimensional character and very complicated charge kinetics of the corona discharge.

A negative corona in air is generally non-steady-state and exists in the form of periodic current pulses (Trichel pulses [1]). In experiments, the time-averaged corona current is usually measured. The relation between the time-averaged corona current I and the applied voltage U (i.e., the steady-state current–voltage characteristic) is the integral Ohm's law for a discharge gap, which, from the electrotechnical standpoint, can be regarded as an inhomogeneous and nonlinear conductor. Knowledge of the time-averaged current–voltage characteristic is important for many practical applications, in particular, engineering calculations of various gas-discharge devices based on a negative corona in air.

To date, a large number of mathematical methods for calculating the time-averaged current–voltage characteristic of a negative corona have been developed (see review [2]). These methods are commonly based on simplified physical concepts of the structure of a negative corona in air. It is assumed that the corona is steady-state and consists of two regions: a narrow generation zone, which is adjacent to the point electrode, and a negatively charged drift region, which occupies the entire discharge gap. In the former region, ionization processes dominate, whereas in the latter, ionization is absent and the current is carried by negatively charged ions. The current–voltage characteristic is only calculated for the corona drift region. To simplify computations, it is usually suggested that the configuration of the electric field lines in the drift region differs slightly from the initial field line configuration in the gap.

The most doubtful point of the above methods is the (at first glance, quite obvious) assumption that the boundary of the steady-state drift region is closely adjacent to the surface of the corona point electrode. The problem is that an actual corona pulsates and a significant contribution to the total corona current is made by the displacement current [3, 4]. In this case, the discharge region in which the electric field varies greatly with time ($\delta E/\bar{E}$ is on the order of or even much higher than one, where δE and $\bar{E}$ are the fluctuating and average local electric fields, respectively) can be rather extended and can occupy not only the generation zone but also part of the drift region. Indeed, two-dimensional numerical simulations of a negative point-to-plane corona [4] showed that, in the pulsation regime, the distance between the boundary of the quasi-steady drift region (in which $\delta E/\bar{E} \ll 1$ and the field can be regarded as nearly steady-state) and the point electrode significantly exceeds the point radius.

The above circumstance indicates that the correct calculation of the averaged current–voltage characteristic of a pulsating corona in a steady-state model is not so easy matter as it seems at first glance, because it requires a priori information about the position of the boundary of the drift region with respect to the point electrode. Taking into account this circumstance is of particular importance when calculating negative coronas in narrow (a few centimeters long) gaps, because, in this case, the transient region with a non-steady-state electric field can occupy a significant fraction of the gap.

The above problem about the boundary of the quasi-steady drift region can be resolved using the results of dynamic calculations in the two-dimensional numerical model [4], which most comprehensively incorporates the actual charging processes. Such calculations are extremely important for revealing the physics of negative coronas; however, they are very cumbersome and time-consuming, which impedes their wide use in practice. Nevertheless, the calculations of the current–voltage characteristic of the steady-state drift region can be

1063-780X/03/2908-0717$24.00

significantly simplified using the concept of the effective current tube averaged over time and radius.

Obviously, the time-averaged current density monotonically decreases with distance from the axis of the point–plane gap; however, we can assume that the entire current in the drift region flows inside a finite-size tube and the corona parameters are uniform over the tube cross section. The current tube in the drift region begins at a certain distance x_0 from the point electrode and monotonically broadens with distance from it. Information about the cross-sectional area $S(x)$ of the effective current tube and the position x_0 of its boundary is of great importance not only for computing the current–voltage characteristic, but also for various practical applications of a corona discharge (e.g., in electrostatic precipitators).

One of the first studies in which the concept of a current tube was introduced is a paper by Sigmond [5]. In that paper, the current–voltage characteristic of a negative corona at voltages higher than the corona ignition voltage was analytically estimated. However, the shape of the current tube was not studied and, in calculations, only information about the effective tube area (at a level of 0.5) at the anode was used.

The calculations were based on the equation for the evolution of the charge density $\rho(t)$ of an ion cloud that has a constant mobility μ_i and drifts along the electric field lines:

$$\frac{1}{\rho(t)} - \frac{1}{\rho_0} = \frac{\mu_t}{\varepsilon_0}(t - t_0), \tag{1}$$

where t is the time during which the ion cloud moves along the field line from the boundary of the drift region near the point electrode (this motion begins at the instant $t_0 = 0$), $\rho_0 = \rho(t_0)$ is the charge density at the starting point, and ε_0 is the permittivity of free space. Equation (1) is valid for the drift region, in which no charged particles are either produced or lost and the ion density changes only due to a change in the cross-sectional area of the corona.

In a three-dimensional corona, the charge density ρ_0 near the tip of the point electrode greatly exceeds its density ρ_a near the plane anode. Hence, it follows from Eq. (1) that

$$\rho_a \cong \frac{\varepsilon_0}{\mu_i}\frac{1}{t_a}; \tag{2}$$

i.e., the ion density near the anode is determined by the time $t_a = \int_0^L \frac{dl}{\mu_i E(l)}$, during which the ion cloud drifts from the point electrode to the anode along a given electric field line. In [5], it was proposed to calculate t_a only for the axial field line, whose length is known: $L = d$, where d is the interelectrode distance. It was assumed that the electric field is homogeneous along the corona axis; i.e., $E_a \cong U/d$, where U is the applied voltage. In this case, we have $t_a \cong \frac{d^2}{\mu_i U}$ and the current density at the center of the anode is $j_0 = \mu_i E_a \rho_a \cong \frac{\mu_i \varepsilon_0 U^2}{d^3}$.

In [5], the relationship between j_0 and the total current I was taken from the experiment in which the current density at the center of the anode was measured. It was also assumed that $j_0 \cong I/S_a$, where S_a is the effective area of the current tube at the anode. For sufficiently long discharge gaps ($d \geq 30$ mm), S_a is approximately equal to $2d^2$. As a result, one obtains a simple relation between the current and voltage:

$$I \cong \frac{\mu_i \varepsilon_0 S_a U^2}{d^3}. \tag{3}$$

The concept of the effective current tube was used in 1.5-dimensional calculations of a corona with a fixed point-to-plane distance [3]. However, analysis of the shape of the current tube as a function of the interelectrode distance d and the determination of the distance between the point electrode and the boundary of the quasi-steady drift region were beyond the scope of that study.

In the present paper, we propose a method for determining the effective area of the current tube at anode S_a as a function of d. We also propose a method for determining the position x_0 of the boundary of the steady-state drift region and fitting the longitudinal profile of the cross-sectional area $S(x)$ of the time-averaged current tube for different values of d. The former method can be described as follows. In 1965, Loeb [6] suggested that the time-averaged current–voltage characteristic can be approximated by a universal parabolic dependence

$$I = kU(U - U_0), \tag{4}$$

which can be used to describe the corona current in any geometry. In the case of point–plane geometry, the proportionality factor k and the corona ignition voltage U_0 depend on the tip radius r_0 of the point electrode and the interelectrode distance d.

The key idea of our approach is to express the coefficient k in Eq. (4) in a form similar to that in Eq. (3):

$$I = kU(U - U_0) \cong \frac{\mu_i \varepsilon_0 S_a}{d^3} U(U - U_0). \tag{5}$$

From Eq. (5) one can obtain the effective area of the current tube at the anode,

$$S_a(d, r_0) \cong \frac{k(d, r_0) d^3}{\mu_i \varepsilon_0}, \tag{6}$$

which is seen to be independent of the corona current.

Having measured the current–voltage characteristics for different values of d and r_0, we can determine the corresponding coefficients k and, thus, the effective area S_a of the current tube at the anode as a function of d and r_0. The next step is to employ the steady-state 1.5-dimensional model [3], which allows one to find the longitudinal profile of the cross-sectional tube area $S(x)$ that provides the best fit between the calculated and measured current–voltage characteristics at a given S_a value.

Although the idea of the approach proposed is rather simple, its practical implementation requires that special measures be taken to reduce an uncontrolled change in the shape of the current tube when determining the current–voltage characteristic. The literature data on the dependence of the coefficient k on the interelectrode distance d and the tip radius r_0 of the point electrode show that such an uncontrolled change is quite probable. For example, in [7], the experimental current–voltage characteristics of negative coronas ignited on very thin needles ($0.003 \le r_0 \le 0.035$ mm) were fitted by the scaling

$$I(\mu\text{A}) \cong \frac{52}{d^2(\text{mm})} U(\text{kV})(U - U_0); \quad (7)$$

i.e., $k \sim 1/d^2$.

In [2], another scaling was proposed for corona discharges ignited on massive and sharply tapered rods:

$$I(\mu\text{A}) \cong \frac{3}{d(\text{mm})}\left(1 + \frac{42}{d}\right)\frac{1}{(1 - 0.15r_0(\text{mm}))^2} \times U(\text{kV})(U - U_0); \quad (8)$$

i.e., $k \sim 1/d^2$ for small d and $k \sim 1/d$ for large d.

In [5], the following analytic dependence of I on U was obtained:

$$I(\mu\text{A}) \cong \frac{4}{d(\text{mm})} U^2(\text{kV}). \quad (9)$$

When obtaining this dependence, the ion mobility in formula (3) was assumed to be equal to the generally accepted mobility of negative ions in atmospheric air, $\mu_i = 2.25 \times 10^{-4}$ m^2/(V s); i.e., $k \sim 1/d$.

A comparison of the currents given by the above scalings at the same values of U and d shows that, depending on the gap length, the difference between these currents can attain one order of magnitude. In this context, a question arises about the reasons for such a discrepancy and cautions that should be undertaken to provide unambiguous experimental results.

In the papers cited above, coronas with different shapes of the point electrodes and different point-to-plane distances were investigated. Thus, in [7], low-current ($I < 30$ μA) corona discharges in narrow interelectrode gaps ($d \le 15$ mm) were studied. In [2], experiments were carried out with longer interelectrode gaps ($d \ge 50$ mm) and currents of up to $I \cong 150$ μA. Sigmond [5] studied corona discharges at large d and high currents (which, in [5], were referred to as corona saturation currents).

However, the discrepancy between the above scalings is mainly related to the uncontrolled change in the shape of the current tube of a corona discharge rather than to the different ranges of the currents and interelectrode distances. We remember that, for a negative point-to-plane corona, there are two geometrical effects related to the cathode shape that can lead to an uncontrolled change in the shape of the current tube. One of them stems from the fact that the corona spot is not always localized at the very tip of the point electrode [6, 8]. Moreover, the cathode spot usually does not remain on one place: the larger the tip radius of the point electrode, the larger the area within which the cathode spot moves. The fast motion of the cathode spot around the tip of the corona electrode is usually observed for the point electrodes with a relatively large radius of curvature ($r_0 \ge 0.3$ mm). By the way, it is the unsteady position of the cathode spot that results in the known effect of a hissing corona.

Another effect is related to the fact that additional cathode spots can arise on the side surface of the cathode. The number of these spots increases with the applied voltage. These running spots increase the transverse size of the current tube; hence, the corona current also increases, although the applied voltage is fixed. This effect is especially pronounced at large interelectrode gaps ($d \ge 30$ mm) and large (≥3 mm) longitudinal and transverse dimensions of the corona electrode. Because of this effect, the corona currents differ greatly in different experiments even at the same values of r_0 and d. Unfortunately, in the literature devoted to the measurements of the current–voltage characteristics, this effect did not receive proper attention and no information about the side surface area of the corona electrode (especially, a massive one) occupied by running cathode spots was presented.

In experiments, the former effect is difficult to control. One can only reduce its influence by decreasing the tip radius of the corona point electrode. However, the influence of the latter effect on the corona current–voltage characteristic can be eliminated. For this purpose, a metallic ball 12–16 mm in diameter was set on the corona point electrode (see Fig. 1). The length of the prominent part of the electrode was approximately the ball radius. For larger interelectrode distances, it was required to somewhat increase the ball diameter. This method allowed us to avoid the generation of cathode spots on the side surface of the point electrode over the entire range of the interelectrode distances and for all of the corona discharge regimes under study.

There is also one more effect the ignorance of which can result in different corona currents at the same values of r_0, d, and U. This effect is related to the trans-

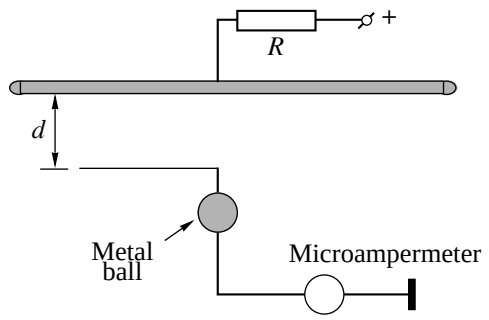

Fig. 1. Schematic of the measurements of the current–voltage characteristic of a negative point-to-plane corona with the controlled geometry of the current tube.

verse dimensions of the anode plate, whose characteristic size should be no less than 3*d* [9]. The decrease in the anode transverse size to less than 3*d* leads to a decrease in the corona current; the smaller the anode diameter, the larger the decrease.

The aim of this study is to find the numerical coefficients for a parabolic fit of the measured current–voltage characteristic of a negative corona with controlled discharge geometry. These data are used to determine the boundary position and shape of a time-averaged current tube that can be used to describe the drift region of a negative point-to-plane corona in a 1.5-dimensional model.

2. EXPERIMENTAL SETUP AND RESULTS

Figure 1 shows a schematic of the measurements of the current–voltage characteristic of a corona with the controlled geometry of the current tube. The interelectrode distance could be varied from 1.5 to 150 mm. A needle with a diameter of no larger than 2.2 mm (in most cases, the diameter was 0.5 mm) and small tip radius (typically, r_0 = 0.06 mm) was used as a corona electrode.

Besides the geometry of the discharge, the corona current also depends on the temperature *T*, pressure *P*, and air humidity. Variations in these parameters (first of all, the pressure and humidity) were governed by atmospheric conditions. The experiments were carried out at an air temperature of $T = 19 \pm 3$°C, a pressure of $P = 740 \pm 15$ torr, and a relative humidity of 60 ± 15%. Within these ranges, the corona current deviated from its average value by no more than 10%, all other conditions being the same.

The reduced current–voltage characteristics of a negative corona in air for different values of r_0 and *d* are shown in Figs. 2–4. A significant effect of the humidity on the current–voltage characteristic is illustrated in Fig. 2, which presents the data obtained for very dry air in which the partial pressure of water vapor corresponded to a dew-point temperature of –50°C.

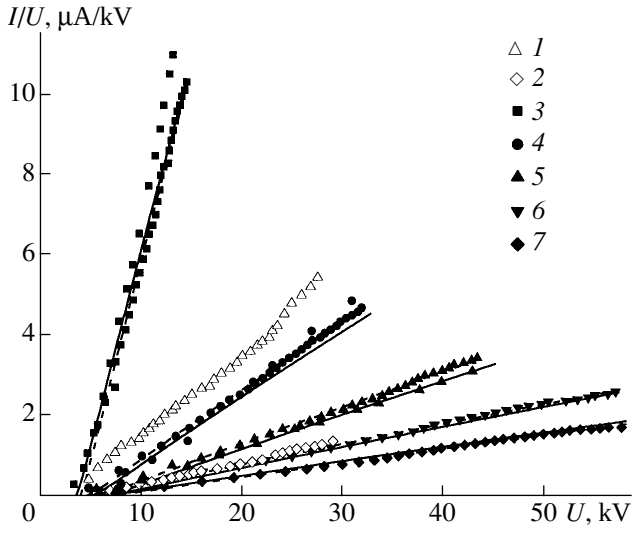

Fig. 2. Measured and calculated reduced current–voltage characteristics of a negative point-to-plane corona in dry air for *d* = (*1*) 50 and (*2*) 100 mm and room air for *d* = (*3*) 10, (*4*) 30, (*5*) 50, (*6*) 75, and (*7*) 100 mm. The needle-tip radius is r_0 = 0.06 mm. The symbols and the fitting dashed lines show the results of measurements. The calculations by the 1.5-dimensional model are represented by the solid lines.

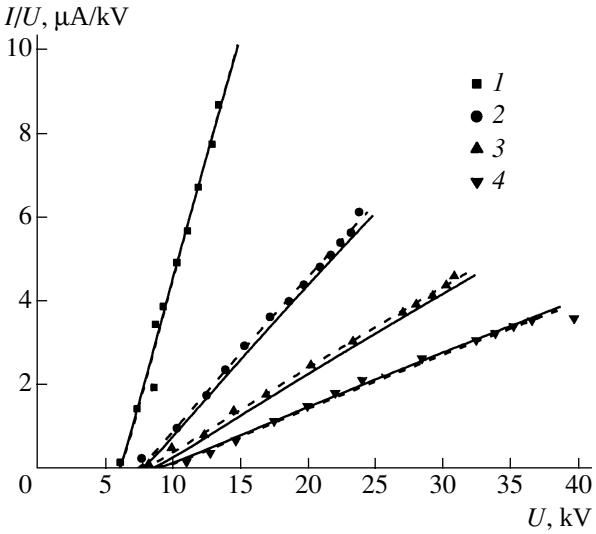

Fig. 3. Measured and calculated reduced current–voltage characteristics of a negative point-to-plane corona in room air for *d* = (*1*) 10, (*2*) 20, (*3*) 30, and (*4*) 40 mm. The needle-tip radius is r_0 = 0.275 mm. The symbols and the fitting dashed lines show the results of measurements. The calculations by the 1.5-dimensional model are represented by the solid lines.

3. FITTING OF THE CURRENT–VOLTAGE CHARACTERISTIC AND THE SHAPE OF THE CURRENT TUBE

The current–voltage characteristic of a negative corona in room air was fitted by the generally adopted expression $I = kU(U - U_0)$. Here, the factor k characterizes the slope of the so-called reduced current–voltage characteristic (remember that reduced current–voltage characteristic is the dependence of I/U on U, which is close to linear). The reduced current–voltage characteristic was fitted by a linear function $I/U = k(U - U_0)$ by using the least squares method.

We processed a great number of current–voltage characteristics measured under different experimental conditions (see Figs. 2–4). As a result, we propose the following fit for the time-averaged current–voltage characteristic:

$$I \cong \frac{2.92}{d}\left(1 + \frac{22.6}{d}\right)\left(1 + \ln\frac{r_0}{0.06}\right)^{1/8} \times \left(\exp\left(\frac{4r_0}{d}\right)\right)U(U - U_0), \quad (10)$$

where the current I is in μA, the voltage U is in kV, and the interelectrode distance d and the tip radius of the point electrode r_0 are in mm.

The range of applicability of this fit is $I \le 150$ μA, $d \le 100$ mm, and $r_0 \le 1.1$ mm. The deviation of the current calculated by formula (10) from the experimental one does not exceed 10%. The degree to which the fitting factor k is close to the value k_{exp} determined from the slope of the measured current–voltage characteristic can be seen in Fig. 5, in which both the measured values of k and those calculated by formula (10) are presented as a function of d for different needle-tip radii.

It can be seen that, in formula (10), the dependence of the factor k on the interelectrode distance for large and small values of d is in qualitative agreement with the corresponding dependence in formulas (7)–(9). As for quantitative agreement, our fit at small d is close to formula (7) but significantly differs from formula (8) because the latter is inapplicable for small interelectrode gaps. At an interelectrode distance of $d \cong 50$ mm, which is in the range of applicability of both (8) and (10), formula (8) gives somewhat higher currents at the same experimental conditions. As was mentioned above, this may be related to an uncontrolled change of the current tube in [2]. Indeed, according to the private communication of I.P. Vereshchagin, in those experiments, additional cathode spots were observed on the side surface of a massive cathode, which resulted in an increase in the corona current at a fixed applied voltage. In the case of thin needles ($4r_0/d \ll 1$), large interelectrode distances d, and high voltages ($U \gg U_0$), our fit is close to Sigmond's formula (9).

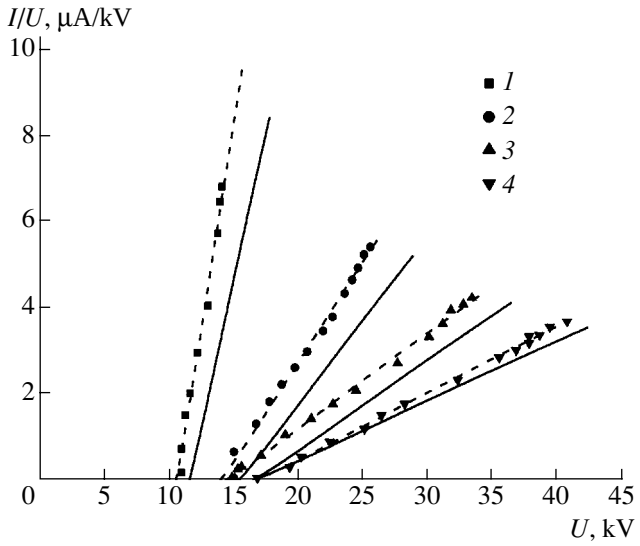

Fig. 4. Measured and calculated reduced current–voltage characteristics of a negative point-to-plane corona in room air for d = (*1*) 10, (*2*) 20, (*3*) 30, and (*4*) 40 mm. The needle-tip radius is r_0 = 1.1 mm. The symbols and the fitting dashed lines show the results of measurements. The calculations by the 1.5-dimensional model are represented by the solid lines.

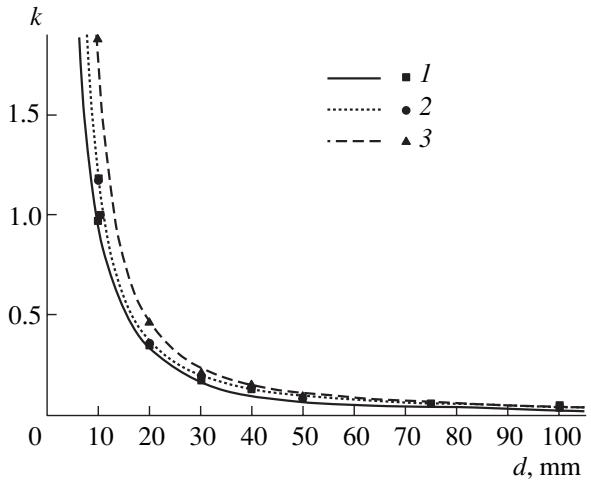

Fig. 5. Comparison of the fitted values of the factor k (curves) with the factor k_{exp} (symbols) determined from the slope of the measured current–voltage characteristic of a negative point-to-plane corona in room air for different needle-tip radii: r_0 = (*1*) 0.06, (*2*) 0.275, and (*3*) 1.1 mm.

Thus, using expressions (6) and (10), we can determine the area of the current tube on the anode for a negative point-to-plane corona in air:

$$S_a(d) \cong 1.46\left(1 + \ln\frac{r_0}{0.06}\right)^{1/8}\left(\exp\left(\frac{4r_0}{d}\right)\right)d(22.6 + d), \quad (11)$$

where r_0 and d are in mm. The dependence of S_a on d for different needle-tip radii is shown in Fig. 6.

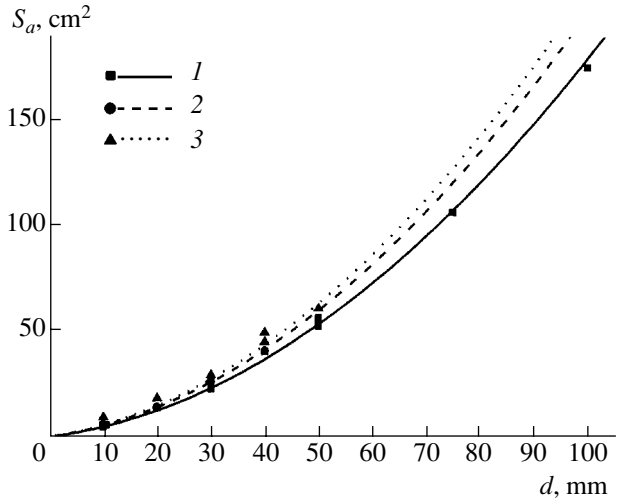

Fig. 6. Area S_a of the current tube on the anode vs. the interelectrode distance d for different needle-tip radii: r_0 = (*1*) 0.06, (*2*) 0.275, and (*3*) 1.1 mm. The symbols show the experimental results, and the curves show the results of calculations by formula (11).

In our opinion, the factor $\left(1 + \ln\frac{r_0}{0.06}\right)^{1/8}\exp\left(\frac{4r_0}{d}\right)$ reflects the increase in the transverse size of the time-averaged current tube with increasing r_0 due to the increase in the area on the needle tip within which the cathode spot moves. The presence of this factor indicates that the tip of the needle electrode cannot be regarded as a structureless point, as is sometimes done in the literature. The fact that the position of the cathode spot is not fixed results in the additional widening of the time-averaged current tube. This widening is most pronounced at large needle-tip radii. The reason why the cathode spot of a negative corona is not fixed to the very tip of a needle electrode with a relatively large tip radius, but moves around it, is still unknown.

Formula (11) for the area of the current tube on the anode was used in 1.5-dimensional numerical calculations of the current–voltage characteristic. The results of these calculations were used to find the cross-sectional area S of the current tube in a point–plane gap as a function of x.

4. CALCULATION OF THE CURRENT–VOLTAGE CHARACTERISTIC AND COMPARISON OF THE CALCULATED RESULTS WITH THE MEASUREMENTS AND FITS

The time-averaged current–voltage characteristic of a negative corona in air was calculated using the 1.5-dimensional model developed in [3]. An axisymmetric point-to-plane corona was represented by a current tube expanding away from the point electrode. In each cross section of the discharge, the corona parameters were assumed to be uniform and steady-state. Since a real corona pulsates and the discharge parameters near the point electrode change periodically in time, the boundary of the quasi-steady drift region, in which $\delta E/\bar{E} \ll 1$ and the electric field can be treated as steady-state, should be set at a sufficiently large distance from the point electrode. The dynamic calculations of a pulsating corona discharge [3, 4, 10] and the dynamic measurements of the glow intensity near the point electrode [11] under different discharge conditions show that this distance is no less than 1.5 mm, which is much larger than the thickness of the generation zone and the length of the transient region in which negative ions are produced due to electron attachment. In this case, in order to calculate the corona parameters, it is sufficient to use the time-independent equations describing the drift of negative ions in the quasi-steady region. This means that the drift region of the corona is only modeled. The voltage drop across the generation zone and the transient region, which, according to estimates, was about ~500 V, was included in the total voltage balance.

Basic equations for the current density $j(x)$ and electric field $E(x)$ in the drift region have the form

$$\frac{d}{dx}(S(x)j(x)) = 0, \quad \frac{1}{S(x)}\frac{d}{dx}(S(x)E(x)) = \frac{\rho(x)}{\varepsilon_0}, \quad (12)$$

where $\rho(x) = \frac{j(x)}{\mu_i E(x)}$ is the space-charge density averaged over the cross section of the current tube. The tip of the point electrode is at $x = 0$, and the anode coordinate is $x = d$.

The cross section of the current tube $S(x)$ as a function of the distance from the point electrode was described by a quadratic dependence, such that, at $x = d$, $S(d)$ is equal to the value of S_a given by formula (11):

$$S(x) = S_0 + \left[\alpha\frac{x - x_0}{d - x_0} + (1 - \alpha)\left(\frac{x - x_0}{d - x_0}\right)^2\right](S_a - S_0), \quad (13)$$

where x_0 corresponds to the boundary of the drift region and x_0 and α are the fitting parameters that provide the best match between the calculated and measured current–voltage characteristics. The first term in square brackets corresponds to the rapid increase in the current-tube radius $R(x)$ with distance from the point electrode ($R \sim \sqrt{x/d}$, where $x/d < 1$). The second term is linear in x; hence, it corresponds to a slower increase in R at $x/d < 1$.

From Eqs. (12), we find the electric field profile along the current tube:

$$E(x) = \frac{1}{S(x)}\sqrt{(S_0E_0)^2 + \frac{2I}{\varepsilon_0\mu_i}\int_{x_0}^{x} S(\xi)d\xi}, \quad (14)$$

where $I = j(x)S(x)$ is the corona current, $\mu_i = 2.25 \times 10^{-4}$ m^2/(V s) is the generally adopted mobility of neg-

ative ions in atmospheric air [2], and $S_0 \cong 2\pi(r_0 + x_0)^2$ and $E_0 \cong 30$ kV/cm are the current-tube cross section and the electric field at the boundary of the drift region on the side of the point electrode at the distance $x = x_0$ from it. Actually, the equipotential surfaces near the point electrode are close to hemispheres, which is reflected in the expression for the effective area S_0. The chosen value of E_0 is an estimate from above for the electric field; below this value, the ionization rate is lower than the attachment rate and no electrons are generated in the drift region. Approximately the same electric field is usually taken as a boundary value on the surface of a corona point electrode in the calculations cited in [2].

The discharge voltage is determined by the formula

$$U \cong \int_{x_0}^{d} E(x)dx + 500. \quad (15)$$

The results of calculations of the reduced current–voltage characteristic of a corona discharge for different interelectrode distances and needle-tip radii are shown in Figs. 2–4 by the solid lines.

The obtained fitting parameters x_0 and α can be approximated by the following expressions

$$x_0 \cong d_0(1 - A_x \exp(-B_x d)),$$
$$\alpha \cong 1 - \exp\left(-\left(\frac{d - d_0}{D}\right)^{A_\alpha}\right) - B_\alpha \exp\left(-\left(\frac{d - d_0}{D}\right)\right), \quad (16)$$

where $d_0 = 3.3$ mm, $D = 65$ mm, all the other spatial dimensions are in mm, $A_x = 0.79$, $B_x = 3.26 \times 10^{-2} - 2.46 \times 10^{-2}\exp(-3r_0)$, $A_\alpha = 0.66 - \dfrac{0.24}{1 + \exp\left(\dfrac{0.7 - r_0}{0.13}\right)}$, and $B_\alpha = 0.95 - 0.96\exp(-0.81r_0)$.

Figures 7 and 8 compare the obtained fitting parameters x_0 and α with the values given by formulas (16). We note that the physics underlying the obtained dependences of x_0 and α on d is beyond the scope of this study. The advantage of formulas (16) is that, setting r_0 and d, we can determine the cross-sectional area of the current tube $S(x)$ by formula (13) and thus calculate the current–voltage characteristic of a negative corona with a point electrode that has no unsteady cathode spots on its side surface.

The calculated cross-sectional area of the current tube for different values of r_0 and d is shown in Figs. 9 and 10. We note that, for a large needle-tip radius and small interelectrode distance (1.1 and 10 mm, respectively), the calculated cross-sectional area of the current channel varies nonmonotonically with the distance from the cathode (see Fig. 9): first, it slightly narrows and, then, expands. Probably, this is an artifact that stems from the insufficiently tight localization of the current spot in experiments with a blunt needle electrode. In this case, the difference between the instantaneous cross section of a real current tube that rests on an unfixed cathode spot and the cross section within which a real current tube fluctuates turns out to be so large that the use of the concept of the effective (i.e., time-averaged and uniform over the cross section) current tube no longer reflects the actual situation near the point electrode.

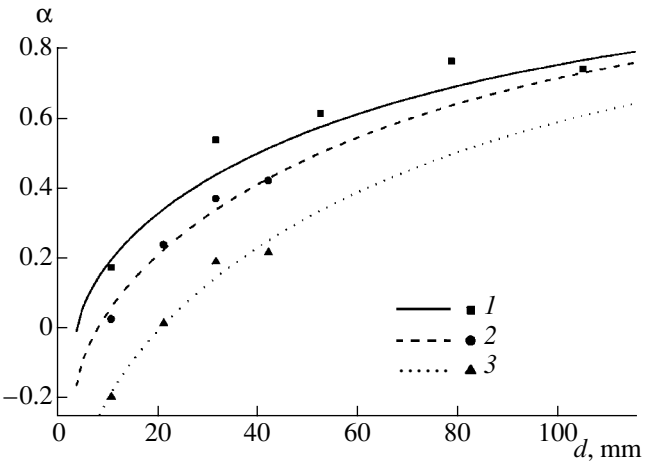

Fig. 7. The parameter α as a function of the interelectrode distance d for different needle-tip radii: r_0 = (*1*) 0.06, (*2*) 0.275, and (*3*) 1.1 mm. The symbols show the values of α that were used to fit the experimental results, and the curves show the approximation by the second formula in (16).

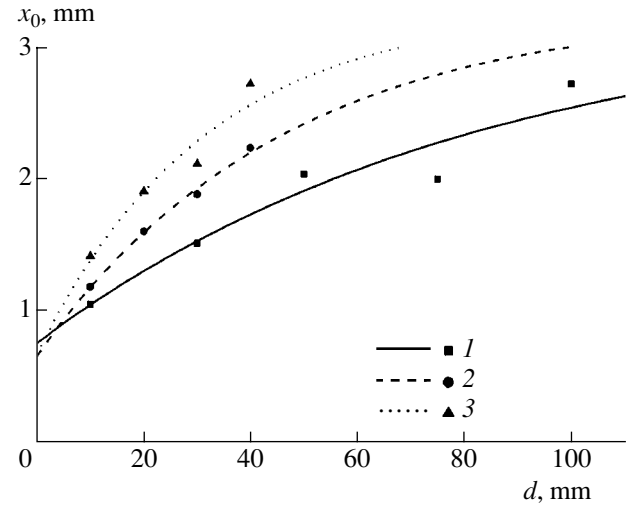

Fig. 8. The parameter x_0 as a function of the interelectrode distance d for different needle-tip radii: r_0 = (*1*) 0.06, (*2*) 0.275, and (*3*) 1.1 mm. The symbols show the values of x_0 that were used to fit the experimental results, and the curves show the approximation by the first formula in (16).

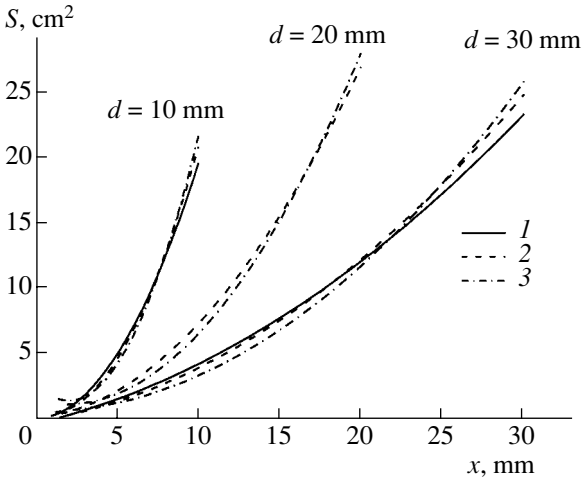

Fig. 9. Axial profiles of the cross-sectional area $S(x)$ of the current tube of a corona discharge for r_0 = (*1*) 0.06, (*2*) 0.275, and (*3*) 1.1 mm and d = 10, 20, and 30 mm. The ordinates of the curves corresponding to d = 10 and 20 mm are magnified by factors of 4 and 2, respectively, as compared to their true values.

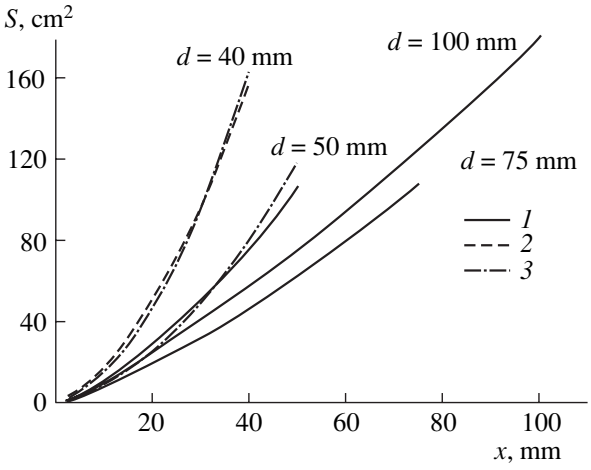

Fig. 10. Axial profiles of the cross-sectional area $S(x)$ of the current tube of a corona discharge for r_0 = (*1*) 0.06, (*2*) 0.275, and (*3*) 1.1 mm and d = 40, 50, 75, and 100 mm. The ordinates of the curves corresponding to d = 40 and 50 mm are magnified by factors of 4 and 2, respectively, as compared to their true values.

5. DISCUSSION

It can be seen from the first formula in (16) that the boundary beyond which the drift region can be regarded as steady-state is located at a sufficiently large distance from the point electrode and that this distance increases with the interelectrode distance. Between the point electrode and the quasi-steady drift region, the electric field of an actually pulsating corona varies strongly with time. An important role in closing the electric current through this gap is played by the displacement current. The period-averaged displacement current is zero; however, its amplitude can exceed or be on the order of the conduction current. Hence, the use of the steady-state approximation to calculate this part of the discharge is indeed incorrect.

Using the obtained value of S_0, the amplitude of the displacement current in this gap can be estimated from below as

$$I \cong \frac{\varepsilon_0 E_0 S_0}{T} = 2\pi\varepsilon_0 E_0 x_0^2 f,$$

where T and f are the period and frequency of the current pulsations of a negative corona in air. It can be seen that the current is proportional to the pulsation frequency, which is in agreement with experiment [1, 12]. For $x_0 \cong 2$ mm and $f \cong 100$ kHz, the displacement current amounts to ~70 μA, which is typical of a negative point-to-plane corona at this frequency.

Note that, as the interelectrode distance increases, the variations in the shape of the current tube cannot be described by a self-similar dependence because the coefficients that characterize the parabolic dependence $S(x)$ in expression (13) depend on d. In other words, the configurations of the current tubes are not geometrically similar at different d. It is impossible to match the calculated and experimental results using a self-similar model. These results also cannot be matched by formally placing the boundary of the steady-state drift region on the surface of the needle tip.

Analysis of the shape of the current tube as a function of d shows that, at small gap lengths, the main fraction of the gap is occupied by a weakly expanding current tube with a field slowly decreasing with distance from the boundary of the drift region. At large interelectrode distances, the tube strongly expands from the very beginning, which corresponds to a rapid decrease in the field with increasing distance from the boundary; as a result, the electric field in the major part of the interelectrode gap is low. Such a behavior of the shape of the current tube and the electric field in the gap agrees with an experimentally observed abrupt decrease in the threshold current at which the corona transforms into a spark (see, e.g., [9]) as the interelectrode distance decreases.

The results obtained reveal an interesting feature of a negative point-to-plane corona for which the condition $r_0/d \ll 1$ is satisfied. It follows from the second formula in (16) that, as d increases, α approaches unity. This corresponds to a linear increase in the cross-sectional area of the current tube of a point-to-plane corona with increasing x, as is the case with a coaxial wire–cylinder corona discharge. In this case, we obtain an analytic expression for the current–voltage characteristic of a point-to-plane corona that is mathematically equivalent to the current–voltage characteristic of a coaxial corona.

Remember that, under the assumption that the coaxial corona is homogeneous and steady-state, its cur-

rent–voltage characteristic is described by the transcendental expression [2, 13, 14] (the voltage drop across the generation zone is neglected):

$$U \cong E_0 r_0 \left\{ \sqrt{1+bR^2} - 1 - \ln\left(\frac{1+\sqrt{1+bR^2}}{1+\sqrt{1+br_0^2}} \frac{r_0}{R} \right) \right\}, \quad (17)$$

where $b = \dfrac{I}{2\pi\varepsilon_0\mu_i r_0^2 E_0^2}$; I is the corona current per unit length of the cylinders; R and r_0 are the radii of the outer and inner cylinders, respectively; and E_0 is the electric field at the corona electrode. In view of the results obtained, we note that the use of r_0 as the boundary of the steady-state drift region of a real pulsating coaxial corona is incorrect.

In the low-current limit ($I \longrightarrow 0$, br_0^2, and $bR^2 \ll 1$), expression (17) transforms into the linear Townsend formula [15]

$$I \cong \frac{8\pi\varepsilon_0\mu_i}{R^2 \ln(R/r_0)} U_0 (U - U_0), \quad (18)$$

where $U_0 = E_0 r_0 \ln(R/r_0)$ is the corona ignition voltage.

At high currents ($I \longrightarrow \infty$, bR^2, and $br_0^2 \gg 1$), the current–voltage characteristic (17) is quadratic in voltage and is similar to the current–voltage characteristic obtained by Sigmond [5] for the so-called corona saturation regime:

$$I \cong \frac{2\pi\varepsilon_0\mu_i}{R^2} U^2. \quad (19)$$

At large d, the steady-state current–voltage characteristic of a point-to-plane corona can easily be derived from Eq. (15) by neglecting the voltage drop across the generation zone:

$$U \cong E_0 d \frac{S_0}{S_a} \left\{ \sqrt{1 + a\left(\frac{S_a}{S_0}\right)^2} - 1 - \sqrt{1-a} \ln\left(\frac{\sqrt{1-a} + \sqrt{1 + a(S_a/S_0)^2}}{1+\sqrt{1-a}} \frac{S_0}{S_a} \right) \right\}, \quad (20)$$

where $a = \dfrac{I}{\varepsilon_0\mu_i E_0^2} \dfrac{d}{S_a}$ and I is the total corona current.

A comparison of expressions (17) and (20) shows that, from the mathematical standpoint, the current–voltage characteristic of a point-to-plane corona in wide gaps is similar to the current–voltage characteristic of a coaxial corona. Indeed, in the low-current limit ($I \longrightarrow 0$, $a(S_a/S_0)^2 \ll 1$), the linear Townsend regime can also be derived from formula (20):

$$I \cong \frac{S_a}{2\pi d} \frac{8\pi\varepsilon_0\mu_i}{d^2 \ln(S_a/S_0)} U_0 (U - U_0), \quad (21)$$

where $U_0 = E_0 d \dfrac{S_0}{S_a} \ln\dfrac{S_a}{S_0}$. In the high-current limit ($a \longrightarrow 1$; i.e., the current tends to the limiting current that formally corresponds to the Sigmond saturation current: $I \longrightarrow \dfrac{\varepsilon_0\mu_i E_0^2 S_a}{d}$), we obtain an expression that is quadratic in voltage:

$$I \cong \frac{\varepsilon_0\mu_i S_a}{d^3} U^2. \quad (22)$$

This expression is similar to the Sigmond formula. A comparison of formulas (19) and (22) shows that, under the condition $R = d$ and the same voltages, a point-to-plane corona operating in the Sigmond regime provides the same current as a segment of a coaxial corona with the length $\Delta = \dfrac{S_a}{2\pi d}$ (which is approximately equal to $d/3$).

6. CONCLUSIONS

(i) The point electrode of a negative corona is not, in fact, a structureless point. The unsteady position of the cathode spot on the tip of the point electrode and the expansion of the current area within which the cathode spot moves lead to an uncontrolled increase in the transverse size of the effective current tube. In this paper, a method for suppressing cathode spots on the side surface of the point electrode has been proposed.

(ii) Based on the experimental results obtained with controlled discharge geometry, an analytical fit of the current–voltage characteristic of a negative point-to-plane corona has been proposed. The time-averaged cross-sectional area $S(x)$ of the current tube has been determined, which significantly simplifies the calculation of the steady-state current–voltage characteristic and provides important information about the transverse size of the corona as a function of the gap length.

(iii) It has been shown that, when computing the steady-state current–voltage characteristic of a negative corona in air, it is necessary to take into account the fact that the current of an actual corona pulsates. Because of the presence of a significant displacement current in the vicinity of the point electrode, it is incorrect to assume that the boundary of the steady-state drift region is adjacent to the surface of the point electrode, as is often done in the literature.

(iv) It has been shown that, at large interelectrode distances, the scaling for the current–voltage characteristic of a negative point-to-plane corona is equivalent to

that of a coaxial corona. The conditions are determined under which the currents in these corona discharges are the same.

The results obtained give a general picture of the time-averaged background against which ionization instabilities can develop in a negative diffuse corona. Therefore, this study is a necessary stage in investigating the mechanisms of the origin of the current spots on the electrodes of a negative corona and of the propagation of the current channels across the interelectrode gap.

ACKNOWLEDGMENTS

We are grateful to A.P. Napartovich for useful discussions of the results obtained. This study was supported in part by the Russian Foundation for Basic Research, project no. 02-02-16913.

REFERENCES

1. G. W. Trichel, Phys. Rev. **54**, 1078 (1938).
2. I. P. Vereshchagin, *Corona Discharge in Apparatus of Electron–Ion Technology* (Énergoatomizdat, Moscow, 1985).
3. A. P. Napartovich, Yu. S. Akishev, A. A. Deryugin, *et al.*, J. Phys. D **30**, 2726 (1997).
4. Yu. S. Akishev, I. V. Kochetov, A. I. Loboĭko, and A. P. Napartovich, Fiz. Plazmy **28**, 1136 (2002) [Plasma Phys. Rep. **28**, 1049 (2002)].
5. R. S. Sigmond, J. Appl. Phys. **53**, 891 (1982).
6. L. B. Loeb, *Electrical Coronas* (Univ. of California Press, Berkeley, 1965).
7. W. L. Lama and C. F. Gallo, J. Appl. Phys. **45**, 103 (1974).
8. H. W. Bandel, Phys. Rev. **84**, 92 (1951).
9. Yu. S. Akishev, M. E. Grushin, V. B. Karal'nik, *et al.*, Fiz. Plazmy **29**, 198 (2003) [Plasma Phys. Rep. **29**, 176 (2003)].
10. D. Graf, in *Proceedings of the 3rd International Symposium on High Voltage Engineering, Milan, 1979*, p. 21.
11. M. R. Laan, Uch. Zap. Tartu Gos. Univ., No. 479, 77 (1979).
12. M. R. Amin, J. Appl. Phys. **25**, 627 (1954).
13. N. A. Kaptsov, *Corona Discharge* (Gostekhizdat, Moscow, 1947).
14. J. Q. Feng, J. Electrostatics **46**, 37 (1999).
15. J. S. Townsend, Philos. Mag. **28**, 83 (1914).

Translated by N.N. Ustinovskiĭ